Graduate School ETD Form 9
(Revised 01/14)

PURDUE UNIVERSITY
GRADUATE SCHOOL
Thesis/Dissertation Acceptance

This is to certify that the thesis/dissertation prepared

By Hongkang Zhou

Entitled
The Essential Role of Stat3 in Bone Homeostasis and Mechanotransduction

For the degree of Doctor of Philosophy

Is approved by the final examining committee:

Dr. R. Claudio Aguilar (Chair)	Dr. Jiliang Li
Dr. James Marrs	
Dr. David Stocum	
Dr. Hiroki Yokota	

To the best of my knowledge and as understood by the student in the *Thesis/Dissertation Agreement. Publication Delay, and Certification/Disclaimer (Graduate School Form 32)*, this thesis/dissertation adheres to the provisions of Purdue University's "Policy on Integrity in Research" and the use of copyrighted material.

Approved by Major Professor(s): Dr. Jiliang Li

Approved by: Dr. Simon Atkinson 03/12/2014

Head of the Department Graduate Program Date

THE ESSENTIAL ROLE OF STAT3 IN BONE HOMEOSTASIS AND MECHANOTRANSDUCTION

A Dissertation
Submitted to the Faculty
of
Purdue University
by
Hongkang Zhou

In Partial Fulfillment of the
Requirements for the Degree
of
Doctor of Philosophy

May 2014
Purdue University
Indianapolis, Indiana

For my family and friends

ACKNOWLEDGEMENTS

I would like to give my genuine thanks to my advisor Dr. Jiliang Li for all his help and guidance. During my studies in his lab, Dr. Li is not only a good teacher and a knowledgeable scholar, but also is a nice mentor willing to give some kind suggestions to his students and helping his students' success. I also would like to thank my advisory committee members, Dr. David Stocum, Dr. James Marrs, Dr. Hiroki Yokota, and Dr. Claudio Aguilar for all their help, advice, and guidance in my research project, setting up, and dissertation preparation. I would like to thank Dr. Keith Condon for teaching me many useful histology techniques. I would like to thank Dr. Matthew Allen for training me how to use micro-CT. I would also like to thank Dr. Joseph Wallace for his help and suggestions in biomechanical testing.

I want to thank Dr. Nicoletta Bivi for her help in mechanical loading experimental data measurement and analysis. I also would like to thank Dr. Lei Li for his help in animal tissue processing and teaching me dissecting skills.

I would like to thank our lab technician Li Jiang for teaching me how to use and repair the diamond wire saw. I want to thank our technician Yongqi Yu for his help with sample processing.

I would like to thank our lab graduate students, America Newnum, Evan Himes, Amy Zhang, and Kylie Corry for their valuable help and friendship. I also want to thank our lab undergraduate students, Kaylie Rambo, Kayla Pepelea, Iman Yousif, Layla Mihuti, Amber Brown, Tomas Meijome, Erika Gramelspacher, Ryne Horn, Tyler Nelson, and Wenyao Li for their assistance with my experiments. It made the time I spent in the lab both educational and enjoyable. It is my pleasure to work with them.

I would like to thank the Department of Biology Chairman Dr. Simon Atkinson for his help and support. I also would like to thank the Department of Biology staff members, Sue Merrell and Shari Dowell for their help and encouragement.

TABLE OF CONTENTS

Page

Page

LIST OF TABLES

LIST OF FIGURES

Figure Page

Figure Page

LIST OF ABBREVIATIONS

ABC solution: Avidin-Conjugated Peroxidase

AD-HIES: Autosomal Dominant-Hyper IgE Syndrome

AP: Anterior Posterior

BFR/BS: Bone Formation Rate

BMC: Bone Mineral Content

BMD: Bone Mineral Density

BMP2: Bone Morphogenetic Protein 2

BSA: Bovine Serum Albumin

B.Pm: Bone Perimeter

B.Ar: Bone Area

BV/TV: Bone Volume/Tissue Volume

CC: Coiled Coil Domain

cDNA: Complementary Deoxyribonucleic Acid

CO_2: Carbon Dioxide

Col: Type I Collagen Promoter

$Ca_3(PO_4)_2$: Calcium Phosphate

$Ca(OH)_2$: Calcium Hydroxide

$Ca_{10}(PO_4)_6(OH)_2$: Hydroxyapatite

CNTF: Ciliary Neurotrophic Factor

CTSK: Cathepsin K

CT-1: Cardiotrophin-1

ddH_2O: Double Distilled Water

DI H_2O: Deionized Water

DMSO: Dimethyl Sulfoxide

DNA: Deoxyribonucleic Acid

DMP-1: Dentin Matrix Protein-1

DAB: 3,3´-Diaminobenzidine

dL.Pm: Double Labeled Perimeter

EGF: Epidermal Growth Factor

EtOH: Ethanol

ES: Eroded Surface

E.Pm: Eroded Perimeter

ECL: Enhanced Chemiluminescence

EDTA: Ethylenediaminetetraacetic Acid

ETC: Electron Transport Chain

FBS: Fetal Bovine Serum

FGF: Fibroblast Growth Factor

FSS: Fluid Sheer Stress

FU: Ultimate Force

GAPDH: Glyceraldehyde 3-phosphate dehydrogenase

G-CSF: Granulocyte-Colony Stimulating Factor gp130: Glycoprotein 130

HBSS: Hank’s Buffered Salt Solution

HIES: Hyper Immunoglobulin E Syndrome

H_2O: Water

H_2O_2: Hydrogen Peroxide

H&E: Hematoxylin and Eosin

HRT: Hormone Replacement Therapy

IUACUC: Indiana University Animal Care and Use Committee

IgE: Immunoglobulin E

IL: Interleukin

Ir.L.Th: Inter-Labeled Thickness

IFN: Interferon

JAK: Janus Kinase

KCl: Potassium Chloride

KH_2PO_4: Potassium Phosphate Monobasic

KO: Knockout

LIF: Leukemia Inhibitory Factor

LRP5: Lipoprotein Receptor 5

MAR: Mineral Appositional Rate

MEM: Minimum Essential Medium

MeOH: Methanol

MMP-9: Matrix Metallopeptidase-9

mRNA: Messenger Ribonucleic Acid

μ-CT: Micro-Computed Tomography

MS/BS: Mineralizing Surface/Bone Surface

ML: Medial Lateral

MMA: Methyl Methacrylate

MOI: Moment of Inertia

NaCl: Sodium Chloride

$NaHCO_3$: Sodium Bicarbonate

$Na_2HPO_4 \cdot 7H_2O$: Sodium Phosphate, Dibasic, 7-Hydrate, Crystal

N.Ob: Osteoblast Number

N.Oc: Osteoclast Number

Ob.Pm: Osteoblast Perimeter

Oc.Pm: Osteoclast Perimeter

Oc.S/BS: Osteoclast Surface/Bone Surface

OS: Osteoid Surface

OSM: Oncostatin M

PBS: Phosphate Buffered Saline

PBF: Phosphate Buffered Formalin

PBST: PBS + 0.3% Triton X-100

PCR: Polymerase Chain Reaction

PDGF: Platelet Derived Growth Factor

PIAS: Protein Inhibitor of Activated STAT

PTH: Parathyroid Hormone

pStat3: Phosphorylated Signal Transducer and Activator of Transcription 3 qPCR: Quantitative Polymerase Chain Reaction

RANKL: Receptor Activator of Nuclear Factor Kappa-B Ligand

RNA: Ribonucleic Acid

ROS: Reactive Oxygen Species

RT: Room Temperature

RT-PCR: Real Time-Polymerase Chain Reaction

rMAR: Relative Mineral Appositional Rate

rMS/BS: Relative Mineralizing Surface/Bone Surface

rBFR/BS: Relative Bone Formation Rate/Bone Surface

S: Stiffness

sL.Pm: Single Labeled Perimeter

SDS: Sodium Dodecyl Sulfate

S.E.M.: Standard Error of Mean

SERM: Selective Estrogen Receptor Modulator

Ser727: Serine Residue 727

SH2: Src Homology 2

SOCS: Suppressors of Cytokine Signaling

SOST: Sclerostin

STAT: Signal Transducer and Activator of Transcription

T.Ar: Tissue Area

TB: Toluidine Blue

Tb.N: Trabecular Bone Number

Tb.Sp: Trabecular Bone Separation

Tb.Th: Trabecular Bone Thickness

TBST: Tris Buffered Saline Tween-20

TGF-β: Transforming Growth Factor-β

TRAP: Tartrate Resistant Acid Phosphate

Tw: Tween

Ty705: Tyrosine Residue 705

TYK: Tyrosine Kinase

U: Work to Failure

UV: Ultra Violet Light

VEGF: Vascular Endothelial Growth Factor

WT: Wild Type

LIST OF UNITS

bp: base pairs

°C: degree Celsius

cm: centimeter

dyn: dynes

g: gravity

hrs: hours

Hz: Hertz

lbs: pounds

N: Newtons

Kb: Kilobase

µg: micrograms

µl: microliter

µm: micrometer

mA: milliamps

mins: minutes

mJ: millijoules

ml: milliliter

mm: millimeter

mM: millimole

nm: nanometer

ng: nanogram

p0: phase (n)

rpm: revolutions per minute

sec: second

V: Volts

v: velocity

wks: weeks

ABSTRACT

Zhou, Hongkang. Ph.D., Purdue University, May 2014. The Essential Role of Stat3 in Bone Homeostasis and Mechanotransduction. Major Professor: Jiliang Li.

Signal Transducer and Activator of Transcription 3 (Stat3) is a transcription factor expressed in bone and joint cells that include osteoblasts, osteocytes, osteoclasts, and chondrocytes. Stat3 is activated by a variety of cytokines and growth factors, including IL-6/gp130 family cytokines. These cytokines not only regulate the differentiation of osteoblasts and osteoclasts, but also regulate proliferation of chondrocytes through Stat3 activation. In 2007, mutations of Stat3 have been confirmed to cause a rare human immunodeficiency disease – Job syndrome which presents skeletal abnormalities like: reduced bone density (osteopenia), scoliosis, hyperextensibility of joints, and recurrent pathological bone fractures. Changes in the Stat3 gene alter the structure and function of the Stat3 proteins, impairing its ability to control the activity of other genes. However, little is known about the effects of Stat3 mutations on bone cells and tissues.

To investigate the *in vivo* physiological role of Stat3 in bone homeostasis, osteoblast/osteocyte-specific Stat3 knockout (KO) mice were generated via the Cre-LoxP recombination system. The osteoblast/osteocyte-specific Stat3 KO mice showed bone abnormalities and an osteoporotic phenotype because of a reduced bone formation rate.

Furthermore, inactivation of Stat3 decreased load-driven bone formation, and the disruption of Stat3 in osteoblasts suppressed load-driven mitochondrial activity, which led to an elevated level of reactive oxygen species (ROS) in cultured primary osteoblasts. Stat3 has been found to be responsive to mechanical stimulation, and might play an important role in mechanical signal transduction in osteocytes. To investigate the role Stat3 plays in mechanical signaling transduction, osteocyte-specific Stat3 knockout (KO) mice were created. Inactivation of Stat3 in osteocytes presented a significantly reduced load-driven bone formation. Decreased osteoblast activity indicated by reduced osteoid surface was also found in osteocyte-specific Stat3 KO mice. Moreover, sclerostin (SOST) protein which is a critical osteocyte-specific inhibitor of bone formation, its encoded gene *SOST* expression has been found to be enhanced in osteocyte-specific Stat3 KO mice.

Thus, these results clearly demonstrated that Stat3 plays an important role in bone homeostasis and mechanotransduction, and Stat3 is not only involved in bone-formation-important genes regulation in the nucleus but also in mediation of ROS and oxidative stress in mitochondria.

CHAPTER 1. INTRODUCTION

1.1 Introduction to Bone Structure and Function

The human skeletal system contains a wide variety of bones and cartilage, ligaments, and other connective tissues that stabilize or interconnect them. Bones are more than scaffolds that muscles simply hang from. They support our weight and work together with nerves and muscles to generate precisely controlled movements.

In a typical human adult skeleton, there are 206 bones. However, the number of bones changed with the inclusion of sesamoid bones. At birth, the human bones number 270. The number decreases with fusion. The growth of the skeleton not only decreases the number of bones but also increases the size and proportion of our body. The bony skeleton begins to form about six weeks after fertilization. Subsequently, the bones undergo dramatic change by fusing into fewer but larger bones, in all three dimensions. Bone growth continues through adolescence, and portions of the skeleton will not cease growing until about age 25[101,102]. The entire process is carefully regulated, and abnormal or irregular bone developmental processes will ultimately affect the whole skeletal system and other body systems.

The mature bone structure can be divided into two tightly connected portions: the axial skeleton which consists of the bones of the skull, vertebral column, sternum, and ribs and the appendicular skeleton consisting of the bones of the limbs and the associated bones that connect limbs to the trunk at the shoulders and pelvis. The bones of the skeleton are complex and dynamic organs, which have many functions. First function, both the axial and appendicular skeletons provide structural support for the entire body. Individual bones or groups of bones provide a framework for the attachment of soft tissues and organs. Second function, bones regulate calcium and phosphate contents in body fluids. The calcium and phosphate salts in bones also represent valuable minerals which are vital in body fluids and all physiological functions. Calcium is the most abundant mineral ion in the human body. A typical human body has approximately 1-2 kg of calcium, and more than 98 percent of it is deposited in the bones of the skeleton. Third function, in the bone marrow stem cell niches, mesenchymal stem cells can differentiate into adipocytes, chondrocytes, and osteoblasts. In the red bone marrow, red blood cells, white blood cells, and platelets are produced from hematopoietic stem cells. Fourth function, delicate tissues and organs are often protected by skeletal elements. The rib cage protects the heart and lungs in the chest, and the skull encases the brain, providing solid vital protection. The vertebrae shield the spinal cord, and the pelvis cradles delicate digestive and reproductive organs. The fifth and last common function of the skeleton is leverage; many bones of the skeleton function as levers[101]. Directed by the nervous system and implemented by skeletal muscles, the magnitude and directions of the leveraged force can change in space and time. The movements produced range from a precisely controlled finger motion to the powerful motility of a change in the entire body posture.

Compromised bone development and subsequently bone abnormality can lead to significant effects on human body function and daily quality of life.

1.2 Bone Cells

Bone contains a distinctive cell population, specializing in bone tissue homeostasis. In the bone development process and daily bone turnover activities, the active and basic units of bone metabolism consist of six types of cells: osteoprogenitor cells, chondrocytes, osteoblasts, osteocytes, bone lining cells and osteoclasts[101].

1.2.1 Osteoprogenitor Cells

Osteoprogenitor cells are a group of progenitor cells with small numbers differentiated from mesenchymal stem cells and found on the very inner layer of the periosteum and in the endosteum lining the medullary cavities. Osteoprogenitor cells are committed to differentiating into osteoblasts and acting as a reservoir providing the major supply for osteoblast cell populations. Maintaining a substantial population of osteoprogenitor cells is essential for daily bone turnover, and the capability to produce additional osteoblasts becomes extremely important after bone cracks or bone fracture. The bone fracture healing process requires larger numbers of osteoblasts, which can be produced from the osteoprogenitor cells[101].

1.2.2 Chondrocytes

Chondrocytes are the only cells found in cartilage which are also differentiated from mesenchymal stem cells. The early stage of bone development begins with endochondral bone formation. Mesenchymal stem cells aggregate, form clusters, and differentiate into chondrocytes to form the basic shape of bone. Through chondrocyte proliferation and hypertrophy the bone enlarges and grows longitudinally. In the mature bone, chondrocytes are located in the cartilage on the surface end of joints or reside in the growth plate of the bone providing smooth and flexible support and bone growth, respectively. Chondrocytes live in small chambers known as lacunae. The extracellular matrix secreted by chondrocytes provides tensile and resilience properties. Chondrocytes can maintain their cell population by undergoing division in lacunae or by chondroblasts differentiation into chondrocytes. Their daughter cells produce additional matrices. Chondrocytes produce a chemical that discourages the formation of blood vessels, thereby rendering cartilage avascular; all nutrients and waste-product exchange must occur by diffusion through the matrix[101].

1.2.3 Osteoblasts

Osteoblasts are cuboidal and columnar in shape with a central nucleus found on the inner or outer bone surfaces. These cells attach to the bone surface and secrete the organic components of bone matrix. These layers of bone matrix are called osteoid, which is composed mainly of type I collagen. Later the osteoid becomes mineralized through an unknown mechanism. Osteoblasts are responsible for the production of new bone and regulating the mineralization of the bone. The process of new bone formation is called osteogenesis. Usually a group of osteoblasts work together to deposit the organic matrix, they synchronize and coordinate the activity by communicating with each other through gap junctions with neighboring osteoblasts. Although the exact stimulus of osteogenesis is unknown, it has been thought that the osteoblast may respond to mechanical or hormonal stimuli to initiate osteogenesis, since osteoblasts have receptors for hormones, such as vitamin D, estrogen, and parathyroid hormone (PTH). They secrete factors that activate osteoclasts (RANK ligand) and other factors which communicate with other cells. In the osteogenic process, osteoblasts are gradually embedded in bone matrix and then differentiate into osteocytes[101].

1.2.4 Osteocytes

Osteocytes are star shaped mature bone cells composing 90% to 95% of all bone cells in adult bone and are the longest lived bone cells within their mineralized environment[103]. Osteocytes occupy small chambers in calcified bone matrix and the little chamber spaces are called lacunae. Osteocytes are networked to each other via long cytoplasmic extensions that occupy tiny canals called canaliculi, which are used for the exchange of nutrients and waste through tightly connected gap junctions. Although osteocytes have reduced synthetic activity for secreting bone extracellular matrix and are incapable of mitotic division, they are actively involved in the routine turnover of bony matrix. Each osteocyte directs both the release of calcium from bone to blood and the deposition of calcium salts in the surrounding matrix. Through various mechanosensory mechanisms the osteocyte networks play an essential role in bone formation stimulation and bone mineral homeostasis[101].

1.2.5 Bone Lining Cells

Bone lining cells are the flat and pancake shaped cells with a nucleus in the center that line inactive bone surfaces. They are differentiated from active osteoblasts which have become inactivated, flattened, and arranged along bone surfaces. The bone lining cells cover the entire surface of the bone protecting the bone from chemicals in the blood which dissolve mineral crystals. Bone lining cells are connected to other bone lining cells through gap junctions for rapid intercellular communication. And they are able to send cell processes through canaliculi to contact osteocyte networks. They are responsible for immediate release of calcium from the bone when the blood calcium is too low. There are many hormone and growth factor receptors on the bone lining cells that can initiate bone metabolism[101].

1.2.6 Osteoclasts

Osteoclasts are large multinucleated cells in charge of bone resorption. They are derived from the same hematopoietic stem cells that give rise to monocytes and neutrophils. Osteoclasts are formed by the fusion of multiple monocyte/macrophage derived cells into one large cellular structure. At the bone resorption site, osteoclasts secrete acids through the exocytosis of lysosomes. The acids dissolve the calcified matrix and release amino acids. These dissolved ions are absorbed into small vesicles and subsequently absorbed by endocytosis into osteoclasts. They then move across the cell and eventually are released into the extracellular fluid, thus increasing levels of the calcium and phosphate ion concentrations in the blood. Osteoclasts always break up mineralized bone matrix and release minerals; therefore, the balance between the number and activity of osteoclasts and those of osteoblasts is very important for maintaining the gross bone mass and density. When osteoclasts remove bone materials faster than osteoblasts deposit them, bone density becomes weaker and bone mass decreases. When osteoblast activity predominates, bones become stronger and bone volume becomes larger[101].

1.3 Bone Modeling

Bone modeling is a process that mainly occurs during bone growth (Figure 1). In children, the osteoblasts and osteoclasts constantly build up new bone and shape the bone size during development by adding new material to bone surfaces, thereby shaping the bone size according to a genetic blueprint[1]. Bone modeling also happens in the adult skeleton. In an adaptive response to prevailing mechanical loading, bone size and shape are modified according to loading strength and directions[2]. An interesting example of bone modeling in response to mechanical loading was demonstrated in the *in vivo* study of competitive tennis players[3]. The dominant playing arm radius of the tennis players had a denser cortex and enlarged diameter than the radius of the non-playing arm. Bone modeling leads to significant net bone gain due to more osteoblast activity than osteoclast activity. However, bone resorption without subsequent bone formation is also modeling and occurs on the endocortical, intracortical, and trabecular components of the inner or endosteal surface, digging and absorbing a marrow cavity during growth and establishing bone's cortical and trabecular architecture[4]. Bone modeling is different from bone remodeling in the fact that bone formation is not tightly coupled with a prior cycle of bone resorption and the bone formation and bone resorption processes happen at different sites (Figure 2). Bone remodeling is also surface dependent but occurs predominantly on the bone's endosteal surface rather than the periosteal surface[5]. Furthermore, in adults bone modeling occurs less frequently than bone remodeling[6].

1.4 Bone Remodeling

Bone remodeling is a process of removing previously formed bone by osteoclasts, followed by adding new bone matrix to the absorption place, which is subsequently mineralized (Figure 2). When bone growth occurs, osteoblasts are creating more bone matrix than osteoclasts are removing. In new bone development, bone remodeling may involve a change in the shape or internal architecture of a bone or a change in the total amount of minerals deposited in the skeleton. In adults, bone remodeling does not change the size or shape of bone. But osteocytes are continually removed and replaced by bone remodeling. Osteoblast activity and osteoclast activity are in balance and the bone formation rate and bone resorption rate are equal. However, in bone remodeling osteoblasts and osteoclasts are active throughout life, and the rate of mineral turnover is quite high in young adults, and each year almost one-fifth of the adult skeleton is demolished and then rebuilt or replaced[101]. But in elderly individuals, osteoblast activity decreases faster than osteoclast activity. As a result, bone resorption exceeds bone deposition, and gradually the skeleton gets weaker and weaker.

There are three significances of bone remodeling. The first significance is it replaces old or fatigued bone with new and sound bone to maintain bone mechanical strength and structural integration. The second is the role of bone mineral homeostasis by providing the body with bone mineral ions like calcium, potassium, magnesium, and phosphorus that are stored in bone[7]. The third significance is that bone remodeling has an important function in bone repair. Initiated in response to microcracks in bone, the bone remodeling process replaces the damaged bone with freshly formed new bone materials[8,9].

The remodeling of bone is accomplished mainly by four distinct phases: activation, resorption, reversal, and formation (Figure 3). Bone remodeling is believed to be initiated by microcracks caused by osteocyte apoptosis in fatigue-damaged bone[10,11,12].

The first phase of remodeling begins with activation. The apoptotic osteocytes at the damaged bone site attract mononucleated osteoclast precursors that infiltrate the bone lining cell layer and then fuse into multinucleated pre-osteoclasts. The pre-osteoclasts attach themselves to the damaged bone matrix to create a sealing zone. The formation of a tightly sealed compartment between an osteoclast and matrix creates a unique microenvironment for bone rebsorption[13].

The second phase in bone remodeling is resorption. After the sealed compartment is formed, proton pumps in the osteoclast membrane transfer protons to the resorption compartment, which decrease the pH value to as low as 4.0 in the sealed compartment[14]. The lower pH value results in acidification of the bone matrix. Simultaneously, osteoclasts secrete digestive enzymes called proteases, such as TRAP, cathepsin K (CTSK), MMP-9, and gelatinase into the sealed compartment[15]. These proteases, which are activated by the low acidity in the resorption compartment, dissolve and digest the mineral and organic parts of matrix creating a resorption bay called Howship’s Lacunae on the eroded bone surface. The end of the resorption phase occurs when osteoclasts undergo apoptosis[16].

The third phase of bone remodeling is reversal. Reversal starts when mononuclear cells appear on the bone surface and osteocytes are released from the bone by osteoclasts[17]. In the reversal phase, the coupling signals are sent out from the absorption site to attract osteoblasts and guide them to the resorption cavities to deposit new bone materials, replacing the bone that had been removed. The exact mechanism of signal coupling is still unknown. Interestingly, factors released from the bone matrix during bone resorption may contribute to the recruitment of osteoblasts and subsequent new bone formation during the reversal phase[18].

The last phase of bone remodeling is bone formation. There are two steps in this phase. First, the osteoblasts synthesize and deposit organic bone matrix, and second, they regulate mineralization. Mineralization is triggered by vesicles containing concentrated calcium and phosphate ions, and the enzymatic degradation of inhibitors of mineralization to initiate mineral deposition[19]. As bone formation continues, osteoblasts gradually embedded in bone matrix and become osteocytes[20]. The osteoblasts that are not becoming osteocytes either undergo apoptosis or remain on the bone surface to become bone lining cells.

The consequence of these bone remodeling cycles is the formation of new osteons resulting in increased new bone volumes[21]. The bone balance in remodeling between the periosteal and endosteal surfaces of cortical bone changes with aging. As individuals grow older, there is less new bone formation and greater bone resorption on both the endosteal and periosteal surfaces, which results in a decrease of cortical bone thickness with advancing age. The balance on the trabecular bone surface is also negative with age, leading to a reduced volume and number of trabecular bones[22].

1.5 Bone Mineral Homeostasis Regulation

In the mineralized matrix of bone, calcium phosphate, $Ca_3(PO_4)_2$, comprises almost two-thirds of the weight of bone. The calcium phosphate reacts with calcium hydroxide $Ca(OH)_2$ to form crystals of hydroxyapatite $Ca_{10}(PO_4)_6(OH)_2$. As they form, these crystals also incorporate other calcium salts, such as calcium carbonate, and ions such as sodium, magnesium, and fluoride. These inorganic components give bones the strength to resist compression. Roughly one-third of the weight of bone is from collagen fibers, which contribute tensile strength to bone. Osteocytes and other cell types account for only 2 percent of the mass of a typical bone[101].

Calcium phosphate crystals are very strong in nature. If only crystals come together, the result is a bone with almost no flexibility. Although they can withstand strong compression, crystals are likely to shatter under bending, twisting, or sudden impacts. Collagen fibers are tough and flexible. They can easily tolerate stretching, twisting, and bending. But organic materials like collagen fibers are not tough enough to constantly maintain a rigid structure when strong weight and compression are applied. In bone, collagen fibers provide an organic framework and scaffold for the formation of mineral crystals. The hydroxyapatite crystals form small plates that lie alongside the collagen fibers (Figure 4). The result is a combination of collagen fibers and hydroxyapatite crystals with the properties of flexibility and resistance to bending, an ideal structure for bone.

As calcium plays a significant role in daily bone metabolism, there is a demand for a substantial calcium supply, which requires adequate dietary calcium. After calcium is absorbed by the digestive system, it enters the blood stream. Through the blood vessels in bone, the skeletal tissue will be supplied with oxygen, nutrients, and calcium ions. Because calcium is critical to bone mineral metabolism, the body's plasma calcium concentration is very closely regulated by three important hormones. They are parathyroid hormone (PTH), calcitriol (vitamin D_3), and calcitonin[102].

These three hormones regulate the movement of calcium between bones, kidneys, and intestines. Among those hormones, parathyroid hormone and calcitriol are the most important in adult humans. The main function of parathyroid hormone (PTH) is to increase plasma calcium concentrations. There are three ways for PTH to raise plasma calcium; first, PTH mobilizes calcium from bones by increasing bone resorption by osteoclasts; second, PTH enhances renal reabsorption of calcium; third, PTH indirectly increases intestinal absorption of calcium through its influence on vitamin D_3. The major function of calcitriol (vitamin D_3) is to enhance intestinal absorption of calcium. The third hormone involved with calcium metabolism is calcitonin. Calcitonin seems to play a minor role in daily calcium homeostasis in adult humans. Calcitonin decreases bone resorption and increases renal calcium excretion[102].

Calcium and phosphate homeostasis are tightly linked in bone mineral homeostasis. Phosphate is the second key component in the hydroxyapatite of bone. And more importantly, most phosphate in the body is found in bone. Phosphate metabolism is parallel to that of calcium. Phosphate is absorbed in the intestines, filtered and reabsorbed in the kidneys, and distributed between bone, extracellular fluid, and intracellular compartments. PTH promotes phosphate renal excretion, and Vitamin D_3 enhances intestinal absorption of phosphate and promotes its renal reabsorption[102].

1.6 Diseases Associated with Decreased Bone Density (Osteopenia and Osteoporosis)

Increased bone resorption and a decreased bone formation lead to decreased bone density. With aging, the bones of the skeleton become thinner and relatively weaker. Lower bone mass, lower bone density, and lower ossification than normal is called osteopenia, and every individual becomes slightly osteopenic as they age. Between ages of 30 and 40 the bone mass starts to decrease. During this period of time, osteoblast activity begins to decline while osteoclast activity continues at previous levels. Every decade, women lose roughly 8 percent of their skeletal mass. For men the reduction rate is slower, about 3 percent per decade[23]. Osteopenia is considered by many physicians to be a precursor of osteoporosis.

With progressive reduction of bone mass, bone density decreases significantly, and the microstructure changes increase, which compromises normal bone function and increases susceptibility to fracture. These are characteristic of osteoporosis, one of the best known pathologies of bone function[22,23,24]. Osteoporosis is much more severe than osteopenia in the degree of bone density loss and bone micro-structure change (Figure 5). Osteoporosis is most common in women after menopause, when estrogen concentrations fall. According to the World Health Organization (WHO), 35 percent of women older than 65 years of age have osteoporosis, while a smaller proportion of older men suffer from osteoporosis[23,25].

Most osteoporotic bone resorption happens in spongy trabecular bone, particularly, in the vertebrae, hips, and wrists where bones have a larger proportion of trabecular to cortical bone. Due to the excessive fragility of osteoporotic bones, they break more easily when a person uses excessive force or in accidental falls. And the subsequent fracture healing is impaired. More seriously, vertebrae may collapse, distorting the vertebral articulations and putting pressure on spinal nerves.

Osteoporosis is a common bone disease that affects approximately 44 million Americans, making it a public health problem for society[26,27]. In the United States, about 8 million women and 2 million men over the age of 50 are estimated to have the disease, which is affecting approximately 10 million individuals[26,28]. In addition, approximately 34 million individuals have low bone mass (osteopenia), which places them at risk for developing osteoporosis or an osteoporosis-related fracture[27]. As the population ages, these numbers are expected to increase to an estimated 14 million individuals with osteoporosis and more than 47 million cases of osteopenia by 2020[26]. The medical cost of osteoporosis is huge. In the United States alone the cost in 2005 was estimated to be between $13.7 billion and $20.3 billion[29]. Furthermore, by the year 2025, the projected medical expenditures related to osteoporosis treatment and its related fracture treatment will reach 25.3 billion each year[26,30]. Due to the high prevalence of osteoporosis, its bone fracture consequences, and its huge cost, treatment options, especially osteoporosis drug development, is attracting the attention of medical health providers and is the subject of dynamic research.

For many years, estrogen or estrogen/progesterone hormone replacement therapy (HRT) was widely used as a treatment for osteoporosis in older individuals. However, estrogen therapy alone increases the risk of endometrial cancer and might cause other cancers, and some research suggested that a combined estrogen/progesterone HRT might increase the risk of heart attacks and strokes. In recent years, a selective estrogen receptor modulator (SERM) called raloxifene has been used to treat osteoporosis. The most efficient way to prevent or treat osteoporosis is to impact the mechanisms that cause bone loss. Bisphosphonate is a drug inducing osteoclast apoptosis and thus suppression of bone resorption. Teriparatide is a PTH derivative that stimulates formation of new bone. Current clinical research has been focused on studies of combining bisphosphonate and teriparatide to fight more efficiently against osteoporosis than either drug alone. The most effective drugs to prevent and treat osteoporosis act directly on the bone loss mechanism, while these drugs simultaneously reducing side effects. Development of future osteoporosis drugs will be facilitated by study of the molecular mechanisms of bone metabolism.

Besides drug intervention to avoid osteoporosis in elderly people, it is a great help for young women to maintain substantial dietary calcium intake and at the same time perform weight-bearing exercises, such as running, weight lifting, or aerobics, which increase bone density at a young age and help maintain bone mass at an older age.

1.7 The Stat Protein Family

Signal transducer and activator of transcription 3 (Stat3) is a transcription factor expressed ubiquitously in many kinds of cells, including embryonic stem cells[38], osteoblasts, osteoclasts, and osteocytes. Stat3 plays important roles in cell differentiation and proliferation[39,40,41] and belongs to the Stat family. The Stat family consists of Stat1, Stat2, Stat3, Stat4, Stat5α, Stat5β, and Stat6. The Stat3 pathway is broadly studied because of its many functions in animal cell growth regulation, inflammation, immune response, and early embryonic development resulting from diverse stimuli[42,43]. Stat3 appears to be involved in the regulation of multiple systematic signal pathways and acts as a multi-functional protein.

Stat proteins are a group of dormant, eukaryotic, cytoplasmic proteins activated by extracellular signals. Stat proteins were initially discovered in the study of transcriptional activation in response to interferon-α (IFN-α) and interferon-β (IFN-β) while exploring the relationship between extracellular signaling molecules and their effect on transcription[39,44]. Prior to the Stat proteins discovery, it had been known for some time that transmembrane receptors played a critical role in allowing cells to respond to the outside environment by altering cellular activity, but the details of how this proceeded had not yet been determined. By using biochemistry and gene cloning techniques combined with somatic cell genetics, researchers were able to provide evidence that a family of proteins responsible for transcription activation existed and responded to extracellular signals through transmembrane protein receptor binding and phosphorylation[39]. These newly discovered proteins were appropriately referred to as signal transducers and activators of transcription, or Stat proteins.

A total of seven Stat proteins have been identified to date: Stat1, Stat2, Stat3, Stat4, Stat5α, Stat5β, and Stat6. These proteins are between 750 and 850 amino acids in length. Stat 1,3,4,5α, and 5β are between 750 and 795 amino acids long, Stat2 and Stat6 are approximately 850 amino acids long and are known to have roles in a variety of biological activity[45,46]. Though much research has been done in an attempt to uncover additional members of the Stat protein family, these attempts have thus far been unsuccessful[47].

The complete three dimensional crystal structures of two of the Stat proteins were determined, Stat1 and Stat3[47]. Within the Stat3 protein the following domains exist: amino terminal domain, coiled coil domain, Src Homology 2 (SH2) domain, linker domain, DNA binding domain, and transcriptional activation domain (Figure 7)[48]. It has been determined that all Stat proteins contain several of the same domains and associated functions: an N-terminal DNA binding domain, an SH2 domain that binds to a specific phosphotyrosine in a receptor cytoplasmic domain, and a C-terminal domain with a critical tyrosine residue[49]. In the cytosol, the Stat proteins exist as monomers. Upon the initial extracellular signal binding of the receptor, an autophosphorylation event occurs creating a Stat docking site[50]. Upon the Stat binding to the receptor's intracellular docking site, a second phosphorylation event leads to dimerization of the protein which is rapidly exported to the nucleus where Stat proteins bind DNA and participate in a wide variety of gene regulation events[48].

1.8 The Stat Activation Pathway

Stat proteins are classified as transcription factors[51] that reside in the cytosol in an inactive state without the activation of specific receptors[50]. However, when activated Stat proteins dimerize. They quickly translocate to the nucleus, bind DNA, and induce or repress specific target genes[46,51].

The activation of Stat proteins requires extracellular signals to bind to the cell surface receptor. Certain protein sequences, in conjunction with their respective extracellular signaling molecules, have been shown to be critical determinants for recruitment to the receptor[52]. Signaling molecules in the Stat pathway are known as growth factors and cytokines. The cytokines, as a family of signaling molecules, are generally small, about 160 amino acids in length. These secreted molecules play critical roles in a wide variety of cellular functions[49]. There are more than 35 cytokines known to activate various Stats. Some important activators include Interferon-γ and interferon-α, which were critical in the discovery of the Stat protein family[44]. Interleukin-6, another important cytokine for

Stat signaling activation, has been implicated in the physiological regulation of decreased bone mass in post-menopausal osteoporosis, besides various other cellular functions[53]. The interferons and interleukins play an important role in many immune processes through Stat signaling pathways[31,49].

The full activation of Stat proteins requires a series of phosphorylation events to make it happen. Several tyrosine residue phosphorylations ultimately result in Stat protein activation[49]. Once the cytokines bind to their receptor domains on the surface of the cell membrane, the process of activation begins. The ligand binding causes a conformational change to the receptor bringing the associated receptor domains together to be dimerized. This results in autophosphorylation by JAK at the receptors' tyrosine residue, subsequently leading to the activation of the receptor kinase associated with the transmembrane receptors[45,49,50]. This process is carried out by the receptor's associated Janus kinase. The Janus kinase commonly known as JAK, is the most important kinase in the JAK-Stat pathway. Currently there are four JAK proteins found in mammals. They are JAK1, JAK2, JAK3, and TYK2[47]. The JAK-Stat pathway transmits the signal directly to target genes in the nucleus without using second messengers, providing a mechanism for concise and rapid signal transduction. Both JAK and Stat proteins are highly conserved among vertebrates[50].

The autophosphorylation event typically occurs at the sites on the cytoplasmic tails of the receptors serving as protein docking sites. Inactive Stat proteins in the cytoplasm are recruited, recognize the receptor phosphotyrosine, and associate with the activated receptor[45]. This is achieved by Stat SH2 domain recognition of a specific amino acid sequence surrounding the receptor's phosphotyrosine residue. Then, active JAK phosphorylates the tyrosine residue of the C-terminal domains of Stat proteins that are attached to the receptor. The phosphorylation on tyrosine residue causes the Stat proteins to be fully activated. The phosphorylated tyrosine residue of one Stat protein recognizes the site of the SH2 domain of another phosphorylated Stat monomer to form a homo-dimer (Figure 7). Dimerized Stat proteins translocate to the nucleus where they bind promoter sequences in target genes. Typically this involves dimeric binding to the nine base pair DNA sequence TTCCGGGAA[45,46]. In Stat3 the phosphorylated tyrosine residue is Tyr705.

In Stat3 signaling pathways, the JAK-Stat signaling pathway is the primary pathway for Stat activation. Stat3 proteins are expressed in the cytoplasm of unstimulated target cells[45,64]. Stat3 can be activated by phosphorylation through the JAK-Stat pathway by binding of extracellular ligands such as growth hormones, IL-6 family cytokines, and G-CSF[65,66,67]. In response to ligand binding, JAKs associated receptors undergo oligomerization which leads to their transphosphorylation. These JAKs phosphorylate the cytoplasmic domain of the cytokine receptor and subsequently phosphorylate tyrosine residue of Stat3.

Phosphorylated Stat3 proteins form dimers that are translocated to the nucleus where they bind specific DNA sequences that promote transcription of target genes (Figure 8)[68,69]. Stat3 can be regulated by G protein pathways. G protein subunits $G\alpha\iota$ and $G\alpha o$ activate c-Src tyrosine kinase. It is currently not known how Gαι or Gαο activates c-Src, but some studies indicate possible direct interactions between Gα subunits and tyrosine kinases. Later on c-Src phosphorylates Stat3 to form dimers. The G protein pathway can regulate signals from c-Src tyrosine kinase to Stat3 and to the Rap pathways[70]. But the physiological consequences of G protein pathway regulated Stat3 are still unknown. Stat3 can also be activated by non-receptor tyrosine kinases such as SRC and ABL. Constitutive activation of Stat3 by ontogeny mutated SRC and ABL tyrosine phosphorylation causes oncogenesis[71]. After tyrosine phosphorylation, Stat3 molecules dimerize and translocate to the nucleus. Once the activated Stat3 dimers recognize a target promoter, the transcription rate from this promoter is dramatically increased. The ability to induce transcription of target genes is an intrinsic property of the Stat3 dimers, reflecting the ability of Stat3 transcription domains to recruit nuclear co-activators that mediate chromatin modifications and communication with core promoters. These characteristics of Stat3 indicate that Stat3 is an essential signaling molecule involved in many key pathways and is competent to regulate a variety of functions by promoting corresponding gene expression.

Phosphorylation, dimerization, and transcriptional activation are the most common functions for a Stat3 protein. But interestingly, Stat3 was also shown to work monomerically as an adaptor coupling another signaling pathway for recruitment of phosphatidylinositol-3-OH kinase to its receptor[54]. In addition, due to the fact that Stat3 shows an increased abundance in the cytosol of cancerous cells, despite the fact that less than one third of these molecules ever translocate into the nucleus, some researchers are now also considering the possibility of a cytoplasmic function of the Stat3 protein[55]. In recent years, researchers have found that cytoplasmic Stat3 plays a critical role in cellular respiration in mitochondria that indicates a diversified and essential role Stat3 plays in cellular function[56].

1.9 The Stat3 Protein Function

The direct function of Stat3 is acting as a transcriptional factor binding DNA in activation of transcription. The results of the activation span a variety of physiological processes, and Stat3 proteins are involved in a staggering number of biological events and activities, with different Stat3 proteins activating different genes in different cells. Stat3 protein function has been studied in detail in cell culture systems. Those *in vitro* studies revealed that Stat3 proteins are involved in a complex variety of cellular processes including, but not limited to, induction of acute-phase response, proliferation of B lymphocytes, activation of terminal differentiation and growth arrest in monocytes, maintenance of pluripotency in stem cells, activation of osteoclasts and osteoblasts in bone tissue, remodeling of skeletal muscle, mediation of bone marrow stem cell VEGF production, and hyper IgE syndrome[31-48].

Stat3 was first discovered in the immune system due to its role in inflammation as a result of interleukin-6 (IL-6) release. Stat3 null mice have demonstrated an impaired immune response in the form of symptoms similar to that of Crohn’s disease, an autoimmune disease in which the immune system begins to attack sections of the gastrointestinal tract leading to chronic inflammation. The absence of Stat3 in mice is associated with an overproliferation of neutrophils and macrophages. However, these neutrophils lack a certain basic functionality and are less effective in dealing with infection, which leads to eventual chronic inflammation[57]. Suppression of Stat3 in the liver leads to apparent impairment of the acute-phase response, as well as impaired survival of T cells[44]. Another known immune deficiency disease linked with Stat3 is hyper IgE syndrome (HIES), a deficiency evidenced from the highly elevated level of serum IgE. This immune disorder has the symptoms of an increase in bacterial infection, skin rashes, and often bone abnormalities. HIES has been shown to be directly connected with mutations in the Stat3 DNA binding domain[31].

Functions of Stat3 have been revealed in addition to its function in the immune system. Stat3 activation is sufficient to maintain an undifferentiated state of mouse embryonic stem cells and that loss of Stat3 causes premature differentiation in embryonic stem cells[38,58,59]. Targeted disruption of the mouse Stat3 gene leads to embryonic lethality, indicating that Stat3 is essential for early embryonic development[60]. In skin, in the absence of Stat3, hair cycle and wound healing processes are severely compromised in epidermal Stat3 KO mice, which indicate defects in hair follicle stem cells and wound healing responsive stem cells[61]. In the brain, Stat3 is activated by ciliary neutrophic factor (CNTF) and leptin. Stat3 loss in the brain results in perinatal lethality[62]. In some human cancer studies, it has been demonstrated that constitutive activation of Stat3 is sufficient to induce tumor formation[40,63]. Cancer caused by continual Stat3 activation has anti-apoptotic activity, and there is significant evidence showing Stat3 controls cell motility. Stat3 is involved in cytoskeletal reorganization, focal adhesion, and digestion of extra cellular matrix, all critical processes in cellular movement[55]. Collectively, this evidence demonstrates that Stat3 regulates cell differentiation and proliferation in response to stimuli during development and tissue turnover. Stat3 loss-of-function causes serious problems in cell function.

In bone, Stat3 was also shown to be connected with the activation of human osteoblastic cells[53]. This, combined with the results of studies of HIES bone phenotypes, has shown that Stat3 is involved in both osteoblastic and osteoclastic differentiation thereby demonstrating the importance of Stat3's role in proper osteoblast function and bone formation *in vivo*. However, little research has been done to reveal the mechanisms that cause these bone abnormalities.

1.10 Stat3 in Response to Mechanical Loading

Daily physiological dynamic loading leads to anabolic bone formation and bone modeling. The response of bone to weight bearing exercise is essential for maintaining normal bone structure and strength. Thereby, mechanical loading plays an important role in skeletal development and the maintenance of skeletal architectural integrity. Increased mechanical loading stimulates bone formation and suppresses bone resorption, leading to an increase in bone mass[108]. Conversely, reduction in mechanical loading results in loss of bone mass through an inhibition of bone formation along with an increase in bone resorption[109]. A significantly increased frequency and strength of physiological loading results in an enhanced bone structure and strength. For example, professional baseball players demonstrated enhanced bone mass, structure, estimated strength, and resistance to torsion in the midshaft humerus of their throwing arms compared to their non-throwing arms[72]. In contrast, prolonged bed rest causes immobilization-induced bone loss; in the patella bone mineral content (BMC) deceases 3.2% and in the tibia the BMC decreases 0.7%[73]. During space flight, due to the zero gravity, much less stress is experienced by human skeleton, bone mineral density (BMD) in astronauts decreases 1.0% and 1.5% in the spine and hip, respectively, per month[74,75].

The mechanisms of gene expression were studied in bone mechanosignal transduction. These studies showed that mechanical loading affects signaling pathways and gene expression in loaded bone[76,77]. And they found that the gene expression patterns are time-dependent, with early activities stimulating a chain reaction of events that directly affects bone cell behavior and ultimately leads to bone formation. Interestingly, in a bone loading study, Stat3 was found in the early-response gene expression cluster, which was upregulated 4 hours after a single loading session[78]. Furthermore, in another loading study, increased periosteal bone formation was found in a loaded arm but not in a non-loaded arm. Gene expression assays were conducted 6 hours after loading. Total Stat3 expression was increased two fold in the loaded group compared with that of non-loaded control group[79]. This data demonstrates that expression of Stat3 in response to bone mechanical loading is rapidly enhanced in response to loading. However, the response mechanism and the role that Stat3 plays in load-induced bone formation have not been studied previously. In our study, Stat3 protein functions were specifically eliminated in osteoblasts and osteocytes to investigate the role of Stat3 protein plays in load-induced bone formation.

1.11 The Hyper IgE Syndrome and Its Bone Phenotypes

In 2007, dominant-negative mutations in the DNA-binding domain of signal transducer and activator of transcription 3 (Stat3) were determined to be the cause of hyper IgE syndrome (HIES)[31]. HIES is a multisystem disorder and a rare primary immunodeficiency disease not only characterized by eczema, recurrent skin[32] and lung infections, brain abnormalities[33], highly elevated serum IgE, and various connective tissue, and vascular abnormalities, but also prominent skeletal abnormalities[34].

In HIES patients, bone features include craniosynostosis, scoliosis, minimal trauma fractures, osteopenia, osteoporosis, joint hyperextensibility and degenerative joint disease[35]. Scoliosis is common in most of HIES patients, and often appears during adolescence, similar to the case with idiopathic scoliosis, but in other HIES phenotypes may also be associated with leg length discrepancy or be worsened by lung damage or resections. Minimal trauma fractures occur in about half of individuals with HIES, and they frequently involve the ribs and long bones. Hyperextensibility of the small and large joints is frequent and may contribute to early degenerative joint disease, which is especially apparent in the cervical spine. Osteopenia and osteoporosis also have been found in HIES patients, and decreased bone density and compromised bone structure make HIES patients suffer from recurring fractures in long bones and ribs (Figure 6). On the tissue level, bone histology of HIES patients shows increases in osteoclasts and osteomalacia. On the cellular level, cultured and differentiated osteoclasts from peripheral blood of HIES patients demonstrated increased osteoclast activity and bone resorption compared to cultures from normal patients. Osteoclast-mediated bone resorption is abnormal in HIES and is likely related to osteopenia, osteoporosis and fractures[36,37]. The abnormal skeletal features of HIES patients with mutated Stat3 suggested that the Stat3 signal is required for proper bone development and that mutations of Stat3 might cause osteopenia and osteoporosis.

From the HIES phenotypes discussed above we can summarize that mutations in Stat3 cause irregulated bone development, decreased bone density (osteopenia and osteoporosis), and increased osteoclast activity. However, the mechanisms causing those bone abnormalities are still unknown. And the Stat3 might play a critical role in pathogenesis of osteopenia and osteoporosis. In our research, in order to investigate the role of the Stat3 played in bone modeling and bone remodeling, bone tissue-specific Stat3 knockout mice were created. By utilizing this animal model, we can systematic study the mechanism of null Stat3 causing bone abnormalities.

1.12 The Bone-Specific Stat3 Deficiency Mouse Models

The function of Stat3 has been studied extensively in cell culture and has been found to be critical in embryogenesis. Removal of Stat3 in embryonic stem cells leads to cell mortality *in vitro*[44]. Stat3 deficient mice generated by Stat3 gene targeting, results in embryonic lethality. The Stat3 null embryos rapidly collapsed and showed no sign of mesoderm formation between 6.5 and 7.5 days of embryogenesis[60], although the exact mechanism how Stat3 affects embryonic development and causes embryonic lethality is still unclear. Stat3 mRNA was exclusively expressed in visceral endoderm in the embryo[60]. The visceral endoderm has an important function in metabolic exchange between embryo and maternal blood[80]. This evidence might suggest that impaired functions of visceral endoderm leads to insufficient nutritional supply to the embryo resulting in the compromised embryonic development.

Due to the characteristic lack of viability in Stat3 null mice embryos, the study of Stat3 function is compromised. Researchers cannot further monitor the development of Stat3 deficient mice to study its function in different organs and tissues. However, tissue or organ specific Stat3 gene ablation or deletion is available. This is achieved by using the Cre-LoxP recombination system[44]. The Cre- LoxP system consists of an enzyme, Cre recombinase, which catalyzes recombination of target sequence between two LoxP sites which will lead to deletion of DNA sequences in the middle of two loxP sites. The Cre-LoxP recombination system was first introduced into the mouse genome to activate gene expression in mammalian cell lines and transgenic mice[81,82]. In the case of Stat3, since embryonic Stat3 knockouts are lethal, a conditional knock out mouse model was developed. The Cre recombinase gene can be inserted into the tissue or cell specific promoter and loxP sites can be introduced between exons of the Stat3 gene by homologous recombination. Then with both Cre and LoxP transgenes presented in the genome of the experimental mice, Stat3 gene expression can be disrupted in a tissue or cell specific manner.

In our research, transgenic mice were generated by Dr. Xin-Yuan Fu’s lab, mice with both Stat3 alleles in which exons 18-20 are flanked by LoxP sequences. Deletion of exons 18-20, which encode the Src Homology (SH2) domain of Stat3 is expected to not only impair Stat3 gene expression, but also disrupt Stat3's function to form functional dimers through the phosphorylated tyrosine and SH2 domain interaction. And it is believed to eliminate the function of Stat3 proteins[57]. Type I collagens are dominantly expressed in osteoblasts. Strains of mice for bone cell specific gene deletion were used, where Cre expression is driven by type I collagen promoter 2.3 fragments (Col2.3-Cre) and 3.6 fragments (Col3.6-Cre) [83,84]. Since Cre is a transgene originally developed from bacteriophage and is not normally expressed in mammalians, these mice express Cre only in osteoblasts and later osteocytes. Moreover, Col3.6-Cre promoter is activated in early osteoblast differentiation and Col2.3-Cre promoter is activated in mature osteoblasts[85]. Dentin matrix protein 1 (encoded by *DMP1*) is an extracellular matrix protein highly expressed in osteocytes but not expressed in osteoblasts[86]. Mice were generated in which Cre was expressed specifically in osteocytes under the control of dentin matrix protein 1 (Dmp1-Cre) promoter (8kb)[87].

Osteoblast or osteocyte cell specific Stat3 knockout (KO) mice were created by breeding the Cre expression mice and two LoxP sites flanked Stat3 mice. Conditional Stat3 KO mice are carrying osteoblast-specific or osteocyte-specific Cre expression gene and both alleles of Stat3 gene flanked with two LoxP sites. The way this system works is that the Cre recombinase cleaves the genomic DNA at the LoxP sites and recombines the ends only in osteoblasts or osteocytes. This process efficiently removes the exons 18-20 of Stat3 gene.

1.13 Research Goals

In previous studies, researchers have found that Stat3 mutations cause Hyper IgE syndrome (HIES). And in HIES patients apparent bone phenotypes like irregulated bone development, joint diseases, and bone fractures haven been characterized. The interesting facts catching more attention from researchers are the osteopenia and osteoporosis presented in HIES patients. These studies strongly suggest that Stat3 proteins play a critical role in bone formation and that the absence of Stat3's proper function results in bone abnormalities and decreased bone density. Our objective is to reveal the mechanism by which bone cell specific null Stat3 causes bone abnormalities and decreased bone density. Our hypothesis is that Stat3 plays an important role in bone development and bone density achievement. Null Stat3 in bone leads to phenotypes like scoliosis, smaller body size, shorter bone length, decreased bone mineral density, and decreased trabecular bone number and size. At the tissue level, null Stat3 leads to apparent changes in bone geometric structure and decreased bone mechanical strength. At the cellular level, null Stat3 causes deceased osteoblast activity and increased osteoclast activity. Null Stat3 leads to accumulated reactive oxygen species in osteoblast mitochondria and increases sclerostin (SOST) expression in osteocytes. To test this hypothesis we have created an unique animal model consisting of two strains of conditional KO mice to disrupt Stat3 function in bone: one specifically knocks out Stat3 in osteoblasts (*Col3.6-Cre;Stat3*$^{flox/flox}$) and another knocks out Stat3 in osteocytes (*Dmp1-Cre;Stat3*$^{flox/flox}$). By utilizing these two strains of mice, we can differentiate the role that Stat3 plays in osteoblasts and osteocytes, which will give us an insight into Stat3 function in different bone cell types.

In recent bone loading studies, the discovery of upregulation of Stat3 proteins in response to mechanical loading also strongly suggests that Stat3 proteins might play an important role in mechano signal transduction to promote new bone formation by osteoblasts[78,79]. Furthermore, osteocytes have been considered to be the most important mechanosensory cells because of their location in bone and their complex dendritic network[88,89,90]. We hypothesized that Stat3 plays a critical role in mechanotransduced bone formation in osteoblasts and that Stat3 proteins are important signaling molecules in the mechanosignal transduction of osteocytes, predicting that the level of activated Stat3 in osteoblasts will increase in response to mechanical loading force and that knockout of Stat3 in osteocytes will lead to reduced bone formation in response to anabolic mechanical loading.

CHAPTER 2. MATERIALS AND METHODS

2.1 Experimental Animals

All animal studies were reviewed and approved by the Indiana University Animal Care and Use Committee (IUACUC). In Col3.6-Cre mice, Cre expression dominates in osteoblasts and is driven by a type I collagen promoter. These mice were kindly provided by Dr. Barbara Kream[84] (University of Connecticut Health Center). The Cre recombinase transgenic mice expressing Cre specifically in osteocytes (Dmp1-Cre mice) under the control of dentin matrix protein 1 (DMP1) 8 kb promoter were generated as previously described and kindly provided by Dr. Teresita Bellido[87] (Department of Anatomy and Cell Biology, Indiana University School of Medicine). The two LoxP sites floxed exons 18-20 of Stat3 gene mice (Stat3$^{flox/flox}$ mice) were created and generously provided by Dr. Xin-Yuan Fu (Department of Biochemistry, National University of Singapore Yong Loo Lin School of Medicine). The two LoxP sites flank exons 18-20 of the Stat3 gene which encodes the SH2 domain of Stat3 protein. The SH2 domain is required for Stat3 activation[57].

2.2 Mice Breeding Scheme

In order to generate osteoblast-specific Stat3 knockout (KO) mice, there were two steps of mice breeding. In the first step, the homozygous Col3.6-Cre transgenic mice were bred with homozygous Stat3$^{flox/flox}$ mice to create F_1 offspring carrying both heterozygous Col3.6-Cre and heterozygous Stat3$^{flox/+}$ genes in the mice genome. The F_1 offspring possessed the genotype of Col3.6-Cre; Stat3$^{flox/+}$. In the second step, F_1 offspring male and female mice were cross bred with each other: Col3.6-Cre;Stat3$^{flox/+}$ × Col3.6-Cre;Stat3$^{flox/+}$ to generate an F_2 generation which mainly had three different genotypes, which were used for experiments. They were Col3.6-Cre; Stat3$^{flox/flox}$, Col3.6-Cre;Stat3$^{flox/+}$, and Col3.6-Cre;Stat3$^{+/+}$.

Mice with the genotype of Col3.6-Cre; Stat3$^{flox/flox}$ containing the Cre expression gene and both homozygous alleles of the floxed Stat3 gene were considered osteoblast-specific knockout (KO) mice. Mice with the Col3.6-Cre;Stat3$^{flox/+}$ genotype were carrying both the heterozygous Cre gene and heterozygous floxed Stat3 gene, which were used for breeding new offspring to generate more experimental animals. Mice of Col3.6-Cre;Stat3$^{+/+}$ genotype only had osteoblast-specific Cre gene expression, but no floxed Stat3 gene, and were used as wild type (WT) littermate controls.

For generating osteocyte-specific Stat3 knockout mice, the same two-step scheme for breeding osteoblast-specific Stat3 knockout mice was used (Figure 9). Also mainly three different genotypes of mice were created for experiments: Dmp1-Cre;Stat3$^{flox/flox}$, Dmp1-Cre;Stat3$^{flox/+}$, and Dmp1-Cre;Stat3$^{+/+}$. The osteocyte-specific Stat3 knockout (KO) mice were determined to have the genotype of Dmp1-Cre;Stat3$^{flox/flox}$. The mice with the Cre gene and heterozygous floxed Stat3 gene possessing the genotype of Dmp1-Cre;Stat3$^{flox/+}$

were used for breeding new experimental animals. And mice with the genotype of Dmp1-Cre;Stat3$^{+/+}$ were used as wild type (WT) littermate controls.

2.3 Genotyping of Knockout Mice and Wild Type Mice

In order to indentify the genotypes of offspring, genomic total DNA were extracted from 2-3 mm long mice tails with 100 μl of lysis buffer composed of 50 mM Tris pH 8.0, 50 mM KCl, 2.5 mM EDTA, 0.4% NP-40, 0.45% Tween-40, and 10 mg/ml Proteinase K (Thermo Fisher Scientific Inc., Waltham, MA) in a 56 °C water bath overnight. Later mice tail samples with genomic DNA were placed in a 95 °C dry bath for 10 minutes to inactivate the Proteinase K. Then 100 μl of autoclaved Milli-Q water was added to dilute each mice tail sample. 1 μl of tail lysis with genomic DNA from each sample was used for PCR amplification.

For detecting the Cre transgene, PCR was performed by using JumpStart™ REDTaq® ReadyMix™ Reaction Mix (Sigma-Aldrich, St. Louis, MO, USA) according to the manufacturer's protocol with forward primer 5'-GAGTGATGAGGTTCGCAAGA-3' and reverse primer 3'-CTACACCAGAGACGGAAATC-5' to amplify a 615 bp fragment[84]. Thirty-nine cycles were performed with a total volume of 20 μl per reaction: 94 °C, 30s; 55 °C, 30s; 68 °C, 30s. 12 μl of amplified DNA from each reaction was analyzed, using 2.5% agarose gel electrophoresis and SYBR® Safe DNA Gel Stain (Life Technologies Corporation, Carlsbad, CA, USA).

The presence of a 615 bp DNA band for the transgene encoding Cre recombinase indicated the mice were carrying Cre transgene (Figure 10). The mice that didn't contain the Cre recombinase showed no band, since Cre is not an endogenous gene expressed in mammalian species. The same PCR reagents and procedures for Cre gene amplification were also used for detecting the LoxP site in the Stat3 gene exons 18-20. The primers were designed to flank the LoxP site upstream and downstream in the Stat3 gene sequence, by differentiating the length of the PCR product to determine the presence of the LoxP site in the Stat3 gene exons 18-20 (Figure 11). Stat3 forward primer 5'-ATTGGAACCTGGGACCAAGTGG-3' and reverse primer 5'-ACATGTACTTACAGGGTGTGTGC-3'were used for amplifying the LoxP site. The PCR for detecting the DNA sequence of the LoxP site amplified a 520 bp DNA band for Stat3$^{flox/flox}$ and a 480 bp DNA band for Stat3$^{+/+}$, while the PCR for the heterozygous Stat3 floxed mice (Stat3$^{flox/+}$) amplified both 520 bp and 480 bp bands[57] (Figure 10). The expression of Cre only in osteoblasts and osteocytes of these genotyped mice was driven by the expression of type I collagen 3.6 kb fragments and dentin matrix protein 8 kb fragments, respectively. Therefore, the expression of Cre was limited to bone tissue and Cre expression deleted the Stat3 gene exons 18-20 only in osteoblasts and osteocytes.

2.4 Immunohistochemistry

2.4.1 Bone Demineralization and Fixation

Wild type mice and Stat3 knockout mice that were 8-9 weeks old were euthanized using CO_2. Before bone fixation, in order to get ideal results of tissue preservation, both of the wild type and Stat3 knockout mice were processed using 4% phosphate buffered formalin

(PBF) perfusion through the circulatory system. Then, both femurs and tibiae were extracted. The bones were cleared of all muscles and other excess soft tissue by a No.11 surgical blade. Bone specimens were fixed by immersing them in 4% PBF in 4 °C fridge for 48 hours. Bone samples were demineralized in 7:3 10% EDTA and 4% PBF in 4 °C for a week on a shaker. And the demineralization solution had been changed 3 times in that week. When demineralization was completed, bone specimens were washed in running deionized (DI) water or tap water for 1 hour, and then stored in 70% ethanol (EtOH).

2.4.2 Bone Specimens Paraffin Embedding and Cutting

After decalcification and formalin fixation, bone specimens were cut into appropriate portions and placed in embedding cassettes. The bone specimens were then dehydrated in graded alcohols: 70%, 95%, 100%, and 100% (45 minutes per step), cleared in xylene, and embedded into paraffin blocks for paraffin infiltration. Thin sections (4-10 μm) of bone specimens were cut by using a rotary microtome equipped with disposable steel knives. Sections were flattened on a heated water bath, floated onto microscope slides, and dried.

2.4.3 Deparaffinization and Rehydration

At room temperature (RT) the glass slides with paraffin embedded thin bone sections were placed in slide staining jars and immersed in a series of chemicals for immunocytochemistry. The slides were immersed in sequential steps of chemicals: Xylenes I, Xylenes II, Xylenes III, 100% EtOH, and 100% EtOH respectively; each step lasted for 5 minutes. Then, slides were moved to 95% EtOH for 3 minutes, and they later were moved to 70% EtOH for 3 minutes. After slides were removed from the 70% EtOH solution, they were transferred and immersed into phosphate buffered saline (PBS) pH 7.4. Slides were then individually taken out from the PBS and dried around the section with Kimwipes® paper, and a circle was drawn in with Imm-Edge Pen (Cat. #: H-4000; Vector Laboratories, Inc., Burlingame, CA). After the slides were done, the specimens on the glass slides were rehydrated. These slides were placed back into the PBS, so they would not dry out.

2.4.4 Epitope Retrieval

At RT, all procedures were immersed in a variety of chemicals by using slide staining jars. The slides were first immersed in DeCal Retrieval Solution (Cat. #: HK089-5K; Biogenex, San Ramon, CA) for 30 minutes. Slides were then transferred and immersed into a series of chemicals: 100% methanol (MeOH), 100% MeOH, 70% MeOH, respectively; each immersion lasted for 5 minutes. After removing the slides from the last change of the MeOH solution, they were placed into PBS I solution for 5 minutes then moved to PBS II for 5 minutes. After the PBS II step was finished, the slides were placed into a PBS + 0.3% Triton X-100 solution for 10 minutes. Finally, slides were stored back into a PBS solution for at least 5 minutes to keep them from drying out.

2.4.5 Peroxidase Inactivation, Blocking, and Primary Antibody Probing

At the beginning, a 3% H_2O_2 / Methanol solution was prepared by combining 100 µl of 30% H_2O_2 (Cat. #: H1009-500ML; Sigma-Aldrich Co. St. Louis, MO) with 900 µl

MeOH in a microcentrifuge tube. The solution was mixed thoroughly by vortexing. The following steps were done on slides using humidity chambers. Slides were taken out from the PBS and the PBS was carefully drained using Kimwipe® paper. Then the slides were immersed in 200 µl of 3% H_2O_2 / Methanol solution for 5 minutes. The 3% H_2O_2 / Methanol solution was shaken off, and the specimen was covered with PBS for 5 minutes. While the PBS was sitting for 5 minutes, a 1.5% goat serum blocking solution was prepared in a disposable test tube by combining 10 ml PBS with 3 drops (150 µl) normal goat serum from the Vectastain Elite ABC Kit (Rabbit IgG; Cat. #: PK-6101; Vector Laboratories, Inc., Burlingame, CA). The PBS was carefully drained from the section using Kimwipe® paper, and 200 µl of the blocking solution was applied to each slide for 30 minutes.

While the blocking solution was sitting on the slides, the primary Stat3 antibody (C-20; Cat. #: sc482; Santa Cruz Biotechnology, Santa Cruz, CA) was getting prepared. The solution was prepared in1:200 dilutions by combining 1000 µl of 1.5% goat serum blocking solution with 5 µl of Stat3 antibody. The blocking solution was carefully drained from the slide using Kimwipe® paper, and 200 µl of primary antibody solution was applied to each slide. Then, all those slides in humidity chambers were placed in a refrigerator overnight at a temperature of 4 °C. The solution stayed on the slides for at least 16 hours.

2.4.6 Secondary Antibody, Avidin-conjugated Peroxidase, and Chromagen Development

All the steps were done in the humidity chambers. A solution of biotinylated secondary antibody was prepared by using a VectaStain ABC kit. In a disposable test tube, 10 ml PBS, 3 drops (150 µl) goat serum, and 1 drop (50 µl) secondary antibody were combined together and mixed thoroughly. The primary antibody was gently shaken off the slide, and the sections were washed 5 times with PBS + 0.1% Tween 20 solution. The PBS + 0.1% Tween 20 solution was then carefully drained from the slide using Kimwipe® paper, and PBS was added to cover the slide and left sitting on slide for 5 minutes. The slide was drained to remove the PBS, and 200 µl of the secondary antibody was applied and left to cover the slides for 45 minutes.

Immediately after applying the secondary antibody solution, the Avidin-conjugated Peroxidase (ABC) solution (VectaStain ABC Kit) was prepared. The ABC solution was prepared by mixing 5 ml of PBS, 2 drops of reagent A, and 2 drops of reagent B sequentially. The solution was mixed well by gently shaking it and left to set for 30 minutes prior to use. After 45 minutes, the secondary antibody was gently shaken off of the slide and washed 5 times with PBS + 0.1% Tween 20 solution. After the final wash, PBS was added to the slide, and it covered the specimen for 5 minutes. The PBS was drained from the slide and 200 µl of ABC solution was applied to the sections and left to set for 30 minutes. While the ABC solution was setting, the Peroxidase substrate solution (0.05% DAB + 0.01% H_2O_2) was prepared. The Peroxidase substrate solution was prepared by diluting 30% H_2O_2 into 3% H_2O_2 with PBS, and then in a separate tube, 10 mg of 3,3′-Diaminobenzidine (DAB, Sigma-D0426, SIGMAFAST™, Sigma-Aldrich, USA) tablet was dissolved in 20 ml of PBS. The ABC solution was gently shaken off of the slides, and sections were washed 4-5 times with PBS. Sections were carefully drained and 200 µl DAB solution was applied to each slide. The stained tissue gradually developed a dark brown color, and it was monitored under a dissecting microscope. The reaction was stopped by repeated washes with PBS. The DAB stain reaction took approximately 60 seconds for the Stat3 KO mouse femur. Slides were kept covered with PBS until all sections developed. Methyl Green nuclear stain could have counterstained the slides; however, it was not used.

2.4.7 Dehydration and Mounting

All procedures are done in slide staining jars. In the following steps, slides were undergoing a series of chemical immersions. Slides with specimens on them were probed by Stat3 antibody and placed in a variety of graded alcohol and chemical solution changes: PBS, 70% EtOH, 95% EtOH, 100% EtOH, 100% EtOH, Xylenes I, and Xylenes II. The specimens were immersed in each step for 3 minutes. After the dehydration was done, all slides were covered with Eukit and coverslipped with appropriate cover glasses. All slides were left over night to dry in a fume hood. Finally, those slides were fully prepared for measurement and analysis under a microscope.

2.5 *In vivo* Ulna Loading

In order to examine the role of Stat3 in load-induced bone formation, the 16-week-old adult conditional Stat3 KO mice and the WT littermate control mice were subjected to dynamic axial ulna loading (Figure 12). The right ulna of 16-week-old experimental mice were loaded under general anesthesia with 3-5% isoflurane (Sigma-Aldrich, St. Louis, MO, USA) with a force of 2.5 N for female mice, 2.8 N for male mice, and 120 cycles/day at 2 Hz for 3 consecutive days by utilizing an electromagnetic actuator (Bose ElectroForce 3200 series, EnduraTEC). The left ulna of each mouse was used as an internal control. The loading forces were selected to ensure that both male and female mice experienced similar peak strains during loading. In a pilot load-strain calibration experiment using 3 mice randomly selected from each gender and strain of mouse, *in situ*, mechanical strains achieved during loading were measured on the medial surface of the ulnae as described previously by our group[79,91]. The peak force of 2.5 N produced about ~2800 and ~2970 microstrains at the midshaft of ulnas of female control mice and conditional Stat3 KO mice, respectively. The peak force of 2.8 N produced about ~2800 and ~2940 microstrains at the midshaft of ulnas of male control mice and conditional Stat3 KO mice, respectively. All mice were allowed normal cage activity between and after loading sessions.

Because of calcein and alizarin are able to incorporate into newly calcifying bone, an intraperitoneal injection of calcein (green flurochrome label, 30 mg/kg body weight, Sigma-Aldrich) was administered on day 5 after the first bout of loading. Then, another fluorescent dye, alizarin (red flurochrome label, 50 mg/kg body weight, Sigma-Aldrich), was also intraperitoneally injected on the 11th day after the first bout of loading. There were 6 days apart between the calcein and alizarin injection dates. All loaded experimental mice were euthanized 16 days after loading, and a series of bone specimens were extracted and preserved for studies (Table 1). The ulna, radius, femur, tibia, and vertebra were extracted from loaded mice. The bones were cleared of all excess soft tissue using forceps.

2.6 Bone Specimens Plastic Embedding and Sectioning

The ulnae, right femur, and vertebra body lumbar L5 were immersed in 10% neutral buffered formalin for specimen preservation (histology). After 10% neutral buffered formalin fixation, bone specimens were dehydrated through a graded series of ethanols (4 hours per step), cleared in xylenes for 4 hours, and infiltrated first with unpolymerized methyl methacrylate (MMA) for 4 hours, and then for 3 to 7 days with unpolymerized methyl methacrylate containing 4% dibutyl phthtalate, a softening agent. The specimens were then embedded in a medium of methyl methacrylate + 3% dibutyl phthalate + 0.25% Perkadox 16 (catalyst) and allowed to polymerize at room temperature. Excess plastic from the blocks was removed using a band saw, and the blocks were shaped using a dental model trimmer. Thin sections of 4-10 μm, primarily cancellous bone were cut using a rotary microtome equipped with a tungsten-carbide knife. Thick sections of over 80 μm, primarily cortical bone were obtained using a diamond wire saw. When necessary, thick sections were reduced to their final thickness using 600 grit wet/dry silicon carbide paper (LECO).

For dynamic histomorphometry (vital stains), thin sections were left un-deplasticized and were cover-slipped using a Eukitt mounting reagent. For static histomorphometry, thin sections were deplasticized in acetone and stained by two different procedures: (1) a modification of the Von Kossa/MacNeal's (VKM) Tetrachrome protocol[92] and (2) a tartrate-acid resistant acid phosphatase (TRAP) stain[93]. For the VKM slides, mineralized bone was stained using the Von Kossa silver method, and the unmineralized tissue was counter-stained with MacNeal's tetrachrome. For TRAP staining, the sections were pre-incubated in 0.2 M acetate buffer (pH = 5.0), rinsed, and incubated in a warmed acid phosphatase solution. Afterwards, the sections were counterstained with Gill's Hematoxylin No. 3, allowed to air dry, and cover-slipped with an aqueous based mounting media. Additional thin section stains included Goldner's Trichrome (GT), Toluidine Blue (TB), and hematoxylin and eosin (H&E).

For dynamic histomorphometry of thick sections, the sections were briefly cleared in xylenes and cover-slipped with a Eukitt mounting reagent. For static histomorphometry, unattached, un-deplasticized sections were stained using Goldner's Trichrome and then mounted to glass slides by cover-slipping them with a Eukitt mounting reagent. The stains of the additional thick section included TB and H&E.

2.7 Histomorphometry

2.7.1 Ulna Dynamic Histomorphometry

The right ulnas with radius (loaded) and left ulnas (non-loaded control) were matched length and tied together using copper wiring for two circles. The lengths of both right and left ulnas were measured, and the midshaft position of both ulnas was marked by a pencil. The ulna specimens were placed into tissue cassettes and stored in 70% EtOH in 4 °C and later prepped for dehydration in graded alcohols. After the dehydration, ulnas from the cassettes were embedded into small glass tubes using 4% MMA. The tubes were then frozen overnight to allow the MMA to harden. When the MMA was hard enough, the glass tubes were broken with a hammer. Using a diamond-embedded wire saw (Histo-saw, Delaware Diamond Knives, Wilmington, DE), three consecutive transverse thick sections (70 μm) were cut at the ulnar midshafts, ground to a final thickness of 30 μm, mounted on microscope slides, then coverslipped with Eukit.

Three sections in each midshaft ulna were cut and used for bone dynamic histomorphometry (Figure 13), with an OLYMPUS fluorescence microscope (Olympus BX51, Olympus America Inc., Center Valley, PA) using OsteoMeasure™ histomorphometry software (Osteometric Inc., Decatur, GA). The following primary data were collected from the periosteal surface of ulna cortical bone, at 400 X magnification: total perimeter (B.Pm), single labeled perimeter (sL.Pm), double labeled perimeter (dL.Pm), and inter-labeled width (Ir.L.Th). There were 6 days apart between the two fluorescent labels (Figure 14). These primary data were generated from both loaded (right) and non-loaded (left) ulna by tracing the whole ulna periosteal perimeter, two fluorescent dyes labeled perimeters, and the distance between two flurochrome labels. From these primary data, the following quantified data were derived: mineralizing surface [MS/BS = (dL.Pm+1/2sL.Pm)/B.Pm×100 (%)], mineral appositional rate [MAR = Ir.L.Th / 6 days (μm/day)], and bone formation rate [BFR/BS = MAR × MS/BS × 365 ($\mu m^3/\mu m^2$/year)]. Furthermore, in order to normalize data of load-induced bone formation, the ulna’s natural bone growth was excluded from load-induced bone growth, and then a series of relative data were generated. The relative mineralizing surface (rMS/BS) equals MS/BS in the right ulna minus MS/BS in the left ulna. The relative mineral appositional rate (MAR) equals MAR in the right ulna minus MAR in the left ulna. The relative bone formation rate (BFR/BS) equals BFR/BS in the right ulna minus BFR/BS in the left ulna.

2.7.2 Femur Dynamic Histomorphometry

In order to assess and compare the difference of bone growth between conditional Stat3 KO mice and WT control mice, dynamic histomorphometry of mid-shaft femurs (cortical bone) and distal femurs (trabecular bone) were examined.

Right femurs of KO and WT mice were extracted and immersed in 10% neutral buffered formalin for 48 hours at 4 C°, then stored in 70% Ethanol at 4 C°. Total lengths of the femurs were measured, and the mid-shaft femurs were marked with a pencil around their entire circumference. Each femur was cut into two parts: the proximal femur + the mid-shaft femur, and the distal femur (about 1.5 mm distal to the mid-shaft mark). Both segments of femur mid-shaft and distal femur parts were dehydrated in graded alcohols, cleared in xylene, and embedded in Methyl Methacrylate (MMA) plastic. Using the diamond-embedded wire saw at femur mid-shaft, three consecutive transverse sections were cut approximately at a 120 μm thickness. Sections were ground to the desired thickness of 20-30 μm using 600 grit sand paper. Sections were mounted on microscope slides, cleared in xylenes, and cover-slipped with Eukitt.

Under OLYMPUS fluorescence microscope, using OsteoMeasure™ system , at 400 X magnification: total perimeter (B.Pm), single labeled perimeter (sL.Pm), double labeled perimeter (dL.Pm), and inter-labeled width (Ir.L.Th) of femur cortical periosteal surface were generated as primary data from mid-shaft femur cortical bone sections. These primary data were harvested by tracing the whole femur periosteal perimeter, two fluorescent dyes labeled perimeters, and the distance between two flurochrome labels. There were 6 days apart between two fluorescent labels. From those primary data the quantified data were derived: MS/BS = (dL.Pm+1/2sL.Pm)/B.Pm × 100 (%), MAR = Ir.L.Th/6 days (μm/day) and BFR/BS = MAR × MS/BS × 365 ($\mu m^3/\mu m^2$/year).

For the distal femurs, longitudinal thin sections were cut at 4-10 μm by microtome equipped with a tungsten-carbide knife. Three unstained sections were mounted to a microscope slide. Total of five microscope slides were prepared and processed: slide 1 (Fluorochrome), slide 2 (unstained), slide 3 (Von Kossa/MacNeal stain), slide 4 (Tartrate-acid Resistant Acid Phosphatase stain), and slide 5 (Fluorochrome). By using the slide 1 or slide 5 which maintains flurochrome in newly mineralized bone, the primary data were measured from the distal femur trabecular bone region 0.4 mm distal to growth plate and 0.5 mm away from intracortical surface. Under OLYMPUS fluorescence microscope, using OsteoMeasure™ system , at 200 X magnification: Tissue Area (T.Ar), Bone Area (B.Ar), total perimeter (B.Pm), single labeled perimeter (sL.Pm), double labeled perimeter (dL.Pm), and inter-labeled width (Ir.L.Th) of trabecular bone surface were generated as primary data. These primary data were produced by tracing and measuring the area of trabecular bone region of interest (Tissue Area), individual trabecular bone perimeter (B.Pm) and area (Bone Area), single fluorescent dye labeled perimeter (sL.Pm), double fluorescent dyes labeled overlaying perimeters (dL.Pm), and the distance between two flurochrome labels or also called inter-labeled width (Ir.L.Th). There were 6 days apart between two fluorescent labels. From these primary data the quantified data were derived: Bone area/tissue area (BV/TV) = B.Ar/T.Ar (%), MS/BS = (dL.Pm+1/2sL.Pm)/B.Pm×100 (%), MAR = Ir.L.Th / 6 days (μm/day), and BFR/BS = MAR × MS/BS × 365 ($\mu m^3/\mu m^2$/year).

2.7.3 Distal Femur Static Histomorphometry (Von Kossa/MacNeal's Stain)

For the purpose of evaluating the osteoblast activity, a modification of the Von Kossa/MacNeal's (VKM) stain protocol[92] was employed to provide the most reliable discrimination between black stained mineralized bone and pale blue stained osteoid and osteoblast cell morphology. VKM stain also provides clear presentation of osteoclasts absorbed cortical bone surface (absorption bay or eroded bone surface) which can be used to assess osteoclast activity.

Longitudinal cut distal femur sections on slide 3 were deplastified in either acetones (preferred) or MMA + xylenes (osteoid is slightly bluer with acetone). Sections were hydrated through 100% EtOH, 95% EtOH, 70% EtOH, and twice distilled water immersion. Alternatively, the linear stainer was used for this. Later sections were stained in 5% Silver Nitrate solution for 10 minutes in the dark and rinsed in Distilled water for 3 times, 1 minute each. Sections were stained in Sodium Carbonate-Formaldehyde solution for 2 minutes and rinsed in distilled water twice for 1 minute each. Simultaneously Potassium Ferricyanide to Farmer's stain solution was added. Then sections were stained in Farmer's diminisher for 30 seconds and washed in running tap water for 20 minutes.

Sections were rinsed in distilled water for 1 minute and stained in 2% MacNeal's tetrachrome solution (Cat. # 200190, Sigma-Aldrich) for 20 minutes. Sections were rinsed in distilled water three times for 1 minute each. Sections then dehydrated in 1 change of 70% EtOH, 95% EtOH and 100% EtOH; blot between changes of alcohol; alternatively, the linear stainer was used for this. Finally, sections were cleared in 2 changes of xylenes for 5 minutes minimum each. Sections were coverslipped with xylenes-based mounting media.

For osteoblasts activity measurement, under bright field of OLYMPUS fluorescence microscope, using OsteoMeasure™ system, at 400 X magnification, the primary data were measured from the distal femur trabecular bone region 0.4 mm distal to growth plate and 0.5 mm away from intracortical surface (region of interest). By tracing the total area of region of interest, trabecular bone area and perimeter, osteoid perimeter, osteoclasts absorbed surface perimeter (Eroded Surface) and osteoblast covered surface, counting osteoblast number in the region of interest, Tissue Area (T.Ar), Bone Area (B.Ar), total perimeter (B.Pm), osteoid surface (OS), Eroded surface (E.Pm), osteoblast number (N.Ob), osteoblast surface (Ob.Pm) were generated as primary data from Von Kossa/MacNeal's stained sections. From those primary data the quantified data were derived: Bone Volume/Tissue Volume (BV/TV) = B.Ar/T.Ar, Osteoid Surface/trabecular bone surface = OS/B.Pm, Osteoblast surface/trabecular bone surface = Ob.Pm/B.Pm, Eroded surface/Trabecular Bone surface (ES/BS) = E.Pm/B.Pm (%), Osteoblast number/trabecular bone surface = N.Ob/B.Pm, and Osteoblast number/osteoblast surface = N.Ob/Ob.Pm.

2.7.4 Distal Femur Static Histomorphometry (TRAP Stain)

In order to quantify the osteoclast number and activity, Tartrate-acid Resistant Acid Phosphatase (TRAP) stain was used to specifically label osteoclasts[93]. Osteoclasts were specifically stained with red color by TRAP stain and other cells were nuclear stained with Toluidine Blue.

All procedures of TRAP stain were done in Coplin slide staining jars. Coplin jars were pre-warmed to 37 °C in water bath. Distal femur sections on Slide 4 were deplastified in three times of Acetone incubation with agitation at room temperature (RT). Each of the incubations lasted for 20 minutes. Deplastified sections were then rehydrated in graded alcohols: 100% EtOH, 100% EtOH, 95% EtOH, and 70% EtOH, 3 minutes per alcohol change. Sections were stored in double distilled water (ddH$_2$O). Slides were then pre-incubated in 0.2 M acetate buffer (pH 5.0) (CAS 127-09-3; FW 82.03; Sigma-Aldrich 241245) with 50 mM sodium tartrate dibasic dehydrate(CAS 6106-24-7; FW 230.08; Sigma-Aldrich T6251) for 20 minutes at RT. Slides were transferred (drained briefly) from pre-incubation to incubation media with 0.2M acetate buffer (pH 5.0), napthol AS-MX phosphate (0.5 mg/ml) (CAS 1596-56-1; FW 371.3; Sigma-Aldrich N4875), and fast red TR salt (1.1 mg/ml) (CAS 51503-28-7; FW 440.90; Sigma-Aldrich F6760) for 2 hours in 37 °C water bath. Then incubation media was discarded and slides were covered with ddH$_2$O for 5 minutes at RT. Slides were counterstained by Toluidine Blue (Sörensen's Buffer). Finally, all slides were coverslipped with aqueous-based mounting media.

To quantify osteoclasts activity, under bright field of OLYMPUS fluorescence microscope, using OsteoMeasure System™, at 400 X magnification, the primary data were measured from the distal femur trabecular bone region 0.4 mm distal to growth plate and 0.5 mm away from intracortical surface (region of interest). By tracing the total area of region of interest, trabecular bone area and perimeter, and osteoclast covered surface, counting osteoclast numbers in the region of interest trabecular bone surface, Tissue Area (T.Ar), Bone Area (B.Ar), total perimeter (B.Pm), Osteoclast number (N.Oc), and Osteoclast surface (Oc.S) were measured as primary data. From those primary data the quantified data were derived: Bone Volume/Tissue Volume (BV/TV) = B.Ar/T.Ar (%), Osteoclast surface/Trabecular Bone surface (Oc.S.BS) = Oc.S/B.Pm (%), and Osteoclast number/Trabecular Bone surface (N.Oc/BS) = N.Oc/B.Pm (#/mm).

2.7.5 Measurement of Cortical Bone Porosity

In order to assess the potential difference of cortical bone porosity between Stat3 KO mice and WT mice, the histomorphometry analysis of cortical bone porosity was performed by using the OsteoMetrics® System (OsteoMetrics Inc., Decatur, GA). A cross-section of MMA embedded femur was cut from the mid-shaft. Section was grinded and polished to a desired thickness of 30-40 μm. The femur mid-shaft cross-section image was used for measuring large pores (e.g. Harversian canals, and blood vessels) but excluding lacunae of osteocytes. The image for analyze big pores in cortical bone cross-section was acquired from the 200 X magnification under bright field of fluorescence microscope. Primary data were generated by counting the number of pores, area of pores, and total cortical bone area of femur mid-shaft cross-section. The secondary data were derived: number of pores/cortical bone area and total pore area/cortical bone area.

2.8 High Resolution X-ray Imaging

Conditional Stat3 Knockout (KO) mice with bone abnormalities and their bone specimens like femur and vertebra were assessed by high resolution radiographic imaging by Bioptics piXarray 100 Digital Specimen Radiography System (Bioptics Inc., Tucson, AZ, USA). High resolution X-ray images provide direct bone morphological phenotypes of conditional Stat3 KO mice and their littermate controls.

2.9 Peripheral Dual-energy X-ray Absorptionmetry (PixiMUS)

To quantify bone mineral properties, Bone Mineral Density (BMD, g/cm^2) and Bone Mineral Content (BMC, g) of the left femurs of experimental mice were assessed. The BMD and BMC were measured and calculated by using peripheral dual-energy X-ray absorptionmetry (pDXA, PIXIMus II, GE-Lunar Co.).

2.10 Micro Computed Tomography (Micro-CT) Analysis

16-weeks-old adult WT mice (n=6), osteocyte-specific Stat3 KO male mice (n=8), WT female mice (n=14), and osteocyte-specific Stat3 KO female mice (n=13) were euthanized by CO_2 inhalation and cervical dislocation. Left femurs were immediately extracted, stripped of soft tissue, wrapped in 0.85% phosphate buffered saline (PBS, pH 7.4) soaked clean gauze, and placed in labeled small self-seal plastic bags placed in dry ice and stored in -20 °C freezer for micro-CT (μCT) scan. Femurs were brought to room temperature and scanned by using μCT (SkyScan 1172, Bruker-microCT, Kontich, Belgium). The next step after scanning is reconstruction. This is the process by which the raw projection images are converted into individual cross-section slices. Reconstruction can be done by using the SkyScan NRecon software (Bruker-microCT, Kontich, Belgium). Bone X-ray profile images were then reconstructed into three-dimensional (3D) structure and ready for SkyScan CT-Analyser (CTAn) (Bruker-microCT, Kontich, Belgium) software analysis.

For distal femur trabecular bone micro-CT analysis, left femurs were wrapped in parafilm to keep specimens moist, held in Styrofoam, and stabilized on scanning stage of micro-CT machine. By using the scanning parameter setting: Voltage: 60kV, Resolution: 6 μm, Binning mode: 2K, Filter: Al 0.5 mm, Rotation step: 0.7°, and Averaging frame: 2, femur specimens were rotating scanned totally for 180° to generate raw projection images per Rotation step (0.7°). Then these raw projection images were reconstructed by SkyScan NRecon software. To optimize cross-section slides and 3D bone structure reconstruction, reconstruction parameters include that: Post alignment: variable, Smoothing: 2, Ring artifact reduction: 5, Beam hardening: 20, Threshold: 0-0.11 (could differ by study) and File format: BMP. By using the SkyScan CtAn software, bone cross-section images and 3D structure was analyzed 1 mm of tissue with trabecular bone (171 cross-section slides) right above distal femur growth plate. By scrolling through Raw Image file window to find the starting point where the femoral condyle disappears and the cortex is relatively intact. Scrolling images upward through Raw Image file again to find the closest image that is 1 mm above the starting position. In order to analyze the distal femur trabecular bone characteristics, distal trabecular bone region (region of interest) was defined by tracing the trabecular bone region in each cross-section slide but trying to stay away from the cortical bone. In the binary images processing, the Index axis of the Histogram is set to 80 (the selected threshold). In the last step of analysis, a set of 3D analysis basic values and results were generated and saved. From these basic values we mainly report some important results such as: Bone Volume/Tissue Volume (BV/TV), Trabecular Bone Thickness (Tb.Th), Trabecular Bone Number (Tb.N), and Trabecular Bone Separation (Tb.Sp).

In order to evaluate the impact of conditional Stat3 KO on mid-shaft femur's cross-sectional geometric properties. We conducted micro-CT scan at the site of femur mid-shaft in both WT and KO groups by utilizing the same method as distal femur micro-CT scan. Femurs were brought to room temperature and scanned by using μCT with a 12 μm pixel size (SkyScan 1172, Bruker-microCT, Kontich, Belgium). And three-dimensional images were reconstructed. Each three-dimensional data set was arranged as a series of 12 μm thick slices oriented along the long axis of the femur. The femur mid-shaft position was determined by calculated half length site of femur proximal end to distal end distance. Bone geometric properties were then analyzed from mid-shaft 7 sections (3 sections before + 1 midshaft section + 3 sections after) of each bone by using the SkyScan Software CTAn and a MATLAB script wrote by Professor Joseph Wallace at Indiana University-Purdue University Indianapolis, Department of Biomedical Engineering (BME) and edited by BME graduate student Michael Ryne Horn. For the measurement of geometric properties, each section was thresholded into bone and nonbone voxels using a previously defined method[94,95]. Mid-shaft femur geometric properties were reported as described before: cross-sectional area, cortical area, marrow area, average cortical thickness, anterior-posterior (AP) width, medial-lateral (ML) width, AP to ML Ratio, cortical area to total area percentage, and periosteal bone perimeter[96].

2.11 Biomechanical Testing

Femurs after micro-CT scan were used for 3-point biomechanical bone testing. These femurs were wrapped in 0.85% phosphate buffered saline (PBS, pH 7.4) soaked in clean gauze, placed in labeled small self-seal plastic bags and stored in a -20 °C freezer. For later 3-point bending, Femurs were brought to room temperature slowly (approximately 2 hours) and placed in four 100 mm × 20 mm petri dishes (for WT male, KO male, WT female, and KO female groups) which were filled with PBS (pH 7.4) to prevent the bones from drying out.

All femurs were measured from proximal end to distal end to determine overall length. The shortest femur was used as the limiting bone span when determining the span of the bottom two points. The span was set at 6.84 mm and the top point was set at the center of this span at a distance of 3.42 mm. Each femur was then loaded into a 500 lbs actuator with a 25 lbs loading cell (TestResources Inc., Shakopee, MN 55379, USA) (Figure 15) anterior side upward and the distal end to the right. The mid-point of the bone was placed under the top bending cell tip. The loading was done at a rate of 0.03 mm per second up to failure at 30 N, and force-displacement data were collected every 0.04 seconds. The breaking point of each bone was assessed by measuring from the distal end to the break point on the anterior face of the bone due to the oblique fracturing.

During each test, load and deflection were recorded, from which a force-displacement curve was constructed and structural strength (yield force and ultimate force), stiffness (the slope of the linear portion of the force vs. displacement curve), deformation (yield deformation, failure deformation and post-yield deformation), and work (pre-yield work, post-yield work, and total work) were derived at the whole bone level from a force-displacement curve[97,98].

In order to present solely material properties of femurs in a bending test, we need to exclude the effects of geometric structural factors which contributed to resistance to bending. To normalize the data we need to determine the cross-sectional geometry characteristics in a femur fracture site.

To calculate material properties from biomechanical testing of whole bones, the cross-sectional geometry at the breaking site is extracted. Bone geometry was analyzed from midsection slides of each bone scanned using μCT with a 12 μm pixel size (SkyScan 1172, Bruker-microCT, Kontich, Belgium). The μCT scans were then taken to be processed by using the SkyScan Software, DataViewer and CTAn (Bruker-microCT, Kontich, Belgium). In DataViewer the bones were aligned at the distal end with respect to the condyles, with the anterior surface facing right and the midshaft of the bones straightened, so that mediolateral axis coincided with the x-axis. The μCT scan projection images were then reconstructed into cross-sectional slices and one 3D structure then placed into CTAn for analysis. The slice at which the break most nearly occurred was processed, along with 3 slices from the left and the right of the breaking point, for a total of 7 slices. The images were saved as a binary image and used in a MATLAB script written by Professor Joseph Wallace and edited by Michael Ryne Horn[96].

Based on the mid-shaft femur micro-CT image, the second moment of inertia (MOI) of each bone slice was calculated. The MOI is a purely geometric parameter that takes into account the displacement of a material around the centroid to determine the ability to resist bending. A higher MOI will result in a structure that is harder to bend as opposed to a structure with a low MOI.

In order to normalize the material properties of femurs, the force-displacement graphs were transformed into strain-stress curves. The strain-stress transformation was done by taking the force-displacement curve generated by the bending machine and the following equations for 3 point bending:

$$Stress = \sigma = \frac{FLc}{4I}$$

$$Strain = \varepsilon = \frac{12cd}{L^2}$$

Where F is the applied force, L is the bottom span of the 3 point bending, c is the distance from the centroid to the region in compression, I is the MOI, and d is the deformation of the bone. Once transformed, properties such as yield point, Young's modulus, and toughness were calculated.

Bone material properties were calculated such as: ultimate stress (the highest force per area of a material can hold before failure), ultimate strain (maximum deformation representing the bending displacement relative to two bottom point span), Young’s modulus (the slope of the linear region of the stress-strain curve), and total toughness (the area under the stress-strain curve).

2.12 Cell Culture

2.12.1 Primary Bone Marrow Stromal Cell Culture

Conditional Stat3 KO (Col3.6-Cre;Stat3$^{flox/flox}$) mice and their WT littermate control (Col3.6-Cre;Stat3$^{+/+}$) mice between 6-8 weeks old were euthanized with CO_2 and rinsed with 70% EtOH. The skin on the legs was removed and the joint directly above the femur head was cut. The legs were quickly placed in an iced transport medium of α-MEM medium supplemented with 10% FBS, 1% L-glutamine, and 5% antibiotics/antimycotics. The tissues were rinsed with 70% EtOH and the ligaments and muscle tissue surrounding the bones were removed. The exposed bones were washed with HBSS at RT then placed into separate petri dishes containing α-MEM complete medium. The distal and proximal ends of the bones were cut to expose the bone marrow cavities. The marrow was flushed out with α-MEM complete medium into 15 ml sterile centrifuge tubes. The flushing was performed 3 more times until the bone became white. The cells were then resuspended and counted using a hemacytometer. The cells were seeded (passage 0) at 12,000 cells/mm^2 in α-MEM complete medium. After 5 days, the medium was changed using α-MEM complete medium supplemented with 50 μg/ml ascorbic acid and was thereafter changed with the same medium 3 times per week.

2.12.2 Subculturing Cells

The T-75 flask was removed from the 37 °C incubator and the media was aspirated out. A quick wash of the flask was performed with 3 ml of 0.25% trypsin/EDTA in 37 °C incubator, then immediately aspirated out. A second round of 0.25% trypsin/EDTA was added to the flask before the flask was placed back into the incubator for 2-5 minutes at 37 °C. The flask was removed from the incubator and banged by hand to loosen the cells from the flask. The flask was observed under the microscope to verify that the cells were loose from the flask. Once the cells were loose and suspended in the 0.25% trypsin/EDTA, 10 ml of 10% FBS in α-MEM was added to the flask to inactivate the trypsin. All of the fluid in the flask was transferred into a centrifuge tube and centrifuged at 1,000 rpm for 10 minutes. The supernatant was then aspirated leaving only the cell pellets at the bottom. Cells were then re-suspended in 5 ml of 10% FBS in α-MEM for each T-75 flask that was added to the centrifuge tube by pipetting the solution up and down. 5 ml of the re-suspended mixture was added to the T-75 flasks along with 10 ml of 10% FBS in α-MEM.

2.13 Fluid Sheer Stress Study

2.13.1 Coating with Type I Collagen

The slides were autoclaved and placed into petri dishes. A volume of 3 ml collagen was added onto the top of each slide in a uniform manner, and then the slides were left to sit for 3 minutes at RT underneath the biological safety cabinet. Any extra collagen that did not coat the slide was aspirated out. The slides were then left uncovered underneath a UV light overnight. The next day the slides were ready for seeding cells.

2.13.2 Seeding on Type I Collagen Slides

Prior to seeding, the slides coated with type I collagen were prepped by adding 12 ml of 1 X PBS and left to set for 5 minutes. After the 5 minutes, the PBS was aspirated out of the Petri dish. The T-75 flask containing the MC3T3-E1 osteoblasts was removed from the incubator and the media was aspirated out. A quick wash of the flask was performed with 5 ml 0.25% trypsin/EDTA, then immediately aspirated out. A second round of 0.25% trypsin/EDTA was added to the flask before it was inserted into the incubator for 2-5 minutes at 37 °C. The flask was then removed from the incubator and banged by hand to loosen the cells from the flask. Once the cells were loose and suspended in the 0.25% trypsin/EDTA, 10 ml of 10% FBS in α-MEM was added to the flask to inactivate the trypsin. All of the fluid in the flask was transferred into a centrifuge tube through a BD Falcon filter and ran at 1,000 rpm for 10 minutes at 4 °C. The supernatant was aspirated out leaving only the cells at the bottom of the tube. The cells were then re-suspended in 6 ml of 0.2% FBS in α-MEM per T-75 flask then vortexed. A volume of 2 ml of the re-suspended culture was placed on each collagen coated glass slide and left to set under the biological safety cabinet for 2 minutes at RT. The slides were transferred to the incubator to set for 60 minutes at 37 °C. After removal of the slides from the incubator, 12 ml of 10% FBS in α-MEM was added to cover the slide then placed in the incubator for 1-2 days at 37 °C. Once the incubation was complete, the fluid was aspirated and replaced with 12 ml 0.2% FBS in α-MEM and incubated overnight at 37 °C. The cells were then ready for sheering flow in the following day.

2.13.3 *In vitro* Fluid Sheer Stress Applied to MC3T3-E1 Osteoblasts

The fluid flow apparatus was assembled and filled with 0.2% FBS. Two 1 ml syringes were filled with 0.2% FBS and attached to a flow apparatus. After both syringes were attached, the chambers were prepped for cells. The chamber was filled with 0.2% FBS. After filling the chambers, all the bubbles that may have formed were removed. A thin layer of fluid was applied to the interface surface of the chamber and the bubbles were cleared again. A slide of MC3T3-E1 osteoblasts was placed cell-side down on the interface surface. The chamber was sealed and attached to the fluid flow apparatus. Two gas tubes from the CO_2 tank were connected to the chamber for air supply. The CO_2 supply was turned on and set to level 3. Once the apparatus was setup, the desired force of 12 dyn/cm^2 was programmed into the computer and ran for the desired times of 0, 30, 60, and 90 minutes (Figure 16). After the desired time had passed, the slides were removed from the chamber and placed back into its petri dish and was ready for protein or RNA extraction.

2.14 Protein Analysis

2.14.1 Protein Extraction

Inside the biological safety cabinet, each petri dish was washed with 12 ml of cold 1 X PBS twice then aspirated. The slides were then removed from the petri dishes and their edges were blotted, and the bottom was wiped, with a Kimwipe. The cell surface was then blotted very carefully with a Kimwipe. 200 µl of SDS lysis buffer contained 62.5 mM Tris, 2% sodium dodecyl sulfate (SDS), 10% glycerol (v/v), 5 mM EDTA, and 1% protease inhibitor cocktail (Sigma-Aldrich, St. Louis, MO) with a 1% addition of

Proteinase inhibitor cocktail (Sigma-Aldrich, St. Louis, MO) was added to the cell surface side of the slide. The lysis buffer was then spread all over the slide using a cell scraper. The cells were scraped to one corner of the slide and poured into an eppendorf tube. The eppendorf tube filled with cells was then boiled 10 minutes to denature the proteins. After removing the cells from the boiling water, they were placed into a centrifuge and ran at full speed of 14,000 x g for 10 mins at 4 °C to remove any cellular debris for 10 minutes. Protein assay was performed using a Bio-Rad detergent compatible (DC) protein assay. Twenty micrograms of whole cell lysates were separated by 10% SDS polyacrylamide gel electrophoresis and electrotransferred to a nitrocellulose membrane. The supernatant was then collected and frozen. The protein was then available for analysis.

2.14.2 Electrophoresis

Samples were quantitated using BIORAD protein assay (BIORAD Laboratories, Hercules, CA), then read on a spectrophotometer at a wavelength of 650 nm. Reading results were then used to calculate the concentration of protein in the samples to determine the accurate volume to be added to the gel. 10 μg of the total protein sample, 2.5 μl of 4 X NuPage LDS Sample Buffer (Invitrogen, Carlsbad, CA) and 1 μl of 10 X NuPage Reducing Agent (Invitrogen, Carlsbad, CA) was added to each of the tubes. If the volume was less than 10 μl, Nuclease-Free Water (Invitrogen, Carlsbad, CA) was added until the total volume of 10 μl was reached. The samples were then heated in a dry bath at 70 °C for 10 minutes.

The NuPage 10% Bis-Tris Gel 1.0 mm × 12 wells (Invitrogen, Carlsbad, CA) were rinsed with Milli-Q water and the wells were exposed. The cassette wells were gently washed twice with 1 X running buffer (Invitrogen, Carlsbad, CA) and the cassette was placed into the lower buffer chamber. The upper buffer chamber was filled with 200 ml of running buffer (Invitrogen, Carlsbad, CA) and 500 µl of NuPage antioxidants (Invitrogen, Carlsbad, CA). The samples were carefully added to the sample wells. The loading buffer was placed in each well to assure proper flow. Once the samples were ready, the lower buffer was filled with approximately 600 ml of running buffer (Invitrogen, Carlsbad, CA). The samples were then run at 200 V and 120 mA for 40 minutes. After the run had completed, the gel was ready for Western Blot.

2.14.3 Western Blot

Using approximately 700 ml of transfer buffer (Invitrogen, Carlsbad, CA), the nitrocellulose membranes, sponge pads, and filter papers were soaked. Placing onto the blot module, the materials were added in this order: blotting pad, blotting pad, filter paper, first gel, transfer membrane, filter paper, blotting pad, filter paper, second gel, transfer membrane, filter paper, blotting pad, and blotting pad. The constructed blot module was placed into the lower buffer chamber and locked in with a gel tension wedge. The blot module was then filled with transfer buffer (Invitrogen, Carlsbad, CA) until the membrane assembly was completely submerged. In the outer buffer chamber, approximately 650 ml of Milli-Q water was poured between the front of the blot module and the front of the lower chamber. The Western Blot was then run at 30 V constant and a current of 170 mA for 1 hour.

After the Western Blot was finished, the membranes were placed into Blotto (Invitrogen, Carlsbad, CA) and mixed at room temperature on shaker level 2 for 45-60 minutes. The membranes were removed from the shaker and washed with Tris-buffered saline containing 5% nonfat dry milk and 0.1% Tween-20 (TBST) briefly to remove the Blotto solution. The membranes were then divided and placed into 10 µl of rabbit anti-pStat3 Ser727 (Santa Cruz Biotechnology Inc., Santa Cruz, CA) and 10 µl of rabbit anti-pStat3 B-7 (Santa Cruz Biotechnology Inc., Santa Cruz, CA) antibodies with 1:1000 dilution (200 µg/ml) diluted with 10 ml TBST for 60 minutes on shaker level 2 (can be stored overnight on shaker level 2 in 4 °C). The membranes were removed from the primary antibody solutions and washed 5 times for 5 minutes in TBST on shaker level 5. The membranes were removed from TBST and placed in 2 µl of 1:5000 diluted goat anti-rabbit IgG hydroperoxidase conjugated secondary antibodies solution (Santa Cruz Biotechnology Inc., Santa Cruz, CA), which was diluted with 10 ml TBST. The membranes in the solution were placed on a shaker for 30 minutes on level 2. The membranes were then removed from the secondary antibody solution and washed 5 times for 5 minutes in TBST on shaker level 5. Once the washing had completed the Pierce Enhanced Chemiluminescence (ECL) Western Blotting Substrate (Thermo Fisher Scientific Inc., Waltham, MA) was mixed on some plastic wrap on the lab bench. The membranes were placed protein side down on the ECL mixture (Thermo Fisher Scientific Inc., Waltham, MA) and swirled in it for 60 seconds. After applying ECL, the membranes were covered and developed.

2.15 Gene Expression Analysis

2.15.1 Long Bone Osteocytes Extraction

8 weeks old osteocyte-specific Stat3 KO (*Dmp1-Cre;Stat3*$^{flox/flox}$) mice and their WT littermate control (*Dmp1-Cre;Stat3*$^{+/+}$) mice were sacrificed by CO_2 euthanization. Experimental mice were sterilized with 70% EtOH. Rapidly remove legs and arms and place in 5 ml tubes with 3 ml of α-MEM (Sigma-Aldrich, St. Louis, MO) with 1% penicillin and streptomycin (Life Technologies Corporation, Carlsbad, CA) (α-MEM+ solution). And later legs and arms were transferred to 10 cm cell culture plates with α-MEM+ solution immediately. Skin and soft tissues were removed. Usually we use three 10 cm plates; Plate 1 was used for removing soft tissue and cut both ends of the long bone. Plate 2 was used for cleaning bones. Plate 3 solution was for flushing out bone marrow.

Under the dissection microscope, while long bones (femurs, tibiae, and humeri) were in α-MEM+ solution (Plate 1), most of the muscles were removed. The bone shafts were free of muscles. By using new scalpels, scraping off periosteum and rocking back and forth on tips of the bone, epiphyseal region and part of the growth plate were removed, exposing the trabecular and bone marrow. These long bones were in the size of 1 to 1.3 cm long without the joint and growth plate region, Long bone cylinders can be cut longitudinally for the next steps.

The long bone cylinders were transferred into a new dish (plate 2) with α-MEM+ solution. Bone marrow was flushed out by using α-MEM+ in an 1 ml syringe with a 26 G needle until the bones became white and no reddish color. The bone cylinders were then placed in Plate 3 and stored in the cell culture incubator at 37 °C. Then the bones were placed in a 3 ml 0.2% Collagenase solution (Collagenase, Type II, *Clostridium histolyticum*, EMD Millipore Corporation, Billerica, MA, USA) in 5 ml tubes and on a shaker at 37 °C and rotated for 30 minutes at 150 rpm. Usually, 2-6 bone cylinders from the same animal were placed in the same 5 ml tube. Repeat the previous step by aspirating out the old solution and adding a new 3 ml 0.2% Collagenase solution to 5 ml tubes with bone cylinders at 37 °C and rotation for 20 minutes at 150 rpm. 3 ml of 0.2% Collagenase solution was changed and the 20 minutes at 150 rpm rotation was done for the third time. For RNA and protein isolation, bone cylinders were washed with cold PBS 3 times. Then they were transferred to 1.5 ml eppendorf tubes. Bone cylinders were snap frozen in liquid nitrogen and stored at -80 °C.

2.15.2 RNA Extraction

Inside the fume hood, bone cylinders from -80 °C were placed in the autoclaved mortar filled with liquid nitrogen. Bone cylinders were then smashed and grinded by the autoclaved pestle into small fragments and powders in the presence of liquid nitrogen. Bone fragments were then transferred into a new sterile 5 ml cell culture tube with liquid nitrogen. 3 ml of TRIzol (Invitrogen, Carlsbad, CA) was added to the tube with smashed bone fragments and mixed well by shaking the tube. The lysate was incubated with TRIzol at RT for 5 minutes to allow complete dissociation of nucleoprotein complexes. Tubes with lysate were centrifuged at 12,000 x g for 10 minutes at 2 to 8 °C. The liquid phase of lysate was collected into new tubes by pouring. Pellets were discarded. 600 μl chloroform (Sigma-Aldrich, St. Louis, MO) (Chloroform : Trizol = 1:5) was added into each tube. The tubes were then capped and shaken vigorously by hand for 15 seconds. They were then incubated again at RT for 3 minutes or may let it sit on ice for 15 minutes. After incubation, the samples were centrifuged at 12,000 x g for 15 minutes at 4 °C. After being centrifuged, the mixture will have separated into three phases: Lower phase, red, phenol-chloroform (with proteins and lipids) Inter-phase, thin white layer (with DNA), Upper phase (aqueous), colorless (with RNA). Supernatant was transferred from the upper ¾ of the aqueous phase (RNA contained) to a new 5 ml falcon sterile cell culture tube with pipette upright to transfer. 1.5 ml isopropyl alcohol (Isopropanol : TRIzol = 0.5 : 1) was added into the new tube and mixed thoroughly. Samples were incubated at RT for 10 minutes. New tubes were then centrifuged at 12,000 x g for 10 minutes at RT. Supernatant was carefully decanted and discard by placing the centrifuge tube upside down on absorbent paper to get rid of the isopropanol. The inside wall of the tube may be wiped with kimwipe. 3 ml of 75% EtOH was added to the centrifuge tube and was vortexed which completely dissolved the RNA pellet. Any visible precipitate that had formed was removed. Dissolved RNA samples were then centrifuged at 7,500 x g for 5 minutes at RT. Supernatant was removed and the pellet was saved. The pellet was then transferred with a new 1 ml of 75% ETOH into a new 1.5 ml Rnase-free eppendorf tubes and was vortexed. The eppendorf tubes were centrifuged at 7,500 x g for 5 minutes at RT in the mini-centrifuge machine. And then supernatant was removed as much as possible and the pellet was let air dry. The final pellet was resuspended in 20 µl of UltraPure™ DNase/Rnase-Free Distilled Water (Invitrogen, Carlsbad, CA). Isolated RNA samples were then transferred into new Rnase-free PCR tubes on ice. 2 µl of RNA was used for

Nanodrop 2000/2000C (Thermo Fisher Scientific Inc., Waltham, MA) to test RNA concentration. The OD at 260 and 280 nm wavelength was measured to calculate the A260/A280 ratio (A260/A280=1.95 indicates the pure of RNA, if < 1.65, not pure). Purified RNA samples were stored in the -80 °C freezer for Real-Time PCR.

2.15.3 Quantitative Real-Time PCR Analysis

Purified RNA samples were subjected to cDNA synthesis. A quantity of 5 μg of total RNA were reverse transcribed in a 20 μl reaction mixture containing 50 ng/μl ramdom hexamers mixed together with 200 U/μl of Superscript® III reverse transcriptase according to the manufacturer's instructions for Superscript® III first strand synthesis system for RT-PCR (Invitrogen, Carlsbad, CA). GAPDH, Stat3, Sclerostin (SOST), Type I Collagen, and Osteocalcin were selected for quantitative Real-Time PCR (qPCR) analysis. All the qPCR reactions contained the first-strand cDNA corresponding to 25 ng of total RNA. Quantitative Real-Time PCR was carried out by using the FastStart Universal SYBR Green Master (ROX) (Roche Diagnostics, Mannheim, Germany) following the manufacturer's protocol to quantify the relative gene expression, with GAPDH as an endogenous control. 7300 Real-Time PCR System (Applied Biosystems, Foster City, CA) was used for Real-Time PCR analysis according to the manufacturer's instructions. The relative expression of mRNA was calculated based on a relative standard curve and normalized to GAPDH. All qPCR analysis used triplicates of each of the biological samples. The primers of genes used in qPCR were listed as follows: endogenous control gene: *GAPDH* forward primer: 5'-CGTGGGGCTGCCCAGAACAT-3', reverse primer: 5'-

TCTCCAGGCGGCACGTCAGA-3’. Experimental genes: *Stat3* forward primer: 5’-ATTGGAACCTGGGACCAAGTGG-3’, reverse primer: 5’-ACATGTACTTACAGGGTGTGTGC-3’, *SOST* forward primer: 5’-TCCTCCTGAGAACAACCAGAC-3’, reverse primer: 5’-TGTCAGGAAGCGGGTGTAGTG-3’. *Type 1 Collagen* forward primer: 5’-CAGGGAAGCCTCTTTCTCCT-3’, reverse primer: 5’-ACGTCCTGGTGAAGTTGGTC-3’. *Osteocalcin* forward primer: 5’-AAGCAGGAGGGCAATAAGGT-3’, reverse primer: 5’-TTTGTAGTCGGTCTTCAAGC-3’. All primers were synthesized by Integrated DNA Technologies Inc. (Coralville, IA, USA).

2.16 Measurement of Reactive Oxygen Species (ROS)

The cell-permeable dye, 2,7-dichlorodihydrofluorescein diacetate (2,7-DCF-DA) (Sigma-Aldrich St. Louis, MO), was employed as an indicator of the ROS level[99]. First, approximately 3×105 cells isolated from Stat3 KO (Col3.6-Cre;Stat3$^{flox/flox}$) and control (Col3.6-Cre;Stat3$^{+/+}$) calvarias were plated in 6 well plates in full serum media for 24 hours. Then, cells were treated with 10 mM hydrogen peroxide (H_2O_2) (as a positive control), in the presence and absence of 50 mM AG-490 (Stat3 inhibitor) for 2 hours[100]. Cells were then suspended with 10 mM DCFDA, and assayed for ROS using flow cytometry.

2.17 Measurement of NAD^+/NADH Ratio

In order to study whether inactivation of Stat3 affects mitochondrial functions in response to mechanical stimulation, NAD^+/NADH ratio in the mitochondria Complex I was evaluated. Stat3 KO and control calvarial cells were subjected to oscillatory fluid shear stress (FSS at 12 dyns/cm^2) for1 hour. The cells without FSS served as a control. Immediately following FSS, cells were collected and quantitative determination of NAD^+/NADH was conducted using an EnzyChrom NAD^+/NADH assay kit (BioAssay Systems, Hayward, CA). Both NAD^+ and NADH concentrations were measured and normalized by protein contents. The ratio of NAD^+/NADH was then calculated. NADH is oxidized to NAD^+ at mitochondrial Complex I. We compared the ratio of NAD^+/NADH between wild type and Stat3 deficient mice in order to demonstrate the accumulation of NADH in Stat3 deficient osteoblasts due to the dysfunction of mitochondrial Complex I.

2.18 Statistical Analysis

All the data were expressed as mean ± S.E.M. (standard error of the mean). Bartlett’s test (a test of the homogeneity of variances among groups) indicated that group variances were equal ($P > 0.5$), suggesting that the parametric statistical tests were valid. Phenotypic values among the selected genotypes for a given sex were compared by one-way analysis of variance (ANOVA). Gender comparisons were performed using a two-way ANOVA with sex and genotype as independent variables. Differences between parameters in the loaded (right) and non-loaded (left) ulnae were tested using paired t tests. Difference among group means were tested for significance by ANOVA, followed by Fisher’s protected least significant difference test (PLSD) for pair-wise comparisons. Statistical significance was assumed if $P < 0.05$.

CHAPTER 3. RESULTS

3.1 Verification of Osteoblast/osteocyte-specific Stat3 Knockout Mice by Immunohistochemistry

The conditional Stat3 knockout animal models were generated as previously described in Chapter 2. The type I collagen promoter drove the expression of the Cre gene, specifically in osteoblasts, which deletes two LoxP sites flanked exons 18-20 of the Stat3 gene. As mentioned in Chapter 2, mice with the genotype of Col3.6-Cre;Stat3$^{flox/flox}$ were used as Stat3 knockout mice. And Col3.6-Cre;Stat3$^{+/+}$ mice were used as the littermate wild type controls. The genotypes were determined by PCR amplification as described in Chapter 2. The PCR for Stat3 knockout mice amplified a Stat3 band of 520 bp and a 615 bp Cre band. But for the littermate control mice, PCR amplified a 490 bp Stat3 band and a 615 bp Cre band (Figure 10). Since osteocytes are differentiated from osteoblasts, the Stat3 knockout event first happens in osteoblasts and subsequently in osteocytes. Therefore, Stat3 is eliminated in both osteoblasts and osteocytes in Col3.6-Cre;Stat3$^{flox/flox}$ mice. After the experimental mice had been genotyped, an immunohistochemical staining was done to verify the elimination of Stat3 by the Cre-LoxP system in osteoblasts and osteocytes (Figure 17). Stat3 proteins were not presented in either the osteoblasts or osteocytes of Col3.6-Cre;Stat3$^{flox/flox}$ mice (Figure 17). This demonstrated that Stat3 expression was inhibited in osteoblast/osteocyte specific Stat3 knockout mice.

3.2 Phenotypes of Osteoblast/osteocyte-specific Stat3 Knockout Mice

After the Stat3 KO mice were bred, it was observed that about 10% of the Stat3 deficient mice were extremely small in body size and exhibited a spine deformity, which was noticeable at the age of 3-4 weeks in Col3.6-Cre;Stat3$^{flox/flox}$ mice (Figure 18). Those mice were unable to survive longer than 8 weeks and were excluded in further studies.

The bone phenotypes were characterized when they were 18 weeks old. The female Col3.6-Cre;Stat3$^{flox/flox}$ mice had significantly smaller body weights. Their body weights were 11% lower when compared with the WT littermate controls (P=0.02). Whereas, the average body mass was not statistically different in male KO and littermate control mice (Table 2). For both sexes, femur lengths were significantly shorter in Col3.6-Cre;Stat3$^{flox/flox}$ mice than their littermate controls (Table 2). A radiograph analysis was also performed on the femurs of the Col3.6-Cre;Stat3$^{flox/flox}$ mice and their littermate control mice. The radiograph showed that the femurs of osteoblast/osteocyte-specific Stat3 knockout (KO) mice were shorter (Figure 19).

The pixiMUS analysis of the conditional Stat3 KO mice determined that the BMC and BMD were significantly lower in the KO mice than control littermates (Table 2). In the KO female mice, the BMC was 13% lower (p<0.01) and the BMD was 7% lower

($p<0.05$). Similarly, in the KO male mice, the BMC was 11% lower ($p<0.05$) and the BMD was 12% lower ($p<0.001$).

Osteoblast/osteocyte-specific Stat3 KO mice exhibit a lower bone mass phenotype for BMC and BMD in both genders. Von Kossa/MacNeal's stained distal femur of the conditional Stat3 KO mice was then examined under a light microscope to determine the trabecular bone size and number. The image of the distal femur showed a decrease in both trabecular bone size and number in the KO mice compared to the control mice (Figure 20). The bone phenotype of the lumbar vertebra was further examined for each mouse, and a micro-CT was performed on the 4th lumbar vertebra (L4). The micro-CTs demonstrated lower trabecular numbers for the conditional Stat3 KO mice than for the littermate controls (Figure 21).

3.3 Osteoblast/osteocyte-specific Stat3 KO Mice Present a Decrease in Bone Formation

In order to investigate if the decreased bone mass and density seen in the osteoblast/osteocyte-specific Stat3 knockout mice was caused by a decrease in bone formation or increased bone resorption or both, bone dynamic (fluorescent labels) and static histomorphometry (Von Kossa/MacNeal's stain) were conducted using trabecular bones at distal femurs of 18-week-old adult mice. In this study, we examined both osteoblast recruitment and activity, along with osteoclast number and activity (TRAP stain).

The static histomorphometry (Von Kossa/MacNeal's stain) results presented the following results: at the distal femur, for both female and male mice, bone volume was significantly less in the KO (Col3.6-Cre;Stat3$^{flox/flox}$) mice than their wild type littermate controls (Figure 20). The bone volume in the distal femur was quantified. Compared to their littermate controls, in females, the bone volume of the conditional Stat3 KO mice was 39% lower ($p<0.05$). In males, the bone volume of the conditional Stat3 KO mice was 38% lower ($p<0.05$) (Table 2). Furthermore, the TRAP stain results demonstrated that the number of osteoclasts was statistically similar between the KO mice and their WT control mice. However, the osteoclast surfaces were significantly greater in the KO mice. Compared to their littermate controls, in females, the osteoclast surfaces of the conditional Stat3 KO mice were 39% greater ($p<0.05$), and in males, the osteoclast surfaces of the KO mice were 40% greater ($p<0.05$) (Table 2).

The dynamic histomorphometry results demonstrated that both the recruitment and activity of osteoblasts was compromised in the conditional Stat3 KO mice. The red (alizarin) and green (calcein) fluorescent labels of the trabecular bones at the distal femur indicated new calcified bone formation by osteoblasts. The more fluorescent labels found the more new bone formation. The distance between two fluorescent labels was used to demonstrate the rate of new bone formation. The bigger distance between two labels indicates faster new bone formation rate. The conditional Stat3 KO mice presented fewer fluorescent labels and a shorter distance between two labels than the WT control mice, which indicated compromised new bone formation in the KO mice (Figure 22). The quantified data of the dynamic histomorphometry were generated. Compared to wild type control mice, in females, the mineralizing surface (MS/BS) of the KO mice was 24% ($p<0.01$) smaller, and in males, the MS/BS of the KO mice was 29% ($p<0.05$) smaller (Table 2). In the females, the mineral appositional rate (MAR) of the KO mice was 54% ($p<0.001$) lower, and in the males, the MAR of the KO mice was 56% ($p<0.05$) lower (Table 2). And the bone formation rate (BFR/BS) of the KO mice was 63% ($p<0.001$) and 65% ($p<0.05$) lower in the females and the males, respectively (Table 2).

From the above data, we can summarize that lower trabecular bone volume and less new bone formation present in osteoblast/osteocyte-specific Stat3 KO mice compared to littermate controls.

3.4 Osteoblast/osteocyte-specific Stat3 KO Mice Exhibit a Decrease in Bone Biomechanical Properties

In order to evaluate the biomechanical properties of bone in KO (Col3.6-Cre;Stat3$^{flox/fox}$) mice and their wild type littermate controls, the left femurs were subjected to a three-point mechanical bending test. We found the bone strength of the KO mice was significantly lower than that of the WT control mice. Quantified data were generated. For both genders, compared to the WT control mice, the ultimate forces (FU) were 28% ($p<0.01$) lower in the female KO mice and were 27% ($p<0.01$) lower in the male KO mice (Table 2). The stiffness (S) was reduced significantly in the KO mice in comparison with their littermate controls. In the females, the stiffness was 36% ($p<0.01$) lower, and in the males, the stiffness was 40% ($p<0.001$) lower (Table 2). These data suggest that inactivation of the Stat3 specific to osteoblasts and osteocytes significantly decreases bone strength.

3.5 Osteoblast/osteocyte-specific Stat3 KO Mice Exhibit a Decrease in Load-induced Bone Formation

In order to reveal the role of Stat3 in load-induced bone formation, the conditional Stat3 KO (Col3.6-Cre;Stat3$^{flox/flox}$) mice as well as their wild type littermate control mice (Col3.6-Cre;Stat3$^{+/+}$) were subjected to dynamic axial ulna loading as described in Chapter 2 and Figure 12. And their load-induced bone formation responses were evaluated and quantified as mentioned in Chapter 2, Figure13, and Figure 14. The dynamic histomorphometry results demonstrate that load-induced bone formation was suppressed in both the male and female conditional Stat3 KO mice. The histomorphometrical data from the female Col3.6-Cre;Stat3$^{flox/flox}$ mice and their WT (Col3.6-Cre;Stat3$^{+/+}$) controls shows that there is significantly less calcified new bone formation and a lower rate of new bone formation after loading (Figure 23). Quantified data were also generated. Compared to their WT littermate controls, the relative mineralizing surface (rMS/BS), the relative mineral appositional rate (rMAR), and the relative bone formation rate (rBFR/BS) in response to robust axial ulna loading were all significantly lower in the KO mice (Figure 24). In the female mice, for instance, the relative bone formation rate (BFR/BS in the right ulna minus BFR/BS in the left ulna) was roughly 56% lower in the Col3.6-Cre;Stat3$^{flox/flox}$ mice. These loading data support the speculation that Stat3 plays an important role in load-induced bone formation.

3.6 Fluid Shear Stress (FSS) Increases Stat3 Activation in Osteoblasts

In order to study the Stat3 response to mechanical loading, fluid shear stress was employed to apply stress to osteoblasts; fluid shear stress is usually used to mimic *in vivo* mechanical strain on osteoblasts and osteocytes. *In vivo*, bone cells experience interstitial fluid shear stress upon mechanical loading of bone through fluid flow inside the canalicular-lacunar network and trabecular spaces within bone tissue[104]. Mechanical strain and fluid shear stress have also been demonstrated to influence osteodifferentiation and osteoblast proliferation, with load-induced fluid shear stress being shown to have great effects on new bone formation[105-107]. This fluid flow exerts a shear stress at the surfaces of osteoblasts and osteocytes lining canalicular-lacunar spaces, and the shear stress then generates biochemical signals that transduce to the nucleus of bone cells to exert biological effects. The mechanism whereby the shear stress transduces biochemical signals from the membrane to the nucleus by Stat3 proteins is generally referred to as the Stat3 mechanotransduction mechanism and is not well understood.

In this experiment, MC3T3-E1 osteoblasts[110] were seeded on type I collagen layers deposited on a glass slide to mimic the *in vivo* bone matrix. These osteoblasts were subjected to FSS of 12 dyns/cm^2 over time lapses of 0 minutes, 30 minutes, 60 minutes, and 90 minutes. Examination of the phosphorylation of Stat3 at the tyrosine 705 and the serine 727 residues indicated activation of Stat3 in response to stimulation. Western blot analysis showed that phosphorylation of Stat3 at both the tyrosine 705 and the serine 727 residues increased in a time-dependent manner over a 90-minute period (Figure 25). These data indicated that Stat3 protein activation can be stimulated by mechanical loading of FSS. The quantity of phosphorylated Stat3 protein increases with the accumulation of time as FSS is applied to osteoblasts, which demonstrates a time-dependent manner of Stat3 protein activation in response to mechanical FSS.

3.7 Stat3 Deficiency in Osteoblasts Increases the Level of Reactive Oxygen Species (ROS)

Clinical evidence suggests that osteoporosis and age related bone loss is associated with an increased level of ROS-linked oxidative stress[111-117]. Oxidative stress is also known to antagonize Wnt signaling, which is critical in load-induced bone formation[118,119]. Therefore, an increased level of ROS-linked oxidative stress would compromise Wnt signaling pathways and consequently decrease load-induced bone formation.

In recent research, Stat3 proteins have been found to reside within the mitochondria of mouse myocytes and hepatocytes[123]. Without Stat3, an electron transport chain (ETC) that generates energy by oxidative phosphorylation is inhibited and reduction in mitochondrial activity leads to accumulation of ROS, but the number of mitochondria and their protein contents that constituted complexes I and II are not altered[120,121,122]. On the other hand, adding Stat3 to Stat3-null cells can restore oxidative phosphorylation, and this rescue of mitochondrial function does not require the DNA binding domain. However, the expression of Stat3 with a mutation that prevents phosphorylation of the serine 727 does not induce the rescue effect[123]. This data suggests that the conserved serine phosphorylation site on Stat3 is important for regulation of mitochondrial activity.

In order to investigate whether Stat3 deficiency would jeopardize the mitochondrial function of osteoblasts by elevating the level of intracellular ROS, calvarial osteoblasts from Stat3 deficient (Col3.6-Cre;Stat3$^{flox/flox}$) mice and wild type control (Col3.6-Cre;Stat3$^{+/+}$) mice were cultured and assayed for ROS using DCF-DA and flow cytometry. The ROS level was significantly higher in Stat3 deficient osteoblasts than in wild type control cells (Figure 26). Furthermore, the addition of the Stat3 inhibitor AG490 significantly increased the production of ROS in the control cells, but it did not change the ROS level in Stat3 deficient osteoblasts (Figure 26). This data suggests that the inactivation of Stat3 both in KO osteoblasts as well as in AG-490 treated control osteoblasts increases the intracellular ROS level.

3.8 Stat3 Deficiency in Osteoblasts Decreases the NAD$^+$/NADH Ratio in Mitochondria

Recent studies have suggested that Stat3 is involved in mitochondrial functions and Stat3 regulates cellular respiration and metabolism in mitochondria[123,124]. Inactivation of Stat3 in osteoblasts might lead to reduced mitochondrial respiration and impaired mitochondrial function in response to mechanical loading. In order to evaluate mitochondrial function and its response to fluid shear stress (FSS), the NAD$^+$/NADH ratio in mitochondria Complex I was measured. Stat3 KO and control osteoblasts were subjected to oscillatory FSS at 12 dyns/cm^2 for 1 hour. The cells without FSS served as a control. The measurement of NAD$^+$/NADH ratio demonstrated that: first, without FSS, the NAD$^+$/NADH ratio in Stat3 deficient osteoblasts was significantly lower than in control osteoblasts (Figure 27). Second, FSS significantly increased the NAD$^+$/NADH ratio in control osteoblasts (Figure 27). Moreover, the Stat3 deficient osteoblasts presented a 31% lower NAD$^+$/NADH ratio than that of the wild type control osteoblasts (p=0.01). And these Stat3 deficient osteoblasts did not show any alteration in the

NAD^+/NADH ratio in response to FSS. The first data indicates there was an accumulation of NADH in the Stat3 deficient osteoblasts, suggesting the dysfunction of mitochondrial Complex I. The second data shows a mitochondrial respiration response to mechanical loading (FSS) in wild type osteoblasts, and indicates that Stat3 deficiency in osteoblasts impairs mitochondrial respiration in response to FSS.

3.9 Analysis of Osteoblast/osteocyte-specific Stat3 Inactivation

After transgenic mice breeding, the PCR genotyping determined the correct genotypes for osteoblast/osteocyte-specific Stat3 knockout (KO) mice and their age matched wild type (WT) littermate control mice. And the subsequent immunohistochemical staining confirmed the elimination of Stat3 proteins in osteoblast/osteocyte-specific Stat3 knockout mice.

Compared to their age matched wild type littermate control mice, osteoblast/osteocyte-specific Stat3 knockout mice demonstrated some abnormal phenotypes like: smaller body size, smaller body weight, a spinal deformity, and significantly shorter femur length. This data indicates inactivation of Stat3 in osteoblasts and osteocytes impaired normal bone development.

In the bone tissue level, osteoblast/osteocyte specific knockout mice demonstrated a significantly lower bone mass phenotype presented by lower femur bone mineral content (BMC) and lower bone mineral density (BMD) than their age matched wild type littermate controls. In both femur and lumbar vertebra body L4 of Stat3 KO mice, the trabecular bone size and number were significantly smaller than that of their age matched wild type (WT) littermate controls. Furthermore, in Stat3 KO mice, the biomechanical properties of bone were significantly compromised. This data demonstrates that inactivation of Stat3 in osteoblasts and osteocytes reduces bone mass, bone density, and bone strength.

The static bone histomorphometry showed smaller trabecular bone volume and larger osteoclast surfaces in osteoblast/osteocyte-specific Stat3 KO mice compared to their age matched WT littermate control mice. Furthermore, the dynamic bone histomorphometry of KO mice presented a significantly reduced bone formation rate and decreased osteoblast activity than that of WT controls. This data demonstrates that inactivation of Stat3 in osteoblasts and osteocytes significantly increases osteoclast surfaces and decreases osteoblast recruitment and activity, thus reducing new bone formation, which might cause the reduced trabecular bone volume and number, decreased bone mass and density, and reduced bone strength in KO mice.

In the *in vivo* loading study, the osteoblast/osteocyte-specific Stat3 KO mice presented a significantly reduced new bone formation by osteoblasts. This data suggested that inactivation of Stat3 in osteoblasts and osteocytes decreased load-induced new bone formation. However, there might be two reasons that caused the result: first, inactivation of Stat3 in osteoblast might impair differentiation and proliferation of osteoblasts and jeopardize normal osteoblast function of new bone formation. Second, osteocytes are important mechano signal sensoring cells[88,89,90] . Stat3, as a critical signal transducer, might play an important role in transducing mechanical signal into biological signal to promote load-induced new bone formation. Inactivation of Stat3 in osteocytes would strongly reduce the mechanical signal transduction and subsequently reduce load-induced new bone formation.

In the *in vitro* osteoblasts fluid shear stress (FSS) study, both tyrosine and serine phosphorylations of Stat3 increased from 30 to 90 minutes during FSS was applied on the osteoblasts, which indicates that Stat3 is activated in response to mechanical stimulation and suggests Stat3 is an important signaling molecule for mechanical signal transduction. Furthermore, the increased conserved serine phosphorylation of Stat3 which is critical in regulation of mitochondrial activities[123], suggests that Stat3 might play an important role in mitochondrial function of osteoblasts in response to mechanical loading.

In the osteoblastic reactive oxygen species (ROS) study, the basal ROS level of Stat3 deficient osteoblasts was significantly higher than wild type osteoblasts. This data demonstrates that inactivation of Stat3 jeopardized mitochondrial activity, and led to accumulation of ROS in osteoblasts. The impaired mitochondrial function and elevated ROS level in Stat3 deficient osteoblasts might be an important factor in causing decreased bone mass and density in osteoblast/osteocyte-specific Stat3 KO mice, and decrease load-induced new bone formation in Stat3 KO mice.

The measurement of NAD^+/NADH ratio in mitochondria Complex I, which is an important component of the electron transport chain (ETC), indicated that there is a mitochondrial respiration response to mechanical loading (FSS) in wild type osteoblasts. However, osteoblasts with Stat3 deficiency possess a lower basal NAD^+/NADH ratio than that of wild type osteoblasts. And Stat3 deficiency impairs mitochondrial respiration of osteoblasts in response to FSS. These results demonstrated that inactivation of Stat3 impaired mitochondria Complex I function and cellular respiration in osteoblasts, and also jeopardized mitochondrial response to mechanical loading (FSS). Furthermore, Stat3 regulates cell respiration and metabolism in mitochondria[123,124]. Without Stat3, an electron transport chain (ETC) is inhibited and reduction in mitochondrial activity leads to accumulation of ROS[120,121,122]. Therefore, elevation of ROS in osteoblasts might cause reduction of new bone formation in the osteoblast/osteocyte-specific Stat3 KO mice.

3.10 Verification of Osteocyte-specific Stat3 Knockout Mice by Immunohistochemistry

In order to differentiate the role Stat3 plays in osteocytes from osteoblasts, the osteocyte-specific Stat3 knockout mice were created as described in Chapter 2. The dentin matrix protein 1 (DMP1) promoter drove the expression of the Cre gene, specifically in osteocytes, which deletes two LoxP sites flanked exons 18-20 of the Stat3 gene. As mentioned in Chapter 2, mice with the genotype of Dmp1-Cre;$Stat3^{flox/flox}$ were used as conditional Stat3 knockout (KO) mice. And Dmp1-Cre; $Stat3^{+/+}$ mice were used as the littermate wild type (WT) controls. The genotypes were determined by PCR amplification as described in Chapter 2. The PCR for Stat3 knockout mice amplified a Stat3 band of 520 bp and a 615 bp Cre band. Whereas, for the littermate control mice, PCR amplified a 490 bp Stat3 band and a 615 Cre band (Figure 10). The Cre-LoxP recombination mechanism in osteocytes was supposed to disrupt Stat3 gene expression solely in osteocytes[87].

To assess the elimination of Stat3 specifically in osteocytes, an immunohistostaining had been done to probe the presence of Stat3 proteins in osteocytes. The results demonstrated that Stat3 proteins were presented in osteocytes of wild type (Dmp1-Cre;Stat3$^{+/+}$) control mice, but not in osteocytes of conditional Stat3 knockout (Dmp1-Cre;Stat3$^{flox/flox}$) mice (Figure 28).

3.11 Phenotypes of Osteocyte-specific Stat3 Knockout Mice

After osteocyte-specific Stat3 knockout mice were generated, it was observed that both osteocyte-specific Stat3 KO mice and their littermate control mice grew normally. During the early stage of growth, before the age of 8 weeks, there was no apparent bone abnormality noticeable.

The bone phenotypes were characterized when both osteocyte-specific Stat3 KO mice and their littermate control mice were 18 weeks old. Compared to their age-matched littermate wild type (WT) control (Dmp1-Cre;Stat3$^{+/+}$) mice, both male and female KO (Dmp1-Cre;Stat3$^{flox/flox}$) mice demonstrated no significant difference in body weights between WT and KO mice in males (p=0.36) and in females (p=0.45) (Figure 29). For both genders, femur lengths of the WT and KO mice were measured, and the results indicated that there was no significant difference between WT and KO mice in males (p=0.95) and females (p=0.11) (Figure 30). A radiograph analysis was performed on femurs of Dmp1-Cre;Stat3$^{flox/flox}$ mice and Dmp-1Cre;Stat3$^{+/+}$ mice. The radiograph presented that there were no difference of femur lengths between osteocyte-specific Stat3 KO mice and their age-matched littermate controls (Figure 31).

The pixiMUS analysis on femurs of the conditional Stat3 KO mice indicated that compared to wild type control mice, the bone mineral density (BMD) of osteocyte-specific Stat3 KO mice exhibited no significant difference in male groups (p=0.47) and female groups (p=0.68) (Figure 32). And there was no significant difference of bone mineral content (BMC) between WT and KO groups in males (p=0.15) and females (p=0.77) (Figure 32). The BMD and BMC of lumbar vertebra L4 were also measured. There was no significant difference of BMD between WT and KO mice in males (p=0.68) and females (p=0.66) (Figure 33). And there was no significant difference of BMC between WT and KO mice in males (p=0.95) and females (p=0.40) (Figure 33).

Osteocyte-specific Stat3 KO mice presented a normal bone mass and density phenotype for BMC and BMD in both genders. To further evaluate the bone phenotypes of conditional Stat3 KO mice, Von Kossa/MacNeal's stained distal femurs of the Dmp1-Cre;Stat3$^{flox/flox}$ mice were then examined under a light microscope and the trabecular bone size and number were determined. The image of the distal femurs demonstrated that there was no significant difference in both trabecular bone size and number between osteocyte-specific Stat3 KO mice and their age-matched littermate control mice (Figure 34). The bone phenotype of the distal femur trabecular bone was further examined for each mouse, and a micro-CT scan was performed on the distal femur trabecular bone region 1 mm above the growth plate. The three-dimensional images of micro-CTs showed that there was no significant difference of trabecular number and volume between the conditional Stat3 KO mice and their age-matched littermate controls (Figure 35).

3.12 Osteocyte-specific Stat3 KO Mice Exhibit a Decrease in Osteoid Surface

In order to investigate the osteoblast activity and osteoclast activity in osteocyte-specific Stat3 KO mice, static histomorphometry (Von Kossa/MacNeal's stain) was employed to assess trabecular bone volume, osteoid surface, and eroded surface of 18-week-old adult conditional Stat3 KO mice and their age-matched wild type littermate control mice.

The distal femurs of Dmp1-Cre;Stat3$^{flox/flox}$ (KO) mice and Dmp1-Cre;Stat3$^{+/+}$ (WT) mice were stained by Von Kossa/MacNeal's staining. The quantified static histomorphometry data of trabecular bone region 0.5 mm above the growth plate from each experimental mouse was generated. The trabecular bone volume of osteocyte-specific Stat3 KO mice was statistically similar to their age-matched WT littermate controls. Compared to their littermate WT controls, in females, the trabecular bone volume of the conditional Stat3 KO mice demonstrated no significant difference ($p=0.39$). In males, the trabecular bone volume of the conditional Stat3 KO mice also presented no significant difference ($p=0.12$) (Figure 36). However, the osteoid surfaces of trabecular bones (OS/BS) were significantly decreased in conditional Stat3 KO mice. Compared to their littermate controls, in females, the osteoid surfaces of the conditional Stat3 KO mice were 46.2% smaller ($p<0.05$), and in males, the osteoid surfaces of the KO mice were 75.8% smaller

($p<0.01$) (Figure 37). Furthermore, due to Von Kossa/MacNeal’s stain blackening calcified bone, the eroded bone surfaces reabsorbed by osteoclasts are easy to trace, and the eroded trabecular bone surface and total trabecular bone surface were measured. The percentage of eroded trabecular bone surface/total trabecular bone surface (ES/BS) was calculated for each mouse to quantify osteoclast activity. The eroded trabecular bone surfaces of conditional Stat3 KO mice were significantly greater than their age-matched WT littermate controls. Compared to their WT controls, in females, ES/BS of KO mice were 240% greater ($p<0.01$), and in males, ES/BS of KO mice were 364% greater ($p<0.05$) (Figure 38) (Figure 39).

3.13 Osteocyte-specific Stat3 KO Mice Present an Increase in Osteoclast Activity

In order to investigate the osteoclast activity of osteocyte-specific Stat3 KO mice, static histomorphometry (TRAP stain) was used to assess number of osteoclasts and osteoclast surface of 18-week-old adult conditional Stat3 KO mice and their age-matched wild type littermate control mice.

The distal femurs of Dmp1-Cre;Stat3$^{flox/flox}$ (KO) mice and Dmp1-Cre;Stat3$^{+/+}$ (WT) mice were also stained by TRAP staining. The number of osteoclasts and osteoclast surface in the trabecular bone region 0.5 mm above growth plate for each experimental mouse were measured. The quantified static histomorphometry data of osteoclast activity were then generated. The osteoclast number (N.Oc/B.Pm) in Dmp1-Cre;Stat3$^{flox/flox}$ mice was significantly greater than that of Dmp1-Cre;Stat3$^{+/+}$ mice (Figure 40). Compared to their WT controls, in females, N.Oc/B.Pm of KO mice were 104% greater ($p<0.01$), and in males, N.Oc/B.Pm of KO mice were 146% greater ($p<0.01$) (Figure 41). Moreover, the osteoclast surface (Oc.S/BS) of conditional Stat3 KO mice was also significantly greater than that of their WT littermate controls. Compared to their WT controls, in females, Oc.S/BS of KO mice were 110% greater ($p<0.01$), and in males, Oc.S/BS of KO mice were 177% greater ($p<0.01$) (Figure 42).

The significantly greater osteoclast number and greater osteoclast surface in osteocyte-specific KO mice than their age-matched WT littermate controls indicated a significantly higher level of osteoclast activity in KO mice than WT mice.

3.14 Osteocyte-specific Stat3 KO Mice Present a Decrease in Bone Formation

In order to evaluate the new bone formation of 18-week-old osteocyte-specific Stat3 KO mice, the dynamic histomorphometry was used to quantify new periosteal bone formation in midshaft femur and distal femur trabecular bone of 18-week-old KO mice and their WT littermate controls. Thereby, the mineralizing surface (MS/BS), mineral apposition rate (MAR), and bone formation rate (BFR/BS) were measured.

In the periosteum of midshaft femur, the conditional Stat3 KO mice presented fewer fluorescent labels and a shorter distance between two fluorescent labels than the WT control mice, which indicated compromised new bone formation in the midshaft femur of KO mice (Figure 43). The quantified data of the dynamic histomorphometry of midshaft femur periosteum were generated. Compared to wild type control mice, in females, the mineralizing surface (MS/BS) of the KO mice was 40.1% ($p<0.05$) smaller, and in males, the MS/BS of the KO mice was 24.6% ($p<0.05$) smaller (Figure 44). In the females, the mineral appositional rate (MAR) of the KO mice was 17.7% ($p<0.05$) lower, and in the males, the MAR of the KO mice was 51.8% ($p<0.05$) lower (Figure 45). Finally, the bone formation rate (BFR/BS) of the KO mice was 49.3% ($p<0.05$) and 64.8% ($p<0.05$) lower in the females and the males, respectively (Figure 46).

In the distal femur trabecular bone, the conditional Stat3 KO mice also showed less fluorescent labeling and a shorter distance between two fluorescent labels than the WT control mice, which indicated compromised new bone formation in the trabecular bone of KO mice (Figure 47). The quantified data of the dynamic histomorphometry of distal femur trabecular bone were generated. Compared to wild type control mice, in females, the mineralizing surface (MS/BS) of the KO mice was 30% ($p<0.05$) smaller, and in males, the MS/BS of the KO mice was 35.3% ($p<0.01$) smaller (Figure 48). In the females, the mineral appositional rate (MAR) of the KO mice was 41% ($p<0.01$) lower, and in the males, the MAR of the KO mice was 35.6% ($p<0.01$) lower (Figure 49). Finally, the bone formation rate (BFR/BS) of the KO mice was 58.1% ($p<0.01$) and 57.8% ($p<0.01$) lower in the females and the males, respectively (Figure 50).

Lower MS/BS, MAR, BFR/BS in both midshaft femur and distal femur trabecular bone of osteocyte-specific KO mice than their wild type age-matched littermate controls demonstrated that inactivation of Stat3 specifically in osteocytes leads to a significant decrease in new bone formation of 18-week-old adult KO mice.

3.15 Osteocyte-specific Stat3 KO Mice Present a Decrease in Bone Material Properties

In the 3-point biomechanical bending test for femurs of both Dmp1-Cre;Stat3$^{flox/flox}$ (osteocyte-specific Stat3 KO) mice and Dmp1-Cre;Stat3$^{+/+}$ (wild type littermate control) mice, bone structural (extrinsic) properties – ultimate force and stiffness – were measured. Bone material (intrinsic) properties – ultimate stress and Young's modulus – were calculated.

Compared to their wild type littermate controls, the ultimate force of osteocytes-specific Stat3 KO mice demonstrated no significant difference for both male (p=0.73) and female (p=0.33) (Figure 51). Furthermore, the stiffness of KO mice also presented no significant difference for both male (p=0.29) and female (p=0.55) (Figure 52). However, compared to wild type control mice, in males, the ultimate stress of the KO mice was 19.6% (p<0.01) lower, and in females, the ultimate stress of the KO mice was 18.8% (p<0.001) lower (Figure 53). In males, the Young's modulus of the KO mice was 32.3% (p<0.05) smaller, and in females, the ultimate stress of the KO mice was 16.6% (p<0.01) smaller (Figure 54).

3.16 Osteocyte-specific Stat3 KO Mice Exhibited an Increase in Midshaft Femur Size

The moment of inertia (MOI) is a purely geometric parameter that takes into account the displacement of a material around the centroid to determine the ability to resist bending. A higher MOI will result in a structure that is harder to bend as opposed to a structure with a low MOI which has less capability to resist bending. The midshaft femur is an approximately cylindrical structure, and the calculation of MOI of midshaft femur can be used to assess the geometric property for the femur to resist bending.

In order to evaluate the geometric property of both osteocyte-specific Stat3 KO mice and their age-matched wild type (WT) littermate control mice, midshaft femurs of both Dmp1-Cre;Stat3$^{flox/flox}$ (KO) mice and Dmp1-Cre;Stat3$^{+/+}$ (WT) mice were scanned by micro-CT, and the midshaft femur MOI of the KO and WT mice were calculated. Compared to WT control mice, in males, the MOI of the KO mice was 39.5% (p=0.02) greater, and in females, the MOI of the KO mice was 18.5% (p=0.01) greater (Figure 55). The significantly greater number of midshaft femur MOI in both male and female KO mice than their control mice indicated a larger displacement of bone material around the centroid, suggesting the larger midshaft size of KO mice than WT mice.

To evaluate more detailed midshaft femur geometrical properties, cross-sectional area (total area), cortical area, marrow area, average cortical thickness, anterior-posterior (AP) width, medial-lateral (ML) width, AP to ML ratio, cortical area to total area percentage, and periosteal bone perimeter of midshaft femurs were measured by CTAn software.

For both male and female, marrow area was significantly larger in KO mice (+29.6% in male, p<0.01 and +16.2% in female, p<0.001) than their littermate controls (Table 3). Cortical area demonstrated no significant difference between WT and KO mice (in male, p=0.15 and in female, p=0.16) (Table 3). Cross-sectional area was significantly larger in KO mice (+21% in male, p<0.01 and +10.9% in female, p<0.01) than their WT controls

(Table 3). Cortical area to total area percentage was significantly smaller in KO mice (-9.5% in male, p<0.01 and -5.7% in female, p<0.01) (Table 3).

Average cortical thickness showed no significant difference between WT and KO mice (in male, p=0.74 and in female, p=0.52) (Table 3). Anterior-posterior (AP) width was significantly greater in KO mice (+10.1% in male, p<0.05 and +4.3% in female, p<0.05) than their WT control mice (Table 3). Medial-lateral (ML) width was also significantly greater in KO mice (+10.3% in male, p<0.01 and +5% in female, p<0.01) than their WT controls Table 3). However, the AP to ML ratio indicated no significant difference between WT and KO mice (in male, p=0.98 and in female, p=0.74) (Table 3). Furthermore, the periosteal bone perimeter of midshaft femurs was significantly greater in KO mice (+10.1% in male, p<0.01 and +4.5% in female, p<0.01) (Figure 56).

The high resolution X-ray images of femurs indicated the diameter of KO mice were slightly larger than their WT controls (Figure 57). And the cross-sectional micro-CT scan slides of midshaft femurs presented greater periosteal bone perimeters (Figure 56), AP width and ML width (Table 3) in KO mice than WT mice (Figure 58).

To sum up, osteocyte-specific KO Stat3 impacted bone geometry by increase bone modeling process which push bone grow outward to a larger size and greater diameter leading to a larger measurement of bone marrow area, total cross-sectional area, periosteal bone perimeter, anterior-posterior width, and medial-lateral width compared with WT femurs (Figure 58). Furthermore, due to the similar cortical area and average cortical thickness in both WT and KO midshaft femurs, which indicated there was the same amount of bone material in both WT and KO mid-shaft femurs, but there was a larger femoral diameter in KO mice than WT mice, which result in a higher Moment of Inertia (MOI) in KO mice than their WT controls.

3.17 Osteocyte-specific Stat3 KO Mice Present an Increase in Cortical Bone Pore Number

During the dynamic histomorphometrical analysis of midshaft femur in both Dmp1-Cre;Stat3$^{flox/flox}$ (KO) mice and Dmp1-Cre;Stat3$^{+/+}$ (WT) mice, the KO mice exhibited potentially greater cortical bone porosity than their age-matched littermate WT controls (Figure 59). To quantify the cortical bone porosity in the midshaft femur, the pore number/bone area and pore area/bone area of both WT and KO mice were measured. Compared to WT control mice, in males, the pore number/bone area of the KO mice was 112% ($p<0.01$) greater, and in females, the pore number/bone area of the KO mice was 149% ($p<0.01$) greater (Figure 60). However, there were no significant differences of pore area/bone area between KO mice and WT mice in both males ($p=0.31$) and females ($p=0.12$) (Figure 61).

The increased femoral cortical bone pore number in osteocyte-specific Stat3 KO mice might contribute to the decreased bone material properties in KO mice femur biomechanical bending test.

3.18 Osteocyte-specific Stat3 KO Mice Exhibit a Decrease in Load-induced Bone Formation

Osteocytes are the most abundant cells in the bone tissue, composing 90% to 95% of all bone cells in adult bone, and are the longest lived bone cells within their mineralized environment[103]. Osteocytes have been considered to be the most important mechanosensory cells because of their location in bone and their complex dendritic network[88,89,90]. In recent bone loading studies, the discovery of upregulation of Stat3 proteins in response to mechanical loading strongly suggests that the Stat3 protein might be an important messenger in mechanical signal transduction to promote new bone formation by osteoblasts[78,79].

In order to reveal the role of Stat3 play in osteocytes mechanical signal transduction, the conditional Stat3 KO (Dmp1-Cre;Stat3$^{flox/flox}$) mice as well as their wild type (WT) littermate control mice (Dmp1-Cre;Stat3$^{+/+}$) were subjected to dynamic axial ulna loading as described in Chapter 2 and Figure 12. And their load-induced bone formation responses were evaluated and quantified as mentioned in Chapter 2, Figure13, and Figure 14. The dynamic histomorphometry results demonstrate that load-induced bone formation was suppressed in both the male and female osteocyte-specific Stat3 KO mice. The histomorphometrical data from the female Dmp1-Cre;Stat3$^{flox/flox}$ (KO) mice and their WT controls shows that there is significantly less calcified new bone formation and a lower rate of new bone formation after loading (Figure 62).

Quantified data were also generated. Compared to their WT littermate controls, the relative mineralizing surface (rMS/BS) (MS/BS in the right ulna minus MS/BS in the left ulna), the relative mineral appositional rate (rMAR), and the relative bone formation rate (rBFR/BS) in response to robust axial ulna loading were all significantly lower in the KO mice. For both male and female, rMS/BS was significantly lower in KO mice (-49% in male, $p<0.001$ and -56% in female, $p<0.001$) than their WT littermate controls (Figure 63). rMAR was significantly lower in KO mice (-66% in male, $p<0.001$ and -69% in female, $p<0.001$) than their WT littermate controls (Figure 64). rBFR/BS was significantly lower in KO mice (-76% in male, $p<0.001$ and -77% in female, $p<0.001$) than their WT littermate controls (Figure 65).

To sum up, inactivation of Stat3 specifically in osteocytes led to significantly decreased load-induced bone formation. These loading data support the speculation that Stat3 in osteocytes plays an important role in mechanical signal transduction in response to mechanical loading.

3.19 Osteocyte-specific Stat3 KO Mice Presented an Increase in *SOST* Expression

Elimination of Stat3 specifically in osteocytes might affect some genes expression which is important for new bone formation. The protein product of *SOST* gene, sclerostin, a secreted glycoprotein, antagonist to bone morphogenetic protein (BMP), and produced by osteocytes, has anti-anabolic effects on bone formation by inhibiting osteoblasts[125,126,127]. Type 1 collagen is the most abundant material in organic part of bone secreted by osteoblast which strength and support bone tissues. Osteocalcin plays a role in the body's metabolic regulation and is pro-osteoblastic, or bone-building. By its nature, osteocalcin is also implicated in bone mineralization and calcium ion homeostasis[128]. *SOST*, *type 1 collagen*, and *osteocalcin* genes expression were measured from isolated osteocytes of 8-week-old Dmp1-Cre;Stat3$^{+/+}$ (WT) mice and Dmp1-Cre;Stat3$^{flox/flox}$ (KO) mice. The mRNA relative quantification demonstrated that compare to their WT control mice, the *SOST* expression level was significantly higher in osteocytes of male KO mice (Figure 66). However, the *type 1 collagen* expression presented no significant difference in osteocytes of KO mice (Figure 67). The *osteocalcin* gene expression level also presented no significant difference in osteocytes of KO mice (Figure 68).

The increased *SOST* gene expression in osteocyte-specific Stat3 KO mice demonstrated inactivation of Stat3 only in osteocytes led to a higher *SOST* expression level which might contribute to inhibition of new bone formation.

3.20 Analysis of Osteocyte-specific Stat3 Inactivation

The LoxP site and Cre gene detection in Dmp1-Cre;Stat3$^{flox/flox}$ mice indicated the correct genotype for osteocyte-specific Stat3 KO mice. And the subsequent immunohistochemical staining further confirmed the elimination of Stat3 proteins in osteocyte-specific Stat3 knockout mice.

In the early stage of development, before the age of 8 weeks, osteocyte-specific Stat3 KO mice exhibit normal bone growth. In 18-week-old adult mice, compared to their age matched wild type littermate control mice, osteocyte-specific Stat3 knockout mice presented normal phenotypes like: normal body size, normal body weight, and normal femur length. These data indicate inactivation of Stat3 in osteocytes did not affect the KO mice overall bone development. Furthermore, the normal BMC and BMD in femurs and vertebrae of the 18-week-old KO mice demonstrate inactivation of Stat3 in osteocytes did not affect bone mass and bone density achievement. The normal trabecular bone number, size, and volume in KO mice femur indicated inactivation of Stat3 in osteocytes did not affect trabecular bone development.

At the tissue level, there was normal trabecular bone volume in KO mice femurs. However, significantly decreased osteoid surface was found in 18-week-old conditional Stat3 KO mice. Although the bone density and bone mass achievement is normal in osteocyte-specific Stat3 KO mice before the age of 18 weeks, when these KO mice grow older into 18 weeks, due to the absence of Stat3 in osteocytes which might play an important role in mechanical signal transduction for anabolic new bone formation, the osteoblast activity of KO mice might significantly deteriorate faster than WT mice in older age which may cause significantly less osteoid surface was found in KO mice than WT mice.

In the dynamic histomorphometry study, there was significant decreased new bone formation of 18-week-old osteocyte-specific Stat3 KO mice found in both midshaft femur periosteum and distal femur trabecular bone. These data further indicated that the osteoblast recruitment and activity were significantly compromised in KO mice which could lead to less osteoid formation and subsequently less new bone formation by osteoblasts in 18-week-old adult mice.

In the TRAP staining static histomorphometry study, osteoclast number, osteoclast surface, and eroded bone surface of KO mice femur trabecular bone were significantly greater than their WT controls, which demonstrated a significantly increased osteoclast activity in conditional Stat3 KO mice. Moreover, there were significantly larger bone marrow area and greater periosteal perimeter of midshaft femur in osteocyte-specific Stat3 KO mice than their WT controls. These data suggests that the bone modeling activity was significantly increased in KO mice femur to push femur growing outward (Figure 69). The increased bone resorption by osteoclasts in bone marrow cause larger bone marrow area. Simultaneously, the osteoblasts on the periosteum continuously deposit new bone materials to maintain bone thickness and volume. The coordinated action of osteoclasts and osteoblasts leads to larger bone marrow area and greater midshaft femur perimeter in osteocyte-specific Stat3 KO mice than their WT littermate controls.

In the bone biomechanical testing study, the femur bone material properties were significantly lower in osteocyte-specific Stat3 KO mice than WT control mice. These data demonstrated that inactivation of Stat3 specifically in osteocytes decrease femur bone material properties, which might be caused by composition changes in bone matrix materials. Furthermore, in the femur cortical bone porosity measurement, there was a larger pore number in midshaft femur of KO mice than WT controls, which might be an important factor contributing to lower bone material properties of femur in KO mice. Interestingly, the structural properties of KO mice femurs were normal, combined with the results of normal bone mass, bone density, cortical bone area, and average cortical thickness of KO femurs, these data suggest during bone development osteoblasts were functioning well to achieve bone density and bone mass while the Stat3 proteins were eliminated in osteocytes.

In the ulna loading study, significantly decreased load-induced bone formation in osteocyte-specific Stat3 KO mice demonstrated that Stat3, as a critical signal transducer, plays an important role in transducing mechanical signal into biological signal to promote load-induced new bone formation. Inactivation of Stat3 in osteocytes strongly reduces the mechanical signal transduction, and subsequently decreases load-induced new bone formation.

The increased expression level of *SOST* gene might be also another important factor contributed to decreased new bone formation rate of 18-week-old adult KO mice due to sclerostin's nature of inhabitation of osteoblasts[125,126,127].

CHAPTER 4. DISCUSSION

4.1 Skeletal System is Important for Human Body Function

Bone is specialized connective tissue that, together with cartilage and vascular tissue, makes up the skeleton system. Bone tissue possesses a variety of functions, including: first, providing mechanical support (skeleton offers the sites and support for muscle tissue insertion for locomotion); second, protecting vital organs (lungs, heart, brain, bone marrow, etc); third, regulating bone mineral homeostasis (bone is the main reserve of ions for the organism, especially calcium and phosphate). Irregulated bone tissue development and abnormal bone homeostasis would significantly jeopardize normal bone functions and cause bone diseases[129].

Bone tissue homeostasis results from the activities of many cell lineages, including mainly osteoblasts, osteocytes, and osteoclasts. Osteoblasts are bone-forming cells which are progressively transformed into osteocytes embedded in their own secretion products which form lacunae after mineralization. Osteoclasts are multinucleated cells that possess several characteristic features, such as a highly polarized morphology, apical differentiation adjoining the calcified matrix in resorption (a tightly sealed compartment between osteoclasts and bone surface known as the “ruffled border”), and numerous mitochondria[130].

The skeleton is a dynamic organ in which mineralized bone is continuously reabsorbed by osteoclasts, and new bone is formed by osteoblasts throughout the skeleton and throughout life[131,132]. Continual replacements of old bone material by new bone material represent a process known as bone remodeling. Bone remodeling is the process by which bone is continually renewed. This process occurs both within the thick cortical bone that surrounds the marrow space and on the surfaces of the internal trabecular bone network. Bone remodeling provides a mechanism by which calcium levels in the blood can be maintained, a method to restore microscopic regions of damage, and a way of responding to load-bearing, dietary or hormonal changes[133].

4.2 Imbalanced Bone Remodeling Leads to Bone Loss

The bone remodeling depends on a precise balance between bone formation and bone resorption[131,132,133]. During the bone remodeling, osteoblasts and osteoclasts are closely associated in time and space[134]. After receiving a bone stimulus from the lining, osteoblasts and osteoclasts appear on the bone surface and reabsorb the mineral components of bone by an acid extracellular mechanism[135,136]. Subsequently, osteoblasts, stimulated by osteoclasts contacts and/or osteoclastic soluble factors, deposit osteoid on the resorption site, initiating bone formation[137]. Osteoblasts not only initiate but also control bone mineralization. The new bone formation exceeds bone resorption in bone remodeling and leads to an increase in bone mass. Conversely, when bone resorption is more than bone formation, that leads to a decrease in bone density, and the skeleton could potentially develop osteoporosis. During periods of bone growth or in response to repetitive mechanical forces such as increased exercise, the remodeling balance is in favor of bone formation. In contrast, in periods where calcium needs to be released during lactation or during periods of inactivity, the remodeling balance is in favor of bone resorption, and bone mass is lost.

4.3 Many Factors Affect Bone Resorption and Bone Formation

In the bone homeostasis, the balance between bone resorption and bone formation is extensively controlled and maintained by many factors, such as parathyroid hormone (PTH), 1,25$(OH)_2$ vitamin D_3, mechanical loads, estrogen, testosterone, growth factors and other local factors[133,138]. These factors can act directly on osteogenic cells on their precursors and control differentiation, formation and functions (bone matrix formation, mineralization, resorption, etc.). Among the known soluble factors, a pleiotropic cytokine family known as interleukin-6 (IL-6) family, sharing a common signal transducer (gp130) plays an important role during bone remodeling[139]. The interleukin-6 family cytokines include interleukin-6 (IL-6), interleukin-11 (IL-11), oncostatin M (OSM), leukemia inhibitory factor (LIF), cardiotrophin-1 (CT-1), and ciliary neutrophic factor (CNTF). These cytokines all show structural similarities (amino acid sequence, three-dimensional structure) and produce similar activities on a variety of target cells, including haematopoietic cells, hepatocytes, neurons, embryonic stem cells and bone cells[140-148]. Within bone and joint tissue, bone cells express gp130, giving them the ability to respond to gp130-family cytokines[129]. Interestingly, many of these cytokines have been shown to regulate the processes of bone formation and bone resorption (destruction) that are required for skeletal development, growth and maintenance[129,130].

Both osteoblasts and osteocytes are responsive to gp130 cytokines stimulation. IL-6, OSM, and IL-11 were reported to stimulate the differentiation of primary calvarial osteoblasts[149]. Furthermore, OSM, CT-1, IL-11, and LIF all stimulate osteoblast differentiation by stromal cells and simultaneously reduce the ability of these cells to differentiate into adipocytes[150,151]. In the knockout mice models, CT-1, IL-11R, and OSMR deficient mice all demonstrate a low level of bone formation *in vivo* [150,151,152]; however, mice engrafted with LIF-cDNA transfected cells producing high amounts of LIF demonstrated excessive new bone formation[153,154]. Furthermore, in a transgenic mouse model, overexpression of OSM caused the animals to develop osteopetrotic bone tissue, possibly by stimulation of bone formation and inhibition of bone resorption[159], and overexpression of IL-11 in transgenic mice increased bone formation by enhancement of osteoblastogenesis without affecting osteoclastogenesis[165]. The influence of gp130 cytokines on bone formation is not only restricted to an influence on osteoblast commitment but also affects osteocyte signaling pathways. OSM, CT-1 and LIF have been recently reported to strongly inhibit expression of sclerostin (SOST) by osteocytes[151]. SOST protein is an osteocyte-specific and an essential inhibitor of bone formation that acts as a Wnt signaling antagonist[155]. Sclerostin expression by osteocytes is also inhibited by administration of PTH[156], and by mechanical loading[157]. Antibodies neutralizing sclerostin are currently under development as a new therapeutic agent for osteoporosis[158].

4.4 Glycoprotein 130 Family Cytokines are Important for Bone Remodeling

Glycoprotein 130 (gp130) is a transmembrane protein and a cytokine receptor sub-unit capable of intracellular signal transduction in response to wide range of cytokines binding. The most well known of these cytokines are interleukin-6 (IL-6) family cytokines which include interleukin-6 (IL-6), interleukin-11 (IL-11), leukemia inhibitory factor (LIF), cardiotrophin-1 (CT-1), oncostatin M (OSM) and ciliary neurotrophic factor (CNTF)[160]. The binding of IL-6 family cytokines to their receptors induces the homodimerization of gp130 and subsequently activates the gp130-associated Janus kinases (JAKs)[42]. The activated JAKs phosphorylate the tyrosine residues of the YXXQ motif, leading to the recruitment and tyrosine phosphorylation of Stat3[161]. Activated Stat3s dimerize and enter the nucleus, therefore regulating the transcription of various genes that are important for cellular proliferation and differentiation[161](Figure 8).

The gp130 mediated IL-6 cytokine family signal transduction influences osteoclast formation and function. Genetic elimination of CT-1, LIF, and LIFR all lead to increased osteoclast formation *in vivo*[150,162,163]. The injection of recombinant LIF into the hemicalvaria augments bone resorption[166]. These indicate that IL-6 family cytokines are required for normal osteoclastogenesis and normal bone remodeling. Mice lacking gp130 (gp130 knock-out mice) had osteopenia due to increased numbers of osteoclasts[164]. That is, the summed roles of the gp130 signal affects osteoclasts and bone homeostasis. Furthermore, the longitudinal bone growth is determined by the proliferation of chondrocytes at the growth plate. Significant dwarfism has been reported in mice null for gp130 and mice with a mutation in Stat3 signaling downstream of gp130[167,168], which indicates that gp130 is required for normal bone growth. However, it is not known if Stat3 plays critical roles *in vivo* in IL-6-gp130-Stat3-mediated signals regulating bone homeostasis, and the individual physiological roles of Stat3 signaling relayed through IL-6-gp130-Stat3 pathway in osteoblasts and osteocytes *in vivo* were still not clear before our research. This raises an intriguing question about the Stat3's role in IL-6-gp130-Stat3 mediated signals regulating bone homeostasis *in vivo*.

4.5 Stat3 Might Play an Important Role in gp130 Family Cytokines Regulated Bone Formation

To reveal the roles of Stat3 in the IL-6-gp130-Stat3 mediated regulation of bone homeostasis, the Cre-LoxP recombination system was used to specifically delete the Stat3 signal from both cell types: the osteoblasts and osteocytes (Col3.6-Cre;Stat3$^{flox/flox}$ mice), and only one cell type: the osteocytes (Dmp1-Cre;Stat3$^{flox/flox}$ mice). Interestingly, the Col3.6-Cre;Stat3$^{flox/flox}$ mice demonstrated bone abnormalities (Figure 18,19,20,21) and an osteoporotic phenotype (Table 2) as a result of a reduced bone formation rate (Figure 22) (Table2) and an increased osteoclast activity (Table 2). This result clearly indicates that the Stat3 signal is a downstream signaling transducer of IL-6-gp130 signaling pathway regulated bone homeostasis and is essential for osteoblast function and regulates osteoclast function *in vivo*, which shares some similarities with previous studies of IL-6 family cytokines and gp130 signaling pathways[138,149-168]. Moreover, Stat3 proteins were found residing in mitochondria[120-123]and elimination of Stat3 in mitochondria of osteoblasts led to an elevated level of reactive oxygen species (ROS) (Figure 26). Without Stat3, an electron transport chain (ETC) is inhibited and reduction in mitochondrial activity leads to accumulation of ROS, an increased ROS-linked oxidative stress would lead to bone loss[111-117] and compromise Wnt signaling pathways, which consequently decrease load-induced bone formation[118,119]. Therefore, inhibition of bone formation in the Col3.6-Cre;Stat3$^{flox/flox}$ mice may result from the suppression of elevation of ROS in the osteoblasts. In addition, Col3.6-Cre;Stat3$^{flox/flox}$ mice demonstrated a reduction in mechanical properties of mouse long bones (Table 2). This data suggests that Stat3 plays an important role in maintenance of bone strength.

Mechanically load-induced bone formation was founded suppressed in Col3.6-Cre;Stat3$^{flox/flox}$ mice. The mechanical signal transduction seems linked with IL-6-gp130-Stat3 pathway. Osteoblast cells express a group of receptors for IL-6 family cytokines such as IL-6 and IL-11[169]. They are both sharing the common signal transducer gp130[169] and in response to mechanical stimulation. For instance, IL-6 has been found to show a highly increased production in calvarial osteoblasts in response to mechanical loading[170]. And IL-11 has also demonstrated an increased expression in response to loading *in vivo* as well as fluid shear stress *in vitro*[171]. Furthermore, antibody neutralizing IL-11 is shown to block mechanically induced enhancement of bone formation[171]. Thus, it is possible that elimination of Stat3 in osteoblasts of Col3.6-Cre;Stat3$^{flox/flox}$ mice blocked the downstream mechanical signal transduction through IL-6-gp130-Stat3 signaling pathway, and subsequently impaired differentiation and proliferation of osteoblasts.

As a downstream mechanism of IL-6-gp130-Stat3 pathway mediated bone formation, Stat3 regulates osteoblast functions, not only through mitochondria but also through nuclei. Regarding gene regulation in the nucleus, disruption of Stat3 likely alters expression of mechanosensitive genes such as Wnt molecules, and Wnt/β-catenin signaling is a normal physiological response to mechanical loading in bone[175]. In stromal cells transforming growth factor (TGF)-β mediated inhibition of wnt3a is in part through the suppression of Stat3[172]. Moreover, Stat3 has been shown to regulate expression of wnt5a in osteoblasts. Both wnt3a and wnt5a have previously proven to stimulate osteoblast proliferation and differentiation[173,174]. In the future study, by utilizing the osteoblast-specific Stat3 deficient mouse model, the global analysis of load-induced up-stream and down-stream genes in the presence and absence of Stat3 in osteoblasts will provide the gene regulation pattern of Stat3 which affects osteoblasts differentiation and proliferation.

4.6 Stat3 Might be an Important Mechanical Signal Transducer

In the previous studies, Stat3 has been found to be responsive to mechanical loading[78] and indicates an increased level of expression followed by mechanical stimulation[79]. In our research, fluid shear stress (FSS) was applied on osteoblasts; tyrosine and serine phosphorylations of Stat3 were found to be increased from 30 to 90 minutes following FSS (Figure 25). This data suggests the sustained Stat3 expression and activation in response to mechanical stimulation. In the ulna loading studies, Stat3 deficient mice in both osteoblasts and osteocytes (Col3.6-Cre;Stat3$^{flox/flox}$) present a significantly decreased load-induced bone formation (Figure 23 and 24). It has been proposed that osteocytes are mechanosensing cells in bone[103]. Thus, there is a high possibility that suppression of load-induced bone formation in this study is primarily caused by Stat3 deficiency in osteocytes. To further differentiate the role of Stat3 from osteoblasts to osteocytes, osteocyte-specific Stat3 deficient mice (Dmp1-Cre;Stat3$^{flox/flox}$) were subjected to axial ulna loading, and inactivation of Stat3 specifically in osteocytes also shows a significantly reduced load-induced bone formation (Figure 62,63,64,65). This data preliminarily confirmed Stat3 in osteocytes plays a critical role in mechanotransduction, and Stat3 signaling in osteocytes is necessary for anabolic bone formation in response to mechanical loading.

4.7 Stat3 Might Play an Central Role in Regulation of Sclerostin (SOST)

In the osteocyte-specific Stat3 deficient (Dmp1-Cre;Stat3$^{flox/flox}$) mice, a significantly decreased new bone formation rate (Figure 43,44,45,46) and reduced osteoid surface (Figure 37) were found in 18-week-old adult mice. This indicated a potentially decreased osteoblast recruitment and activity in osteocyte-specific Stat3 deficient mice. Mature osteocytes have been shown to produce sclerostin (SOST), encoded by the gene *SOST*, that can inhibit osteoblast activity[125,126,127]. Downregulation of *SOST* may create a permissive response in which Wnt proteins already present can activate the Wnt pathway. *SOST* knockout (KO) mice demonstrate significantly more bone mass than their wild type controls[176]. Mutations of *SOST* cause high bone mass in humans[177]. Sclerostin was discovered to be involved in the Wnt pathway as an antagonist against lipoprotein receptor 5 (LRP5), a positive regulator of bone mass[126,178]. IL-6 family/gp130 cytokines impact the osteocyte signaling pathway. IL-6 family cytokines: OSM, CT-1 and LIF have been recently reported to strongly inhibit expression of sclerostin (SOST) by osteocytes[151]. SOST protein is an osteocyte-specific and an essential inhibitor of bone formation. Moreover, Stat3 is an important downstream signal transducer of OSM, CT-1, and LIF through the gp130-Stat3 signaling pathway[179,180]. Deletion of Stat3 in osteocytes would cause reduced inhibition of *SOST* expression and subsequently an increased level of *SOST* expression, eventually leading to reduced bone formation rate. In our study, osteocyte-specific Stat3 deficient (Dmp1-Cre;Stat3$^{flox/flox}$) mice presented a higher expression level of *SOST* than their wild type control mice (Figure 66). This data strongly suggests that Stat3 protein might be a critical downstream signal transducer of OSM, CT-1, and LIF in osteocytes functioning in inhibition of SOST, and increased expression level of *SOST* might be an important factor contributing to the decreased bone formation rate in Osteocyte-specific Stat3 deficient mice. Furthermore, reduced bone formation in response to unloading was proposed to be due to elevated sclerostin[181,182]. Mechanical loading also has been reported to reduce sclerostin expression[157,182]. The mechanical loading impacts sclerostin expression possibly through gp130-Stat3 pathway. As a critical mechanical signal transducer, elimination of Stat3 signaling in osteocytes might cause increased expression of *SOST* and compromise anabolic bone formation in response to loading in Dmp1-Cre;Stat3$^{flox/flox}$ mice. The possibility of an osteocyte-specific function of Stat3 signal in inhibiting sclerostin expression is an intriguing mechanism that will be clarified in the future. The osteocyte-specific Stat3 knockout (Dmp1-Cre;Stat3$^{flox/flox}$) mice generated for this study can be used for mechanical loading to evaluate the expression level of *SOST* in osteocyte-specific Stat3 deficient mice after loading. By comparing the results from their wild type control mice with the Stat3 conditional knockout mice, the proposed study will further reveal the osteocyte-specific role of Stat3 impacting sclerostin.

4.8 Elimination of Stat3 Might Cause Osteocyte Apoptosis

Osteocytes are considered inducers of osteoclast activation and formation. They can send signals of bone resorption to promote osteoclast formation and activation[183,184]. Both healthy and dying osteocytes can recruit osteoclasts to the sites of remodeling. Microdamage-induced bone remodeling can cause osteocyte apoptosis. Pro-apoptotic molecules are elevated in osteocytes immediately at the microcrack locus, whereas anti-apoptotic molecules are expressed 1 to 2 mm from the microcrack,[185] showing that some osteocytes have protective mechanisms against apoptosis. Apoptotic osteocytes release apoptotic bodies expressing RANKL to recruit osteoclasts[186]. The Wnt/β-catenin signaling pathway is involved in osteocyte apoptosis. Deletion of β-catenin causes apoptosis in osteocytes and results in an increase in osteoclast activity and the generation of a porous bone phenotype[187]. Therefore, the Wnt/β-catenin signaling pathway plays a role not only in bone response to loading but also in osteocyte apoptosis[188]. Interestingly, IL-6 family cytokines (LIF, OSM, IL-6) that utilize the gp130 signal transducer are potent anti-apoptotic agents on osteoblastic cells[189]. For example, oncostatin M can prevent the induction of apoptosis in human osteoblast cells associated with an increase in the ratio of the pro-apoptotic protein bax to the anti-apoptotic protein bcl-2[189]. Moreover, the anti-apoptosis function of IL-6 is acting through transcriptional activation of the p21 gene[190]. As a downstream signaling transducer of IL-6/gp130 family cytokines, Stat3 has been demonstrated to be a critical downstream effector of IL-6/gp130/Stat3 pathway signaling activation and an important mediator of the anti-apoptosis effects on IL-6 family cytokines via activation of the p21 on human osteoblastic cells[190]. In addition, and in support of a mediating role of Stat3 in the activation of the p21 promoter, overexpression of Stat3 potentiated the cytokine effect on the p21 promoter; whereas a dominant negative Stat3, or a mutation of the Stat3 response element on the promoter, significantly reduced the IL-6 cytokine effect[190]. Because osteocytes are descendants of osteoblasts[103], Stat3 might play an important role in the protective mechanism of anti-apoptosis in osteocytes through IL-6/gp130/Stat3/p21 pathway. Deficient Stat3 in osteocytes possibly causes apoptosis in Dmp1-Cre;Stat3$^{flox/flox}$ mice, and subsequently induces an increased level of osteoclast activities which include: increased osteoclast formation and activation (Figure 40,41,42) and an increased bone resorption (Figure 38 and 39). Moreover, potential osteocyte apoptosis might also cause increased porosity of Dmp1-Cre;Stat3$^{flox/flox}$ mice (Figure 69 and 60). In the future study, to further reveal the role Stat3 plays in osteocyte apoptosis, osteocyte apoptosis tests (e.g. caspase-3 immunohistochemistry or TUNEL assay) will be employed to evaluate the osteocyte apoptosis in osteocyte-specific Stat3 deficient (Dmp1-Cre;Stat3$^{flox/flox}$) mice and their wild type control (Dmp1-Cre;Stat3$^{+/+}$) mice.

4.9 The Conclusion

To sum up, Signal transducer and activator of transcription 3 (Stat3) is a transcription factor activated by a variety of cytokines and growth factors, including IL-6 family cytokines through gp130/JAK/Stat3 pathways. IL-6 family cytokines regulate osteoblast differentiation, osteoclast function, and bone formation through Stat3 activation. As a downstream significant effector of IL-6/gp130 pathway and other associated pathways, Stat3 plays an essential role in bone homeostasis and mechanotransduction, and Stat3 is not only involved in load-driven gene activation in nuclei, but also in regulation of reactive oxygen species (ROS) in mitochondria. Furthermore, Stat3 might play an important role in a protective mechanism of anti-apoptosis in both osteoblasts and osteocytes.

In conclusion, Stat3, as an important signal transducer and activator of transcription of IL-6/gp130 cytokine family, has important roles in bone remodeling and mechanical signal transduction. However, many questions remain to be answered before we fully understand the detailed molecule mechanisms of Stat3-involved signaling pathways and the interplay between Stat3 pathways and other important bone pathways (PTH, vitamin D_3, Wnt/β-catenin etc.) and its role in regulating bone remodeling and maintenance of the skeleton in health and disease. The generation of bone- and cartilage-specific gene knockout mouse models lacking expression of Stat3 and lacking expression of each of the gp130 signaling factors will further reveal the signaling pathways of each of the factors in regulating bone structure and integrity. With greater understanding of the functions of Stat3 and IL-6/gp130 cytokines, it would be possible to identify novel therapeutic targets for the prevention of osteoporosis and the bone abnormalities in Hyper IgE Syndrome (HIES).

TABLES

Table 1 Bone specimens extracted from experimental mice after ulna loading and the methods of bone specimens processing

Specimen Name	Purpose of Use	Way of Processing	Way of Storage	Storage Temperature
Right Ulna with Radius	Load-driven bone formation analysis	70% Ethanol	70% Ethanol in small glass bottle	4 °C
Left Ulna	Internal Control	70% Ethanol	70% Ethanol in small glass bottle	4 °C
Left Femur	Micro CT/X-ray Biomechanical Testing	wrapped in 0.9% saline soaked gauze	In labeled self-seal plastic bag	– 20 °C
Right Femur	Histology	10% Neutral Buffered Formalin overnight in 4 °C	70% Ethanol in small glass bottle	4 °C
Left Tibia	Total Protein Isolation	Fresh freezing in liquid N_2	1.5 ml eppendorf tube	– 80 °C
Right Tibia	Total RNA Isolation	Fresh freezing in liquid N_2	1.5 ml eppendorf tube	– 80 °C
L2	Total RNA Isolation	Fresh freezing in liquid N_2	1.5 ml eppendorf tube	– 80 °C
L3	Total Protein Isolation	Fresh freezing in liquid N_2	1.5 ml eppendorf tube	– 80 °C
L4	Micro CT/X-ray Biomechanical Testing	Wrapped in 0.9% saline soaked gauze	In labeled self-seal plastic bag	– 20 °C
L5	Histology	10% Neutral Buffered Formalin overnight in 4 °C	70% Ethanol in small glass bottle	4 °C

L: Lumbar (vertebra)

Table 2 Bone phenotypes of Col3.6-Cre;Stat3$^{flox/flox}$ mice

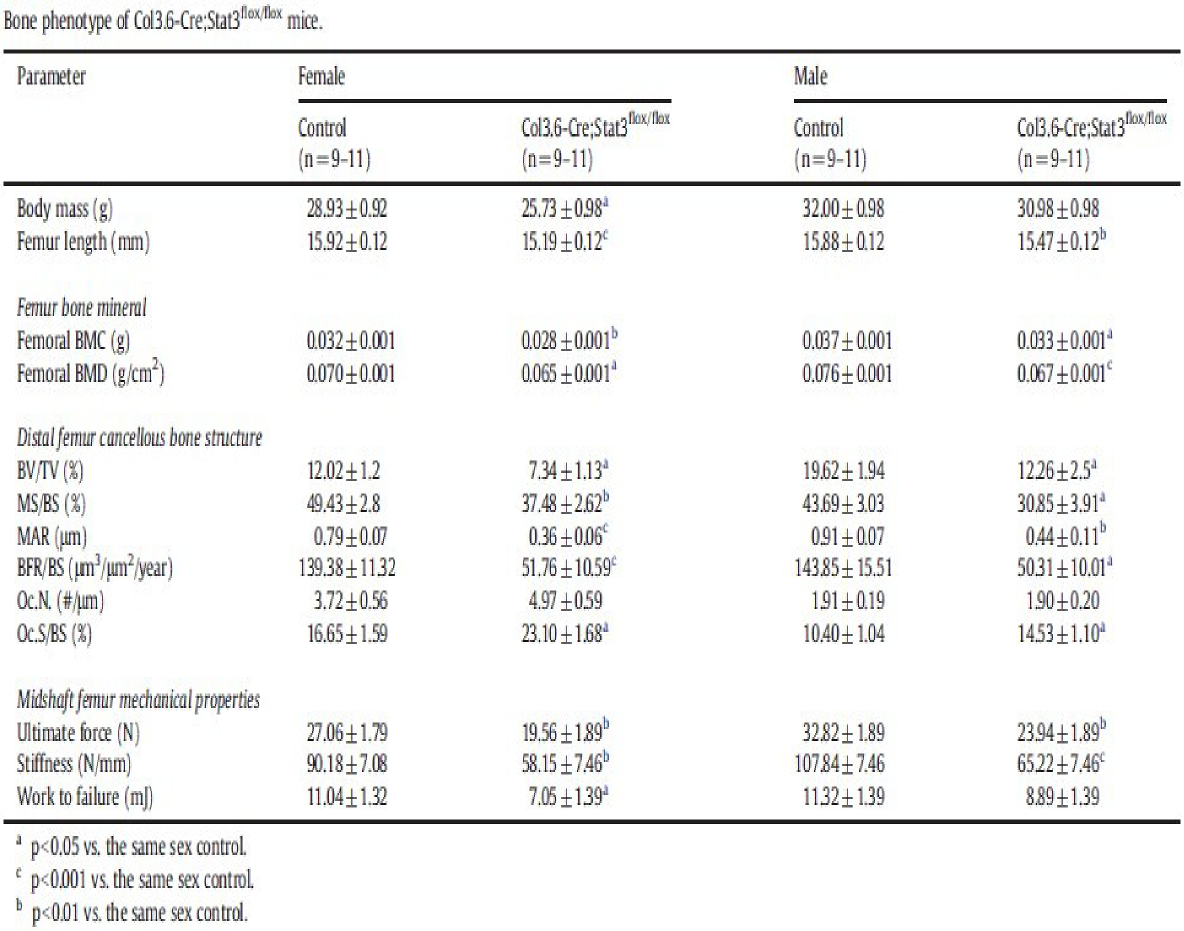

Bone phenotype of Col3.6-Cre;Stat3$^{flox/flox}$ mice.

Parameter	Female		Male	
	Control (n=9–11)	Col3.6-Cre;Stat3$^{flox/flox}$ (n=9–11)	Control (n=9–11)	Col3.6-Cre;Stat3$^{flox/flox}$ (n=9–11)
Body mass (g)	28.93±0.92	25.73±0.98[a]	32.00±0.98	30.98±0.98
Femur length (mm)	15.92±0.12	15.19±0.12[c]	15.88±0.12	15.47±0.12[b]
Femur bone mineral				
Femoral BMC (g)	0.032±0.001	0.028±0.001[b]	0.037±0.001	0.033±0.001[a]
Femoral BMD (g/cm^2)	0.070±0.001	0.065±0.001[a]	0.076±0.001	0.067±0.001[c]
Distal femur cancellous bone structure				
BV/TV (%)	12.02±1.2	7.34±1.13[a]	19.62±1.94	12.26±2.5[a]
MS/BS (%)	49.43±2.8	37.48±2.62[b]	43.69±3.03	30.85±3.91[a]
MAR (µm)	0.79±0.07	0.36±0.06[c]	0.91±0.07	0.44±0.11[b]
BFR/BS (µm^3/µm^2/year)	139.38±11.32	51.76±10.59[c]	143.85±15.51	50.31±10.01[a]
Oc.N. (#/µm)	3.72±0.56	4.97±0.59	1.91±0.19	1.90±0.20
Oc.S/BS (%)	16.65±1.59	23.10±1.68[a]	10.40±1.04	14.53±1.10[a]
Midshaft femur mechanical properties				
Ultimate force (N)	27.06±1.79	19.56±1.89[b]	32.82±1.89	23.94±1.89[b]
Stiffness (N/mm)	90.18±7.08	58.15±7.46[b]	107.84±7.46	65.22±7.46[c]
Work to failure (mJ)	11.04±1.32	7.05±1.39[a]	11.32±1.39	8.89±1.39

[a] $p<0.05$ vs. the same sex control.

[c] $p<0.001$ vs. the same sex control.

[b] $p<0.01$ vs. the same sex control.

Table 3 Midshaft femur cross-sectional geometric properties

Group	Total Area (mm^2)	Marrow Area (mm^2)	Cortical Area (mm^2)	Cortical Thickness (mm)	AP Width (mm)	ML Width (mm)	AP to ML Ratio	Cortical Area/Total Area (%)
WT Male (n=6)	1.660 ± 0.167	0.931 ± 0.124	0.730 ± 0.047	0.185 ± 0.005	1.212 ± 0.077	1.744 ± 0.073	0.695 ± 0.023	44.097 ± 1.834
KO Male (n=8)	2.009 ± 0.246^a	1.207 ± 0.156^a	0.803 ± 0.118	0.182 ± 0.019	1.335 ± 0.094^c	1.923 ± 0.106^a	0.694 ± 0.028	39.924 ± 2.757^a
WT Female (n=14)	1.548 ± 0.106	0.813 ± 0.094	0.736 ± 0.038	0.195 ± 0.011	1.221 ± 0.052	1.621 ± 0.067	0.755 ± 0.043	47.650 ± 2.779
KO Female (n=13)	1.716 ± 0.147^a	0.945 ± 0.083^b	0.772 ± 0.078	0.192 ± 0.013	1.274 ± 0.052^c	1.701 ± 0.088^c	0.750 ± 0.029	44.941 ± 1.919^a

Data were presented as mean ± S.E.M.
[a] $p<0.01$ vs. the same sex control
[b] $p<0.001$ vs. the same sex control
[c] $p<0.05$ vs. the same sex control

FIGURES

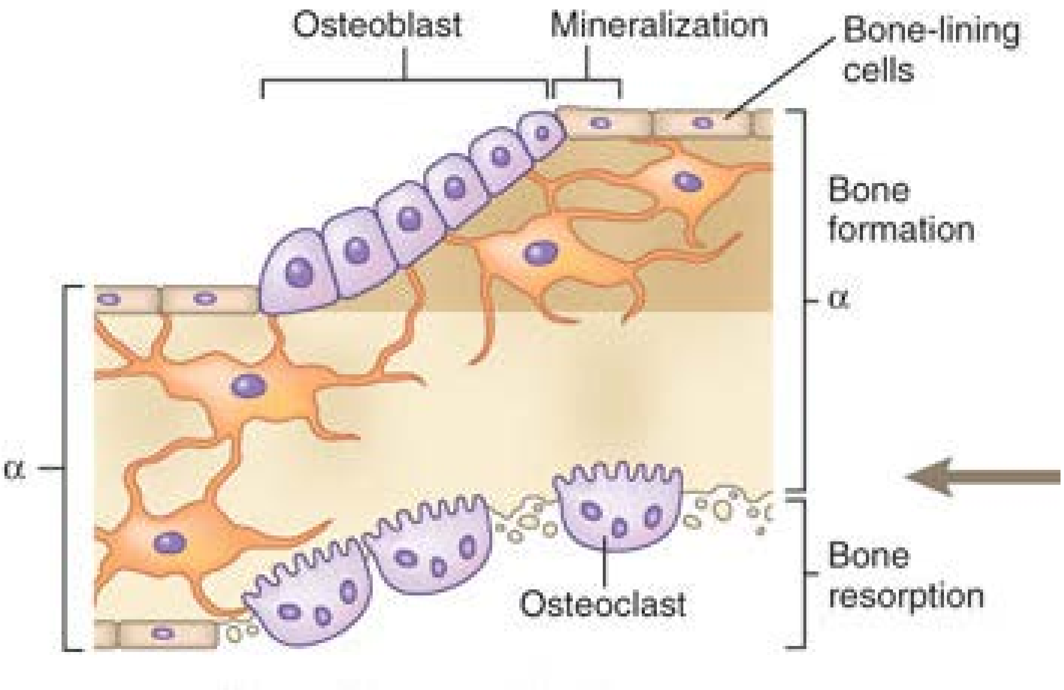

Figure 1: Bone modeling process. Bone modeling is the process that builds up and shapes the bone structures and ensures the acquisition of the appropriate bone morphology and mass during growth. This process occurs at a high rate in young adult bone growth and a low rate throughout an adult individual's life and is required for repair and adaptation to changes in mechanical loading. In this process, bone resorption and bone formation occur in an uncoupled manner and on separate surfaces. α represents the mineralized bone layer containing star shaped osteocytes.

(The figure is reproduced from Baron, R. and Kneissel, M. (2013). WNT signaling in bone homeostasis and disease: from human mutations to treatments. *Nature Medicine*, *19* (2), 179-192.)

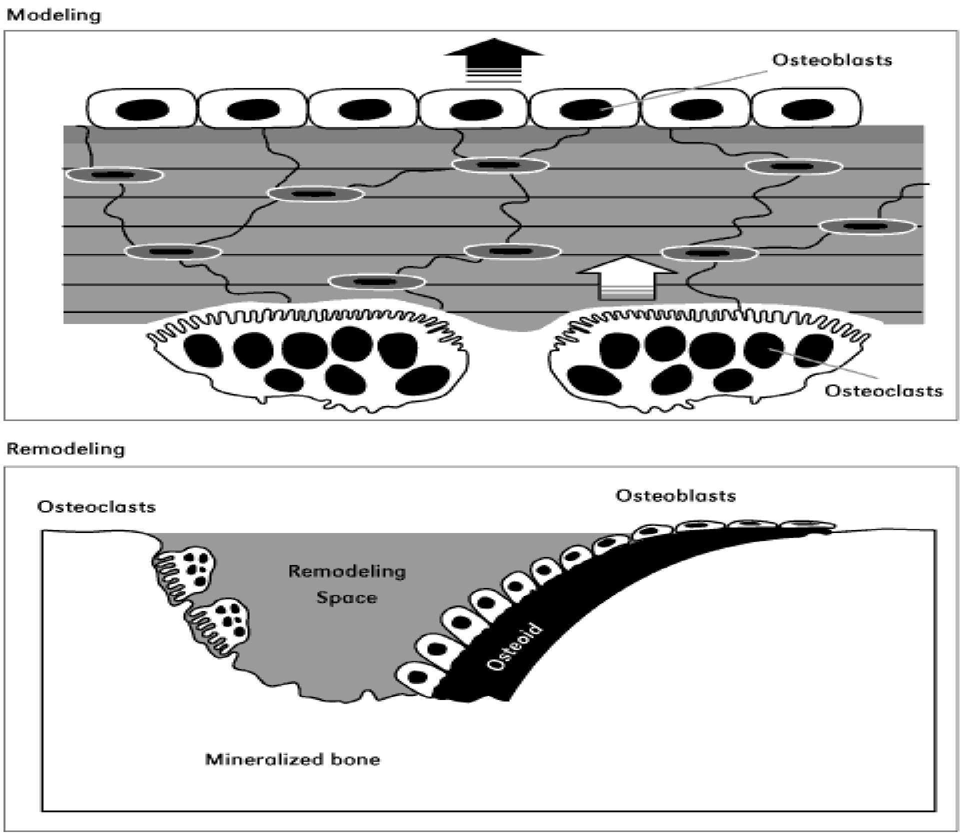

Figure 2: The difference between bone modeling and bone remodeling. In modeling (top figure), osteoblast and osteoclast activities are not coupled because osteoblast and osteoclast actions occur on different surfaces of bone. However, in bone remodeling (lower figure), osteoblasts deposit new bone materials coupled with prior osteoclasts bone resorption. In both bone modeling and bone remodeling, a higher rate of bone formation than bone resorption leads to bone gain. Conversely, a higher rate of bone absorption than bone formation results in bone loss.

(Figure is adapted from Bone Health and Osteoporosis: A Report of the Surgeon General. Chapter 2: The basics of Bone in Health and Disease. 2004)

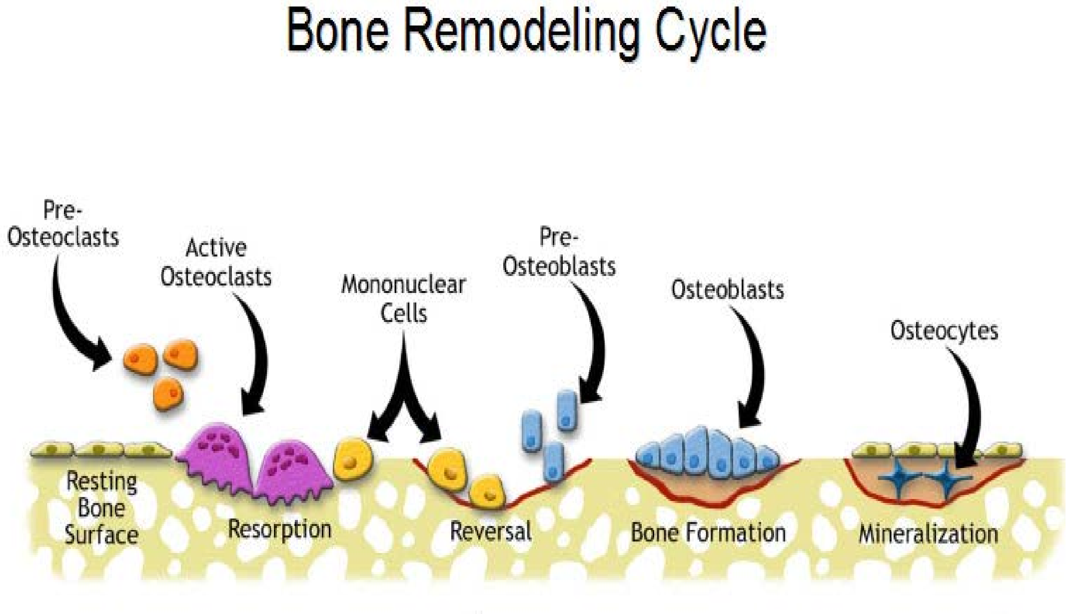

Figure 3: Bone remodeling cycle. The bone remodeling cycle consists of four distinct phases: activation, resorption, reversal, and formation. The sequence of these phases is illustrated. The activation phase is initiated by osteocytes apoptosis which attracts monocyte/macrophage lineage cells to form osteoclasts. In the resorption phase, osteoclasts absorb bone materials. During a brief reversal phase, osteoclasts undergo apoptosis and are released from the bone surface. The osteoblasts are recruited and begin to lay down new bone. Some of the osteoblasts remain inside the bone and are converted to osteocytes which are connected to each other and to the surface bone lining cells. Some other osteoblasts become inactive and flatten into bone lining cells.

(Figure is adapted from http://www.ns.umich.edu/Releases/2005/Feb05/img/bone.jpg)

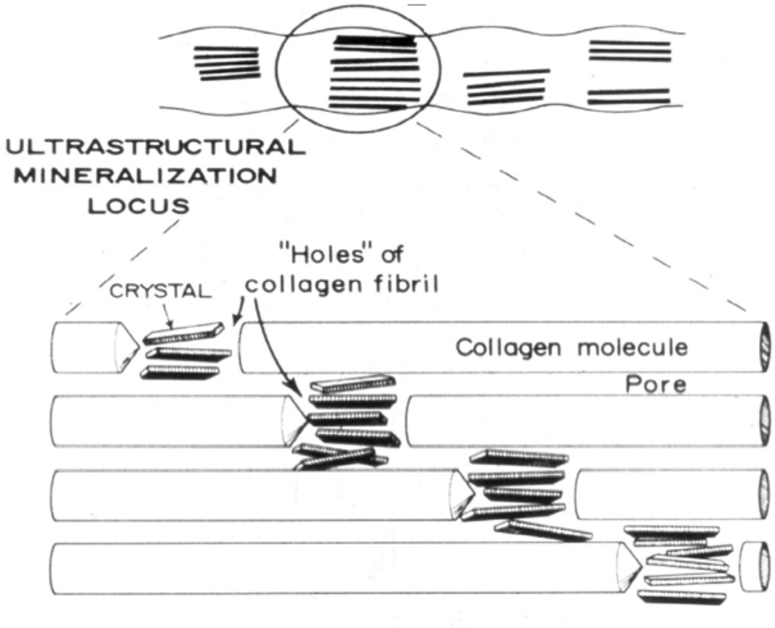

Figure 4: Mineralization of bone. In the collagen fiber ultrastructural mineralization locus, hydroxyapatite crystal plates deposit in holes of collagen fibril between collagen molecules.

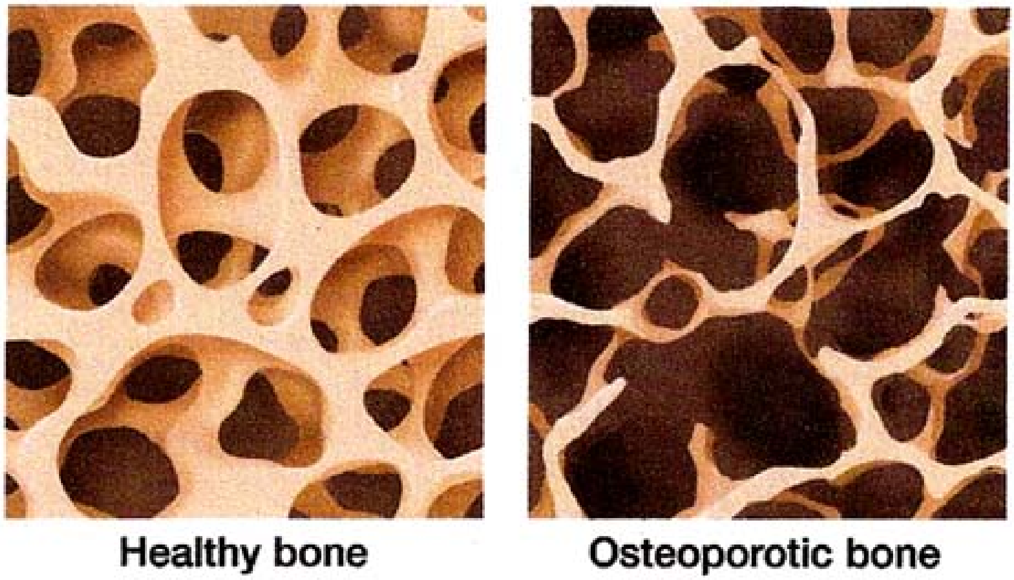

Figure 5: Comparison of healthy bone and osteoporotic bone. The thinner and smaller number of osteoporotic spongy bones leads to changed microstructure and bony weakness, with increased risk of fracture.

(Figure is adapted from http://www.drwolgin.com/Pages/osteoporosis.aspx)

Figure 6: Bone phenotypes of Hyper IgE Syndrome (HIES). A: bone X-ray scan demonstrated spinal scoliosis; B: healed pathologic distal femoral fracture in a HIES patient; C: a 3 year 9 month old patient with HIES showing bowing of the legs.

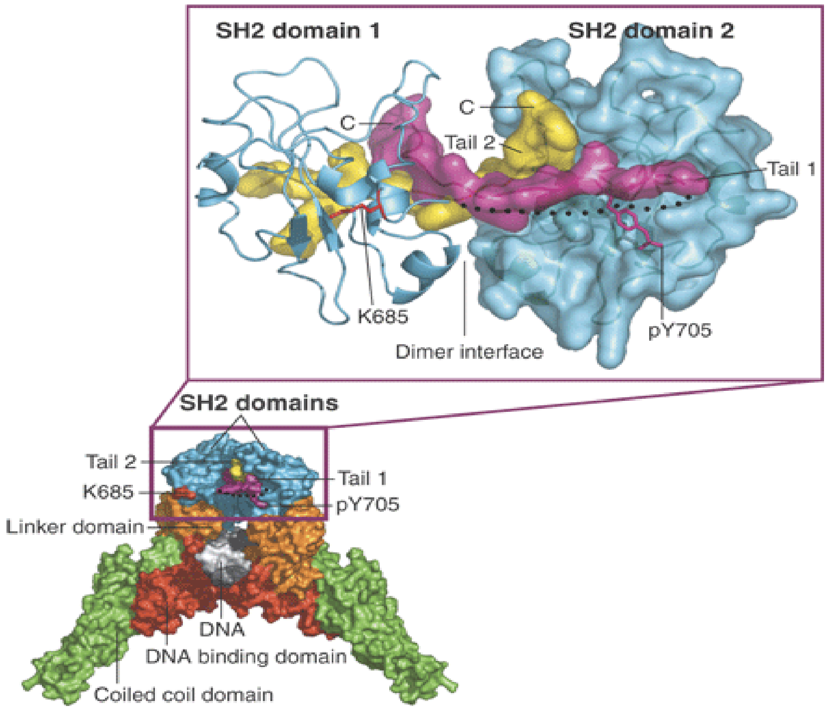

Figure 7: Three-dimensional structure of the activated Stat3 protein dimer. The crystal structure of Stat3 illustrates the location of lysine 685 (red) in the tyrosine-phosphorylated Stat3 dimer. The four recognized domains in each Stat3 monomer are the coiled-coil domain (green), the DNA binding domain (red), the linker domain (orange), and the Src Homology (SH2) domain (cyan). A disordered loop (black dotted curve) connects the SH2 domain on the left to Tail 1 (magenta). Two strands of DNA are shown in white and black held in the center of Stat3 dimer. The other lysine 685 is on the back side of the SH2 domain on the right. The top figure illustrates a detailed view of the dimer interface of the 2 tyrosine-phosphorylated SH2 domains (cyan) of Stat3. Two tail segments are shown in magenta and yellow, and the dotted curve is a disordered loop (residues 689 to 701) connecting the SH2 domain on the left to its tail segment. Lysine 685 is depicted in red and tyrosine 705 is shown in magenta.

(Figure is adapted from O'Shea, J. J., Kanno, Y., Chen, Y., Levy, D. E. (2005). Cell Signaling. Stat acetylation--a key facet of cytokine signaling? *Science*, *307*, 217-218.)

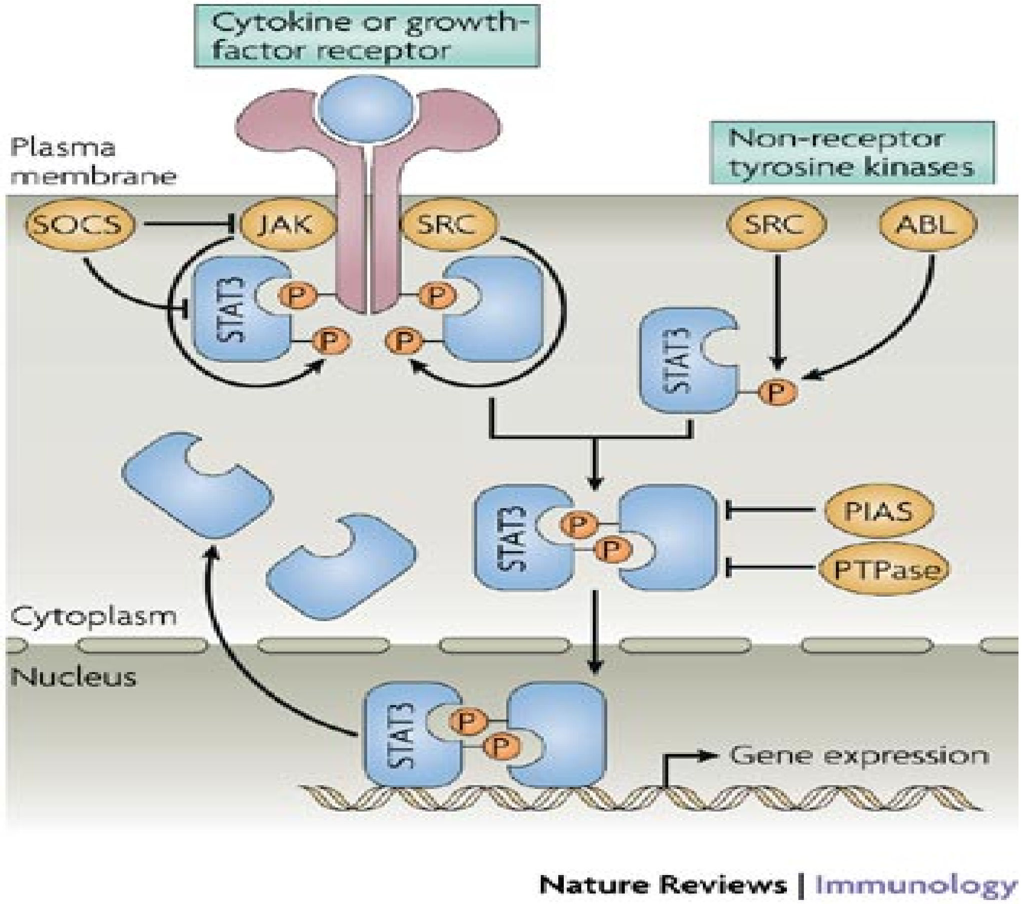

Figure 8: Jak-Stat3 pathway. Upon growth factors or cytokines binding to the receptor, a dimerization of receptor and later cytoplasmic domain autophosphorylation event occurs. The autophosphorylation creates a Stat3 protein docking site. Stat3 monomers are recruited to the receptor. Once a Stat3 monomer binds to the docking site, Janus Kinase (JAK) phosphorylates the tyrosine residue Tyr705 of Stat3 proteins which lead to dimerization of Stat3. The homo-dimer of Stat3 rapidly translocates into a nucleus. It binds with a promoter DNA sequence to regulate targeted gene expression.

(Figure is adapted from Yu, H., Kortylewaski, M., Pardoll, D. (2007). Crosstalk between cancer and immune cells: role of STAT3 in the tumor microenvironment. *Nature Reviews Immunology*, *7*, 41-51.)

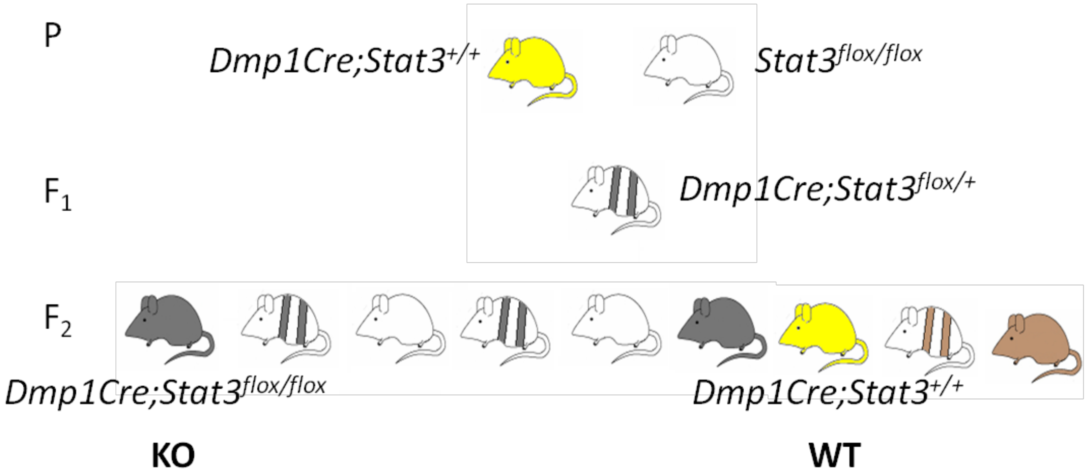

Figure 9: The experimental mice breeding scheme. In the parents' generation (P), the homozygous Cre expression mice (yellow) breed with homozygous Stat3 gene floxed mice (white). The offspring F_1 generation mice (striped) carry the Cre gene and the heterozygous floxed Stat3 gene. The F_1 generation of mice is cross bred to produce the F_2 generation. In the F_2 generation, the homozygous for both floxed Stat3 gene and Cre transgene generate knockout mice (dark grey). Only Cre gene carrying mice are used as wild type littermate controls (yellow).

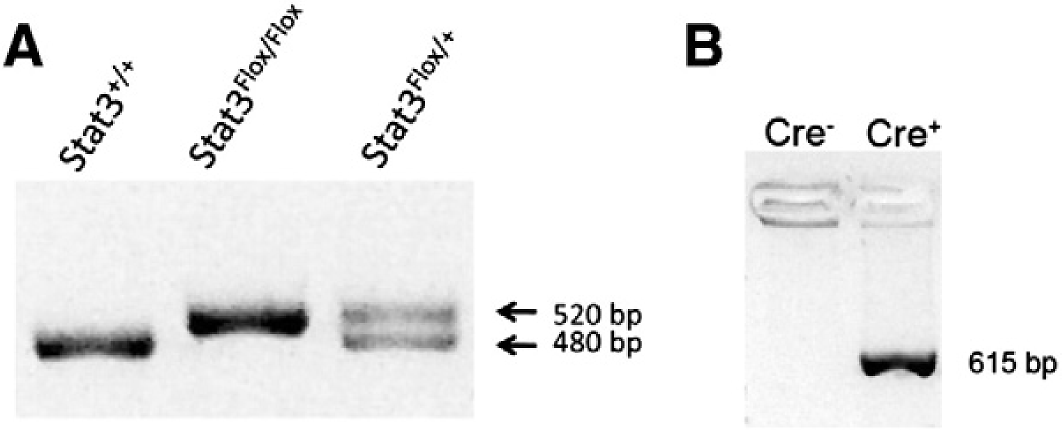

Figure 10: Genotyping for LoxP and Cre gene. A: The Stat3$^{flox/flox}$ allele was detected with the primers amplifying a 520 bp fragment, while Stat3 wild-type allele Stat3$^{+/+}$ gave a 480 bp fragment. And the heterozygous genotype Stat3$^{flox/+}$ has both 520 bp and 480 bp DNA bands. B: The Cre transgene was detected with the primers amplifying a 615 bp fragment.

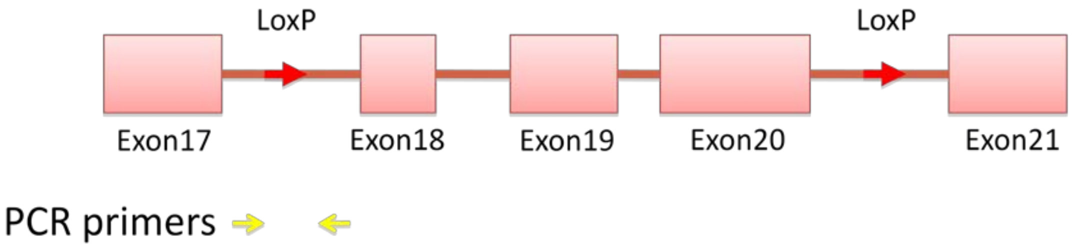

Figure 11: LoxP sites flanked exons of Stat3 gene. Two LoxP sites (red arrowheads) flank exons 18-20 of Stat3 gene. The PCR forward primer 5’-ATTGGAACCTGGGACCAAGTGG-3’ (left yellow arrowhead) and reverse primer 5’-ACATGTACTTACAGGGTGTGTGC-3’ (right yellow arrowhead) are used to amplify a PCR product of 520 bp with LoxP DNA sequence. Without LoxP DNA sequence, the PCR product is 480 bp in length.

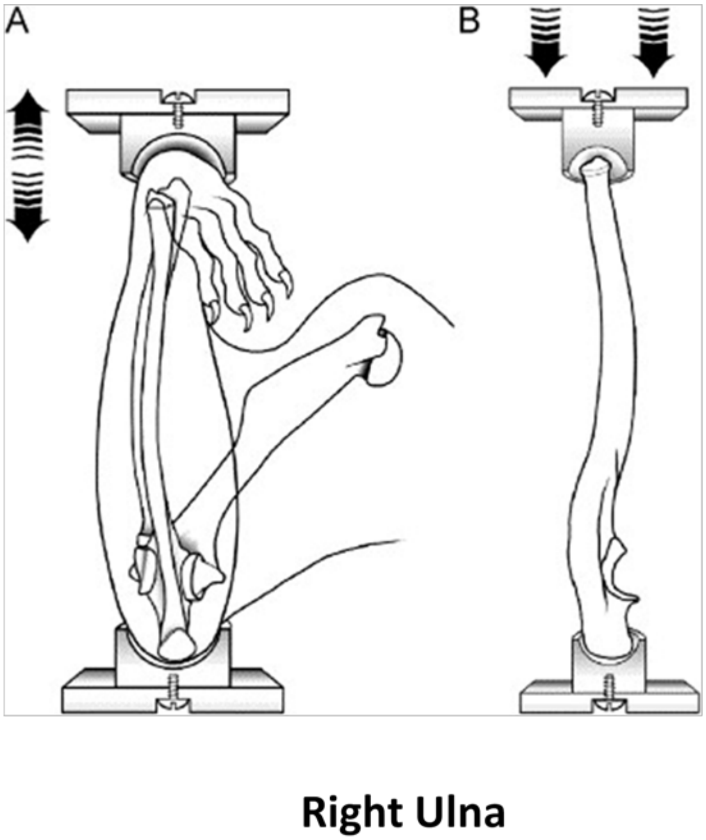

Figure 12: *In vivo* ulna loading illustration. 16 weeks old experimental mice right ulna was loaded with 2.5 N for female, 2.8 N for male, 120 cycles/day at 2 Hz for 3 consecutive days. Left ulna was used as an internal control. Calcein (green) was administered on day 5 after first loading. Alizarin (red) was administered on day 11, after first loading. Mice were euthanized and ulnas were dissected out16 days after loading. Ulna histomorphometry of bone formation rate and bone mineral apposition rate were measured.

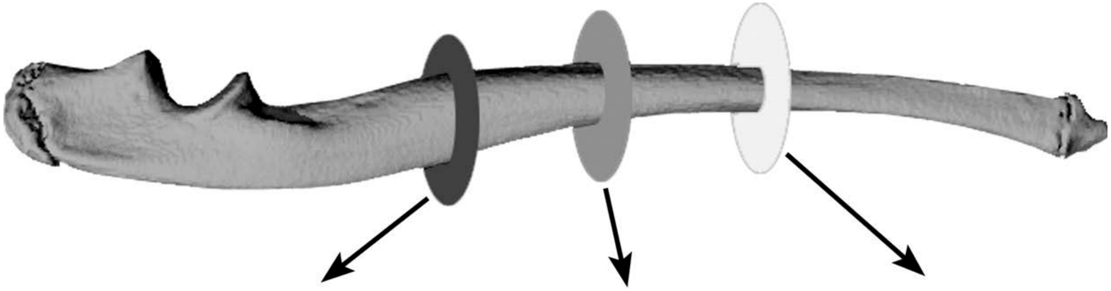

Figure 13: Illustration of midshaft ulna sections. Right ulna with radius and left ulna were embedded in MMA plastic. 3 pieces of transverse sections were cut in the midshaft ulna (0.070 mm). Ulna specimens were grinded to a thickness of 0.030 mm and mounted to the microscope slides for dynamic histomorphometry measurement.

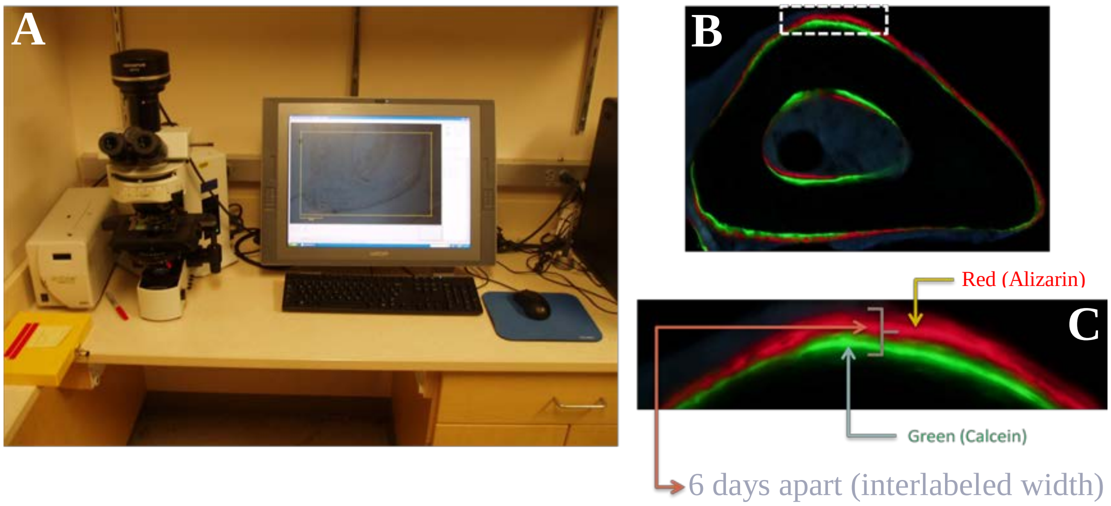

Figure 14: Ulna loaded-induced bone formation dynamic histomorphometry. A: OsteoMetrics® System with an OLYMPUS fluorescence microscope and OsteoMeasure™ histomorphometry software. B: at 100 X magnification, a midshaft section of the dynamic axial loaded right ulna. The new bone formation was presented by green and red fluorescent dye labeling. C: at 400 X magnification, the enlarged image of white dashed rectangle covered area in picture B. Red fluorescent dye indicated Alizarin labeling new bone and Green fluorescent dye presented Calcein labeling new bone. There were 6 days apart between two fluorescent dyes labeling.

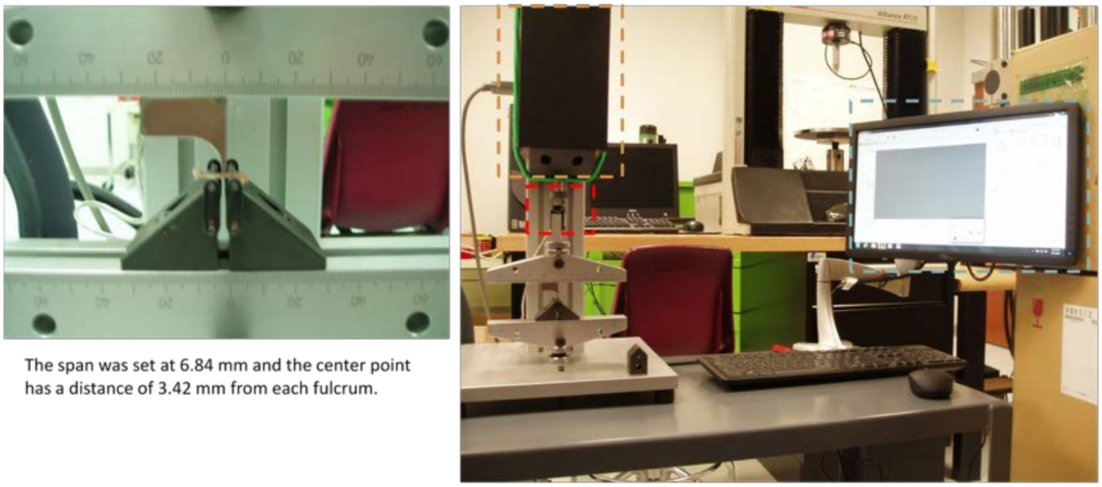

The span was set at 6.84 mm and the center point has a distance of 3.42 mm from each fulcrum.

500 lbs. Actuator
Serial Number: 1112011-02A
Assembly Number: 111215-16
Part Number: 20045402

25 lbs. Load Cell
Model: SM-25-294
Capacity: 25 lbs.
Serial: 672358

R Controller
Version 3.13.02
R controller Firmware
Version SIMULATIONS

Figure 15: Three point bending machine. During the bending process, the sensory system (TestResources Inc., Shakopee, MN 55379, USA) in the loading machine recorded primary data such as bending force (N) and bone displacement (deformation) (µm). From previous data, force and displacement curve was constructed by the controller system of the bending machine (R Controller, Version 3.13.02).

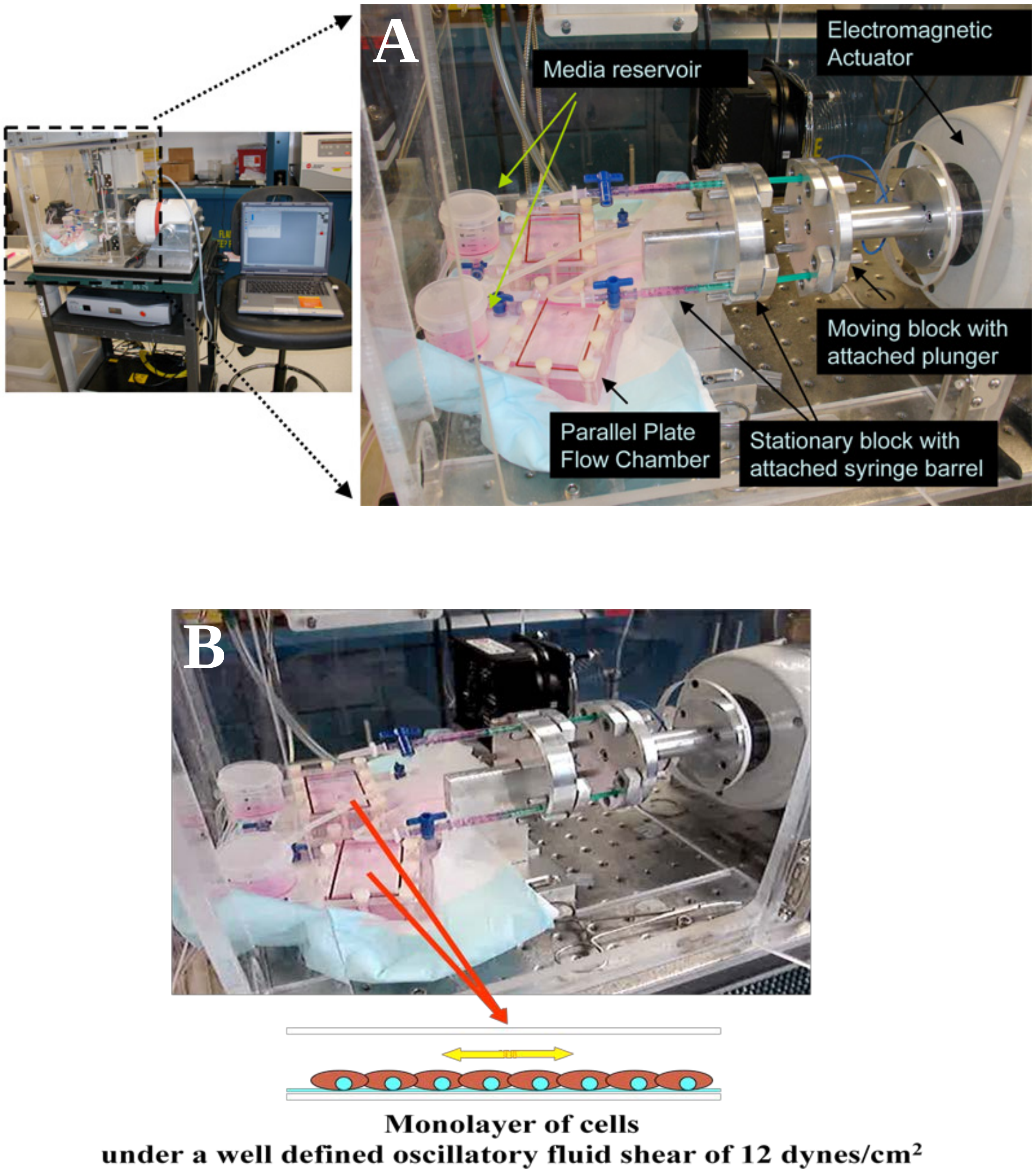

Figure 16: Fluid Shear Stress (FSS) generating equipment. The FSS is applied to the MC3T3-E1 osteoblasts in the chamber in a multidirectional manner. A: Electromagnetic Actuator generates the motion of attached plunger to propel a well defined oscillatory sheering fluid of 12 dynes/cm^2 in tightly sealed flow chambers. B: Monolayer of MC3T3-E1 osteoblasts were seeded on flow chambers experiencing oscillatory fluid sheer stress at 37 °C with a 5% CO_2 supply.

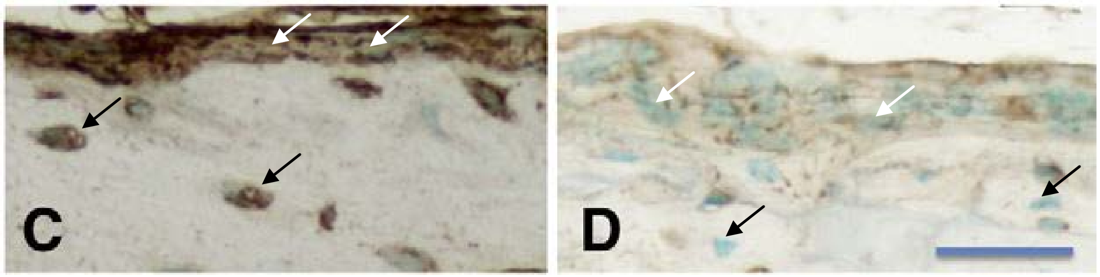

Figure 17: Immunohistochemical staining of experimental mice femurs.
(C) Immunohistochemical staining for wild type control with Stat3 protein present in periosteal osteoblasts (white arrow) and osteocytes (black arrow). (D) Immunohistochemical staining for KO (Col3.6-Cre;Stat3$^{flox/flox}$) mice without Stat3 protein in osteoblasts (white arrow) and osteocytes (black arrow). Nuclei were stained with Methyl Green (Bar=50 μm).

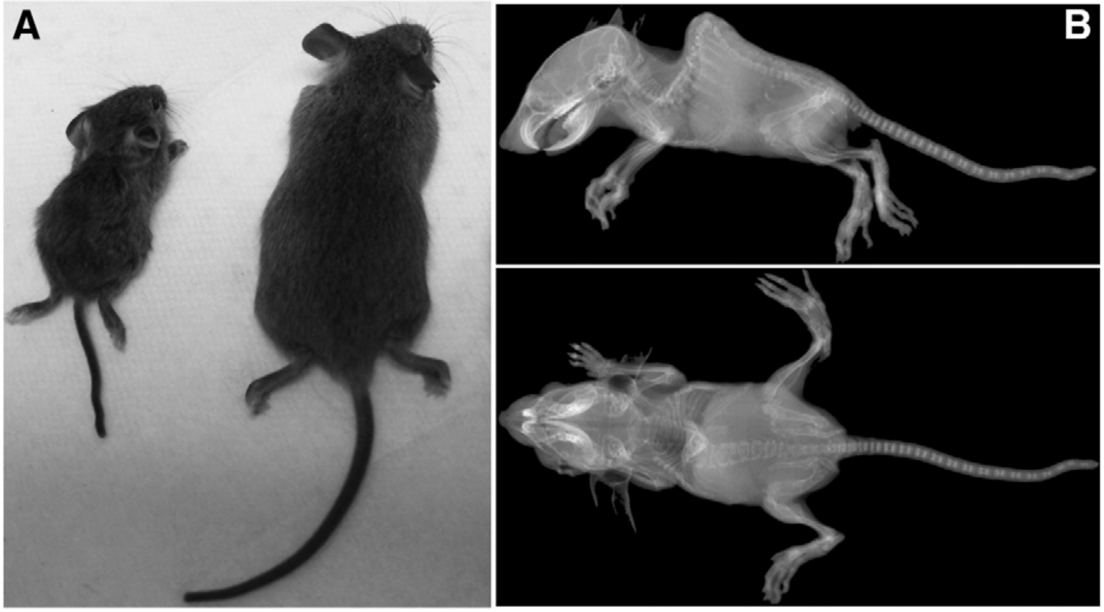

Figure 18: Appearance of the conditional Stat3 KO mice. (A) Col3.6-Cre;Stat3$^{flox/flox}$ mice significantly smaller than its littermate control. (B) Lateral and anterior-posterior X-ray views of the Col3.6-Cre;Stat3$^{flox/flox}$ mouse showing severe spinal deformity.

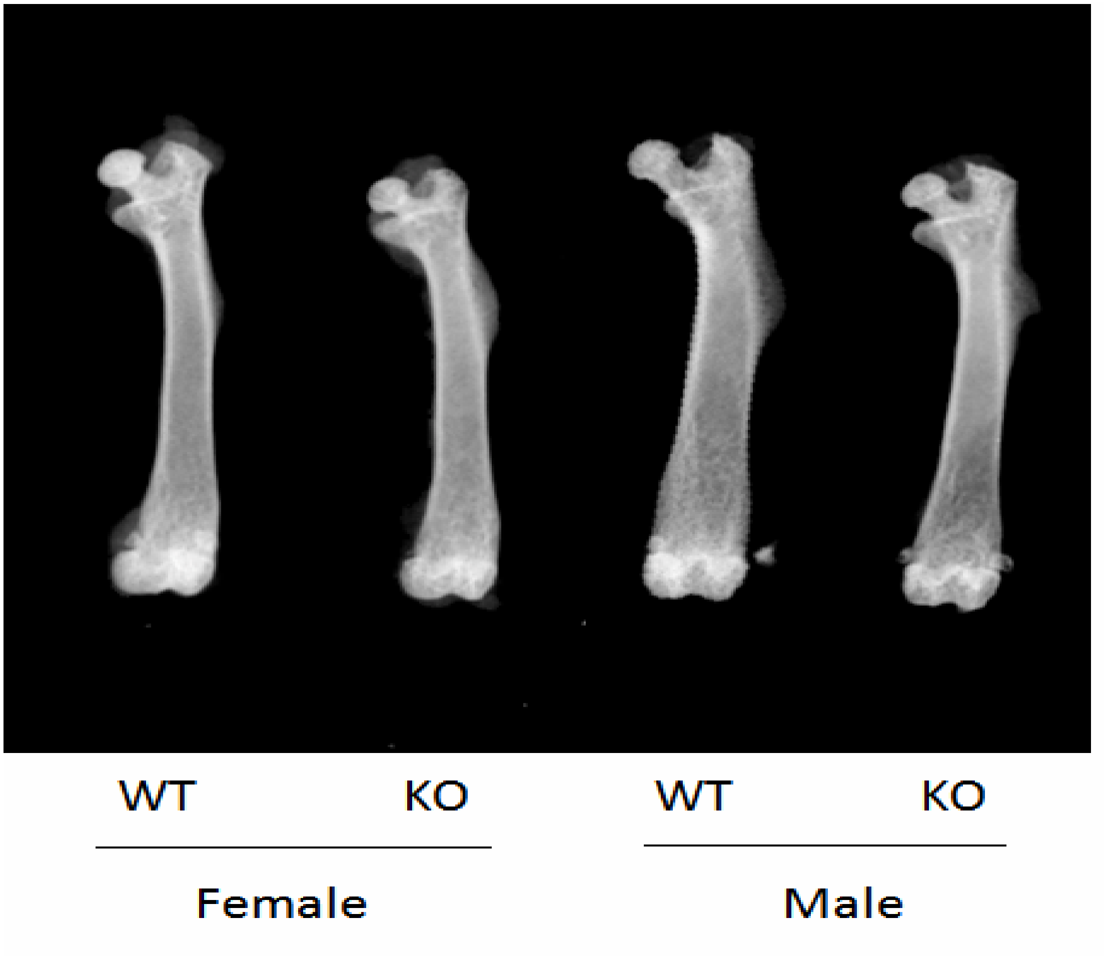

Figure 19: High resolution X-ray images of experimental mice femurs. For both 18 weeks old adult female and male, Col3.6-Cre;Stat3$^{flox/folx}$ (KO) mouse femur length was significantly shorter than its littermate control (WT) mouse femur.

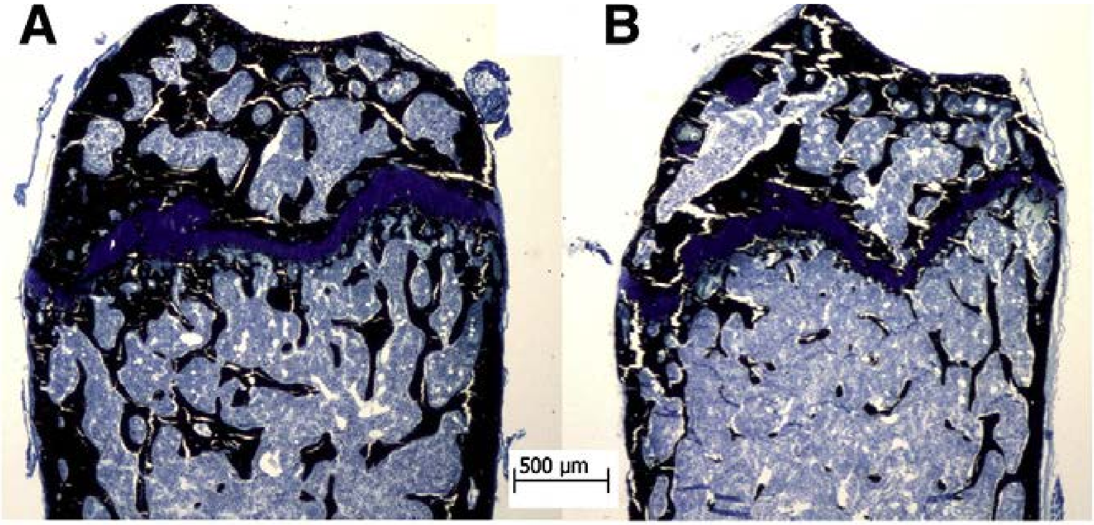

Figure 20: Von Kossa/MacNeal’s stained distal femurs. Calcified bones were stained black and cartilage was stained dark blue. Trabecular bone size and number decreased in Col3.6-Cre;Stat3$^{flox/flox}$ mouse (B) compared to wild type control (A). Scale bar=500µm.

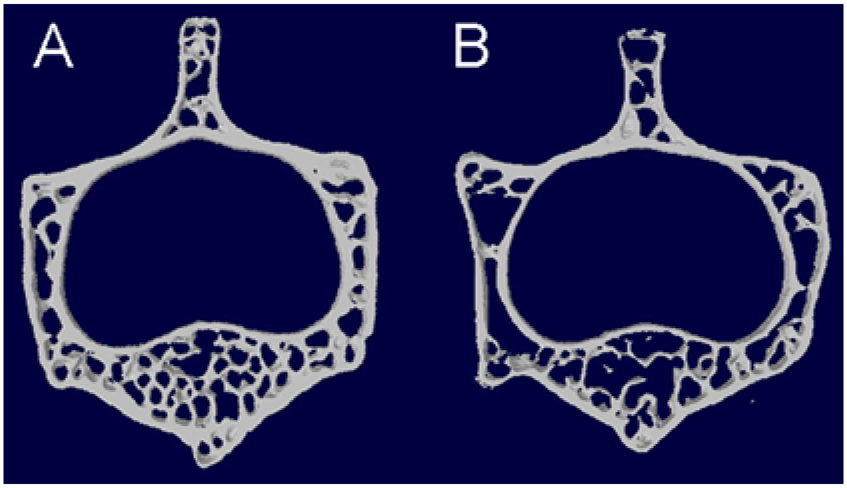

Figure 21: Cross-sectional μCT images of the 4th lumbar vertebrae (L4). L4 of Col3.6-Cre;Stat3$^{flox/flox}$ mouse (B) demonstrates less trabecular bone number than the wild type littermate control (A).

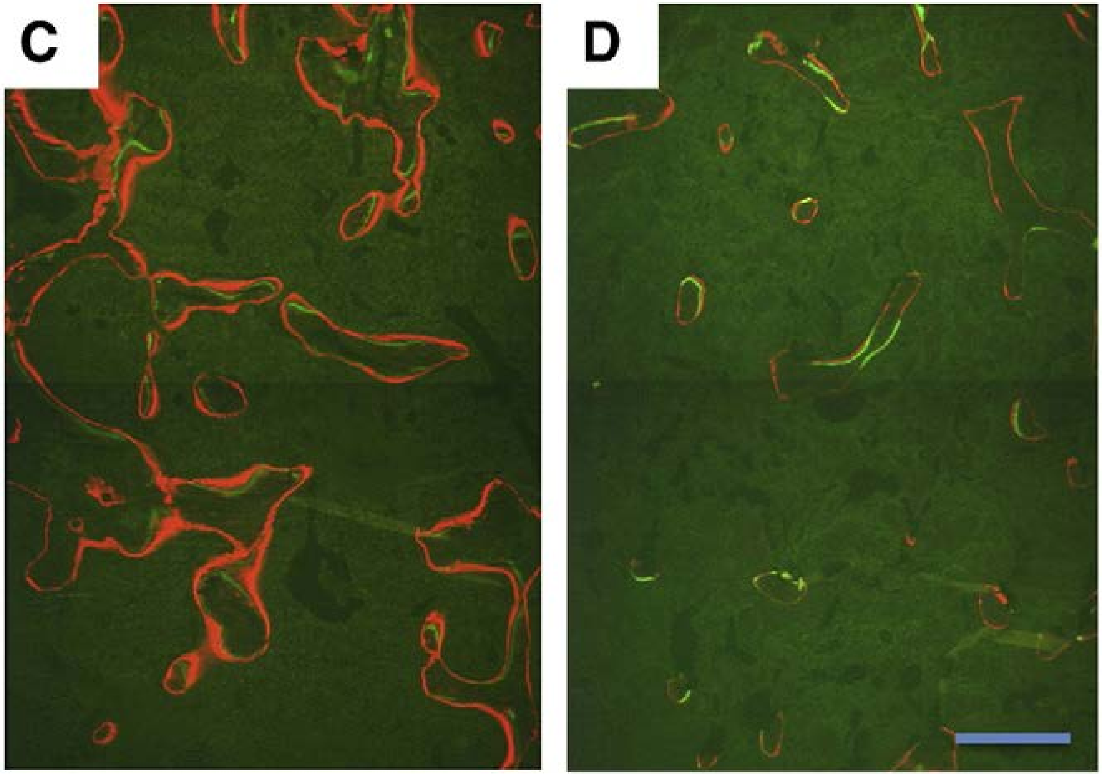

Figure 22: The fluorescent labels of experimental mice distal femurs. The red (alizarin) and green (calcein) fluorescent labels of trabecular bone at the distal end of the femur in (C) wild type littermate control mice and (D) conditional Stat3 knockout (Col3.6-Cre;Stat3$^{flox/flox}$) mice, indicating mineralizing surface (MS/BS), mineral appositional rate (MAR) and bone formation rate (BFR/BS). (Bar=200μm).

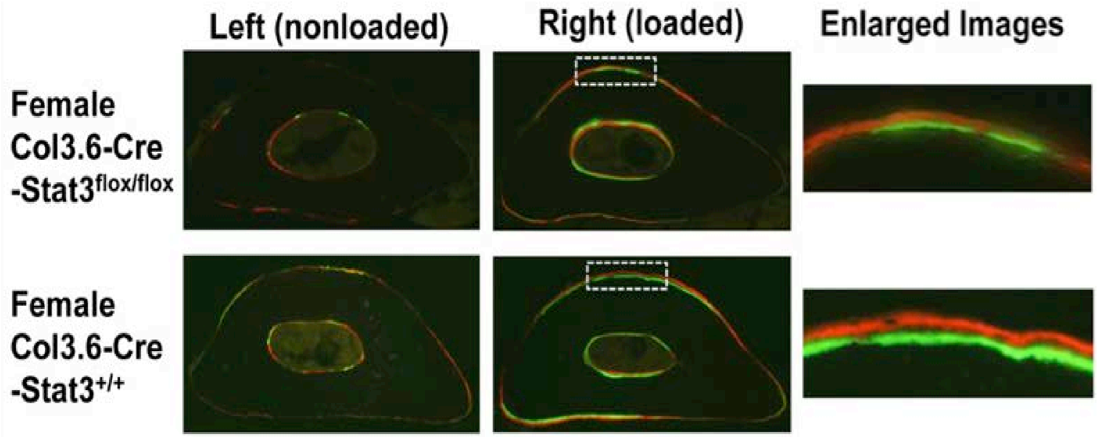

Figure 23: Midshaft sections of experimental mice ulnas. Midshaft ulnar sections from the non-loaded and loaded forearms of female WT control (Col3.6-Cre;Stat3$^{+/+}$) mice and KO (Col3.6-Cre;Stat3$^{flox/flox}$) mice. Calcein (green) and alizarin (red) were injected after loading to label load-induced new bone formation. Note that the anabolic responses on the medial (square) and lateral surfaces of the loaded control ulna were detected. In the KO mice those responses were significantly decreased in the loaded ulna compared with the loaded ulna of WT mice (enlarged images).

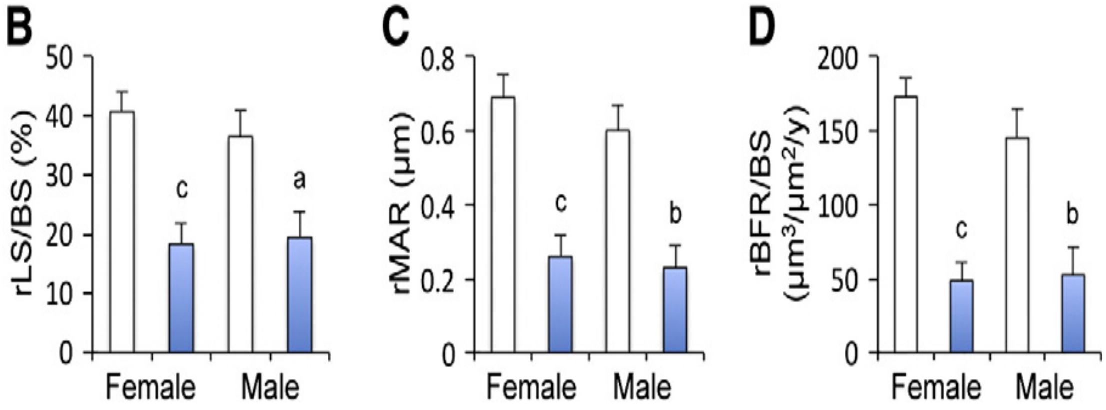

Figure 24: Bone morphometric parameters of female and male experimental mice. WT control mice (Col3.6-Cre;Stat3$^{+/+}$) (open bars) and KO (Col3.6-Cre;Stat3$^{flox/flox}$) mice (solid bars). (B) Relative mineralizing surface (rMS/BS). (C) Relative mineral appositional rate (rMAR). (D) Relative bone formation rate (rBFR/BS). Note that a: $p<0.05$, b: $p<0.01$, and c: $p<0.001$.

p-Y705 STAT3, Tyr705 phosphorylated STAT3

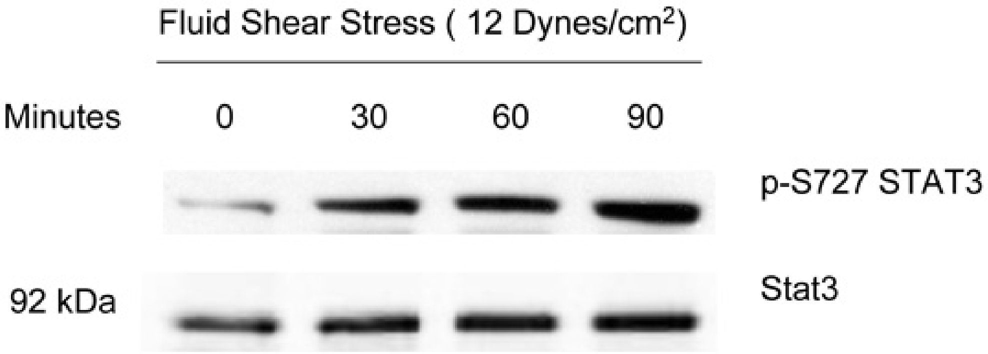

p-S727 STAT3, Ser727 phosphorylated STAT3

Figure 25: Stat3 activation increased in response to Fluid Shear Stress (FSS). Western blot analysis demonstrates that the quantity of phosphorylated Stat3 proteins at Tyrosine 705 (A) and Serine 727 (B) was increased with time from 0 minutes to 90 minutes following FSS at 12 dynes/cm^2. 92 kDa total Stat3 proteins were used as controls to show the total quantity of Stat3 proteins in each time lapse of FSS.

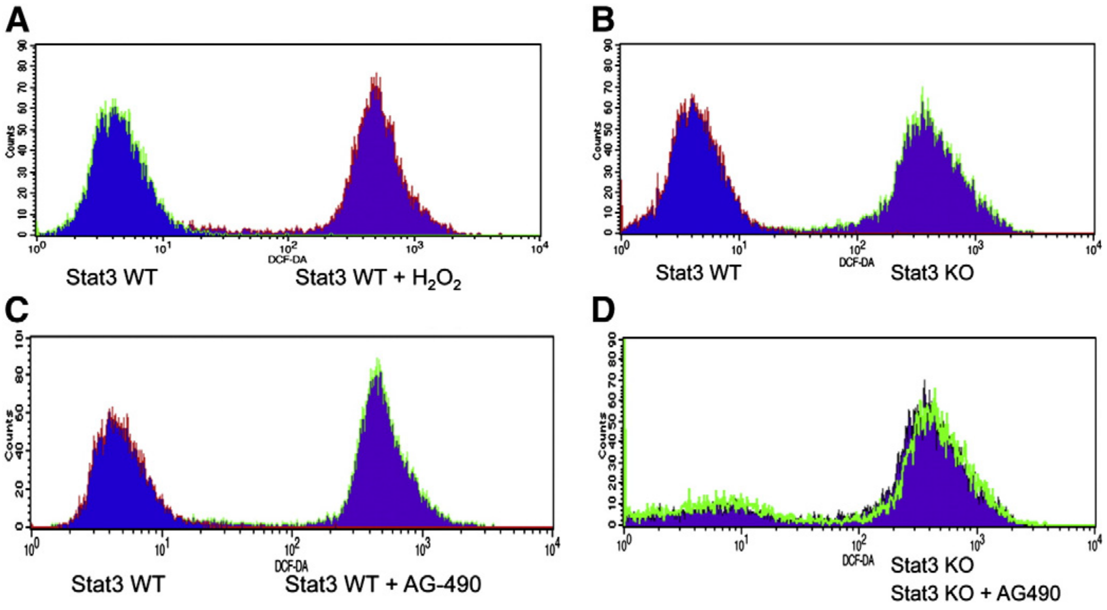

Figure 26: Flow cytometric analysis for the level of Reactive Oxygen Species (ROS). ROS level was monitored by using 2,7-DCF-DA fluorescence (horizontal axis). (A) ROS level increased significantly in wild type (WT) cells when treated with hydrogen peroxide (H_2O_2) (as a positive control). (B) ROS level was significantly higher in Stat3 deficient (KO) calvarial osteoblasts. (C) ROS level increased significantly in wild type cells when treated with AG-490, an inhibitor of Stat3. (D) ROS level did not change in Stat3 deficient cells treated with AG-490.

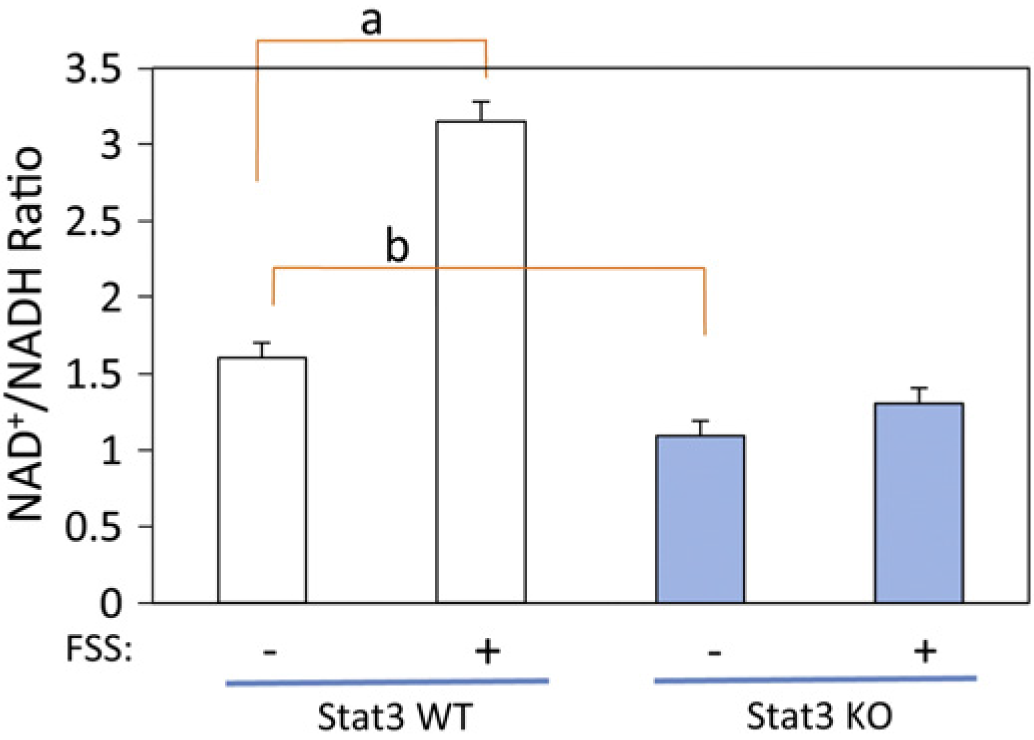

Figure 27: Levels of NAD$^+$/NADH ratios in wild type (WT) and Stat3 KO osteoblasts with and without fluid shear stress (FSS). Note that a: $p<0.001$ and b: $p<0.01$.

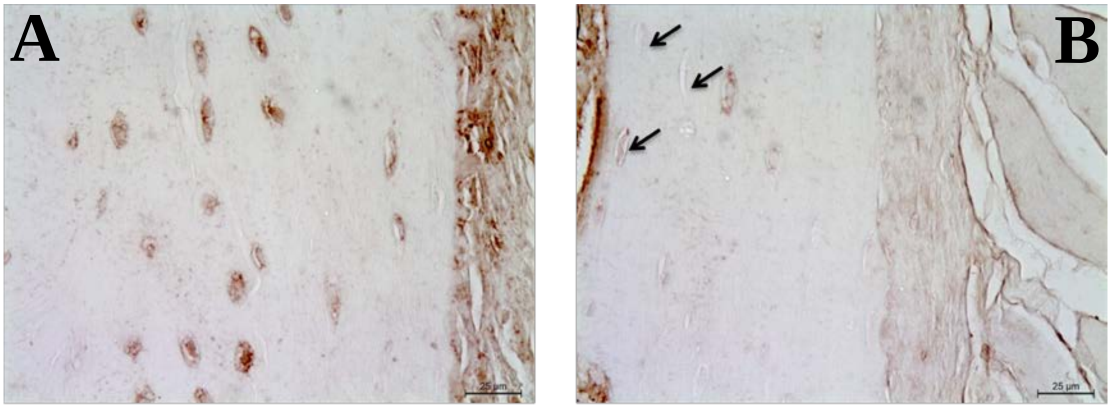

(WT Femur) **(KO Femur)**

Figure 28: Immunohistochemical staining of experimental mice cortical femurs. Immunohistochemical staining demonstrates the expression of Stat3 protein in 8-week-old osteocytes of the Dmp1-Cre;Stat3$^{+/+}$ (WT control) mouse (A). Stat3 proteins in osteocytes were stained brown and dark brown. However, there was no Stat3 protein expression in osteocytes of the Dmp1-Cre;Stat3$^{flox/flox}$ (conditional Stat3 KO) mouse (B). Black arrows indicate osteocytes without Stat3 proteins probed by brown stains in conditional Stat3 KO mouse. (Scale bar=25μm).

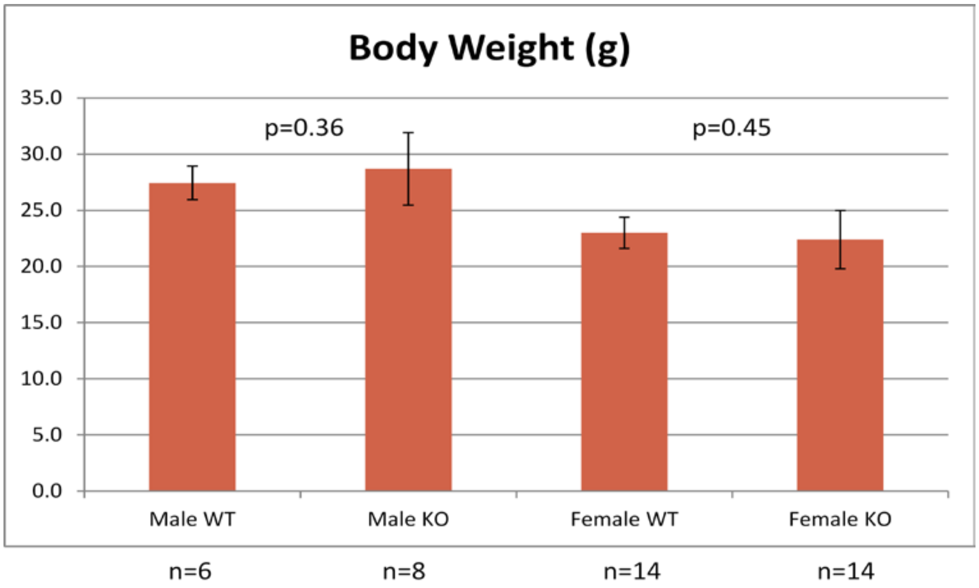

Figure 29: Body weight of experimental mice. For 18-week-old mice, the WT and KO animals' body weights have no significant difference in both genders.

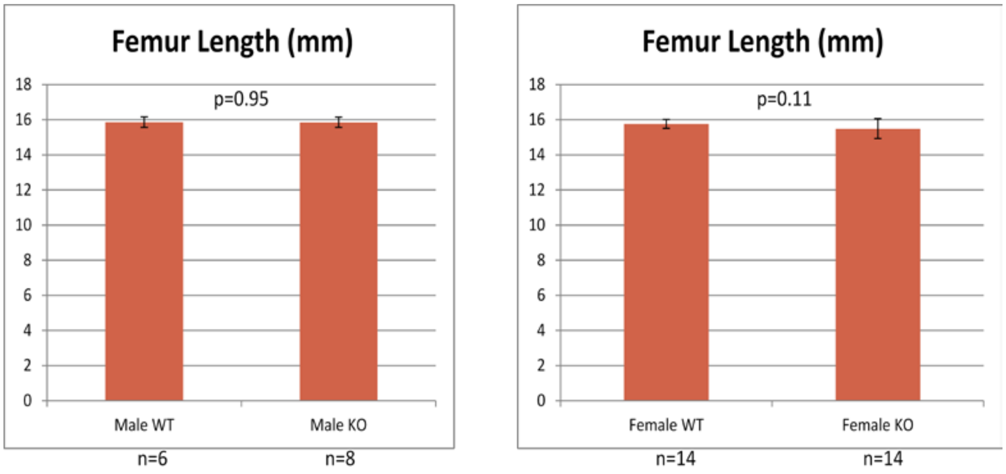

Figure 30: Femur length of experimental mice. The femoral lengths were used as their sex- and age-matched littermate controls. Left femur lengths of each experimental group were measured and indicated that the average femur lengths have no significant difference between 18-week-old KO and WT mice in both genders.

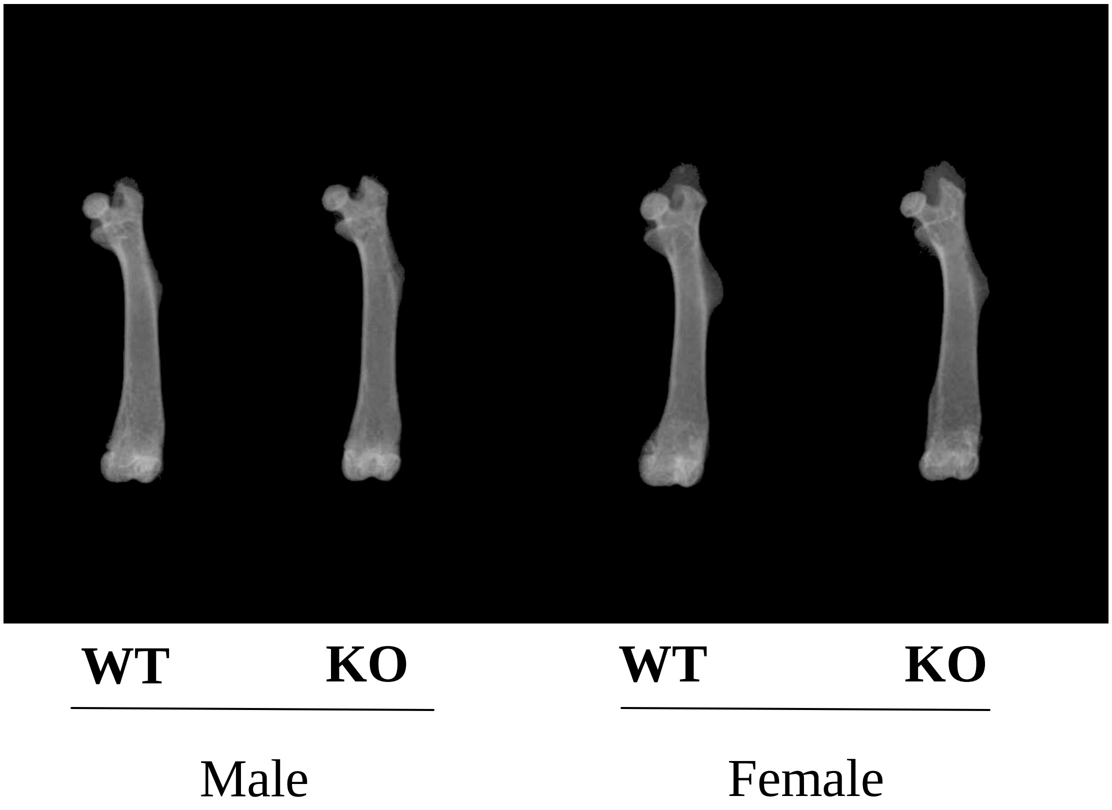

Figure 31: Radiograph of left femurs from Dmp1-Cre;Stat3$^{flox/flox}$ (KO) mice and WT controls. Femurs of both male and female Dmp1-Cre;Stat3$^{flox/flox}$ (KO) mice have no significant difference in length and morphology compared with their age-matched WT littermate controls.

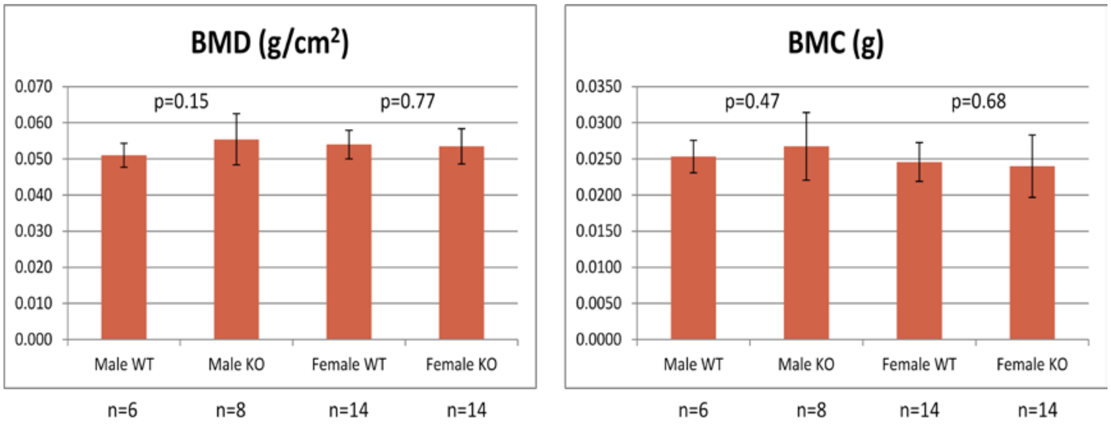

Figure 32: Femoral BMD and BMC of experimental mice. For femoral BMD and BMC of Dmp1-Cre;Stat3$^{+/+}$ (WT) mice and Dmp1-Cre;Stat3$^{flox/flox}$ (KO) mice, the WT and KO mice's femoral BMD and BMC presented no significant difference in both genders.

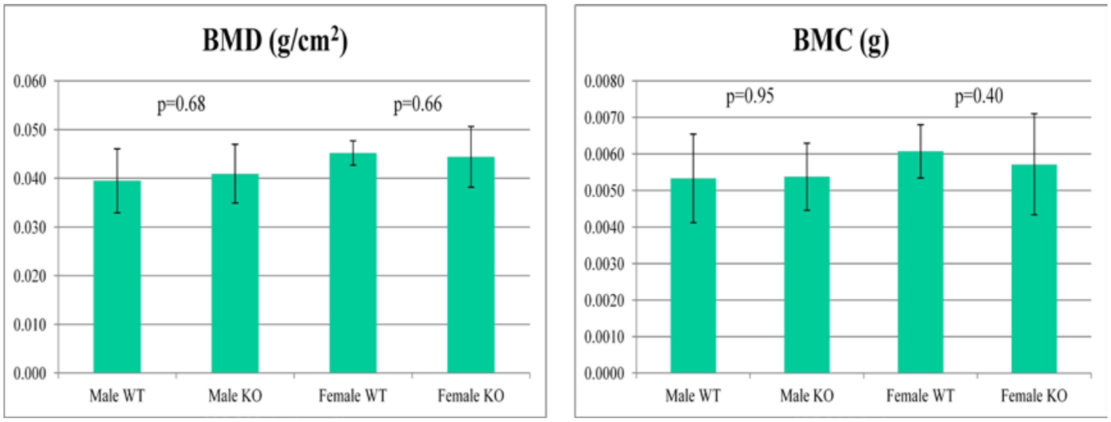

Figure 33: Lumbar vertebral body L4 BMD and BMC of experimental mice. For both Dmp1-Cre;Stat3$^{+/+}$ (WT) mice and Dmp1-Cre;Stat3$^{flox/flox}$ (KO) mice, the WT and KO mice's vertebra L4 BMD and BMC exhibited no significant difference in both genders.

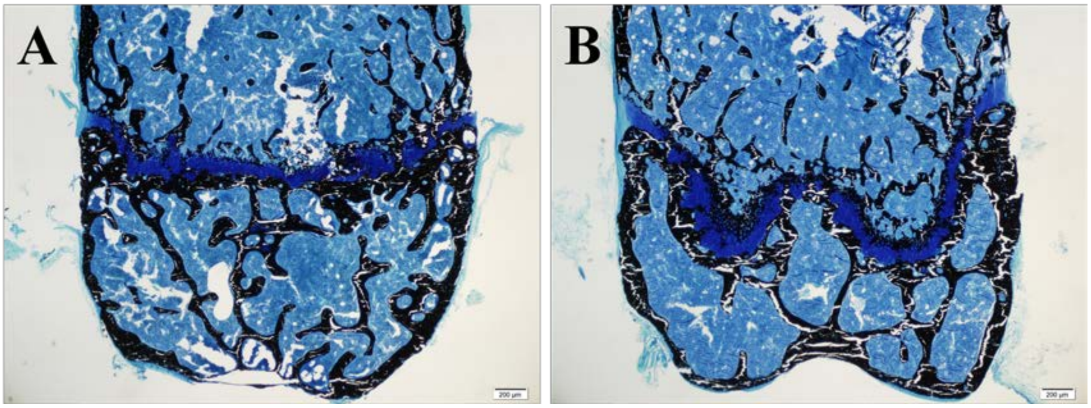

Figure 34: Von Kossa/MacNeal's stained distal femurs. Calcified bones were stained black and cartilage was stained dark blue. Trabecular bone number and volume presented no significant difference in Dmp1-Cre;Stat3$^{flox/flox}$ mouse (B) compared to their age-matched wild type littermate control mouse (A). Scale bar=200µm.

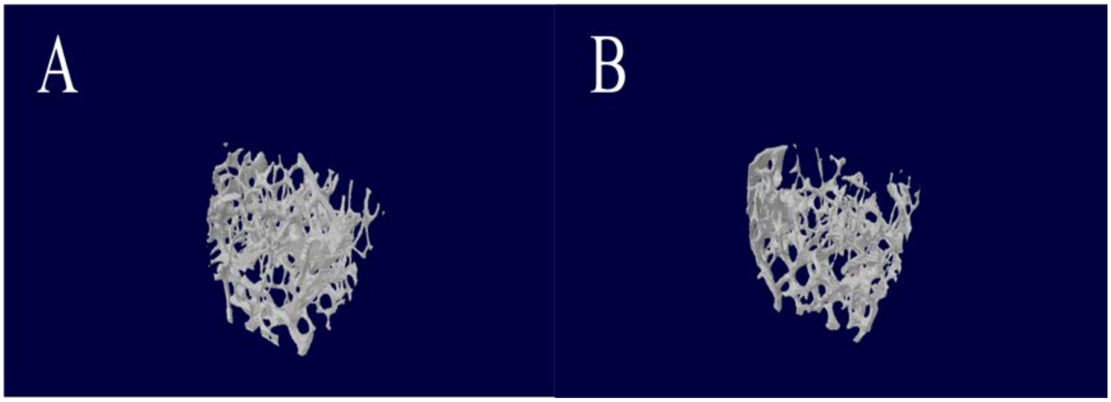

Figure 35: Three-dimensional images of distal femur trabecular bones. In the intracortical area 1 mm above the growth plate, compared to Dmp1-Cre;Stat3$^{+/+}$ (WT) mouse trabecular bones (A), the Dmp1-Cre;Stat3$^{flox/flox}$ (KO) mouse trabecular bones (B) demonstrated no significant difference in trabecular bone number and volume.

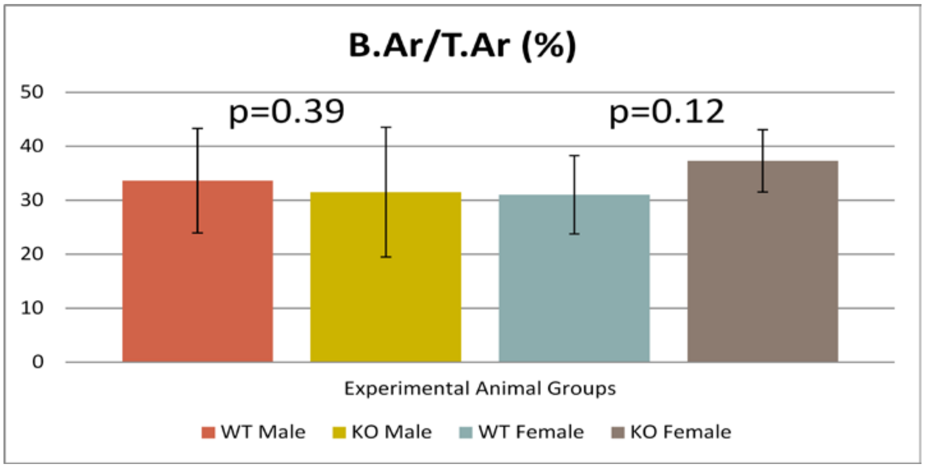

Figure 36: B.Ar/T.Ar of experimental mice trabecular bones. Compared to Dmp1-Cre;Stat3$^{+/+}$ (WT) mice, Dmp1-Cre;Stat3$^{flox/flox}$ (KO) mice presented no significant difference in distal femur trabecular bone volume/tissue volume (B.Ar/T.Ar) for males (p=0.39) and females (p=0.12). In each experimental mice group n=6.

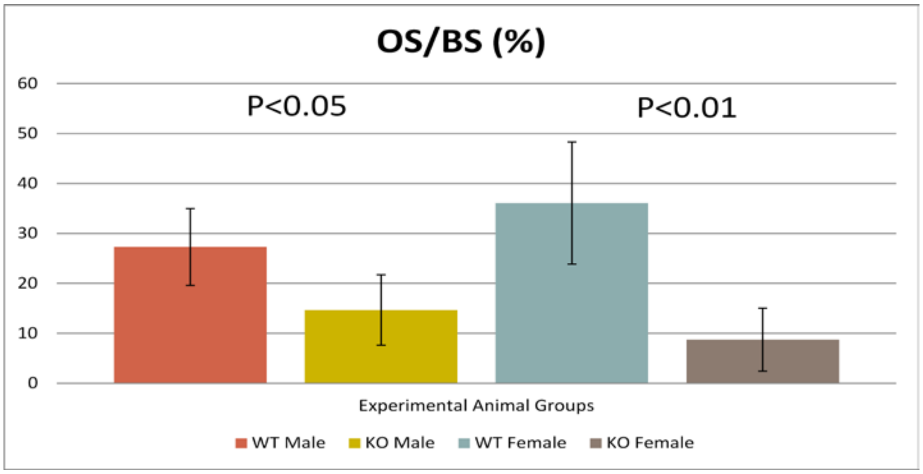

Figure 37: OS/BS of experimental mice trabecular bones. Compared to their littermate controls (Dmp1-Cre;Stat3$^{+/+}$) in males, the osteoid surfaces of the KO mice were 75.8% smaller ($p<0.01$). In females, the osteoid surfaces (OS/BS) of the conditional Stat3 KO (Dmp1-Cre;Stat3$^{flox/flox}$) mice were 46.2% smaller ($p<0.05$). In each experimental mice group n=6.

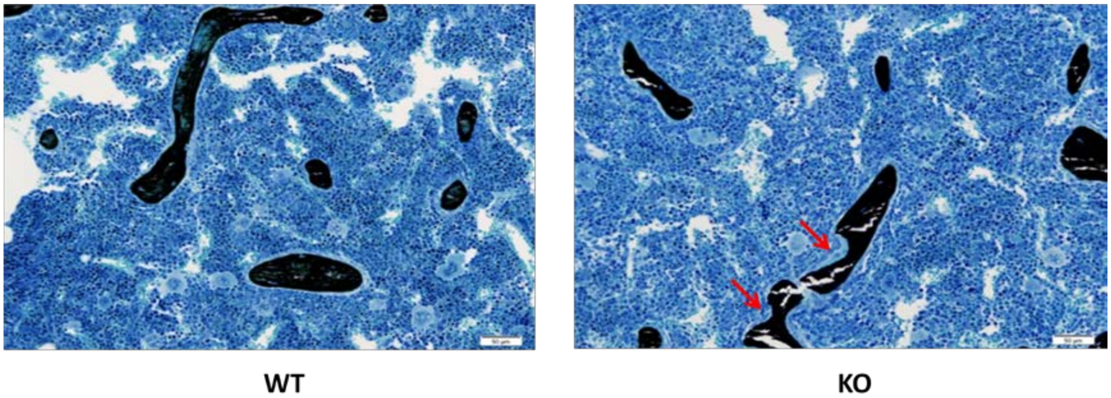

Figure 38: Eroded trabecular bone surface of experimental mice. Compared to Dmp1-Cre;Stat3$^{+/+}$ (WT) mice, Dmp1-Cre;Stat3$^{flox/flox}$ (KO) mice presented more eroded trabecular bone surface (red arrows) in the similar region of distal femur 0.5 mm above the growth plate. Scale bar=50μm.

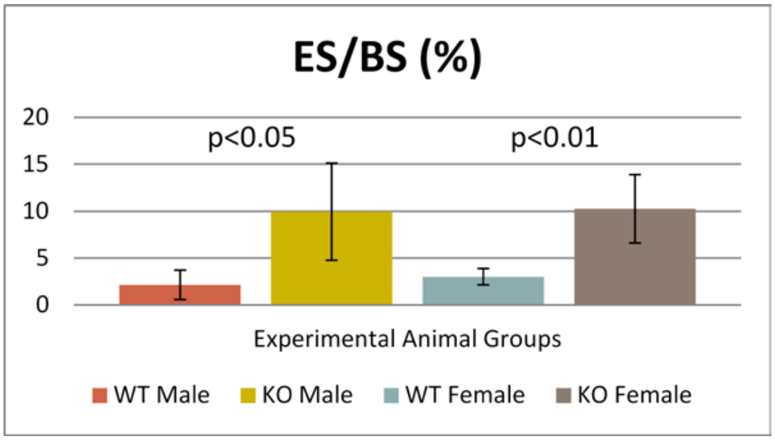

Figure 39: ES/BS of experimental mice trabecular bones. Compared to their WT (Dmp1-Cre;Stat3$^{+/+}$) controls in males, ES/BS of osteocyte-specific Stat3 KO (Dmp1-Cre;Stat3$^{flox/flox}$) mice were 364% greater ($p<0.05$). In females, ES/BS of KO mice were 240% greater ($p<0.01$). In each experimental group n=6.

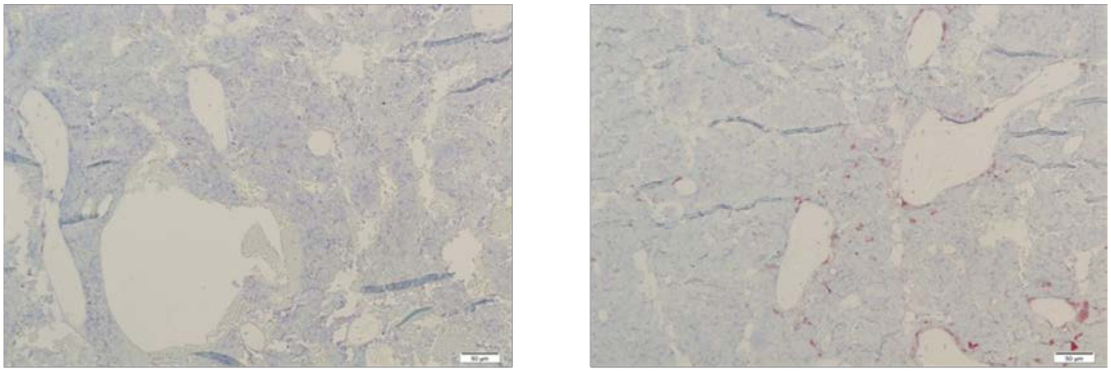

WT **KO**

Figure 40: TRAP stained osteoclasts on trabecular bone surfaces. Compared to Dmp1-Cre;Stat3$^{+/+}$ (WT) mouse, Dmp1-Cre;Stat3$^{flox/flox}$ (KO) mouse presented more osteoclast number and osteoclast surface (red stain on trabecular bone surface) on trabecular bone in the similar region of distal femur 0.5 mm above the growth plate. Scale bar=50μm.

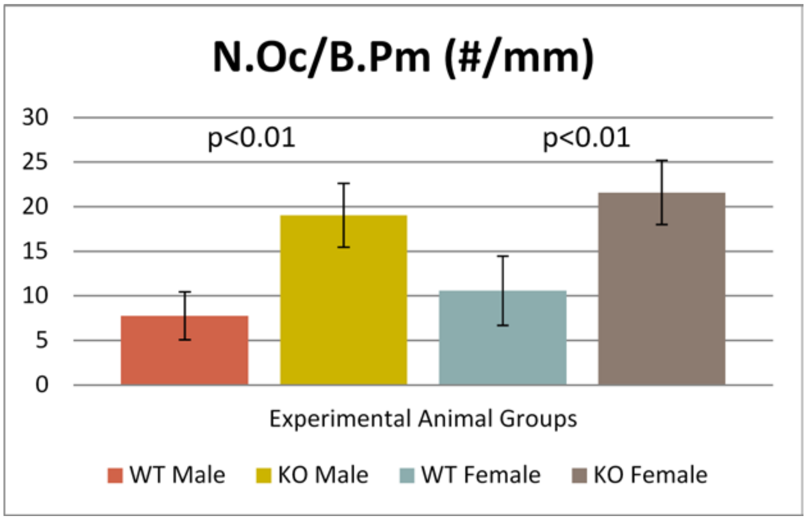

Figure 41: N.Oc/B.Pm of experimental mice trabecular bones. Compared to their WT (Dmp1-Cre;Stat3$^{+/+}$) controls in males, N.Oc/B.Pm of osteocyte-specific Stat3 KO (Dmp1-Cre;Stat3$^{flox/flox}$) mice were 146% greater ($p<0.01$). In females, N.Oc/B.Pm of KO mice were 104% greater ($p<0.01$). In each experimental group n=6.

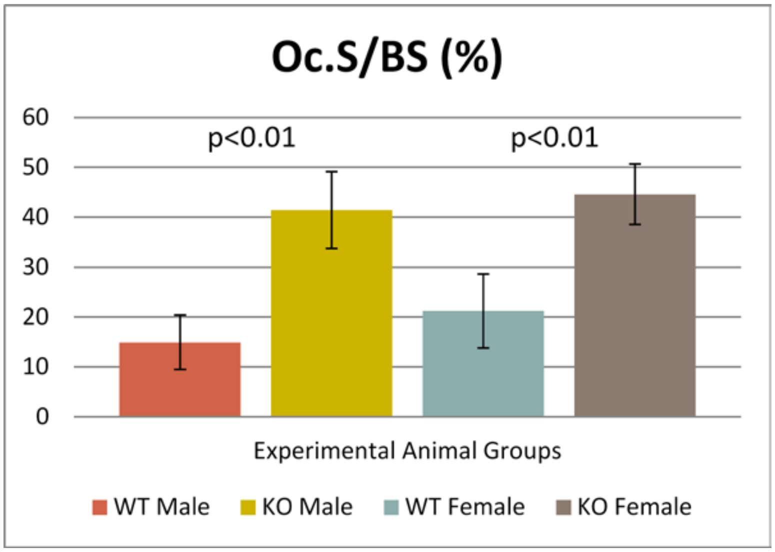

Figure 42: Oc.S/BS of experimental mice trabecular bones. Compared to their WT (Dmp1-Cre;Stat3$^{+/+}$) controls in males, Oc.S/BS of osteocyte-specific Stat3 KO (Dmp1-Cre;Stat3$^{flox/flox}$) mice were 177% greater ($p<0.01$). In females, Oc.S/BS of KO mice were 110% greater ($p<0.01$). In each experimental group n=6.

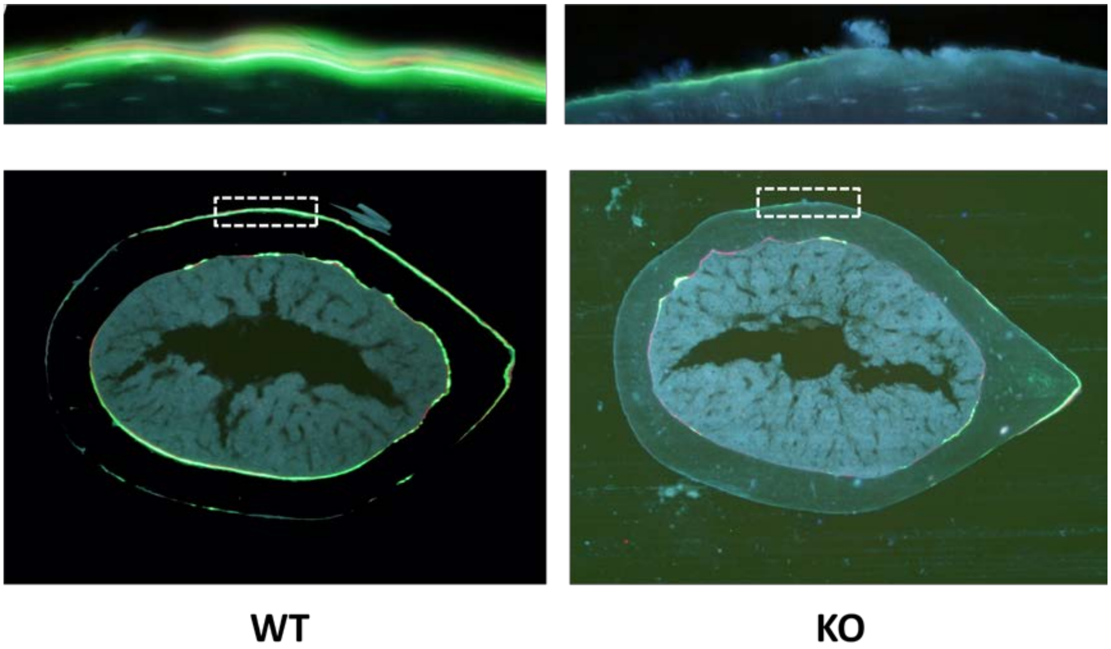

Figure 43: The red (alizarin) and green (calcein) fluorescent labels in the midshaft femurs. Conditional Stat3 KO (Dmp1-Cre;Stat3$^{flox/flox}$) mice demonstrated less fluorescent labels and smaller distance between two labels than wild type (WT) littermate control (Dmp1-Cre;Stat3$^{+/+}$) mice. This indicates mineralizing surface (MS/BS), mineral appositional rate (MAR), and bone formation rate (BFR/BS) were decreased in KO mice.

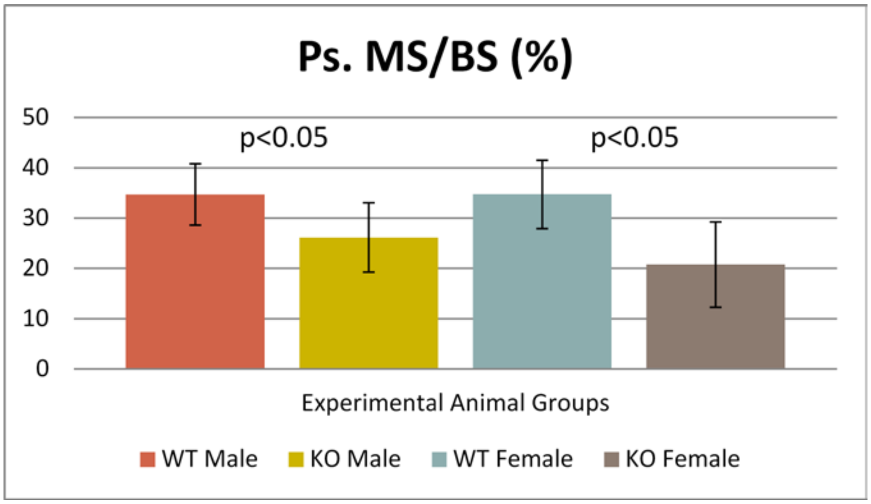

Figure 44: Ps. MS/BS of the midshaft femur cortical bone. On average, compare WT mice (n=6) data to KO mice (n=6) in males and females. The periosteal (Ps.) MS/BS decreased 24.6% ($p<0.05$) and 40.1% ($p<0.05$) respectively.

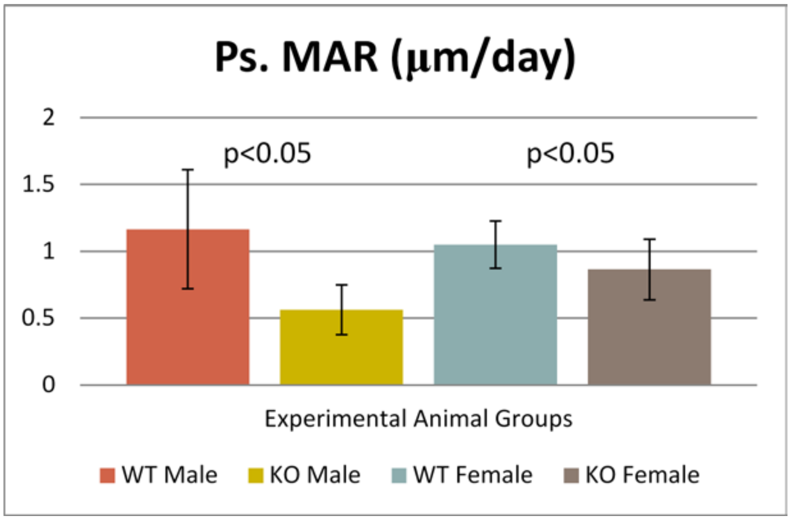

Figure 45: Ps. MAR of the midshaft femur cortical bone. On average, compare WT mice (n=6) data to KO mice (n=6) in males and females. The periosteal (Ps.) MAR decreased 51.8% ($p<0.05$) and 17.7% ($p<0.05$) respectively.

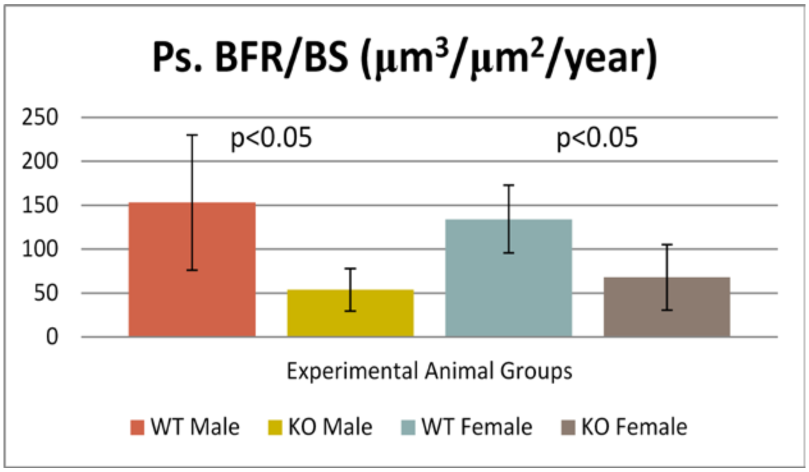

Figure 46: Ps. BFR/BS of the midshaft femur cortical bone. On average, compare WT mice (n=6) data to KO mice (n=6) in males and females. The periosteal (Ps.) BFR/BS decreased 64.8% ($p<0.05$) and 49.3% ($p<0.05$) respectively.

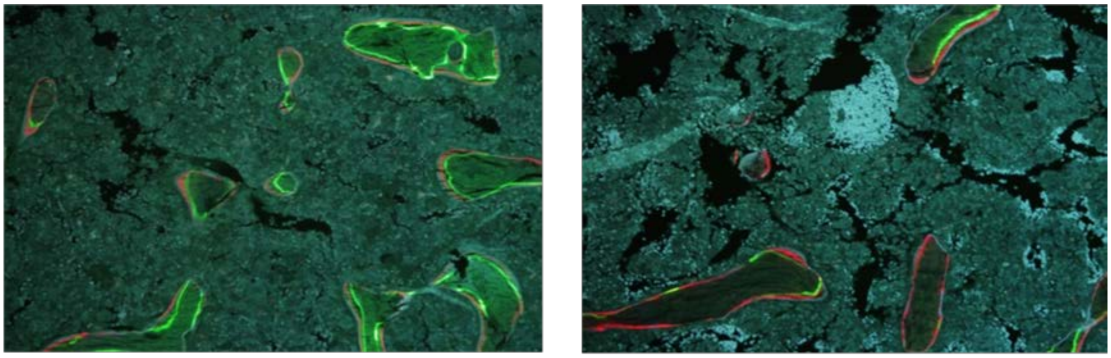

WT **KO**

Figure 47: The red (alizarin) and green (calcein) fluorescent labels in the distal femur trabecular bones. In the similar region of distal femur 0.5 mm above the growth plate, conditional Stat3 KO (Dmp1-Cre;Stat3$^{\text{flox/flox}}$) mice demonstrated less fluorescent labels and smaller distance between two labels than wild type (WT) littermate control (Dmp1-Cre;Stat3$^{+/+}$) mice. This indicated mineralizing surface (MS/BS), mineral appositional rate (MAR), and bone formation rate (BFR/BS) were decreased in KO mice.

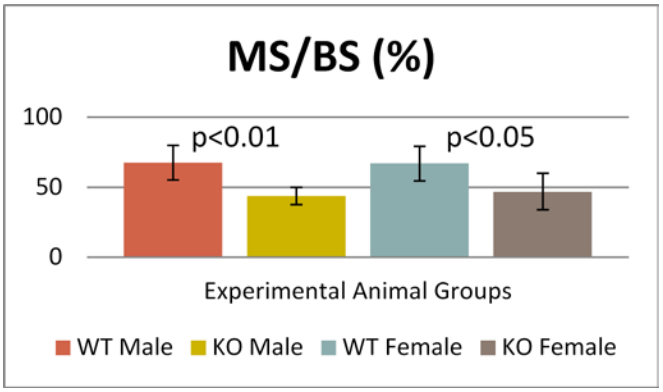

Figure 48: MS/BS of the distal femur trabecular bones. On average, compare WT mice (n=6) data to KO mice (n=6) in males and females. The distal femur trabecular bone MS/BS decreased 35.3% ($p<0.01$) and 30% ($p<0.05$) respectively.

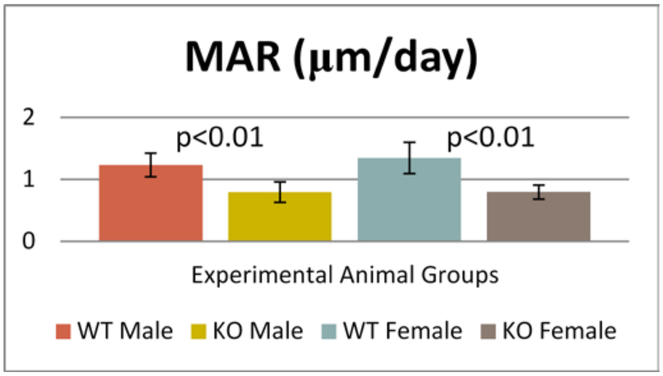

Figure 49: MAR of the distal femur trabecular bones. On average, compare WT mice (n=6) data to KO mice (n=6) in males and females. The trabecular bone MAR decreased 35.6% ($p<0.01$) and 41% ($p<0.01$) respectively.

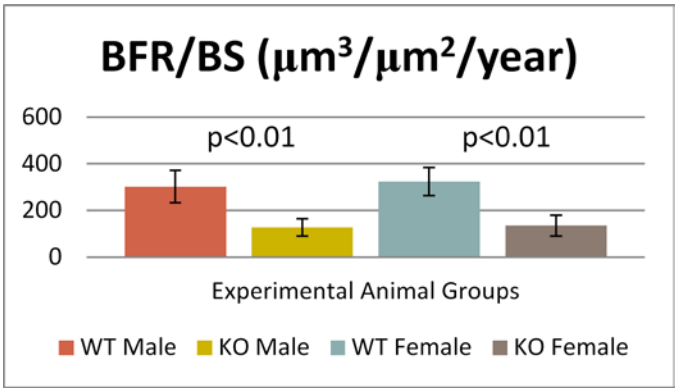

Figure 50: BFR/BS of the distal femur trabecular bones. On average, compare WT mice (n=6) data to KO mice (n=6) in males and females. The trabecular bone BFR/BS decreased 57.8% ($p<0.01$) and 58.1% ($p<0.01$) respectively.

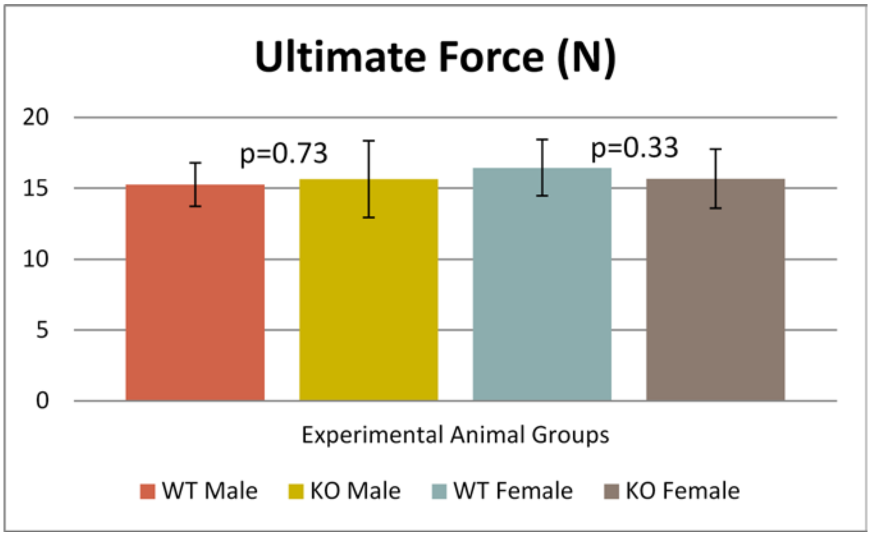

Figure 51: Ultimate force of experimental mice femurs. Data was presented by mean ± S.E.M. There were no significant differences between WT and Stat3 deficient (KO) femurs in ultimate force in both males (p=0.73) and females (p=0.33).

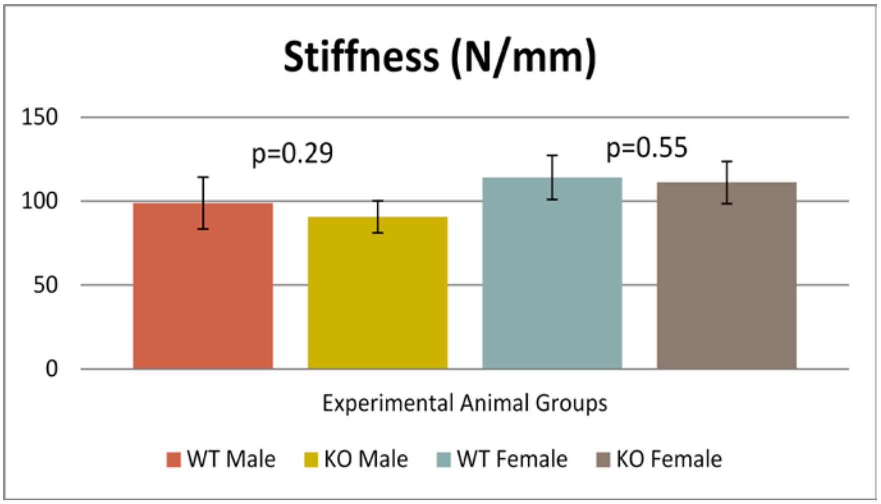

Figure 52: Stiffness of experimental mice femurs. Data was presented by mean ± S.E.M. There were no significant differences between WT and Stat3 deficient (KO) femurs in stiffness in both males (p=0.29) and females (p=0.55).

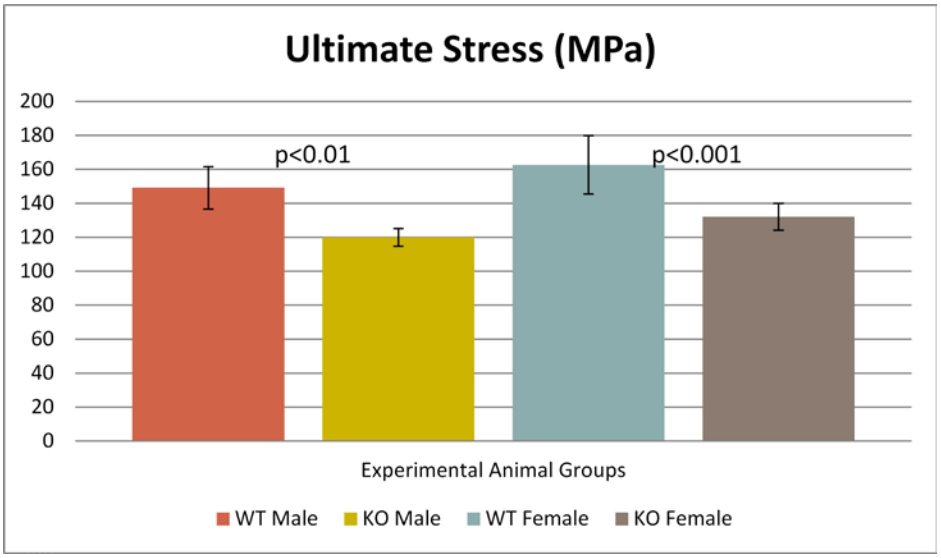

Figure 53: Ultimate stress of experimental mice femurs. Data was presented by mean ± S.E.M. Compared to wild type (WT) control mice, in males, the ultimate stress of the KO mice was 19.6% ($p<0.01$) lower. In females, the ultimate stress of the KO mice was 18.8% ($p<0.001$) lower.

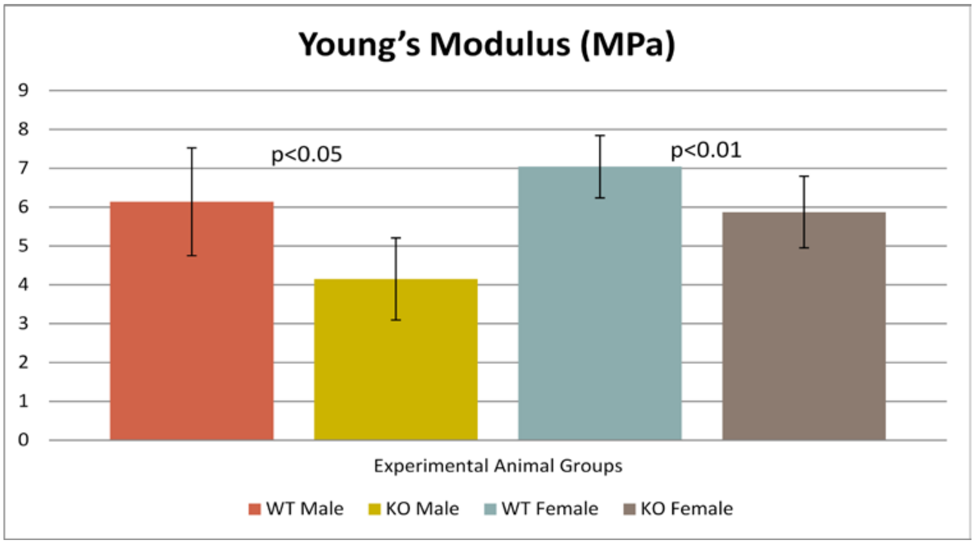

Figure 54: Young's modulus of experimental mice femurs. Data was presented by mean ± S.E.M. Compared to wild type (WT) control mice, in males, the young's modulus of the KO mice was 32.3% ($p<0.05$) smaller. In females, the ultimate stress of the KO mice was 16.6% ($p<0.01$) smaller.

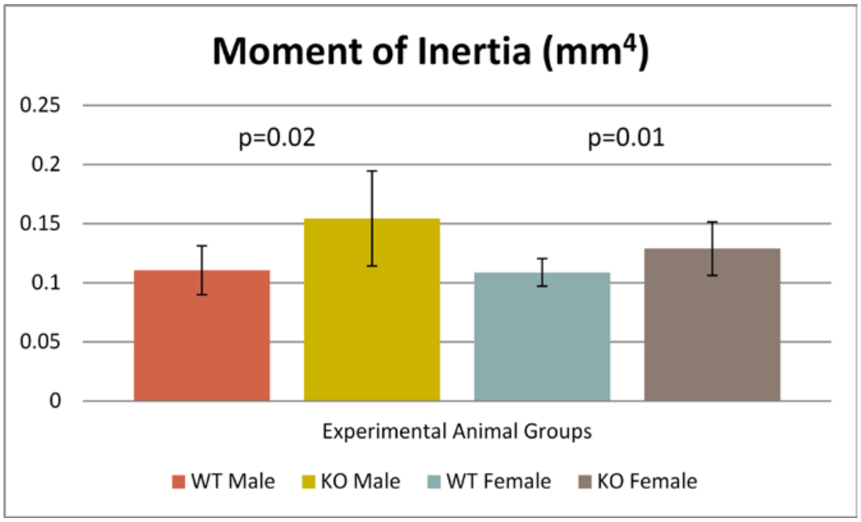

Figure 55: Moment of Inertia (MOI) of the midshaft femurs. Data was presented by mean ± S.E.M. Compared to WT control mice, in males, the MOI of the KO mice was 39.5% (p=0.02) greater. In females, the MOI of the KO mice was 18.5% (p=0.01) greater.

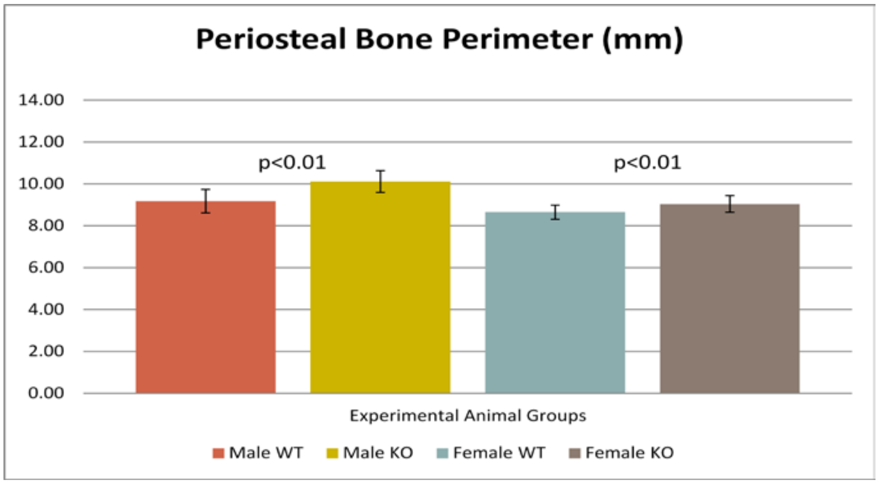

Figure 56: Periosteal bone perimeter of the midshaft femurs. Data was presented by mean ± S.E.M. Compared to their WT littermate controls, the periosteal bone perimeter of midshaft femurs were significantly greater in KO mice (+10.1% in male, p<0.01 and +4.5% in female, p<0.01).

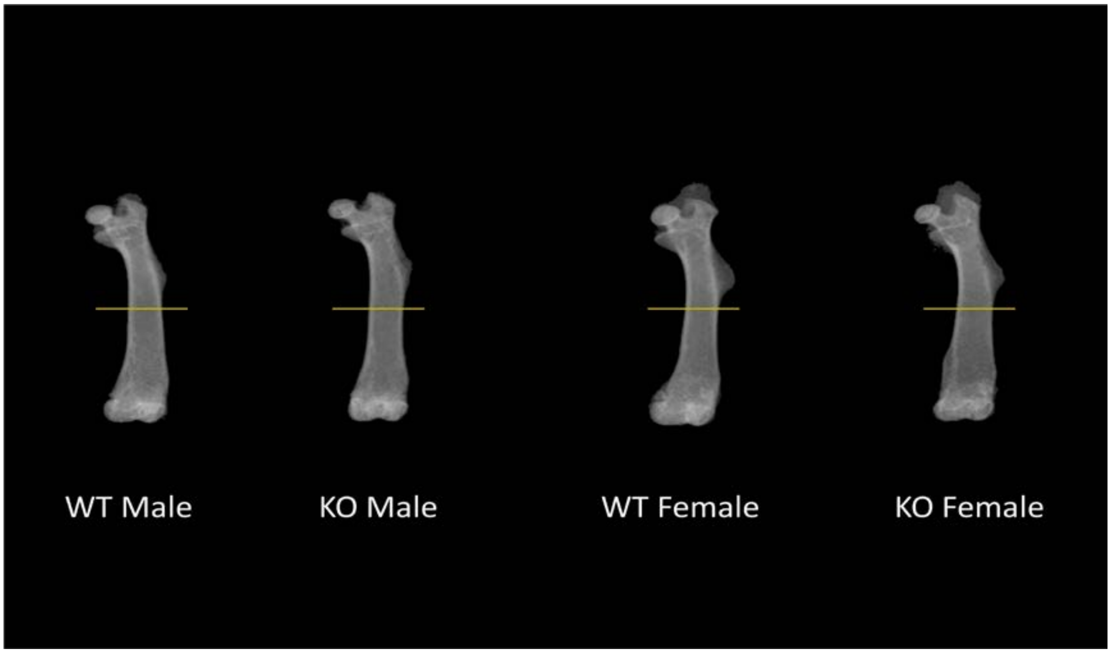

Figure 57: High resolution X-ray images of femurs. The yellow lines indicate the mid-shaft slides which represent the sites of femur mid-shaft transectional μ-CT images analyzed by CTAn software. The total femur lengths of WT and KO mice showed no significant difference. However, while looking closely at the width of the midshaft slides indicated by yellow lines, for both males and females, the diameters of midshaft femurs in KO mice are significantly greater than their WT controls.

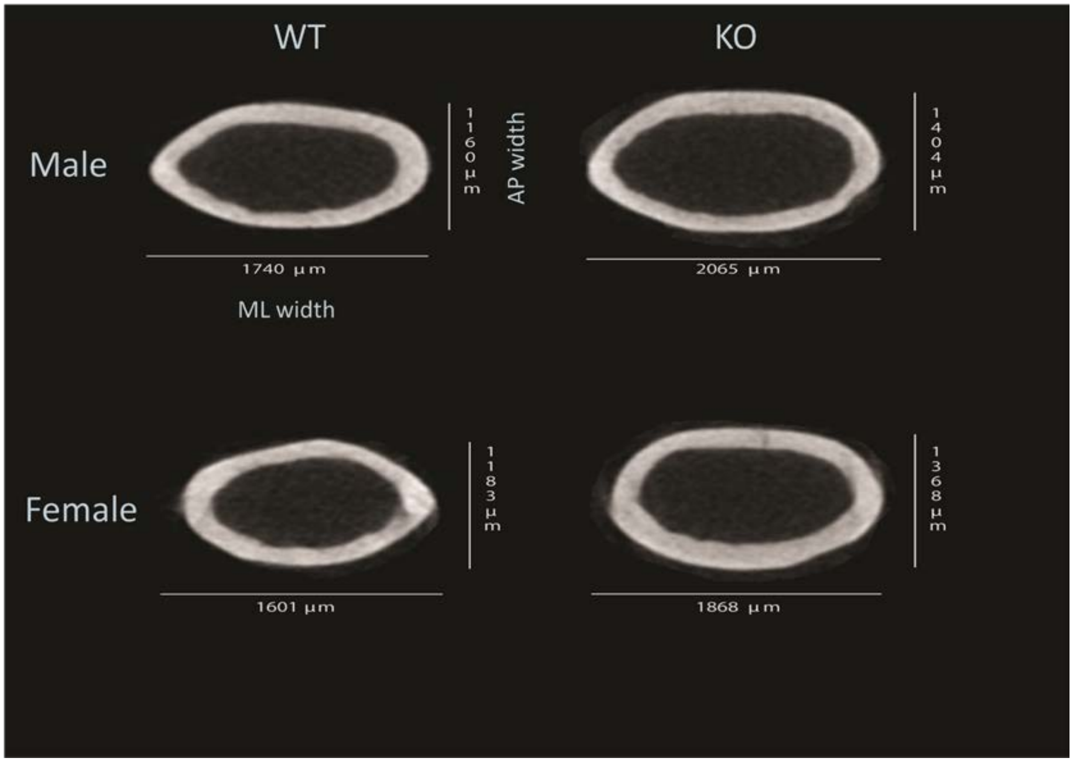

Figure 58: Midshaft femur cross-sectional µ-CT images. Analysis revealed significantly increased total cross-sectional area, marrow area, AP width, ML width, and reduced cortical area to total area percentage in KO mice. However, there were no significant changes in cortical area, average cortical thickness, and AP to ML ratio between KO mice and WT mice.

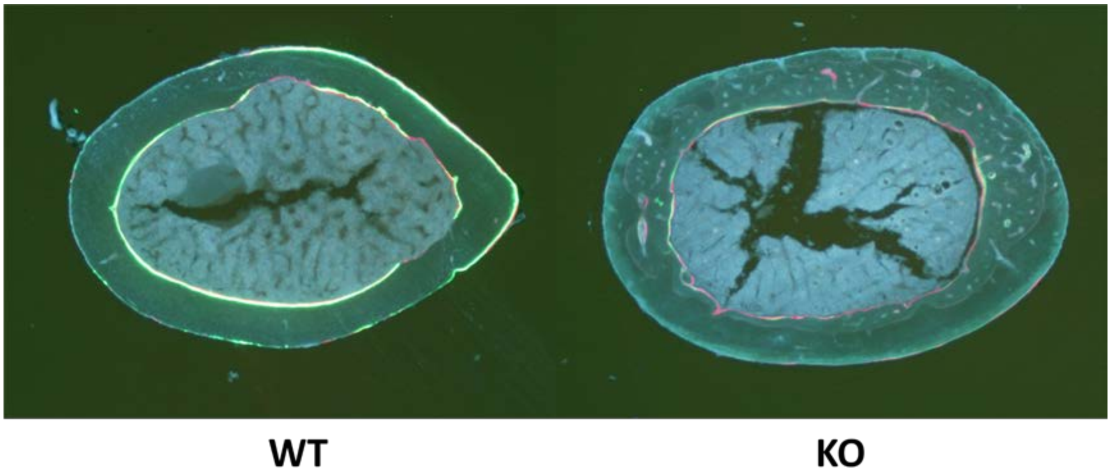

Figure 59: Images of the fluorescent dyes labeled midshaft femurs. Compare midshaft femurs of the 18-week-old Dmp1-Cre;Stat3$^{+/+}$ (WT) mice to the Dmp1-Cre;Stat3$^{flox/flox}$ (KO) mice, KO mice femurs presented noticeably more cortical bone porosity than WT mice femurs.

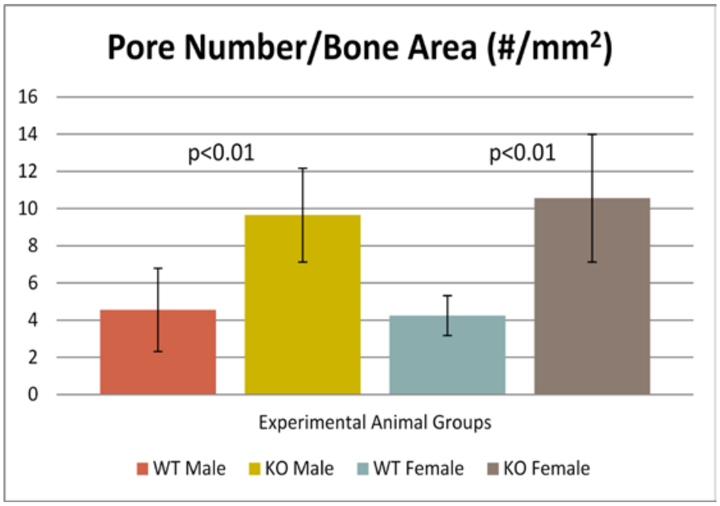

Figure 60: Pore number/bone area of the midshaft femur cortical bone. Data was presented as mean ± S.E.M. Compared to WT control mice (n=6), in males, the cortical bone pore number/bone area of the KO mice (n=6) was 112% ($p<0.01$) greater. In females, the cortical bone pore number/bone area of the KO mice (n=6) was 149% ($p<0.01$) greater.

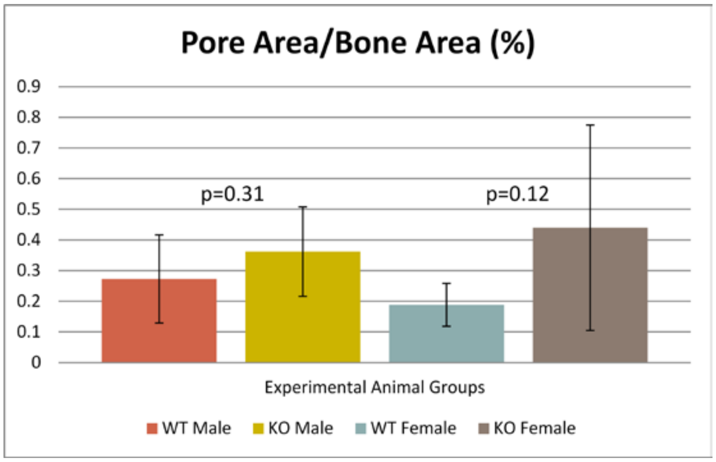

Figure 61: Pore area/bone area of the midshaft femur cortical bone. Data was presented as mean ± S.E.M. There were no significant differences of pore area/bone area between KO mice (n=6) and WT mice (n=6) in both males ($p=0.31$) and females ($p=0.12$).

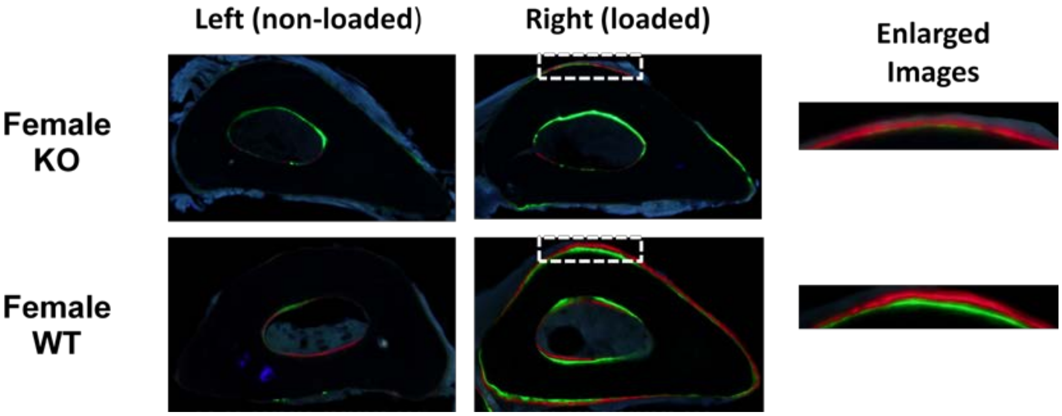

Figure 62: Midshaft ulnar sections from the non-loaded and loaded forearms. In the female WT control (Dmp1-Cre;Stat3$^{+/+}$) mice and KO (Dmp1-Cre;Stat3$^{flox/flox}$) mice, calcein (green) and alizarin (red) were injected after loading to label load-induced new bone formation. Note that the anabolic responses on the medial (square) and lateral surfaces of the loaded control ulna were detected. In KO mice those responses were significantly decreased in the loaded ulna compared with the loaded ulna of WT mice (enlarged images).

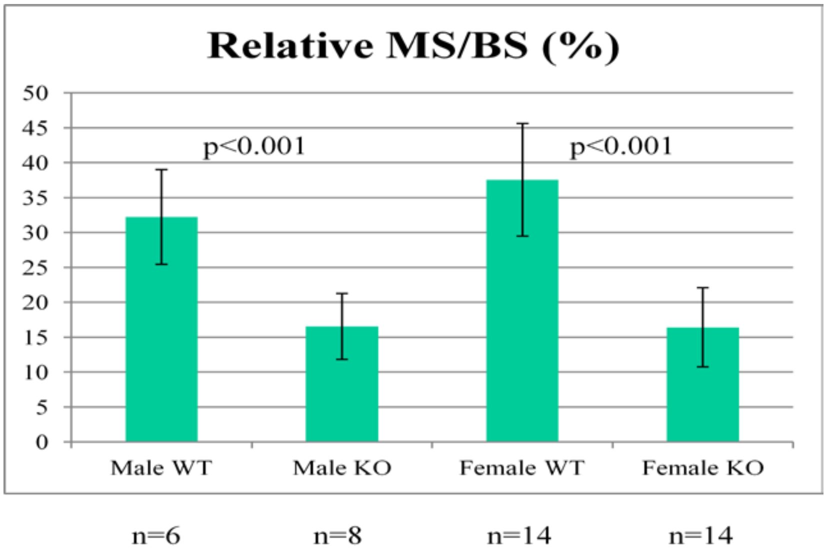

Figure 63: Relative MS/BS of the midshaft ulna cortical bone. Data was presented as mean ± S.E.M. For both males and females, rMS/BS was significantly lower in KO mice (-49% in males, $p<0.001$ and -56% in females, $p<0.001$) than in their WT littermate controls.

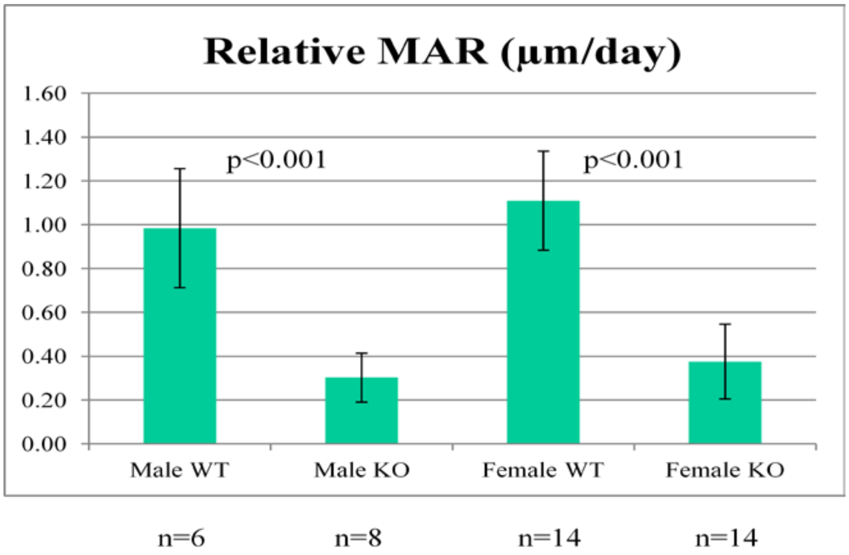

Figure 64: Relative MAR of the midshaft ulna cortical bone. Data was presented as mean ± S.E.M. rMAR was significantly lower in KO mice (-66% in males, $p<0.001$ and -69% in females, $p<0.001$) than in their WT littermate controls.

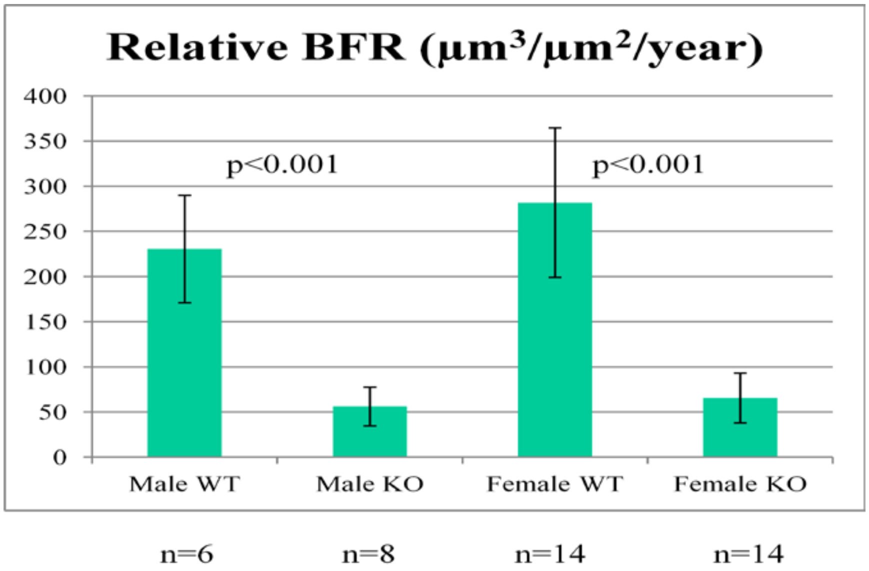

Figure 65: Relative BFR of the midshaft ulna cortical bone. Data was presented as mean ± S.E.M. rBFR/BS was significantly lower in KO mice (-76% in males, $p<0.001$ and -77% in females, $p<0.001$) than in their WT littermate controls.

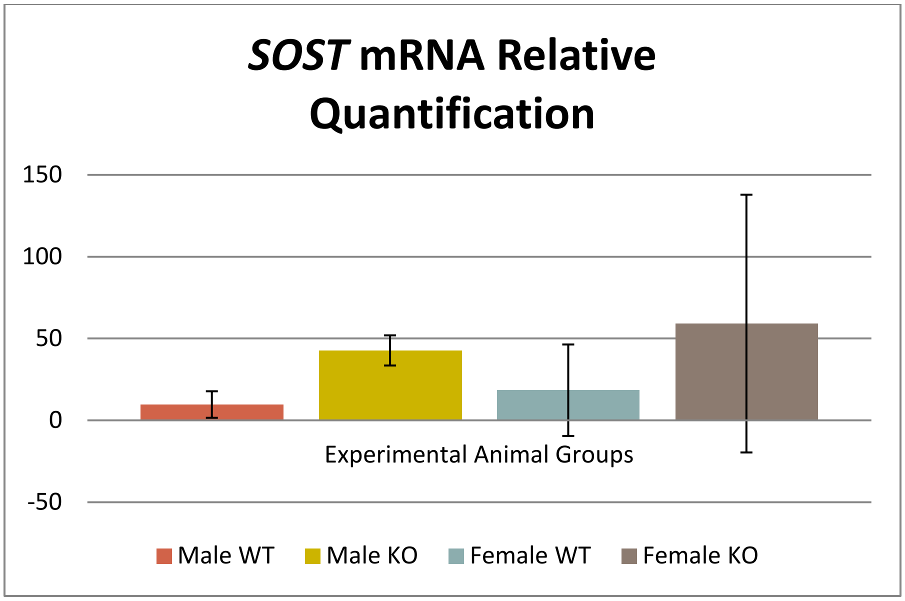

Figure 66: Real-Time PCR analysis of *SOST* gene expression. The total RNA of freshly isolated cortical bone osteocytes was obtained from both WT (Dmp1-Cre;Stat3$^{+/+}$) mice and osteocyte-specific Stat3 KO (Dmp1-Cre;Stat3$^{flox/flox}$) mice in males and females. Higher expression of the *SOST* gene was observed in osteocyte-specific Stat3 KO male mice than in their WT controls. But in the females, due to the high S.E.M, there were no significant difference between WT and KO mice. For each experimental group n=3.

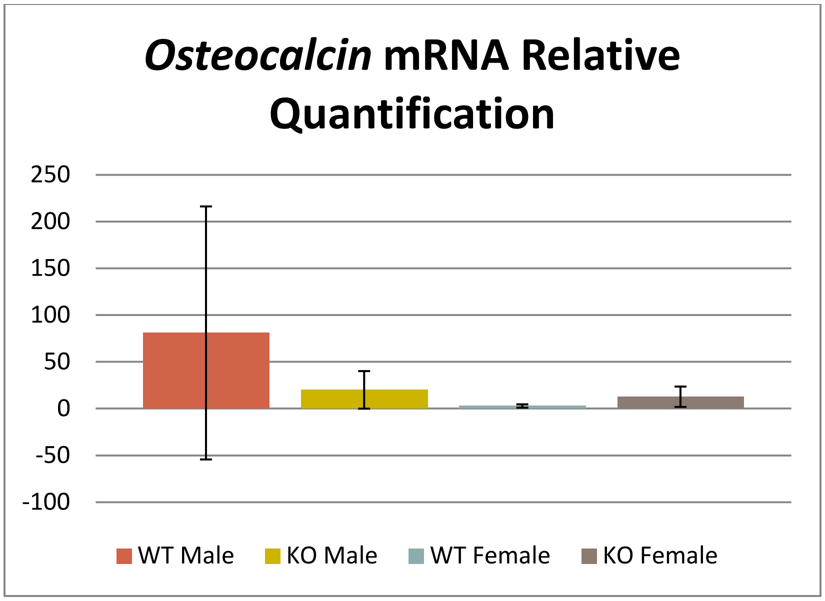

Figure 67: Real-Time PCR analysis of *osteocalcin* gene expression. The total RNA of freshly isolated cortical bone osteocytes was obtained from WT (Dmp1-Cre;Stat3$^{+/+}$) control mice and osteocyte-specific Stat3 KO (Dmp1-Cre;Stat3$^{flox/flox}$) mice in both males and females. There were no differences in the expression of the *osteocalcin* gene between WT and KO mice in males and females. For each experimental group n=3.

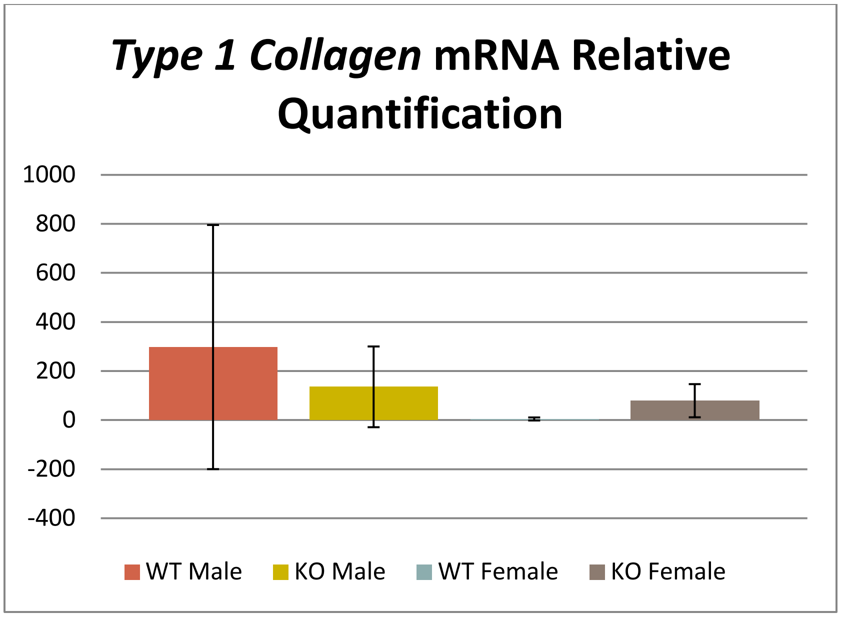

Figure 68: Real-Time PCR analysis of *type 1 collagen* gene expression. The total RNA of freshly isolated cortical bone osteocytes was obtained from WT (Dmp1-Cre;Stat3$^{+/+}$) control mice and osteocyte-specific Stat3 KO (Dmp1-Cre;Stat3$^{flox/flox}$) mice in both males and females. There were no differences in the expression of the *type 1 collagen* gene between WT and osteocyte-specific Stat3 KO in male and female mice. For each experimental group n=3.

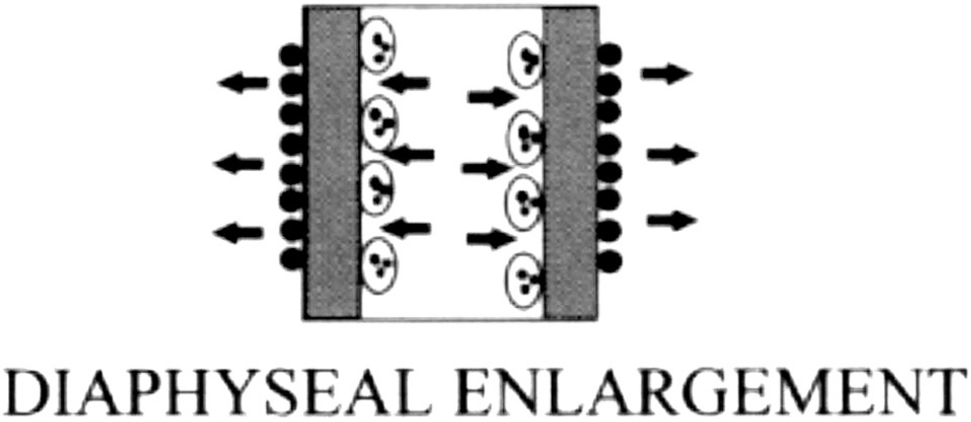

Figure 69: Diaphyseal enlargement of the midshaft femur cortical bone. Midshaft femur bone modeling process demonstrates the osteoclasts in bone marrow absorb the endocortical bone leading to an increased bone marrow cavity, and the osteoblasts make new bone material on the periosteal bone surface to maintain the total cortical bone thickness and volume. The consequence of this type of bone modeling is making the bone grow outward (black arrows).

LIST OF REFERENCES

LIST OF REFERENCES

1. Murray, P. D. F., Huxley, J. S. (1925). Self differentiation in the grafted limb bud of the chick. *Journal of Anatomy*. *59*, 379-384.

2. Currey, J. (2002). Bones: structure and mechanics. Princeton (NJ): *Princeton University Press*, 1-380.

3. Haapasalo, H., Kontulainen, S., Sievanen, H., Kannus, P., Jarvinen, M., Vuori I. (2000). Exercise-induced bone gain is due to enlargement in bone size without a change in volumetric bone density: a peripheral quantitative computed tomography study of the upper arms of male tennis players. *Bone*, *27* (3), 351-357.

4. Hattner, R., Epker, B. N., Frost, H. M. (1965). Suggested sequential mode of control of changes in cell behavior in adult bone remodeling. *Nature*, *206* (983), 489-490.

5. Parfitt, A. M. (1996). Skeletal heterogeneity and the purposes of bone remodeling: Implications for the understanding of osteoporosis [In Marcus, R., Feldman, D., Kelsey, J., editors. *Osteoporosis*. San Diego (CA)]. *Academic Press*, 315-319.

6. Kobayashi, S., Takahashi, H. E., Ito, A., et al (2003). Trabecular minimodeling in human iliac bone. *Bone*, *32* (2), 163-169.

7. Parfitt, A.M. (1995). Problems in the application of in vitro systems to the study of human bone remodeling. *Calcified Tissue International*, *56* (suppl 1), S 5-7.

8. Burr, D. B., Martin, R. B., Schaffler, M. B., Radin, E. L. (1985). Bone remodeling in response to in vivo fatigue microdamage. *Journal of Biomechanics*, *18* (3), 189-200.

9. Mori, S., Burr, D. B. (1993). Increased intracortical remodeling following fatigue damage. *Bone*, *14* (2), 103-109.

10. Hazenberg, J. G., Freeley, M., Foran, E., Lee, T. C., Taylor, D. (2006). Microdamage: a cell transducing mechanism based on ruptured osteocyte processes. *Journal of Biomechanics*, *39* (11), 2096-2103.

11. Noble, B. S., Stevens, H., Loveridge, N., Reeve, J. (1997). Identification of apoptotic changes in osteocytes in normal and pathological human bone. *Bone, 20* (3), 273-282.

12. Verborgt, O., Gibson, G.J., Schaffler, M. B. (2000). Loss of osteocytes integrity in association with microdamage and bone remodeling after fatigue *in vivo*. *Journal of Bone and Mineral Research*, *15* (1), 60-67.

13. Roodman, G. D. (1999). Cell biology of the osteoclast. *Experimental Hematology*, *27* (8), 1229-1241.

14. Silver, I. A., Murrills, R. J., Etherington, D. J. (1988). Microelectrode studies on the acid microenvironment beneath adherent macrophages and osteoclasts. *Experimental Cell Research*, *175* (2), 266-276.

15. Delaisse, J. M., Andersen, T. L., Engsig, M. T., Henriksen, K., Troen, T., Blavier, L. (2003). Matrix metalloproteinases (MMP) and cathepsin K contribute differently to osteoclastic activities. *Microscopy Research and Technique*, *61* (6), 504-513.

16. Reddy, S. V. (2004). Regulatory mechanisms operative in osteoclasts. *Critical Reviews in Eukaryotic Gene Expression*, *14* (4), 255-270.

17. Hadjidakis, D. J., Androulakis, II. (2006). Bone Remodeling. *Annals of the New York Academy of Sciences*, *1092*, 385-396.

18. Mohan, S., Baylink, D. J. (1991). Bone growth factors. *Clinical Orthopaedics Related Research*, *263*, 30-48.

19. Anderson, H. C. (2003). Matrix vesicles and calcification. *Current Rheumatology Reports*, *5* (3), 222-226.

20. Burger, E. H., Klein-Nulend, J. (1999). Mechanotransduction in bone-role of the lacuno-canalicular network. *FASEB Journal*, *suppl 13*, S101-112.

21. Parfitt, A. M. (1994). Osteonal and hemi-osteonal remodeling: the spatial and temporal framework for signal traffic in adult human bone. *Journal of Cellular Biochemistry*, *55* (3), 273-286.

22. Lane, J. M., Russell, L., Khan, S. N. (2000). Osteoporosis. *Clinical Orthopaedics Related Research*, *372*, 139-150.

23. World Health Organization (2003). Prevention and management of osteoporosis: report of a World Health Organization scientific group. Geneva, Switzerland. *World Health Organization*, 1-192.

24. Melton, L. J., III. (1997). Epidemiology of spinal osteoporosis. *Spine*, *22* (suppl 24), S2-11.

25. World Health Organization (1994). Assessment of fracture risk and its application to screening for postmenopausal osteoporosis. Report of a Word Health Organization Study Group. *World Health Organization Technical Report Series*. *843*, 1-129.

26. National Osteoporosis Foundation. Fast Facts. http://www.nof.org/node/40. Published 2012.

27. National Osteoporosis Foundation. America's bone health: the state of osteoporosis and low bone mass in our nation. http://www.osteoporosisnews.org/advocacy/prevalence. Published 2002.

28. U.S. Department of Health and Human Services. Bone health and osteoporosis: a report of surgeon general. Rockville, MD: U.S. Department of Health and Human Services, Office of the Surgeon General. Published 2004.

29. Burge, R., Dawson-Hughes, B., Solomon, D. H., Wong, J. B., King, A., Tosteson, A. (2007). Incidence and economic burden of osteoporosis-related fractures in the United States, 2005-2025. *Journal of Bone and Mineral Research*, *22* (3), 465-475.

30. Roche, J. J., Wenn, R. T., Sahota, O., Moran, C. G. (2005). Effect of comorbidities and postoperative complications on mortality after hip fracture in elderly people: prospective observational cohort study. *British Medical Journal*, *331* (7529), 1374.

31. Minegishi, Y., Saito, M., Tsuchiya, S., et al. (2007). Dominant-negative mutations in the DNA-binding domain of STAT3 cause hyper-IgE syndrome. *Nature*, *448*, 1058-1062.

32. Chamlin, S. L., McCalmont, T. H., Cunningham, B. B., et al. (2002). Cutaneous manifestations of hyper-IgE syndrome in infants and children. *Journal of Pediatrics*, *41*, 572-575.

33. Freeman, A. F., Collura-Burke, C. J., Patronas, N. J., et al. (2007). Brain abnormalities in patients with hyperimmunoglobulin E syndrome. *Pediatrics*, *119*, 1121-1125.

34. Freeman, A. F., Holland, S. M. (2008). The Hyper-IgE Syndromes. *Immunology and Allergy Clinics of North America*, *28*, 277-291.

35. Grimbacher, B., Holland, S. M., Gallin, J. I., et al. (1999). Hyper-IgE syndrome with recurrent infections: an autosomal dominant multisystem disorder. *New England Journal of Medicine, 340*, 692-702.

36. Cohen-Solal, M., Prieur, A. M., Prin, L., et al. (1995). Cytokine-mediated bone resorption in patients with the hyperimmunoglobulin E syndrome. *Clinical Immunology Immunopathology, 76*, 75-81.

37. Leung, D. Y., Key, L., Steinberg, J. J., et al. (1988). Increased in vitro bone resorption by monocytes in the hyper-immunoglobulin E syndrome. *Journal of Immunology, 140*, 84-88.

38. Niwa H., Burdon, T., Chambers, I., Smith, A. (1998). Self-renewal of pluripotent embryonic stem cells is mediated via activation of STAT3, *Genes & Development*, *12*, 2048-2060.

39. Darnell, J. J., Kerr, I., Stark, G. (1994). Jak–STAT pathways and transcriptional activation in response to IFNs and other extracellular signaling proteins. *Science*, *264*, 1415-1421.

40. Buettner, R., Mora, L., Jove, R. (2002). Activated STAT signaling in human tumors provides novel molecular targets for therapeutic intervention, *Clinical Cancer Research*, *8*, 945-954.

41. Schaefer, T., Sanders, L., Nathans, D. (1995). Cooperative transcriptional activity of Jun and Stat3 beta, a short form of Stat3, *Proceedings of the National Academy of Sciences*, *92*, 9097-9101.

42. Hirano, T., Ishihara, K., Hibi, M. (2000). Roles of STAT3 in mediating the cell growth, differentiation and survival signals relayed through the IL-6 family of cytokine receptors. *Oncogene*, *19*, 2548-2556.

43. Shizuo A. (2000). Roles of STAT3 defined by tissue-specific gene targeting. *Oncogene*, *19*, 2607-2611.

44. Levy, D., Lee, C. (2002). What does STAT3 do?. *The Journal of Clinical Investigation*, *109*, 1143-1147.

45. Darnell, J. (1997). STATs and gene regulation. *Science*, *277*, 1630-1635.

46. Becker, S., Groner, B., Muller, C. W. (1998). Three-dimensional structure of the Stat3β homodimer bound to DNA. *Nature*, *394*, 145-151.

47. O'Shea, J. J., Gadina, M., Schreiber, R. D. (2002). Cytokine signaling in 2002: new surprises in the Jak/Stat pathway. *Cell*, *109*, S121-131.

48. Trenerry M. K., et al. (2007). STAT3 signaling is activated in human skeletal muscle following acute resistance exercise. *Journal of Applied Physiology, 102*, 1483-1489.

49. Lodish H., et al. (2007). Molecular Cell Biology Sixth Edition. New York, *New York: W. H. Freeman*.

50. Aaronson, D. S., Horvath, C. M. (2002). A road map for those who don't know JAK-STAT. *Science, 296*, 1653-1655.

51. U.S. Nation Library of Medicine, Genetics Home Reference. (2008) STAT3. Retrieved from http://ghr.nlm.nih.gov/gene/STAT3#location

52. Stahl, N., Farruggella, T. J., Boulton, T. G., Zhong, Z., et al. (1995). Choice of STATs and other substrates specified by modular tyrosine-based motifs in cytokine receptors. *Science, 267*, 1349-1352.

53. Nishimura, R., Moriyama, K., Yasukawa, K., Mundy, G. R., Yoneda, T. (1998). Combination of interleukin-6 and soluble interleukin-6 receptors induces differentiation and activation of JAK-STAT and MAP kinase pathways in MG-63 human oteoblastic cells. *Journal of Bone and Mineral research*, *13*, 777-785.

54. Pfeffer, L. M., et al. (1997). Stat3 as an adaptor to couple phosphatidylinositol 3-kinase to the IFNAR1 chain of the type I interferon receptor. *Science*, *276*, 1418-1420.

55. Gao, S., Bromberg, J. (2006). Touched and moved by STAT3. *Science*, *343*, 30.

56. Wegrzyn J, Potla R, et al. Function of mitochondrial Stat3 in cellular respiration. Science. 323 (2009) 793-797.

57. Welte, T., Zhang, S., Wang, T. (2003). STAT3 deletion during hematopoiesis causes Crohn's disease-like pathogenesis and lethality: A critical role of STAT3 in innate immunity. *Proceedings of the National Academy of Sciences*, *100*, 1879-1884.

58. Matsuda, T., Nakamura, T., Nakao, K., Arai, T., Katsuki, M., Heike, T., Yokota, T. (1999). STAT3 activation is sufficient to maintain an undifferentiated state of mouse embryonic stem cells. *EMBO Journal*, *18*, 4261-4269.

59. Raz, R., Lee, C., Cannizzaro, L. A., d'Eustachio, P., Levy, D. E. (1999). Essential role of STAT3 for embryonic stem cell pluripotency. *Proceedings of the National Academy of Sciences*, *96*, 2846-2851.

60. Takeda, K., Noguchi, K., Shi, W., Tanaka, T., Matsumoto, M., Yoshida, N., Kishimoto, T., Akira, S. (1997). Targeted disruption of the mouse Stat3 gene leads to early embryonic lethality. *Proceedings of the National Academy of Sciences*, *94*, 3801-3814.

61. Sano, S., et al. (1999). Keratinocyte-specific ablation of Stat3 exhibits impaired skin remodeling, but does not affect skin morphogenesis. *EMBO Journal*, *18***,** 4657-4668.

62. Alonzi, T., et al. (2001). Role of STAT3 and PI 3-kinase/Akt in mediating the survival actions of cytokines on sensory neurons. *Molecular and Cellular Neuroscience, 18,* 270-282.

63. Bromberg, J., Wrzeszcznska, M., Devgan, G., Zhao, Y., Pestell, R., Albanese, C., Darnell, J. J. (1999). Stat3 as an oncogene. *Cell*, *98,* 295-303.

64. Jing, N., Tweardy, D. J. (2005). Targeting Stat3 in cancer therapy. *Anti-Cancer Drugs*, *16*, 601-607.

65. Heinrich, P. C., Behrmann, I., Muller-Newen, G., Schaper, F., Graeve, L. (1998). Interleukin-6-type cytokine signaling through the gp130/Jak/STAT pathway. *Biochemical Journal*, *334*, 297-314.

66. Senaldi, G., Varnum, B. C., Sarmiento, U., Starnes, C., Lile, J., Scully, S., Guo, J., Elliott, G., McNinch, J., Shaklee, C. L., Freeman, D., Manu, F., Simonet, W. S., Boone, T., Chang, M. S. (1999). Novel neurotrophin-1/B cell-stimulating factor-3: a cytokine of the IL-6 family. *Proceedings of the National Academy of Sciences*, *96*, 11458-11463.

67. Levy, D. E., Loomis, C. A. (2007). STAT3 signaling and the hyper IgE syndrome. *New England Journal of Medicine*, *357*, 1655-1658.

68. Shuai, K., Liu, B. (2003). Regulation of JAK-STAT signaling in the immune system. *Nature Reviews Immunology*, *3,* 900-911.

69. Levy, D. E., Darnell, J. E. Jr. (2002). Stats: transcriptional control and biological impact. *Nature Reviews Molecular Cell Biology*, *3,* 651-662.

70. Neves, S. R., Ram, P. T., Iyengar, R. (2002). G Protein Pathways. *Science*, *296,* 1636-1639.

71. Yu, H., Kortylewski, M., Pardoll. D. (2007). Crosstalk between cancer and immune cells: role of STAT3 in the tumour microenvironment. *Nature Review Immunology, 7,* 41-51.

72. Warden, S. J., Bogenschutz, E. D., Smith, H. D., Gutierrez, A. R. (2009). Throwing induces substantial torsional adaptation within the midshaft humerus of male baseball players. *Bone*, *45*, 931-941.

73. Rittweger, J., Simunic, B., Bilancio, G., De Santo, N. G., Cirillo, M., Biolo Gianni, Pisot, R., Eiken, O., Mekjavic, I. B., Narici, M. (2009). Bone loss in the lower leg during 35 days of bed rest is predominantly from the cortical compartment. *Bone*, *44*, 612-618.

74. LeBlanc, A., Schneider, V., Shackelford, L., et al. (2000). Bone mineral and lean tissue loss after long duration space flight. *Journal of Musculoskeletal and Neuronal Interactions*, *1*, 157-160.

75. McCarthy, I., Goodship, A., Herzog, R., Oganov, V., Stussi, E., Vahlensieck, M. (2000). Investigation of bone changes in microgravity during long and short duration space flight: comparison of techniques. *European Journal of Clinical Investigation*, *30*, 1044-1054.

76. Ingber, D. E. (2003). Mechanobiology and diseases of mechanotransduction. *Annals of Medicine*, *35*, 564-577.

77. Liedert, A., Kaspar, D., Blakytny, R., Claes, L., Ignatius, A. (2006). Signal transduction pathways involved in mechanotransduction in bone cells. *Biochemical and Biophysical Research Communications*, *349*, 1-5.

78. Roosa, S. M., Liu, Y., Turner, C. H. (2011). Gene expression patterns in bone following mechanical loading. *Journal of Bone and Mineral Research*, *26*, 100-112.

79. Li, J., Liu, D., Ke, H. Z., Duncan, R. L., Turner, C. H. (2005). The P2X7 nucleotide receptor mediates skeletal Mechanotransduction. *Journal of Biological Chemistry*, *280* (52), 42952-42959.

80. Cross, J. C., Werb, Z., Fisher, S. J. (1994). Implantation and the placenta: Key pieces of the development puzzle. *Science*, *266*, 1508-1518.

81. Sauer, B. (1987). Function expression of the cre-lox site-specific recombination system in the yeast *Saccharomyces cerevisiae*. *Molecular and Cellular Biology*, *7* (6), 2087-2096.

82. Sauer, B., Henderson, N. (1988). Site-specific DNA recombination in mammalian cells by the Cre recombinase of bacteriophage P1. *Proceedings of the National Academy of Sciences*, *85* (14), 5166-5170.

83. Dacquin, R., Starbuck, M., Schinke, T., Karsenty, G. (2002). Mouseα1(I)-Collagen promoter is the best known promoter to drive efficient Cre recombinase expression in osteoblast. *Developmental Dynamics*, 224, 245-251.

84. Liu, F., Woitge, H. W., Braut, A., Kronenberg, M. S., Lichtler, A. C., Mina, M., Kream, B. E. (2004). Expression and activity of osteoblast-targeted Cre recombinase transgenes in murine skeletal tissues. *International Journal of Developmental Biology*, *48*, 645-653.

85. Kalajzic, Z., Liu, P., Kalajzic, I., Du, Z., Braut, A., Mina, M., Canalis, E., Rowe, D. W. (2002). Directing the expression of a green fluorescent protein transgene in differentiated osteoblasts: Comparison between rat type I collagen and rat osteocalcin promoters. *Bone*, *31*, 654-660.

86. Toyosawa, S. et al. (2001). Dentin matrix protein 1 is predominantly expressed in chicken and rat osteocytes but not in osteoblasts. *Journal of Bone and Mineral Research*, *16*, 2017-2026.

87. Bivi, N., Condon, K. W., Allen, M. R., Farlow, N., Passeri, G., Brun, L. R., Rhee, Y., Bellido, T., Plotkin, L. (2012). Cell autonomous requirement of connexin 43 for osteocyte survival: consequences for endocortical resorption and periosteal bone formation. *Journal of Bone and Mineral Research*, *27* (2), 374-89.

88. Rubin, C. (1984). Skeletal strain and the functional significance of bone architecture. *Calcified Tissue International*, *36*, S11-18.

89. Turner, C. H., Forwood, M. R., Otter, M. W. (1994). Mechanotransduction in bone: do bone cells act as sensors of fluid flow?. *Federation of American Societies for Experimental Biology Journal*, *8*, 875-878.

90. Robling, A. G., Hinant, F. M., Burr, D. B., Turner, C. H. (2002). Shorter, more frequent mechanical loading sessions enhance bone mass. *Medicine and Science in Sports and Exercise*, *34*, 196-202.

91. Robling A. G., Turner, C. H. (2002). Mechanotransduction in bone: genetic effects on mechanosensitivity in mice. *Bone*, *31*, 562-569.

92. Schenk, R. K., Olah, A. J., Herrmann, W. (1984). Preparation of calcified tissue for light microscopy. In Methods of Calcified Tissue Preparation, GR Dickson, ed. New York, *Elsevier*, 1-56.

93. Erlebacher, A., Derynck, R. (1996). Increased expression of TGB-β2 in osteoblasts results in an osteoporosis-like phenotype. *Journal of Cell Biology*, *132*, 195-210.

94. Kuhn, J. L., Goldstein, S. A., Feldkamp, L. A., Goulet, R. W., Jesion, G. (1990). Evaluation of a microcomputed tomography system to study trabecular bone structure. *Journal of Orthopaedic Research*, *8*, 833-842.

95. Wallace, J. M., Golcuk, K., Morris, M. D., Kohn, D. H. (2009). Inbred strain-specific response to biglycan deficiency in the cortical bone of C57BL6/129 and C3H/He mice. *Journal of Bone and Mineral Research*, *24*, 1002-1012.

96. Wallace, J. M., Golcuk, K., Morris, M. D., Kohn, D. H. (2010). Inbred strain-specific effects of exercise in wild type and biglycan deficient mice. *Annals of Biomedical Engineering*, *38*, 1607-1617.

97. Wallace, J. M., Rajachar, R. M., Allen, M. R., Bloomfield, S. A., Robey, P. G., Young, M. F., Kohn, D. H. (2007). Exercise-induced changes in the cortical bone of growing mice are bone- and gender-specific. *Bone*, *40*, 1120-1127.

98. Wallace, J. M., Rajachar, R. M., Chen, X. D., Shi, S., Allen, M. R., Bloomfield, S.A., Les, C. M., Robey, P. G., Young, M. F., Kohn, D. H. (2006). The mechanical phenotype of biglycan-deficient mice is bone- and gender-specific. *Bone*, *39*, 106-116.

99. Sundaresan, M., Yu, Z. X., Ferrans, V. J., Sulciner, D. J., Gutkind, J. S., Irani, K., et al. (1996). Regulation of reactive-oxygen-species generation in fibroblasts by Rac1. *Biochemical Journal*, *318* (Pt 2), 379-382.

100. Burdelya, L., Catlett-Falcone, R., Levitzki, A., Cheng, F., Mora, L. B., Sotomayor, E., et al. (2002). Combination therapy with AG-490 and interleukin 12 achieves greater antitumor effects than either agent alone. *Molecular Cancer Therapeutics*, *1*, 893-899.

101. Martini, F., Timmons, M., Tallitsch, R. (2008). *Human Anatomy*, 6th edition, PEARSON-Benjamin Cummings, *Chapter 5*, 111-260.

102. Silverthorn, D. (2003). *Human Physiology an Integrated Approach,* 6th edition, PEARSON, 790-796.

103. Bonewald L. F. (2011). The amazing osteocyte. *Journal of Bone and Mineral Research*, *26* (2), 229-238.

104. Norvell, S. M., Alvarez, M., Bidwell, J. P. & Pavalko, F. M. (2004). Fluid Shear Stress induces β-catenin signaling in osteoblasts. *Calcified Tissue International*, *75*, 396-404.

105. Owan, I., Burr, D. B., Turner, C. H., Qiu, J., Tu, Y., Onyia, J. E., Duncan, R. L. (1997). Mechanotransduction in bone: Osteoblasts are more responsive to fluid forces than mechanical strain. *American Journal of Physiology, Cell Physiology, 273*, 810-815.

106. Tanaka, S. M., Sun, H. B., Roeder, R. K., Burr, D. B., Turner, C. H., Yokota, H. (2005). Osteoblast responses one hour after load-induced fluid flow in a three-dimensional porous matrix. *Calcified Tissue International*, *76,* 261-271.

107. You, J., Yellowley, C. E., Donahue, H. J., Zhang, Y., Chen, Q., Jacobs, C. R. (2000). Substrate deformation levels associated with routine physical activity are less stimulatory to bone cells relative to loading-induced oscillatory fluid flow. *Journal of Biomechanical Engineering*, *122*, 387-393.

108. Hillam, R. A., Skerry, T. M. (1995). Inhibition of bone resorption and stimulation of formulation by mechanical loading of the modeling rat ulna in vivo. *Journal of Bone and Mineral Research*, *10*, 683-689.

109. Bikle, D. D., Halloran, B. P. (1999). The response of bone to unloading. *Journal of Bone and Mineral Metabolism*, *17*, 233-244.

110. Quarles, L. D., Yohay, D. A., Lever, L. W., Caton, R. and Wenstrup, R. J. (1992). Distinct proliferative and differentiated stages of murine MC3T3-E1 cells in culture: An in vitro model of osteoblast development. *Journal of Bone and Mineral Research*, *7*, 683-692.

111. Bai, X. C., Lu, D., Bai, J., Zheng, H., Ke, Z. Y., Li, X. M., et al. (2004). Oxidative stress inhibits osteoblastic differentiation of bone cells by ERK and NF-kappaB. *Biochemical and Biophysical Research Communications*, *314*, 197-207.

112. Basu, S., Michaelsson, K., Olofsson, H., Johansson, S., Melhus, H. (2001). Association between oxidative stress and bone mineral density. *Biochemical and Biophysical Research Communications*, *288*, 275-279.

113. Kasper, G., Mao, L., Geissler, S., Draycheva, A., Trippens, J., Kuhnisch, J., et al. (2009). Insights into mesenchymal stem cell aging: involvement of antioxidant defense and actin cytoskeleton. *Stem Cells*, *27*, 1288-1297.

114. Varanasi, S. S., Francis, R. M., Berger, C. E., Papiha, S. S., Datta, H. K. (1999). Mitochondrial DNA deletion associated oxidative stress and severe male osteoporosis. *Osteoporosis International*, *10*, 143-149.

115. Cadenas, E., Davies, K. J. (2000). Mitochondrial free radical generation, oxidative stress, and aging. *Free Radical Biology and Medicine*, *29*, 222-230.

116. Papiha, S. S., Rathod, H., Briceno, I., Pooley, J., Datta, H. K. (1998). Age related somatic mitochondrial DNA deletions in bone. *Journal of Clinical Pathology*, *51*, 117-120.

117. Valko, M., Leibfritz, D., Moncol, J., Cronin, M. T., Mazur, M., Telser, J. (2007). Free radicals and antioxidants in normal physiological functions and human disease. *International Journal of Biochemistry and Cell Biology*, *39*, 44-84.

118. Almeida, M., Ambrogini, E., Han, L., Manolagas, S. C., Jilka, R. L. (2009). Increased lipid oxidation causes oxidative stress, increased PPAR{gamma} expression and diminished proosteogenic Wnt signaling in the skeleton. *Journal of Biological Chemistry*, *284*, 27438-27448.

119. Almeida, M., Han, L., Martin-Millan, M., O'Brien, C. A., Manolagas, S. C. (2007). Oxidative stress antagonizes Wnt signaling in osteoblast precursors by diverting beta-catenin from T cell factor- to forkhead box O-mediated transcription. *Journal of Biological Chemistry*, *282*, 27298-27305.

120. Hajnoczky, G., Hoek, J. B. (2007). Cell signaling. Mitochondrial longevity pathways. *Science*, *315*, 607–609.

121. Myers, Jr. M. G. (2009). Cell biology. Moonlighting in mitochondria. *Science*, *323*, 723-724.

122. Reich, N. C. (2009). STAT3 revs up the powerhouse. *Science Signal*, *2*, 61.

123. Wegrzyn, J., Potla, R., Chwae, Y. J., Sepuri, N. B., Zhang, Q., Koeck, T., et al. (2009). Function of mitochondrial Stat3 in cellular respiration. *Science*, *323*, 793-797.

124. Lufei, C., Ma, J., Huang, G., Zhang, T., Novotny-Diermayr, V., Ong, C. T., et al. (2003). GRIM-19, a death-regulatory gene product, suppresses Stat3 activity via functional interaction. *The EMBO Journal*, *22*, 1325-1335.

125. Winkler, D., Sutherland, M. K., Geoghegan, J. C., Yu, C., Hayes, T., Skonier, J., Shpektor, D., Jonas, M., Kovacevich, B. R., Staehling-Hampton, K., Appleby, M., Brunkow, M. E., Latham, J. A. (2003). Osteocyte control of bone formation via sclerostin, a novel BMP antagonist. *The EMBO Journal*, *22* (23), 6267-6276.

126. Van Bezooijen, R., Roelen, B. A. J., Visser, A., Wee-Pals, L., Wilt, E., Karperien, M., Hamersma, H., Papapoulos, E., Dijke, P., Lowik, C. (2004). Sclerostin is an osteocyte-expressed negative regulator of bone formation, but not a classical BMP antagonist. *The Journal Experimental Medicine*, *199*, 805-814.

127. Poole, K., Bezooijen, L., Loveridge, N., Hamersma, H., Papapoulos, S., Lowik, C., Reeve, J. (2005). Sclerostin is a delayed secreted product of osteocytes that inhibits bone formation. *The FASEB Journal*, *19*, 1842-1844.

128. Lee, N. K., Sowa, H., Hinoi, E., Ferron, M., Ahn, J. D., Confavreux, C., Dacquin, R., Mee, P. J., McKee, M. D., Jung, D. Y., Zhang, Z., Kim, J. K., Mauvais-Jarvis, F., Ducy, P., Karsenty, G. (2007). Endocrine regulation of energy metabolism by the skeleton. *Cell*, *130* (3), 456-469.

129. Sims, N. A., Walsh, N. C. (2010). GP130 cytokines and bone remodeling in health and disease. *Biochemistry and Molecular Biology Reports*, *43* (8), 513-523.

130. Heymann, D., Rousselle, A. V. (2000). gp130 cytokine family and bone cells. *Cytokine*, *12* (10), 1455-1468.

131. Karsenty, G. (2001). Genetic control of skeletal development. *Novartis Found Symposium*, *232*, 16-17.

132. Boyle, W. J., Simonet, W. S., Lacey, D. L. (2003). Osteoclast differentiation and activation. *Nature*, *423*, 337-342.

133. Harada, S., Rodan, G. A. (2003). Control of osteoblast function and regulation of bone mass. *Nature*, *423*, 349-355.

134. Frost, H. M. (1973). Bone remodeling and its relation to metabolic bone diseases. Charles C. Thomas, Springfield Ed., Illinois, USA.

135. Teitelbaum, S. L., Tondravi, M. M., Ross, F. P. (1997). Osteoclasts, macrophages, and the molecular mechanisms of bone resorption. *Journal of Leukocyte Biology*, *61*, 381-388.

136. Athanasou, N. A. (1996). Cellular biology of bone-resorbing cells. *Journal of Bone and Joint Surgery*, *78A*, 1096-1112.

137. Fawcett, D. W., Raviola, E. (1994). *Bone. In: Fawcett DW, Raviola E. (eds) A textbook of histology*, 12th edition. Chapman and Hall, New York, USA, 194-233.

138. Manolagas, S. C. (1995). Role of cytokines in bone resorption. *Bone*, *17*, S63-67.

139. Hibi, M., Murakami, M., Saito, M., Hirano, T., Taga, T., Kishimoto, T. (1990). Molecular cloning and expression of an IL-6 signal transducer, gp 130. *Cell*, *63*, 1149-1157.

140. Gearing, D. P. (1993). The leukemia inhibitory factor and its receptor. *Advances in Immunology*, *53*, 31-58.

141. Pennica, D., Wood, W. I., Chien, K. R. (1996). Cardiotrophin-1: a multifunctional cytokine that signals via LIF receptor-gp130 dependent pathways. *Cytokine and Growth Factor Reviews*, *7*, 81-91.

142. Sariola, H., Sainio, K., Arumae, U., Sarma, M. (1994). Neurotrophin and ciliary neurotrophic factor: their biology. *Annals Medicine*, *26*, 355-363.

143. Piquet-Pellorce, C., Grey, L., Mereau, A., Heath, J. K. (1994). Are LIF and related cytokines functionally equivalent?. *Experimental Cell Research*, *213*, 340-347.

144. Richards, C. D. (1998). Interleukin-6. In: Mire-Sluis, A. R., Thorpe, R. (eds) Cytokines. *Academic Press*, New York, NY, USA, 88-108.

145. Leng, S. X., Elias, J. A. (1997). Interleukin-11. *International Journal of Biochemistry and Cell Biology*, *28*, 1059-1062.

146. Yang, Y. C. (1993). Interleukin 11: an overview. *Stem Cells*, *11*, 474-486.

147. Neben, S., Turner, K. (1993). The biology of interleukin 11. *Stem Cells*, *11* (suppl 2), 156-162.

148. Yang, Y. C., Yin, T. (1992). Interleukin-11 and its receptor. *Biofactors*, *4*, 15-21.

149. Bellido, T., Borba, V. Z., Roberson, P., Manolagas, S. C. (1997). Activation of the Janus kinase/STAT (signal transducer and activator of transcription) signal transduction pathway by interleukin-6-type cytokines promotes osteoblast differentiation. *Endocrinology*, *138*, 3666-3676.

150. Walker, E. C., McGregor, N. E., Poulton, I. J., Pompolo, S., Allan, E. H., Quinn, J. M., Gillespie, M. T., Martin, T. J., Sims, N. A. (2008). Cardiotrophin-1 is an osteoclast-derived stimulus of bone formation required for normal bone remodeling. *Journal of Bone and Mineral Research*, *23*, 2025-2032.

151. Walker, E. C., McGregor, N. E., Poulton, I. J., Solano, M., Pompolo, S., Fernandes, T. J., Constable, M. J., Nicholson, G. C., Zhang, J. G., Nicola, N. A., Gillespie, M. T., Martin, T. J., Sims, N. A. (2010). Oncostatin M promotes bone formation independently of resorption when signaling through leukemia inhibitory factor receptor in mice. *Journal of Clinical Investigation*, *120*, 582-592.

152. Sims, N. A., Jenkins, B. J., Nakamura, A., Quinn, J. M., Li, R., Gillespie, M. T., Ernst, M., Robb, L., Martin, T. J. (2005). Interleukin-11 receptor signaling is required for normal bone remodeling. *Journal of Bone and Mineral Research*, *20*, 1093-1102.

153. Metcalf, D., Gearing, D. P. (1989). A myelosclerotic syndrome in mice engrafted with cells producing high levels of leukemia inhibitory factor (LIF). *Leukemia*, 3, 847-852.

154. Metcalf, D., Gearing, D. P. (1989). Fatal syndrome in mice engrafted with cells producing high levels of leukemia inhibitory factor. *Proceedings of the National Academy of Sciences, 86*, 5948-5952.

155. Van Bezooijen, R. L., ten Dijke, P., Papapoulos, S. E., Lowik, C. W. (2005). SOST/sclerostin, an osteocyte- derived negative regulator of bone formation. *Cytokine and Growth Factor Reviews, 16*, 319-327.

156. Keller, H., Kneissel, M. (2005). SOST is a target gene for PTH in bone. *Bone*, *37*, 148-158.

157. Robling, A. G., Bellido, T., Turner, C. H. (2006). Mechanical stimulation in vivo reduces osteocyte expression of sclerostin. *Journal of Musculoskeletal and Neuronal Interactions, 6* (4), 354.

158. Li, X., Ominsky, M. S., Warmington, K. S., Morony, S., Gong, J., Cao, J., Gao, Y., Shalhoub, V., Tipton, B., Haldankar, R., Chen, Q., Winters, A., Boone, T., Geng, Z., Niu, Q. T., Ke, H. Z., Kostenuik, P. J., Simonet, W. S., Lacey, D. L., Paszty, C. (2009). Sclerostin antibody treatment increases bone formation, bone mass, and bone strength in a rat model of postmenopausal osteoporosis. *Journal of Bone and Mineral Research*, *24,* 578-588.

159. Malik, N., Haugen, H. S., Modrell, B., Shoyab, M., Clegg, C. H. (1995). Developmental abnormalities in mice transgenic for bovine oncostatin M. *Molecular and Cellular Biology, 15*, 2349-2358.

160. Bravo, J., Heath, J. K. (2000). Receptor recognition by gp130 cytokines. *EMBO Journal*, *19*, 2399-2411.

161. Ishihara, K., Hirano, T. (2002). Molecular basis of the cell specificity of cytokine action. *Biochimica et Biophysica Acta*, *1592*, 281-296.

162. Bozec, A., Bakiri, L., Hoebertz, A., Eferl, R., Schilling, A. F., Komnenovic, V., Scheuch, H., Priemel, M., Stewart, C. L., Amling, M., Wagner, E. F. (2008). Osteoclast size is controlled by Fra-2 through LIF/LIF-receptor signaling and hypoxia. *Nature, 454*, 221-225.

163. Ware, C. B., Horowitz, M. C., Renshaw, B. R., Hunt, J. S., Liggitt, D., Koblar, S. A., Gliniak, B. C., McKenna, H. J., Papayannopoulou, T., Thoma, B., Cheng, L., Donovan, P. J., Peschon, J. J., Bartlett, P. F., Willis, C. R., Wright, B. D., Carpenter, M. K., Davison, B. L., Gearing, D. P. (1995). Targeted disruption of the low-affinity leukemia inhibitory factor receptor gene causes placental, skeletal, neural and metabolic defects and results in perinatal death. *Development*, *121*, 1283-1299.

164. Kawasaki, K., Gao, Y. H., Yokose, S., Kaji, Y., Nakamura, T., Suda, T., et al. (1997). Osteoclasts are present in gp130-deficient mice. *Endocrinology*, *138*, 4959-4965.

165. Takeuchi, Y., Watanabe, S., Ishii, G., Takeda, S., Nakayama, K., Fukumoto, S., et al. (2002). Interleukin-11 as a stimulatory factor for bone formation prevents bone loss with advancing age in mice. *Journal of Biological Chemistry*, *277*, 49011-49018.

166. Cornish, J., Callon, K., King, A., Edgar, S., Reid, I. R. (1993). The effect of leukemia inhibitory factor on bone in vivo. *Endocrinology*, *132*, 1359-1366.

167. Shin, H. I., Divieti, P., Sims, N. A., Kobayashi, T., Miao, D., Karaplis, A. C., Baron, R., Bringhurst, R., Kronenberg, H. M. (2004). Gp130-mediated signaling is necessary for normal osteoblastic function *in vivo* and *in vitro*. *Endocrinology*, *145*, 1376-1385.

168. Jenkins, B. J., Grail, D., Inglese, M., Quilici, C., Bozinovski, S., Wong, P., Ernst, M. (2004). Imbalanced gp130-dependent signaling in macrophages alters macrophage colony-stimulating factor responsiveness via regulation of c-fms expression. *Molecular and Cellular Biology*, *24*, 1453-1463.

169. Bellido, T., Stahl, N., Farruggella, T. J., Borba, V., Yancopoulos, G. D., Manolagas, S. C. (1996). Detection of receptors for interleukin-6, interleukin-11, leukemia inhibitory factor, oncostatin M, and ciliary neurotrophic factor in bone marrow stromal/osteoblastic cells. *Journal of Clinical Investigation*, *97*, 431-437.

170. Sanchez, C., Gabay, O., Salvat, C., Henrotin, Y. E., Berenbaum, F. (2009). Mechanical loading highly increases IL-6 production and decreases OPG expression by osteoblasts. *Osteoarthritis Cartilage*, *17*, 473-481.

171. Kido, S., Kuriwaka-Kido, R., Imamura, T., Ito, Y., Inoue, D., Matsumoto, T. (2009). Mechanical stress induces Interleukin-11 expression to stimulate osteoblast differentiation. *Bone*, *45*, 1125-1132.

172. Li, X., Placencio, V., Iturregui, J. M., Uwamariya, C., Sharif-Afshar, A. R., Koyama, T., et al. (2008). Prostate tumor progression is mediated by a paracrine TGF-beta/Wnt3a signaling axis. *Oncogene*, *27*, 7118-7130.

173. Zhou, H., Mak, W., Zheng, Y., Dunstan, C. R., Seibel, M. J. (2008). Osteoblasts directly control lineage commitment of mesenchymal progenitor cells through Wnt signaling. *Journal of Biological Chemistry*, *283*, 1936-1945.

174. Katoh, M. (2009). Transcriptional mechanisms of WNT5A based on NF-kappaB, Hedgehog, TGFbeta, and Notch signaling cascades. *International Journal of Molecular Medicine*, *23*, 763-769.

175. Robinson, J. A., Chatterjee-Kishore, M., Yaworsky, P. J., Cullen, D. M., Zhao, W., Li, C., Kharode, Y., Sauter, L., Babij, P., Brown, E. L., Hill, A. A., Akhter, M. P., Johnson, M. L., Recker, R. R., Komm, B. S., and Bex, F. J. (2006). Wnt/β-catenin signaling is a normal physiological response to mechanical loading in bone. *Journal of Biological Chemistry, 281*, 31720-31728.

176. Li, X., Ominsky, M. S., Niu, Q. T., et al. (2008). Targeted deletion of the sclerostin gene in mice results in increased bone formation and bone strength. *Journal of Bone and Mineral Research, 23*, 860-869.

177. Balemans, W., Ebeling, M., Patel, N., et al. (2001). Increased bone density in sclerosteosis is due to the deficiency of a novel secreted protein (SOST). *Human Molecular Genetics*, *10*, 537-543.

178. Li, X., Zhang, Y., Kang, H., et al. (2005). Sclerostin binds to LRP5/6 and antagonizes canonical Wnt signaling. *Journal of Biological Chemistry*, *280*, 19883-19887.

179. O'Brien, C. A., Gubrij, I., Lin, S. C., Saylors, R. L., Manolagas, S. C. (1999). STAT3 activation in stromal/osteoblastic cells is required for induction of the receptor activator of NF-kappaB ligand and stimulation of osteoclastogenesis by gp130-utilizing cytokines or interleukin-1 but not 1,25-dihydroxyvitamin D_3 or parathyroid hormone. *Journal of Biological Chemistry*, *274*, 19301-19308.

180. Udagawa, N., Takahashi, N., Katagiri, T., Tamura, T., Wada, S., Findlay, D. M., et al. (1995). Interleukin (IL)-6 induction of osteoclast differentiation depends on IL-6 receptors expressed on osteoblastic cells but not on osteoclast progenitors. *Journal of Experimental Medicine*, *182*, 1461-1468.

181. Robling, A. G., Niziolek, P. J., Baldridge, L. A., et al. (2008). Mechanical stimulation of bone in vivo reduces osteocyte expression of Sost/sclerostin. *Journal of Biological Chemistry*, *283*, 5866-5875.

182. Lin, C., Jiang, X., Dai, Z., et al. (2009). Sclerostin mediates bone response to mechanical unloading through antagonizing Wnt/beta-catenin signaling. *Journal of Bone and Mineral Research*, *24*, 1651-1661.

183. Tanaka, K., Yamaguchi, Y., Hakeda, Y. (1995). Isolated chick osteocytes stimulate formation and bone-resorbing activity of osteoclast-like cells. *Journal of Bone and Mineral Metabolism*, *13*, 61-70.

184. Zhao, S., Zhang, Y. K., Harris, S., Ahuja, S. S., Bonewald, L. F. (2002). MLO-Y4 osteocyte-like cells support osteoclast formation and activation. *Journal of Bone and Mineral Research*, *17*, 2068-2079.

185. Verborgt, O., Tatton, N. A., Majeska, R. J., Schaffler, M. B. (2002). Spatial distribution of Bax and Bcl-2 in osteocytes after bone fatigue: complementary roles in bone remodeling regulation? *Journal of Bone and Mineral Research*, *17*, 907-914.

186. Kogianni, G., Mann, V., Noble, B. S. (2008). Apoptotic bodies convey activity capable of initiating osteoclastogenesis and localized bone destruction. *Journal of Bone and Mineral Research*, *23*, 915-927.

187. Kramer, I., Halleux, C., Keller, H., et al. (2010). Osteocyte Wnt/beta-catenin signaling is required for normal bone homeostasis. *Molecular and Cellular Biology*, *30*, 3071-3085.

188. Bonewald, L. F., Johnson, M. L. (2008). Osteocytes, Mechanosensing, and Wnt Signaling. *Bone*, *42*, 606-615.

189. Jilka, R. L., Weinstein, R. S., Bellido, T., Parfitt, A. M., Manolagas, S. C. (1998). Osteoblast programmed cell death (apoptosis): modulation by growth factors and cytokines. *Journal of Bone and Mineral Research*, *13*, 793-802.

190. Bellido, T., O'Brien, C. A., Roberson, P. K., Manolagas, S. C. (1998). Transcriptional activation of the p21 (WAF1, CIP1, SDI1) gene by interleukin-6 type cytokines. A prerequisite for their prodifferentiating and anti-apoptotic effect on human osteoblastic cells. *Journal of Biological Chemistry*, *273*, 21137–21144.

VITA

VITA

Hongkang Zhou
Purdue University Graduate School

Education

Doctor of Philosophy (Ph.D.) in Cell and Developmental Biology
Indiana University-Purdue University Indianapolis (IUPUI), Indianapolis, Indiana, May 2014
Research Dissertation: "The Essential Role of Stat3 in Bone Homeostasis and Mechanotransduction"
Principal Investigator: Dr. Jiliang Li

Master of Science (M.S.) in Cell and Molecular Biology
San Francisco State University (SFSU), San Francisco, California, August 2009
Research Thesis: "Identification of Proteins that Interact with Sperm-specific Phosphatases GSP-3 and GSP-4 in *C.elegans*"
Principal Investigator: Dr. Diana Chu

Bachelor of Science (B.S.) in Biological Sciences
Minzu University of China (MUC), Beijing, China, July 2007
Research Thesis: "Identifying Characteristics of Human Red Blood Cells in Dielectrophoresis (DEP)"
Undergraduate Research Mentor: Dr. Bin Wang

Professional Appointments

2010-2014	Graduate Teaching Assistant (Human Physiology Laboratory Instructor), Department of Biology, IUPUI Course Supervisor: Dr. Patricia Clark Teaching Responsibilities: Provide instructions for N217 Human Physiology Laboratory, including giving 30 minutes lectures, answer questions from students, solve problems during laboratory exercise proceedings, prepare quizzes and exam questions, evaluate laboratory reports, and submit final grades.
2009-2014	Graduate Research Assistant, Li Lab, Department of Biology, IUPUI Research Advisor: Dr. Jiliang Li Ph.D. Research Projects: Investigate the *in vivo* physiological role of Stat3 in bone homeostasis and mechanotransduction. Characterize phenotypes of osteoblast and osteocyte-specific Stat3 knockout mice

from bone tissue level to cellular level. Examine load-induced bone formation and bone formation-important genes in Stat3 knockout mice. Assess the enhanced bone fracture healing by transplantation of blood vessel wall-derived endothelial colony-forming cells on biocompatible materials.

2007-2009 Graduate Student Assistant, Chu Lab, Department of Biology, SFSU
Research Advisor: Dr. Diana Chu
M.S. Research Project: Indentify the interacting partners of GSP-3 and GSP-4 proteins which are required in male fertility in *C.elegans* by utilizing data mining of yeast two-hybrid data base, co-immunoprecipitation, western blot, and mass spectrometry assays.

2006-2007 Undergraduate Student Researcher: Chinese Minority Traditional Medical Center, MUC
Undergraduate Research Advisor: Dr. Bin Wang
B.S. Research Project: Determine the frequency and strength of electric field to isolate red blood cells from whole human blood samples by dielectrophoresis on biochips.

Publications

Zhou, H., Newnum, A. B., Martin, J. R., Li, P., Nelson, M. T., Moh, A., Fu, X. Y., Yokota, H., and Li. J. (2011). Osteoblast/osteocyte-specific inactivation of Stat3 decreases load-driven bone formation and accumulates reactive oxygen species. *Bone*, *49* (3), 404-411.

Chandrasekhar, K. S., **Zhou, H.**, Zeng, P., Alge, D., Li, W., Finney, B. A., Yoder, M. C., and Li, J. (2011). Blood vessel wall-derived endothelial colony-forming cells enhance fracture repair and bone regeneration. *Calcified Tissue International*, *89* (5), 347-357.

Zhou, H. and Li, J. (2014). A critical role of Stat3 in osteocytes mediated mechanotransduction and bone formation (in preparation).

Conferences/Poster Presentations

Go, A., Wu, J. C., Samson, M., **Zhou, H.**, Mirsoian, S., and Chu D. (2009). The conserved Glc7/PP1 phosphatases GSP-3 and GSP-4 regulate sperm morphogenesis. 17th International *C.elegans* Meeting, June 24-28, 2009. University of California Los Angeles, California, U.S.A.

Zhou, H., Li, L., Bivi, N., Himes, E., Mihuti, L., Bellido, T., and Li, J. (2012). Stat3 in osteocytes is required for skeletal mechanotransduction. American Society for Bone and Mineral Research 2012 Annual Meeting, October 12-15, 2012. Minneapolis, Minnesota, U.S.A.

Awards and Scholarships

2010-2014	Graduate Teaching Assistantship, Department of Biology, IUPUI
2009	Research Investment Fund (RIF) Fellowship, Department of Biology, IUPUI
2009	Instructionally Related Activities (IRA) Travel Award, Department of Biology, SFSU
2008	Instructionally Related Activities (IRA) Research Award, Department of Biology, SFSU
2006	Academic Progress Award, College of Life and Environmental Sciences, MUC

Professional Organizations

2007-present	Member, American Association for the Advancement of Science
2010-2014	Member, Biology Purdue University Graduate Student Club
2012-2013	President, Biology Purdue University Graduate Student Club

PUBLICATION

Bone 49 (2011) 404–411

Contents lists available at ScienceDirect

Bone

journal homepage: www.elsevier.com/locate/bone

Osteoblast/osteocyte-specific inactivation of Stat3 decreases load-driven bone formation and accumulates reactive oxygen species

Hongkang Zhou [a], America B. Newnum [a], Joseph R. Martin [a], Ping Li [b], Mark T. Nelson [a], Akira Moh [c], Xin-Yuan Fu [c], Hiroki Yokota [d], Jiliang Li [a,*]

[a] Department of Biology, Indiana University Purdue University Indianapolis, Indianapolis, IN 46202, USA
[b] Department of Surgery, Indiana University School of Medicine, Indianapolis, IN 46202, USA
[c] Department of Microbiology and Immunology, Indiana University School of Medicine, Indianapolis, IN 46202, USA
[d] Department of Biomedical Engineering, Indiana University Purdue University Indianapolis, Indianapolis, IN 46202, USA

ARTICLE INFO

Article history:
Received 22 February 2011
Revised 4 April 2011
Accepted 21 April 2011
Available online 30 April 2011

Edited by: David Fyhrie

Keywords:
Signal transducers and activators of transcription 3
Osteoblast
Mechanotransduction
Reactive oxidative stress
Bone formation
Mitochondria

ABSTRACT

Signal transducers and activators of transcription 3 (Stat3) is a transcription factor expressed in many cell types including osteoblasts, osteocytes, and osteoclasts. STAT3 mutations cause a rare human immunodeficiency disease that presents reduced bone mineral density and recurrent pathological fractures. To investigate the role of Stat3 in load-driven bone metabolism, two strains of osteoblast/osteocyte-selective Stat3 knockout (KO) mice were generated. Compared to age-matched littermate controls, this selective inactivation of Stat3 significantly lowered bone mineral density (7–12%, $p<0.05$) as well as ultimate force (21–34%, $p<0.01$). In ulna loading (2.50–2.75 N with 120 cycles/day at 2 Hz for 3 consecutive days), Stat3 KO mice were less responsive than littermate controls as indicated by reduction in relative mineralizing surface (rMS/BS, 47–59%, $p<0.05$) and relative bone formation rate (rBFR/BS, 64–75%, $p<0.001$). Furthermore, inactivation of Stat3 suppressed load-driven mitochondrial activity, which led to an elevated level of reactive oxygen species (ROS) in cultured primary osteoblasts. Taken together, the results support the notion that the loss-of-function mutation of Stat3 in osteoblasts and osteocytes diminishes load-driven bone formation and impairs the regulation of oxidative stress in mitochondria.

Introduction

Signal transducers and activators of transcription 3 (STAT3) is a ubiquitously expressed transcription factor, mediating cell proliferation, differentiation, and survival [1–5]. STAT3 mutations cause a rare human immunodeficiency disease, Job's Syndrome (also known as hyperimmunoglobulin E syndrome) [6,7], which is characterized by the elevated level of IgE in serum and distorted craniofacial and skeletal features. Most patients present reduced bone mineral density [8], recurrent fractures, hyperextensible joints, and scoliosis. Few studies, however, have investigated the role of STAT3 in bone metabolism.

Stat proteins are latent cytoplasmic transcription factors [2,9], and activated by cytokines including IL6, IL11, oncostatin M, leukemia inhibitory factor, cardiotrophin 1, and neurotrophin 1/B-cell stimulatory factor 3 [10,11]. These cytokines are pleiotropic, sharing a glycoprotein chain gp130 as a common signal transducer [10,12,13]. The binding of these cytokines to their receptors induces the homodimerization of gp130 and activates gp130-associated Janus kinases (JAKs) [14], which phosphorylate a tyrosine residue of Stat3 [15]. Targeted disruption of the mouse Stat3 gene leads to embryonic lethality, indicating that Stat3 is essential for early embryonic development [16].

Recent studies also suggest that Stat3 is involved in mitochondrial functions [17,18]. Stat3 regulates cell respiration and metabolism in mitochondria [17,18]. A fraction of cellular Stat3 has been found to reside within the mitochondria of mouse myocytes and hepatocytes. Without Stat3, an electron transport chain (ETC) that generates energy by oxidative phosphorylation is inhibited and reduction in mitochondrial activity leads to accumulation of ROS, but the number of mitochondria and their content of the protein that constitute complexes I and II are not altered [19–21]. On the other hand, addition of Stat3 in Stat3-null cells can restore oxidative phosphorylation, and this rescue of mitochondrial function does not require the DNA binding domain. However, expression of Stat3 with a mutation that prevents phosphorylation of serine 727 does not induce the rescue effects [17]. These data suggest that the conserved serine phosphorylation site on Stat3 is important for regulation of mitochondrial activity. Clinical evidence suggests interplay between ROS-linked oxidative stress and age-related bone loss [22–28]. Since oxidative stress is known to antagonize Wnt signaling, which is critical in load-driven bone formation [29,30], Stat3 is potentially involved in bone metabolism through regulation of anabolic genes as well as ROS-linked mitochondrial functions.

---

* Corresponding author at: Department of Biology, Indiana University Purdue University Indianapolis, 723 W Michigan Street, SL306, Indianapolis, IN 46202, USA. Fax: +1 317 274 2846.
E-mail address: jilili@iupui.edu (J. Li).

8756-3282/$ – see front matter © 2011 Elsevier Inc. All rights reserved.
doi:10.1016/j.bone.2011.04.020

In this study, we addressed two questions: Is Stat3 necessary for induction of bone formation in response to mechanical loading? Does inactivation of Stat3 in osteoblasts and osteocytes impair mitochondrial functions and lead to accumulation of ROS? Since mechanical loading is known to upregulate expression of Stat3 [31] and activate Wnt signaling [32], we hypothesized that the inactivation of Stat3 specific to osteoblasts and osteocytes would reduce load-driven bone formation and elevate the level of ROS. Stat3 KO mice specific to osteoblasts as well as osteocytes were generated using Cre-loxP recombination by breeding the mice with Cre recombinase driven by a type I collagen promoter with the mice carrying floxed Stat3. The two loxP sites flank the exons 18–20 of the Stat3 gene [33]. Although two lines of transgenic mice using the collagen $\alpha1$(I)2.3 and $\alpha1$(I)3.6 fragments were established [34], herein we mainly presented data collected from the Col3.6-Cre; Stat3$^{flox/flox}$ mice since these two lines exhibited similar responses to mechanical loading. Data collected from the Col2.3-Cre;Stat3$^{flox/flox}$ mice are presented in the Supplementary Data.

Materials and methods

Experimental animals

All procedures performed in this study were in accordance with the Indiana University Animal Care and Use Committee Guidelines. The Cre recombinase transgenic mice and the floxed Stat3 mice were generated as reported previously [33,34] and kindly provided by Dr. Barbara Kream (University of Connecticut Health Center) and Dr. Xin-Yuan Fu (Department of Microbiology and Immunology, Indiana University School of Medicine), respectively. The Cre recombinase transgene is driven by the by the collagen $\alpha1$(I)2.3 and $\alpha1$(I)3.6 fragments (Col2.3-Cre and Col3.6-Cre), while in floxed Stat3 mice (Stat3$^{flox/flox}$) the two loxP sites flank the exons 18–20 of the Stat3 gene [33]. Conditional Stat3 knockout (KO) mice specific to osteoblasts and osteocytes were generated by breeding mice with Cre recombinase driven by the type I collagen promoter and mice with floxed Stat3. Offspring, which were heterozygous or homozygous for the Cre transgene and homozygous for the loxP sites, were used in this study together with their littermate controls.

Two lines of conditional Stat3 KO mice, Col2.3-Cre;Stat3$^{flox/flox}$ and Col3.6-Cre;Stat3$^{flox/flox}$, were established in which Stat3 was deleted using the collagen $\alpha1$(I)2.3 and $\alpha1$(I)3.6 fragments, respectively. A deletion of the exons 18 and 20, which encode the SH2 domain of Stat3, results in a conditional Stat3 KO in osteoblasts and osteocytes (Fig. 1). Note that Col2.3-Cre blocks Stat3 expression in mature osteoblasts and osteocytes, while Col3.6-Cre mutates Stat3 in early and mature osteoblasts as well as osteocytes. The genotype was determined by PCR as described previously [33,34].

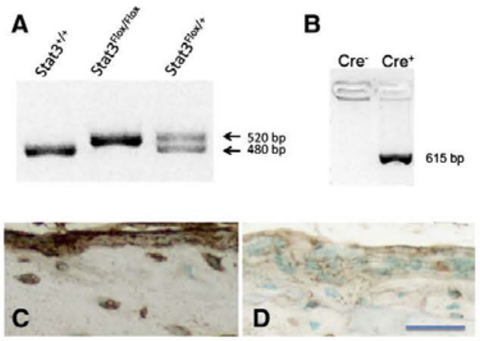

Fig. 1. Characterization of the conditional Stat3 KO mice. (A) Stat3^{flox} allele detected with a pair of PCR primers that generate 520-bp DNA fragments, and Stat3 wildtype allele corresponding to 480-bp fragments. (B) Col2.3-Cre and Col-3.6-Cre transgenes detected with the primers amplifying 615-bp fragments. (C) Immunohistochemical staining for wildtype control with Stat3 protein present in periosteal osteoblasts and osteocytes. (D) Immunohistochemical staining for KO (Col3.6-Cre;Stat3$^{flox/flox}$) mice without Stat3 protein. (Bar = 50 μm).

In vivo ulna loading

To examine the role of Stat3 in load-driven bone formation, we subjected Stat3 deficient mice (Col2.3-Cre;Stat3$^{flox/flox}$ and Col3.6-Cre;Stat3$^{flox/flox}$) and littermate controls (Col2.3-Cre;Stat3$^{+/+}$ and Col3.6-Cre;Stat3$^{+/+}$ mice) to axial ulnar loading as previously described [35,36] and conducted bone histomorphometry. Using 16-week-old mice, dynamic loads (120 cycles/day at 2 Hz, with peak forces of 2.50 N for female and 2.75 N for male mice) were applied under general anesthesia with 3–5% isoflurance for three consecutive days using an electromagnetic actuator (Bose ElectroForce 3200 series; EnduraTEC). The loading forces were selected to ensure that both male and female mice experiences similar peak strains during loading. In a pilot load-strain calibration experiment using 3 mice randomly selected from each gender and strain of mouse, in situ mechanical strains achieved during loading were measured on the medial surface of the ulnae as described previously by our group [35,37]. The peak force of 2.5 N produced about ~2800 and ~2970 microstrains at the midshaft of ulnas of female control mice and conditional Stat3 KO mice, respectively. The peak force of 2.75 N produced about ~2800 and ~2940 microstrains at the midshaft of ulnas of male control mice and conditional Stat3 KO mice, respectively. The left forearms were not loaded and served as nonloaded controls. All mice were allowed normal cage activity between loading sessions and afterward. Intraperitoneal injections of calcein (30 mg/kg body weight; Sigma) and alizarin (50 mg/kg body weight; Sigma) were administered on days 5 and 11 after the first loading bout. All animals were sacrificed after 14 days.

Right (loaded) and left (nonloaded control) ulnas were processed for histomorphometry to evaluate load-induced bone formation. Femurs were used to determine bone size, bone mineral density and mechanical properties. In particular, the right distal femurs of Stat3 deficient mice (Col3.6-Cre;Stat3$^{flox/flox}$) and littermate controls (Col3.6-Cre;Stat3$^{+/+}$ mice) were sectioned and used for measurement of bone formation and resorption.

Peripheral dual-energy X-ray absorptionmetry (pixiMUS)

Bone mineral content (BMC, g) and bone mineral density (BMD, g/mm^2) of the left femurs were evaluated using peripheral dual-energy X-ray absorptiometry (pDXA; PIXIMus II; GE-Lunar Co.).

Biomechanical testing

Femurs were brought to room temperature slowly (~2 h) in a saline bath, and mechanical testing was conducted by three-point bending using a microforce materials testing machine (Vitrodyne V1000; Liveco, Inc., Burlington, VT). Loads were applied at the mid-diaphysis (10 mm apart from a pair of supports) in the anteroposterior direction. Tests were conducted at a cross-head speed of 0.2 mm/s, during which force-displacement curves were generated. We determined ultimate force (F_U; N), stiffness (S; N/mm) and work to failure (U; mJ). Note that F_U represents the strength of the bone, whereas U is a measure of the energy required to break the bone.

Histomorphometry

Bone specimens were immersed in 10% neutral buffered formalin for 48 h. The specimens were then dehydrated in graded alcohols, cleared in xylene, and embedded in methyl methacrylate. Using a diamond-embedded wire saw (Histo-saw; Delaware Diamond Knives, Wilmington, DE), transverse thick sections (70 μm) were cut at the ulnar midshafts, ground to a final thickness of 20 μm, and mounted on microscope slides. Three sections per limb was used for bone histomorphometry with a Nikon Optiphot flurescence microscope (Nikon, Inc., Garden City, NJ) using a Bioquant digitizing system (R&M Biometrics, Nashville, TN). The following primary data were collected from the periosteal surface at 250× magnification: total perimeter (B.Pm); single label perimeter (sL.Pm); double label perimeter (dL.Pm), and double label area (dL.Ar). From these primary data, the following quantities were derived: mineralizing surface ($MS/BS = [1/2sL.Pm + dL.Pm]/B.Pm \times 100$;%); mineral apposition rate ($MAR = dL.Ar/dL.Pm/6$ days; μm/day); and bone formation rate ($BFR/BS = MAR \times MS/BS \times 3.65$; $\mu m^3/\mu m^2$ per year). Furthermore, a set of relative (r) values such as rMS/BS, rMAR, and rBFR/BS was obtained in which the values for the left ulna (nonloaded) were subtracted from the values for the right ulna (loaded).

From the distal femurs, the 5 μm thick frontal sections were cut using a microtome (Leica, Germany). Two unstained sections were mounted on microscope slides, and other sections were stained with McNeal's tetrachrome as well as tartrate-resistant acid phosphatase (TRAP) to identify active osteoclasts. The following primary data were collected from the metaphyseal area, 0.5 mm distal to the growth plate and 0.5 mm away from the intracortical surface, at 250× magnification: tissue area (T.Ar), trabecular bone area (tB.Ar), trabecular bone perimeter (tB.Pm), single label perimeter (sL.Pm), double label perimeter (dL.Pm), double label area (dL.Ar), osteoclast surface (Oc.S), and osteoclast number (Oc.N). From these primary data, the following quantities were derived: bone volume ($BV/TV = tB.Ar/T.Ar \times 100$;%), mineralizing surface ($MS/BS = [1/2sL.Pm + dL.Pm]/B.Pm \times 100$;%), mineral apposition rate ($MAR = dL.Ar/dL.Pm/6$ days; μm/day), bone formation rate ($BFR/BS = MAR \times MS/BS \times 3.65$; $\mu m^3/\mu m^2$ per year), percentage of osteoclast surface ($Oc.S/BS = Oc.S/tB.Pm$;%), and osteoclast number per mm ($Oc.N/BS = Oc.N/tB.Pm$; #/mm).

Cell culture

The pre-osteoblastic cell line, MC3T3-E1 (passages 10–20), was cultured in α-Minimal Essential Medium (α-MEM; Sigma, St. Louis, MO, USA) containing 10% fetal bovine serum (FBS; Atlanta Biologicals, Norcross, GA), 100 U/ml penicillin G (Sigma), and 100 μg/ml streptomycin (Sigma). Cells were maintained in a 95% air/5% CO_2 humidified incubator at 37 °C and subcultured every 72 h. Primary osteoblasts were isolated from calvarial bone of 4.5-day-old Stat3 deficient mice ($Col3.6\text{-}Cre;Stat3^{flox/flox}$) and littermate controls ($Col3.6\text{-}Cre;Stat3^{+/+}$) by sequential digestions with collagenase and trypsin [38]. We added 50 μg/ml ascorbic acid and cultured for 21 days to induce osteoblast differentiation [39]. Then the cells were used for the measurement of ROS and NAD^+/NADH ratio.

Fluid shear stress (FSS) studies

For fluid shear experiments, MC3T3-E1 cells or primary osteoblasts were plated on type I collagen-coated (10 $\mu g/cm^2$, BD Biosciences, Bedford, MA) $75 \times 38\ mm^2$ glass slides (Fisher Scientific, Pittsburgh, PA) at a density of about $1 \times 10^5\ cells/cm^2$. The cells were serum-starved for 24 h in α-MEM supplemented with 0.2% FBS prior to flow. Cells were subjected to oscillatory fluid shear stress (12 dyn/cm^2) in parallel plate flow chambers at 37 °C using a previously described fluid flow device [40]. Hard walled tubing was used to connect the pump to the chamber inlet, and a reservoir was attached to the outlet to allow for movement of the fluid and exchange of 5% CO_2. This system subjected cells to oscillating fluid flow at a frequency of 1 Hz in α-MEM supplemented with 0.2% FBS and antibiotics. Static controls were held in cell culture dishes at 37 °C with 5% CO_2.

Western blot analysis

Immediately after MC3T3-E1 cells were subjected to FSS for 30, 60 and 90 min, the cells were washed quickly with cold PBS (1×) and lysed with SDS lysis buffer. The lysis buffer contained 62.5 mM Tris, 2% sodium dodecyl sulfate (SDS), 10% glycerol (v/v), 5 mM EDTA, and 1% protease inhibitor cocktail (Sigma). After the cell lysates were boiled for 10 min, the protein samples were centrifuged at 14,000 g for 10 min at 4 °C to remove any cellular debris. Protein assay was performed using a Bio-Rad detergent compatible (DC) protein assay. Twenty micrograms of whole cell lysates were separated by 10% SDS-polyacrylamide gel electrophoresis and electrotransferred to a nitrocellulose membrane. Membranes were blocked in Tris-buffered saline containing 5% nonfat dry milk and 0.1% Tween-20 (TBST), and incubated with 200 μg/ml (1:1000) rabbit anti-Stat3 and rabbit anti-p-Stat3 (Ser 727) antibodies (Santa Cruz Biotechnology, Santa Cruz, CA) overnight at 4 °C. Following three washes in TBST, the membranes were incubated with goat anti-rabbit IgG hydroperoxidase conjugated secondary antibodies (1:5000) for 1 h at room temperature. Immunodetection was conducted using the enhanced chemiluminescence (ECL) method.

Measurement of ROS

The cell-permeable dye, 2,7-dichlorodihydrofluorescein diacetate (2,7-DCF-DA) (Sigma-Aldrich), was employed as an indicator of ROS level [41]. First, approximately 3×10^5 cells isolated from Stat3 KO ($Col3.6\text{-}Cre;Stat3^{flox/flox}$) and control ($Col3.6\text{-}Cre;Stat3^{+/+}$) calvarias were plated in 6 well plates in full serum media for 24 h. Then, cells were treated with 10 μM hydrogen peroxide (H_2O_2) (as a positive control), in the presence and absence of 50 μM AG-490 (Stat3 inhibitor) for 2 h [42]. Cells were then suspended with 10 μM DCF-DA, and assayed for ROS using flow cytometry.

Measurement of NAD^+/NADH ratio

In order to study whether inactivation of Stat3 affects mitochondrial functions in response to mechanical stimulation, NAD^+/NADH ratio in mitochondria Complex I was evaluated. Stat3 KO and control calvarial cells were subjected to oscillatory fluid shear stress (FSS at 12 dyn/cm^2) for 1 h. The cells without FSS served as a control. Immediately following FSS, cells were collected and quantitative determination of NAD^+/NADH was conducted using an EnzyChrom NAD^+/NADH assay kit (BioAssay Systems). Both NAD^+ and NADH concentrations were measured and normalized by protein contents. The ratio of NAD^+/NADH was then calculated. NADH is oxidized to NAD^+ at mitochondrial Complex I. We compared the ratio of NAD^+/NADH between wild type and Stat3 deficient mice in order to demonstrate the accumulation of NADH in Stat3 deficient osteoblasts due to the dysfunction of mitochondrial Complex I.

Statistical analysis

The data are expressed as mean ± SEM (standard error of the mean). Phenotypic values among the selected genotypes for a given sex were compared by one-way analysis of variance (ANOVA). Gender comparisons were performed using a two-way ANOVA with sex and genotype as independent variables. Differences between the loaded (right) and nonloaded (left) limbs were tested using paired t-tests. Statistical significance was assumed for $p < 0.05$.

Results

A deletion of the exons 18 and 20 resulted in a conditional knockout of Stat3 protein in the osteoblasts and osteocytes (Fig. 1), which was confirmed by immunohistochemical staining. Note that about 10% of

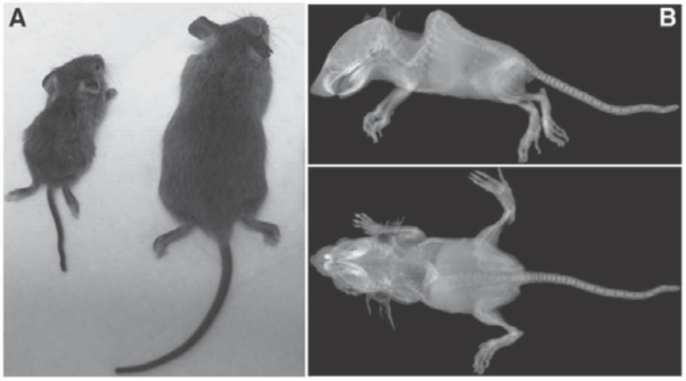

Fig. 2. Appearance of the conditional Stat3 KO mice. (A) Col3.6-Cre;Stat3$^{flox/flox}$ mice significantly smaller than its littermate control. (B) Lateral and anterior-posterior X-ray views of the Col3.6-Cre;Stat3$^{flox/flox}$ mouse showing severe spinal deformity.

the Stat3 deficient mice were extremely small and exhibited a spine deformity, which was noticeable at age of 3–4 weeks in both Col3.6-Cre;Stat3$^{flox/flox}$ mice (Fig. 2) and Col2.3-Cre;Stat3$^{flox/flox}$ mice (Supplementary Fig. 1). Those mice were unable to survive longer than 8 weeks and were excluded in the current study.

The bone phenotypes were characterized when they were 18 weeks old. Female Col3.6-Cre;Stat3$^{flox/flox}$ mice had significantly smaller body weights (-11%, $p=0.02$) compared with Col3.6-Cre; Stat3$^{+/+}$ mice, whereas the average body mass was not statistically different in male KO and littermate mice (Table 1). For both sexes, femur lengths were significantly shorter in Col3.6-Cre;Stat3$^{flox/flox}$ mice than controls (Table 1). The conditional Stat3 KO mice exhibited low bone mass phenotype, and BMC (-13% in female, $p<0.01$ and -11% in male, $p<0.05$) and BMD (-7% in female, $p<0.05$ and -12% in male, $p<0.001$) were significantly lower in KO mice than control littermates (Table 1). Similar bone phenotype can also be seen in Col2.3-Cre;Stat3$^{flox/flox}$ mice as shown in Supplementary Table 1.

Bone histomorphometry was conducted using trabecular bones at distal femurs. For both female and male mice, bone volume was significantly less in KO (Col3.6-Cre;Stat3$^{flox/flox}$) mice (-39% in female, $p<0.05$ and -38% in male, $p<0.05$) than their littermate controls (Table 1, Fig. 3A and B). Furthermore, mineralizing surface (MS/BS, -24% in female, $p<0.01$ and -29% in male, $p<0.05$), mineral appositional rate (MAR, -54% in female, $p<0.001$ and -56% in male, $p<0.05$) and bone formation rate (BFR/BS, -63% in female, $p<0.001$ and -65% in male, $p<0.05$) were significantly smaller in KO mice than control mice (Fig. 3C and D). Although the number of osteoclasts was statistically similar between KO mice and their control mice, osteoclast surfaces were significantly greater in KO mice ($+39\%$ in female and $+40\%$ in male, $p<0.05$) than their littermates (Table 1).

In order to evaluate the mechanical properties of bone in KO (Col3.6-Cre;Stat3$^{flox/flox}$) mice and control mice, the femurs were subject to mechanical testing. For both sexes, the ultimate forces (-28% in female, $p<0.01$ and -27% in male, $p<0.01$) and stiffness

Table 1
Bone phenotype of Col3.6-Cre;Stat3$^{flox/flox}$ mice.

Parameter	Female		Male	
	Control (n = 9–11)	Col3.6-Cre;Stat3$^{flox/flox}$ (n = 9–11)	Control (n = 9–11)	Col3.6-Cre;Stat3$^{flox/flox}$ (n = 9–11)
Body mass (g)	28.93 ± 0.92	25.73 ± 0.98[a]	32.00 ± 0.98	30.98 ± 0.98
Femur length (mm)	15.92 ± 0.12	15.19 ± 0.12[c]	15.88 ± 0.12	15.47 ± 0.12[b]
Femur bone mineral				
Femoral BMC (g)	0.032 ± 0.001	0.028 ± 0.001[b]	0.037 ± 0.001	0.033 ± 0.001[a]
Femoral BMD (g/cm^2)	0.070 ± 0.001	0.065 ± 0.001[a]	0.076 ± 0.001	0.067 ± 0.001[c]
Distal femur cancellous bone structure				
BV/TV (%)	12.02 ± 1.2	7.34 ± 1.13[a]	19.62 ± 1.94	12.26 ± 2.5[a]
MS/BS (%)	49.43 ± 2.8	37.48 ± 2.62[b]	43.69 ± 3.03	30.85 ± 3.91[a]
MAR (μm)	0.79 ± 0.07	0.36 ± 0.06[c]	0.91 ± 0.07	0.44 ± 0.11[b]
BFR/BS (μm^3/μm^2/year)	139.38 ± 11.32	51.76 ± 10.59[c]	143.85 ± 15.51	50.31 ± 10.01[a]
Oc.N. (#/μm)	3.72 ± 0.56	4.97 ± 0.59	1.91 ± 0.19	1.90 ± 0.20
Oc.S/BS (%)	16.65 ± 1.59	23.10 ± 1.68[a]	10.40 ± 1.04	14.53 ± 1.10[a]
Midshaft femur mechanical properties				
Ultimate force (N)	27.06 ± 1.79	19.56 ± 1.89[b]	32.82 ± 1.89	23.94 ± 1.89[b]
Stiffness (N/mm)	90.18 ± 7.08	58.15 ± 7.46[b]	107.84 ± 7.46	65.22 ± 7.46[c]
Work to failure (mJ)	11.04 ± 1.32	7.05 ± 1.39[a]	11.32 ± 1.39	8.89 ± 1.39

[a] $p<0.05$ vs. the same sex control.
[c] $p<0.001$ vs. the same sex control.
[b] $p<0.01$ vs. the same sex control.

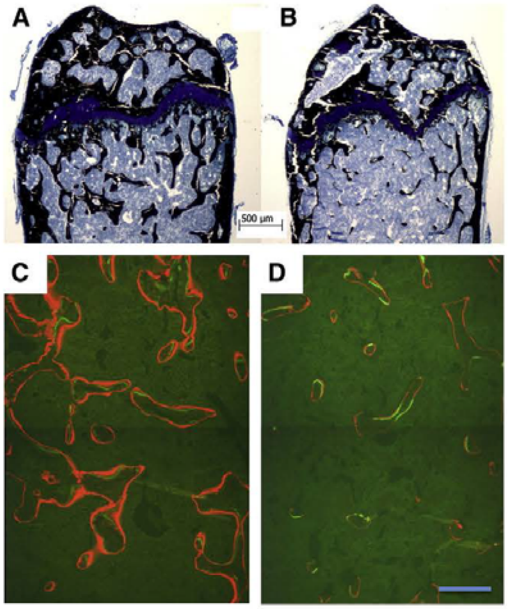

Fig. 3. Trabecular bone in the distal femur in (A) Wildtype control and (B) Col3.6-Cre; $Stat3^{flox/flox}$ mice. Fluorescent labels (Calcein and alizarin) in (C) Wildtype control and (D) Col3.6-Cre;$Stat3^{flox/flox}$ mice, indicating mineralizing surface (MS/BS), mineral appositional rate (MAR) and bone formation rate (BFR/BS). (Bar = 200 µm).

(−36% in female, $p<0.01$ and −40% in male, $p<0.001$) were reduced significantly in KO mice in comparison with their controls (Table 1). Bone strength of Col2.3-Cre;$Stat3^{flox/flox}$ mice was also significantly lower that the littermate controls (Col2.3-Cre;$Stat3^{+/+}$ mice, Supplementary Table 1). These data suggest that inactivation of Stat3 specific to osteoblasts and osteocytes significantly decreases bone strength.

To investigate the role of Stat3 in load-driven bone formation, the Col3.6-Cre;$Stat3^{flox/flox}$ mice as well as their littermate control mice (Col3.6-Cre;$Stat3^{+/+}$) were given ulna loading and their bone formation responses were evaluated. The results showed that load-induced bone formation was suppressed in male and female Col3.6-Cre;$Stat3^{flox/flox}$ mice. The data from female Col3.6-Cre;$Stat3^{flox/flox}$ mice are shown in Fig. 4. In female mice, for instance, the relative bone formation rate (BFR/BS in the right ulna minus BFR/BS in the left ulna) was roughly 56% lower in Col3.6-Cre;$Stat3^{flox/flox}$ mice. These loading data support an important role of Stat3 in load-driven bone formation. The similar loading phenotypes in Col2.3-Cre;$Stat3^{flox/flox}$ mice were also observed (Supplementary Fig. 2).

To demonstrate the Stat3 activation in response to FSS, we examined the phosphorylation of Stat3 at serine 727 using MC3T3-E1 osteoblastic cells in the presence and absence of FSS (12 dyn/cm^2). Western blotting analysis showed that serine phosphorylation of Stat3 increased in a manner dependent on flow duration from 30 to 90 min (Fig. 5).

In order to examine if Stat3 deficiency led to an elevated level of intracellular ROS, calvarial osteoblasts were cultured and assayed for ROS using DCF-DA and flow cytometry. The ROS level was significantly higher in Stat3 deficient osteoblasts than control cells (Fig. 6). Furthermore, administration of Stat3 inhibitor, AG490, significantly increased the production of ROS in control cells, but it did not affect the ROS level in Stat3 deficient osteoblasts. These data suggest that the inactivation of Stat3 both in KO osteoblasts as well as in AG-490 treated control osteoblasts increases the intracellular ROS level.

To evaluate mitochondrial functions in response to FSS, NAD^+/NADH ratio was measured. First, compared to control osteoblasts the NAD^+/NADH ratio was significantly reduced in Stat3 deficient osteoblasts (Fig. 7). Second, FSS increased NAD^+/NADH ratio in control osteoblasts. However, Stat3 deficient osteoblasts exhibited a lower NAD^+/NADH ratio level (31% lower than control, $p = 0.01$) and they did not show any alteration in the NAD^+/NADH ratio to FSS. These data indicate the accumulation of NADH in Stat3 deficient osteoblasts, suggesting the dysfunction of mitochondrial Complex I.

Discussion

The present study demonstrated that inactivation of Stat3 in osteoblasts and osteocytes reduced bone mass, strength, and load-

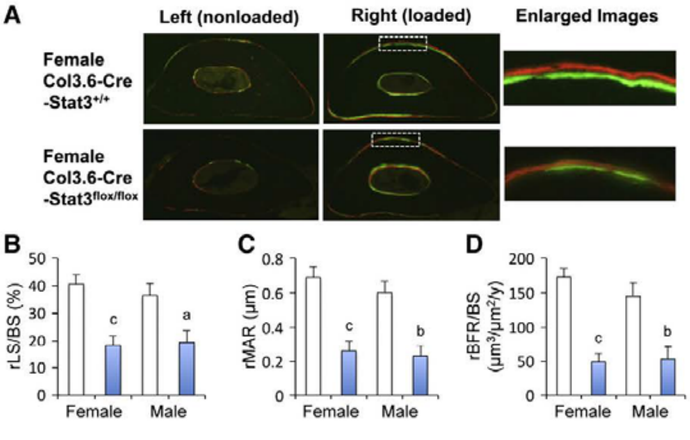

Fig. 4. (A) Midshaft ulnar sections from the control and loaded forearms for female control and Col3.6-Cre; $Stat3^{flox/flox}$ mice. Calcein (green) and alizarin (red) injections were given after loading. Note that the anabolic responses on the medial (square) and lateral surfaces of the loaded control ulna were detected, but those responses were significantly decreased in the loaded ulna of the Stat3 KO mouse. Bone morphometric parameters for control mice (Col3.6-Cre; $Stat3^{+/+}$) (open bars) and Col3.6-Cre; $Stat3^{flox/flox}$ mice (solid bars). (B) Relative mineralizing surface (rMS/BS). (C) Relative mineral appositional rate (rMAR). (D) Relative bone formation rate (rBFR/BS). Note that a: $p<0.05$, b: $p<0.01$, and c: $p<0.001$.

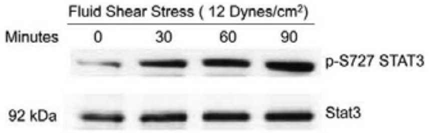

Fig. 5. Serine phosphorylation of Stat3 in response to FSS. Western blot analyses showed that phosphorylation of Stat3 at Serine 727 was increased in response to FSS.

driven bone formation. Furthermore, Stat3 deficient osteoblasts presented a higher basal level of ROS, and mechanical stimulation failed to lower this ROS level. These results clearly show that Stat3 plays a critical role in bone homeostasis and mechanotransduction, and Stat3 is involved not only in load-driven gene activation in nucleus but also in regulation of ROS and oxidative stress in mitochondria.

Consistent with a previous study [43], our study has shown that osteoblast/osteocyte specific knockout of Stat3 results in an osteoporotic phenotype because of suppressed bone formation. We have shown that Stat3 deficiency in osteoblasts/osteocytes does not change the number of osteoclasts, but osteoclast surfaces were significantly greater in KO mice than their littermates. Since osteoclast surface is normalized by bone surface, there is a possibility that the greater osteoclast surfaces in Stat3 deficient mice may result from the reduced bone surfaces due to the inhibition of bone formation. In addition, our study has demonstrated that Stat3 deficiency in osteoblast/osteocyte leads to a reduction in mechanical properties of mouse long bones. These data suggest that Stat3 plays an important role in bone homeostasis and maintenance of bone strength.

Mechanically induced bone formation was suppressed in both male and female conditional Stat3 KO mice. Because of the reduced mineralizing surface and mineral appositional rate, the result indicates that Stat3 deficiency suppresses osteoblast recruitment and activity. The mechanism of Stat3 activation is considered to be linked to the gp130 signaling pathway. Targeted disruption of gp130 gene in mice leads to embryonic lethality [44]. The gp130 knockout mice demonstrate defects in bone development, formation and resorption [45,46]. Osteoblastic cells express a group of receptors for cytokines such as IL6 and IL11, which share the gp130 signal transducer [47].

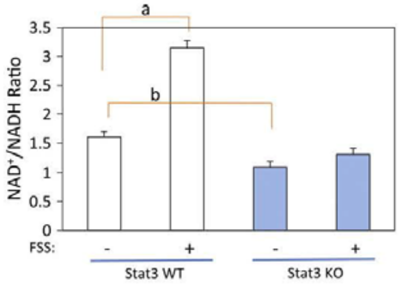

Fig. 7. Levels of NAD$^+$/NADH ratios in wildtype and Stat3 KO osteobalsts with and without fluid shear stress. Note that a: $p<0.001$ and b: $p<0.01$.

IL6, for instance, has been shown to be elevated in calvarial osteoblasts in response to mechanical stimulation [48], and IL11 is also increased in response to loading in vivo as well as fluid shear stress in vitro [49]. Furthermore, anti-IL11 antibody is shown to block mechanically induced enhancement of bone formation. Thus, it is possible that in Stat3 KO mice gp130 signaling is blocked imparing proliferation and differentiation of osteoblasts.

As a downstream mechanism for Stat3-mediated bone formation, Stat3 regulates functions in both nuclei and mitochondria. Stat3 is activated by tyrosine phosphorylation, which dimerizes and translocates it to the nucleus [2]. It binds specific gene-promoter sequences and induces gene expression [2,3,20]. Furthermore, Stat3 regulates cell respiration and metabolism in mitochondria [17,18]. Without Stat3, an electron transport chain (ETC) is inhibited and reduction in mitochondrial activity leads to accumulation of ROS [19–21]. Therefore, inhibition of bone formation in the conditional Stat3 KO mice may result from the suppression of gene expression and elevation of ROS in osteoblasts.

Regarding gene regulation in nucleus, disruption of Stat3 likely alters expression of mechanosensitive genes such as wnt molecules. In stromal cells transforming growth factor (TGF) − β mediated inhibition of wnt3a is in part through the suppression of Stat3 [50].

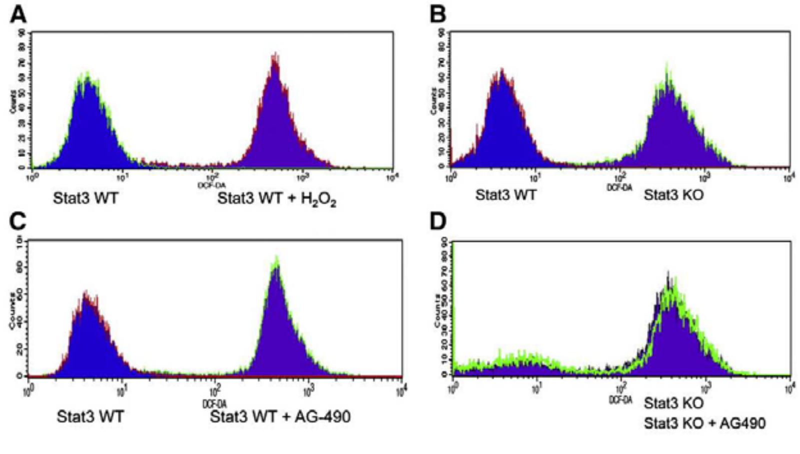

Fig. 6. Flow cytometric analysis for the level of ROS that was monitored by using 2,7-DCF-DA fluorescence (Horizontal axis). (A) ROS increased significantly in wild type cells when treated with hydrogen peroxide (H_2O_2) (as a positive control). (B) ROS level was significantly higher in Stat3 deficient calvarial osteoblasts. (C) ROS increased significantly in wild type cells when treated with AG-490, an inhibitor of Stat3. (D) ROS level did not change in Stat3 deficient cells treated with AG-490.

Our unpublished data also indicate that Stat3 regulates expression of wnt5a in osteoblasts. Both wnt3a and wnt5a have previously shown to stimulate osteoblast proliferation and differentiation [51,52]. Using the conditional Stat3 deficient mice in this study, our future study may include identification of load-driven up-stream and down-stream genes in the presence and absence of Stat3 in osteoblasts.

It has been known that accumulation of ROS is associated with osteoporosis and aging related bone loss. Recently, Stat3 has been shown to connect mitochondrial functions to ROS production in hepatocytes and cardiomyocytes [17]. In order to investigate whether Stat3 activation would regulate the ROS level and mitochondrial functions in osteoblasts, we applied fluid shear stress (FSS) on Stat3 deficient calvarial osteoblasts. First, we showed that serine phosphorylation of Stat3 increased from 30 to 90 min following FSS, suggesting the sustained Stat3 activation in response to mechanical stimulation. Especially, the conserved serine phosphorylation site on Stat3 is critical in regulation of mitochondrial activities [17]. Next, we demonstrated Stat3-driven association of the level of ROS through mitochondrial activity with the effects of mechanical loading on bone formation. The result presented a significant increase in ROS in Stat3 deficient osteoblast, and the mitochondrial function as indicated by the NAD^+/NADH ratio is reduced in Stat3 deficient osteoblasts. Furthermore, FSS reduced the level of ROS through stimulation of mitochondrial activity but it failed to do so in Stat3 deficient osteoblasts. Clinical evidence suggests that age related bone loss is closely associated with oxidative stress [22,23,25,28]. In addition, recent studies have demonstrated that oxidative stress antagonizes Wnt signaling [29,30]. It has yet to be tested whether reduction in load-driven bone formation in Stat3 KO mice is in part caused by an increase in the basal level of ROS and/or insensitivity of ROS levels in response to mechanical loading.

In the current study, both osteoblasts and osteocytes are deficient in Stat3. It has been proposed that osteocytes are mechanosensing cells in bone. Thus, there is a possibility that suppression of load-driven bone formation in this study is primarily caused by Stat3 deficiency in osteocytes. Future studies using osteocyte-specific inactivation of Stat3 might further differentiate the role of Stat3 in osteoblasts and osteocytes.

In conclusion, loss-of-function mutations of Stat3 reduce bone mass and load-driven anabolic responses, and Stat3 plays a critical role in regulation of anabolic pathways in nucleus as well as suppression of ROS in mitochondria.

Supplementary materials related to this article can be found online at doi:10.1016/j.bone.2011.04.020.

Acknowledgments

The authors thank Li Jiang for her assistance with animal care and tissue processing. This study was supported by the research funds from Purdue School of Science, Indiana University Purdue University Indianapolis (JL) and NIHR01AR052144 (HY).

References

[1] Bromberg J. Stat proteins and oncogenesis. J Clin Invest 2002;109:1139–42.

[2] Darnell Jr JE. STATs and gene regulation. Science 1997;277:1630–5.

[3] Reich NC, Liu L. Tracking STAT nuclear traffic. Nat Rev Immunol 2006;6:602–12.

[4] Stepkowski SM, Chen W, Ross JA, Nagy ZS, Kirken RA. STAT3: an important regulator of multiple cytokine functions. Transplantation 2008;85:1372–7.

[5] Zhong Z, Wen Z, Darnell Jr JE. Stat3: a STAT family member activated by tyrosine phosphorylation in response to epidermal growth factor and interleukin-6. Science 1994;264:95–8.

[6] Holland SM, DeLeo FR, Elloumi HZ, Hsu AP, Uzel G, Brodsky N, et al. STAT3 mutations in the hyper-IgE syndrome. N Engl J Med 2007;357:1608–19.

[7] Minegishi Y, Saito M, Tsuchiya S, Tsuge I, Takada H, Hara T, et al. Dominant-negative mutations in the DNA-binding domain of STAT3 cause hyper-IgE syndrome. Nature 2007;448:1058–62.

[8] Grimbacher B, Puck JM, Holland SM. Hyper-IgE recurrent infections syndrome. In: Ochs HD, Smith CIE, Puck JM, editors. Primary immunodeficiency diseases: a molecular & cellular approach. 2nd ed. New York City, New York: Oxford University Press, Inc.; 2007. p. 496–504.

[9] Jing N, Tweardy DJ. Targeting Stat3 in cancer therapy. Anticancer Drugs 2005;16: 601–7.

[10] Heinrich PC, Behrmann I, Muller-Newen G, Schaper F, Graeve L. Interleukin-6-type cytokine signalling through the gp130/Jak/STAT pathway. Biochem J 1998;334(Pt 2): 297–314.

[11] Senaldi G, Varnum BC, Sarmiento U, Starnes C, Lile J, Scully S, et al. Novel neurotrophin-1/B cell-stimulating factor-3: a cytokine of the IL-6 family. Proc Natl Acad Sci U S A 1999;96:11458–63.

[12] Heinrich PC, Behrmann I, Haan S, Hermanns HM, Muller-Newen G, Schaper F. Principles of interleukin (IL)-6-type cytokine signalling and its regulation. Biochem J 2003;374:1–20.

[13] Kishimoto T, Akira S, Narazaki M, Taga T. Interleukin-6 family of cytokines and gp130. Blood 1995;86:1243–54.

[14] Hirano T, Ishihara K, Hibi M. Roles of STAT3 in mediating the cell growth, differentiation and survival signals relayed through the IL-6 family of cytokine receptors. Oncogene 2000;19:2548–56.

[15] Ishihara K, Hirano T. Molecular basis of the cell specificity of cytokine action. Biochim Biophys Acta 2002;1592:281–96.

[16] Takeda K, Noguchi K, Shi W, Tanaka T, Matsumoto M, Yoshida N, et al. Targeted disruption of the mouse Stat3 gene leads to early embryonic lethality. Proc Natl Acad Sci U S A 1997;94:3801–4.

[17] Wegrzyn J, Potla R, Chwae YJ, Sepuri NB, Zhang Q, Koeck T, et al. Function of mitochondrial Stat3 in cellular respiration. Science 2009;323:793–7.

[18] Lufei C, Ma J, Huang G, Zhang T, Novotny-Diermayr V, Ong CT, et al. GRIM-19, a death-regulatory gene product, suppresses Stat3 activity via functional interaction. EMBO J 2003;22:1325–35.

[19] Hajnoczky G, Hoek JB. Cell signaling. Mitochondrial longevity pathways. Science 2007;315:607–9.

[20] Myers Jr MG. Cell biology. Moonlighting in mitochondria. Science 2009;323: 723–4.

[21] Reich NC. STAT3 revs up the powerhouse. Sci Signal 2009;2:pe61.

[22] Bai XC, Lu D, Bai J, Zheng H, Ke ZY, Li XM, et al. Oxidative stress inhibits osteoblastic differentiation of bone cells by ERK and NF-kappaB. Biochem Biophys Res Commun 2004;314:197–207.

[23] Basu S, Michaelsson K, Olofsson H, Johansson S, Melhus H. Association between oxidative stress and bone mineral density. Biochem Biophys Res Commun 2001;288:275–9.

[24] Cadenas E, Davies KJ. Mitochondrial free radical generation, oxidative stress, and aging. Free Radic Biol Med 2000;29:222–30.

[25] Kasper G, Mao L, Geissler S, Draycheva A, Trippens J, Kuhnisch J, et al. Insights into mesenchymal stem cell aging: involvement of antioxidant defense and actin cytoskeleton. Stem Cells 2009;27:1288–97.

[26] Papiha SS, Rathod H, Briceno I, Pooley J, Datta HK. Age related somatic mitochondrial DNA deletions in bone. J Clin Pathol 1998;51:117–20.

[27] Valko M, Leibfritz D, Moncol J, Cronin MT, Mazur M, Telser J. Free radicals and antioxidants in normal physiological functions and human disease. Int J Biochem Cell Biol 2007;39:44–84.

[28] Varanasi SS, Francis RM, Berger CE, Papiha SS, Datta HK. Mitochondrial DNA deletion associated oxidative stress and severe male osteoporosis. Osteoporos Int 1999;10:143–9.

[29] Almeida M, Ambrogini E, Han L, Manolagas SC, Jilka RL. Increased lipid oxidation causes oxidative stress, increased PPAR{gamma} expression and diminished pro-osteogenic Wnt signaling in the skeleton. J Biol Chem 2009;284:27438–48.

[30] Almeida M, Han L, Martin-Millan M, O'Brien CA, Manolagas SC. Oxidative stress antagonizes Wnt signaling in osteoblast precursors by diverting beta-catenin from T cell factor- to forkhead box O-mediated transcription. J Biol Chem 2007;282: 27298–305.

[31] Mantila Roosa SM, Liu Y, Turner CH. Gene expression patterns in bone following mechanical loading. J Bone Miner Res 2011;26:100–12.

[32] Robinson JA, Chatterjee-Kishore M, Yaworsky PJ, Cullen DM, Zhao W, Li C, et al. Wnt/beta-catenin signaling is a normal physiological response to mechanical loading in bone. J Biol Chem 2006;281:31720–8.

[33] Welte T, Zhang SS, Wang T, Zhang Z, Hesslein DG, Yin Z, et al. STAT3 deletion during hematopoiesis causes Crohn's disease-like pathogenesis and lethality: a critical role of STAT3 in innate immunity. Proc Natl Acad Sci U S A 2003;100: 1879–84.

[34] Liu F, Woitge HW, Braut A, Kronenberg MS, Lichtler AC, Mina M, et al. Expression and activity of osteoblast-targeted Cre recombinase transgenes in murine skeletal tissues. Int J Dev Biol 2004;48:645–53.

[35] Li J, Liu D, Ke HZ, Duncan RL, Turner CH. The P2X7 nucleotide receptor mediates skeletal mechanotransduction. J Biol Chem 2005;280:42952–9.

[36] Mosley JR, March BM, Lynch J, Lanyon LE. Strain magnitude related changes in whole bone architecture in growing rats. Bone 1997;20:191–8.

[37] Robling AG, Turner CH. Mechanotransduction in bone: genetic effects on mechanosensitivity in mice. Bone 2002;31:562–9.

[38] Tozum TF, Oppenlander ME, Koh-Paige AJ, Robins DM, McCauley LK. Effects of sex steroid receptor specificity in the regulation of skeletal metabolism. Calcif Tissue Int 2004;75:60–70.

[39] Plotkin LI, Lezcano V, Thostenson J, Weinstein RS, Manolagas SC, Bellido T. Connexin 43 is required for the anti-apoptotic effect of bisphosphonates on osteocytes and osteoblasts in vivo. J Bone Miner Res 2008;23:1712–21.

[40] Jacobs CR, Yellowley CE, Davis BR, Zhou Z, Cimbala JM, Donahue HJ. Differential effect of steady versus oscillating flow on bone cells. J Biomech 1998;31:969–76.

[41] Sundaresan M, Yu ZX, Ferrans VJ, Sulciner DJ, Gutkind JS, Irani K, et al. Regulation of reactive-oxygen-species generation in fibroblasts by Rac1. Biochem J 1996;318 (Pt 2):379–82.

[42] Burdelya L, Catlett-Falcone R, Levitzki A, Cheng F, Mora LB, Sotomayor E, et al. Combination therapy with AG-490 and interleukin 12 achieves greater antitumor effects than either agent alone. Mol Cancer Ther 2002;1:893–9.

[43] Itoh S, Udagawa N, Takahashi N, Yoshitake F, Narita H, Ebisu S, et al. A critical role for interleukin-6 family-mediated Stat3 activation in osteoblast differentiation and bone formation. Bone 2006;39:505–12.

[44] Yoshida K, Taga T, Saito M, Suematsu S, Kumanogoh A, Tanaka T, et al. Targeted disruption of gp130, a common signal transducer for the interleukin 6 family of cytokines, leads to myocardial and hematological disorders. Proc Natl Acad Sci U S A 1996;93:407–11.

[45] Kawasaki K, Gao YH, Yokose S, Kaji Y, Nakamura T, Suda T, et al. Osteoclasts are present in gp130-deficient mice. Endocrinology 1997;138:4959–65.

[46] Shin HI, Divieti P, Sims NA, Kobayashi T, Miao D, Karaplis AC, et al. Gp130-mediated signaling is necessary for normal osteoblastic function in vivo and in vitro. Endocrinology 2004;145:1376–85.

[47] Bellido T, Stahl N, Farruggella TJ, Borba V, Yancopoulos GD, Manolagas SC. Detection of receptors for interleukin-6, interleukin-11, leukemia inhibitory factor, oncostatin M, and ciliary neurotrophic factor in bone marrow stromal/osteoblastic cells. J Clin Invest 1996;97:431–7.

[48] Sanchez C, Gabay O, Salvat C, Henrotin YE, Berenbaum F. Mechanical loading highly increases IL-6 production and decreases OPG expression by osteoblasts. Osteoarthritis Cartilage 2009;17:473–81.

[49] Kido S, Kuriwaka-Kido R, Imamura T, Ito Y, Inoue D, Matsumoto T. Mechanical stress induces Interleukin-11 expression to stimulate osteoblast differentiation. Bone 2009;45:1125–32.

[50] Li X, Placencio V, Iturregui JM, Uwamariya C, Sharif-Afshar AR, Koyama T, et al. Prostate tumor progression is mediated by a paracrine TGF-beta/Wnt3a signaling axis. Oncogene 2008;27:7118–30.

[51] Zhou H, Mak W, Zheng Y, Dunstan CR, Seibel MJ. Osteoblasts directly control lineage commitment of mesenchymal progenitor cells through Wnt signaling. J Biol Chem 2008;283:1936–45.

[52] Katoh M. Transcriptional mechanisms of WNT5A based on NF-kappaB, Hedgehog, TGFbeta, and Notch signaling cascades. Int J Mol Med 2009;23:763–9.